EXPERIMENTAL AND THEORETICAL INVESTIGATIONS OF ANION-PI INTERACTIONS IN METALLACYCLIC ARCHITECTURES OF FIRST-ROW TRANSITION METALS WITH N-HETEROAROMATIC LIGANDS

A Dissertation

by

IAN DEREK GILES

Submitted to the Office of Graduate Studies of
Texas A&M University
in partial fulfillment of the requirements for the degree of

DOCTOR OF PHILOSOPHY

May 2012

Major Subject: Chemistry

Experimental and Theoretical Investigations of Anion-pi Interactions in Metallacyclic Architectures of First-Row Transition Metals and N-Heteroaromatic Ligands

EXPERIMENTAL AND THEORETICAL INVESTIGATIONS OF ANION-PI INTERACTIONS IN METALLACYCLIC ARCHITECTURES OF FIRST-ROW TRANSITION METALS WITH N-HETEROAROMATIC LIGANDS

A Dissertation

by

IAN DEREK GILES

Submitted to the Office of Graduate Studies of
Texas A&M University
in partial fulfillment of the requirements for the degree of

DOCTOR OF PHILOSOPHY

Approved by:

Chair of Committee,	Kim R. Dunbar
Committee Members,	François P. Gabbaï
	Timothy R. Hughbanks
	Winfried Teizer
Head of Department,	David H. Russell

May 2012

Major Subject: Chemistry

ABSTRACT

Experimental and Theoretical Investigations of Anion-pi Interactions in Metallacyclic Architectures of First-Row Transition Metals with N-Heteroaromatic Ligands.

(May 2012)

Ian Derek Giles, B.A., Austin College

Chair of Advisory Committee: Dr. Kim R. Dunbar

Research into anion-π interactions has shifted from attempts to establish the legitimacy of the interaction to the incorporation of anion-π interactions into supramolecular architectures. The research discussed in this dissertation explores the subtle effects of ligand, anion, and metal ion on supramolecular architectures of tetrazine-based ligands in the context of anion-π interactions and their importance in the design and synthesis of supramolecular architectures.

Computational studies highlight the importance of the arene quadrupole moment, molecular polarizability, and substituent effects on the strength of anion-π interactions. More importantly, however, this work establishes that there is a distinct directionality inherent to the anion-π interaction between polyatomic anions and N-heterocycles, which can be used to direct ligands in supramolecular architectures as demonstrated through the work of the Dunbar group in recent years, particularly that of the square and pentagonal metallacycles.

The extension of metallacycles of bptz to Co^{II} and Fe^{II} demonstrates the ability to tune the size of the metallacyclic cavity by simply changing the metal ion and results in the surprising encapsulation of two $[SbF_6]^-$ anions in $[Fe_5(bptz)_5(NCCH_3)_{10}][SbF_6]_{10}$. ^1H NMR spectroscopy and electrochemical studies reveal slight but significant differences characteristic of the square and pentagonal metallacycles and support the presence of anion-π interactions in solution and highlight the importance of the encapsulated anion in the templation and stability of the metallacycles. A study of the interconversion between the square and pentagonal metallacycles *via* ^1H NMR is presented for the first time.

Increasing the π-acidity of the chelating ligand from bptz to bmtz results in the encapsulation of only one $[SbF_6]^-$ anion in $[Fe_5(bmtz)_5(NCCH_3)_{10}][SbF_6]_{10,}$ maximizing anion-π interactions with the ligand despite the tighter fit. A significant hurdle in the incorporation of different anions into the metallacyclic structures was overcome with the development of a new synthetic protocol for $[Fe(NCCH_3)_6]^{2+}$ salts of a wide range of anions from sodium salts and $Fe_4Cl_8(THF)_6$. Also, the nuclearity of the less stable $[Fe_5(bptz)_5(NCCH_3)_{10}][PF_6]_{10}$ metallacycle was established *via* a combination of MS, electrochemistry and ^1H NMR experiments through comparisons with known Fe^{II} metallacycle solution behavior.

DEDICATION

To my parents, Carol and Richard, for their never-ending support and love, for always pushing me to do my best, and for teaching me the value of thinking ahead…thank you will never be enough for all you have done for me.

To my wife, Christina, who, despite the late nights and my sometimes prickly demeanor, is always there to offer a hug, words of encouragement or even a gentle nudge back to work…I love you more than you could ever know.

To my Auntie Patti, who taught me to see the lighter side of life and was always so proud of everything I did…though you are not here in person, I know you have been with me in spirit as I've grown into the person I am today. You are missed so very much.

ACKNOWLEDGEMENTS

The old adage that ‘it takes a village to raise a child’ is certainly applicable to the long and arduous path towards attaining a graduate degree. I would like to thank my research advisor Prof. Kim R. Dunbar for her guidance and support over the years I have spent as a part of her research group. Her genuine joy for chemistry and care for her students is an inspiration to aspiring researchers. Thanks to my committee members Profs. Timothy Hughbanks, François Gabbaï, and Winfried Teizer, whose suggestions and insight have been valuable to the successful completion of my dissertation research. Thanks also to Dr. Steven E. Wheeler and Dr. Lisa M. Pérez for their helpful discussion and guidance with computational work.

I would like to extend my gratitude to Dr. Jane Johnson-Carr who mentored me at the beginning of my undergraduate career. I will never forget my shock when she told me she couldn’t wait for me to get my first ‘B’ in a class, nor will I ever forget the moment it dawned on me how right she was to say so. It helped to temper my perfectionism and allow myself to make mistakes, so long as I learned from them. She also guided me through the early part of my career, especially in encouraging me to seek out NSF-REU programs for extra research experience. Had it not been for those experiences, I would not be where I am today. I would like to thank my undergraduate research advisor and mentor Dr. Andrew Carr who took a chance on a wet-behind-the-ears college sophomore and offered me a position in his research group and also advised me during my time at Austin College. His support and guidance (especially with respect

to the research involved in my honors project) have made a significant impact on me, especially the joy he has for teaching at any level.

I would not be a chemist today if it were not for the influence of my high school chemistry teacher Scott Greenwood, who enthusiasm for the subject was nothing short of contagious. I can still remember the lab experiment in which we recycled aluminum cans and grew large crystals of alum over winter break. In fact, it was his suggestion to apply to my undergraduate institution that set me on the path I am on today. For his inspirational teaching and guidance I will be always grateful.

I must thank my fellow Dunbar group members, both past and present, for their help and camaraderie during my tenure in the group: Dr. Brandi Schottel, for passing to me a wonderful research project and her guidance in the early part of my graduate career; Dr. Eric Reinheimer, for his good-natured ribbing and friendship; Drs. Michael Shatruk, Dafhne Aguirre, Alfredo Angeles, Matthew Hilfiger, Carolina Avendaño, and Ferdi Karadaş for their friendship and help with many aspects of my research; Ed and Dr. Kristen Funck for their friendship and letting me be their 'third wheel' without ever making me feel like it; Dr. Helen Chifotides for being a wonderful friend and a tremendous help with my research; Heather Southerland, for being there to talk about life and its many ups and downs; and last, but certainly not least, Dr. Hanhua Zhao, Dr. Andrey Prosvirin, Sarah Lane, Zhongyue Zhang, Codi Sanders, Andrew Brown, Zhanyong Li, Bruno Peña, Amanda David, Maryfer Ballesteros, Toby Woods, Xuan Zhang, Jill Frank, Mayela Canales, and Charlene Campbell for making my time in the group an enjoyable one.

On a personal note, I must of course thank my parents, Carol and Richard Seril, for their never-ending support and love throughout my life. You have taught me so much about how to live and be a good person. You have also allowed me the freedom to chart my own course while being ready to help when it was truly needed. I love you both and can never, ever repay you for all that you have given me, though I know you would never expect it from me. I am glad that I have grown into a man that you can be proud of and I will endeavor to continue to be someone you can take pride in. Thank you from the bottom of my heart.

I must also thank my wonderful wife Christina for all of her patience and love throughout my college and graduate career. I know the sacrifices you have made to be with me now and I hope you know how much it means to me that you were willing to do so. I cannot wait until we both can distinguish ourselves in our respective careers and, more importantly, do so together. I love you so very much, and I look forward to our long and happy lives together. It's so wonderful having a spouse I can make laugh and who makes my life so much more enjoyable and who is proud of me no matter what I do.

My extended family has been a wonderful support for me over the years and has given me so many wonderful experiences. I would like to thank my grandparents Pat and Tony Albano, with whom I have spent so many wonderful moments with. My grandmother Pat and I have had some wonderful trips together, and I am so very blessed that I had the opportunity to get such a deep appreciation for other cultures and open my mind at such a young age and with such wonderful company. My Uncle Robert (Bob)

McBroom has been so thoughtful and generous throughout my graduate career, buying not only one but two laptops for me without reservation, both of which have been a tremendous aid to my studies. My Aunt Gayle and her family have been so supportive and have cheered me on as I've progressed through my academic studies, and her determination and work ethic are an inspiration to all. Thank you all from the bottom of my heart.

One cannot make it through life without a cadre of great friends who are available and ready to join you in a celebration or just some good-natured stress relief. Thank you to Brandon Baer, Kent and Sarah Gillenwater, Jason Thode, Megan Parker, Robert and Olive Romig, Drew Mondry and Clint and Monica Watson for being those friends. We've had many good times together and I look forward to the times yet to come.

NOMENCLATURE

ADF	Amsterdam density functional theory
Å	Ångstrom
aq	aqueous
a.u.	atomic units
$\alpha_{\|\|}$	Molecular polarizability parallel to principle molecular axis
B	Buckingham
B3	Becke's three-parameter electron exchange functional
$[^{n}Bu_4N]^{+}$	tetrabutylammonium
bppn	3,6-bis(2′-pyridyl)pyridazine
bppz	2,5-bis(2′-pyridyl)pyrazine
bptz	3,6-bis(2′-pyridyl)-1,2,4,5-tetrazine
bmtz	3,6-bis(2′-pyrimidyl)-1,2,4,5-tetrazine
CSD	Cambridge Structural Database
CCDC	Cambridge Crystallographic Data Centre
CCD	Charge-coupled Device
CV	Cyclic Voltammetry
^{o}C	degrees Celsius
C	Coulomb
CIF	Crystallographic Information File
cm^{-1}	wavenumbers
δ	chemical shift

DNA	Deoxyribonucleic Acid
^{o}	degree
DFT	Density Functional Theory
DPV	Differential Pulse Voltammetry
d	distance between anion and arene atoms
ε	extinction coefficient
$E_{1/2}$	Half-potential
$E_{binding}$	Binding energy
EtOH	Ethanol
ECP	Electron Core Potential
ESI	Electrospray Ionization
ESP	Electrostatic Potential
emu	electromagnetic unit
FT	Fourier Transform
g	gram
HAT	hexaazatriphenylene
I	Nuclear spin
IR	Infrared
ICR	Ion Cyclotron Resonance
K	Kelvin
K_a	Association constant
kcal	kilocalorie

kJ	kilojoule
λ_{max}	wavelength of maximum absorbance
LYP	Lee, Yang and Parr's electron correlation functional
L	Liter
LMCT	Ligand-to-Metal Charge Transfer
LUMO	Lowest Unoccupied Molecular Orbital
MO	Molecular Orbital
MPMS	Magnetic Properties Measurement System
m/z	mass to charge ratio
MS	Mass Spectrometry
m	meter
MHz	Megahertz
mg	milligram
mL	milliliter
mmol	millimole
mol	mole
mM	millimolar
M	Molar (L mol^{-1})
MP2	Møller-Plesset 2^{nd} order perturbation theory
ν	vibrational mode
nm	nanometer
NDI	Naphthalenediimide

NMR	Nuclear Magnetic Resonance
ppm	parts per million
PDI	Perylenediimide
Q_{zz}	Quadrupolar moment
Σ_{vdW}	Sum of the van der Waals radii
s	second
S	Electronic spin
SCF	Self-consistent field
SQUID	Superconducting Quantum Interference Device
THF	Tetrahydrofuran
TOF	Time-of-Flight
V	Volt
XRD	X-ray Diffraction

TABLE OF CONTENTS

CHAPTER Page

CHAPTER Page

CHAPTER Page

CHAPTER Page

LIST OF FIGURES

Page

Page

Page

Page

Page

Page

Page

Page

Page

Page

Page

Page

Page

Page

Page

Page

Page

LIST OF TABLES

Page

Page

CHAPTER I

INTRODUCTION TO SUPRAMOLECULAR CHEMISTRY WITH A FOCUS ON ANION-Π INTERACTIONS AND TEMPLATION

Non-covalent intermolecular forces are present in any chemical system and govern the interactions between discrete molecules, directly affecting the packing of the molecules in the solid-state crystal structure and their propensity to dissolve in various solvents. These forces can also dictate the structural characteristics of the molecule itself, best illustrated by biological systems, in higher-order protein folding and the DNA double-helix for which hydrogen bonding between amino acids and base pairs, respectively, plays a key role. Intermolecular interactions form the basis of supramolecular chemistry, which is elegantly described by Jean-Marie Lehn as "chemistry beyond the molecule."[1]

While macromolecules such as proteins and DNA are the most-often cited examples of the importance of intermolecular forces, there are numerous arenas in which these forces play a role in the physical properties exhibited by the molecules as well as the structures. The importance of supramolecular interactions in fields such as magnetochemistry and conductivity has recently become apparent. The current focus on functional devices makes it necessary to take into account the intermolecular interactions between the various active components composing the device to ensure proper operation and reduce spurious responses to unwanted stimuli. Furthermore, these interactions are

---

This dissertation follows the style of the *Journal of the American Chemical Society*.

often key to catalytic activity; the coordination of a specific substrate to the catalyst and the subsequent structural and chemical changes that lead to the ultimate transformation and release of the target molecule. The balance of these intermolecular forces is key to the function; if one designs a catalyst that binds the substrate too strongly (perhaps one extra hydrogen bond), the catalyst fails to turn over, too weak and the substrate fails to bind at all. Understanding the forces at play in these, and many other, molecular systems is critical to the design, analysis, and fine-tuning of the desired (and sometimes undesired) molecular properties.

A. Supramolecular Chemistry

i. Defining supramolecular chemistry

a. A brief history

Ever since the discovery by Pedersen and coworkers in 1967 of crown ethers and their ability to complex various alkali metal cations, the study of supramolecular chemistry has witnessed a steady rise in activity as more chemical systems have been shown to exhibit the intermolecular interactions that are the hallmark of the field. It is becoming increasingly evident that supramolecular interactions are an essential consideration when assessing the properties of systems ranging from materials exhibiting magneto-, electro-, or photochemical phenomena to complex biological systems and their model complexes. The idea of molecular association into higher-order structures, a key feature of supramolecular chemistry, hearkens back further to the late 19th century lock-and-key steric description of receptors binding substrates advanced by Emil Fischer and the "übermoleküles" (supermolecules) of the early 20th century, a term

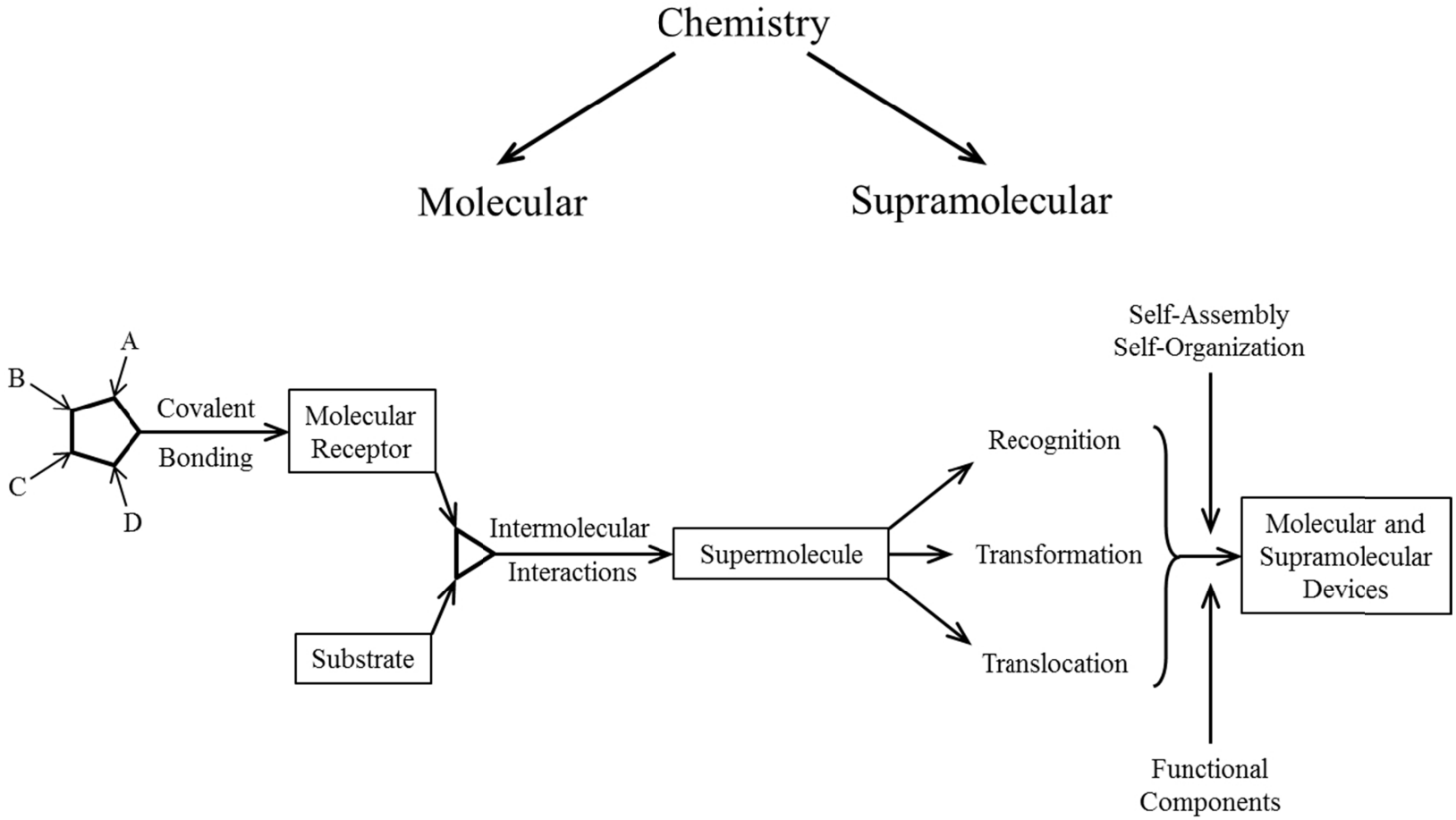

Figure 1. Diagrammatic representation of the relationship between molecular and supramolecular chemistry. Adapted from Lehn.[1]

used to describe higher-order systems comprising coordinatively saturated species. In fact, even Alfred Werner's discovery of the coordination bond can be considered as an important contribution to supramolecular chemistry involving metal ions, as the coordination bond is a key feature in many of these complexes. Understanding the activity and reactivity of biological systems was a significant driving force in the early part of the field, and continues to be to this day.[1,2]

b. Principles of supramolecular chemistry

Supramolecular chemistry is often compared to molecular chemistry and shares many of the same features. In molecular chemistry, small building units (atoms) combine *via* linkages (covalent bonds) to form larger, more complex structures (molecules). In much the same way, supramolecular chemistry stitches together molecules (the small building unit) *via* non-covalent intermolecular interactions (the linkages) to form the larger, more complex supermolecule (Figure 1). The relationship between molecular and supramolecular chemistry is similar to that between the word and sentence in language: letters are combined to form words (molecular) which are subsequently organized into sentences (supramolecular). These supermolecules often have further functionality in terms of molecular recognition (cation/anion sensing/signaling), transformation (catalysis) and translocation (membrane transport). Supermolecules can also be further arranged into organized assemblies combining the functionalities of multiple types of supramolecular species into a supramolecular device (*e.g.* a membrane studded with channel proteins for specific ion translocation), much like sentences are further organized into paragraphs.[1,2]

ii. Interactions governing supramolecular ensembles

As supramolecular chemistry depends upon the non-covalent interactions that hold these higher-order structures together, it is important to briefly discuss them. These interactions include, roughly in order of decreasing strength, ion-ion, ion-dipole (including coordination bonds), cation-π, anion-π interactions, hydrogen bonding, dipole-dipole, dipole-induced dipole (Debye), induced dipole-induced dipole (London dispersion) forces, and hydrophobic effects. Table 1 provides a comparison of approximate energy ranges of these interactions.[2]

a. Ion-ion interactions

By far the strongest of these are ion-ion interactions, electrostatic interactions between a cationic and an anionic species. In its simplest form, the ions are monoatomic and an inorganic salt is formed, such as NaCl. Salts of polyatomic ions, or mixed monoatomic/polyatomic ion salts also fall into this category. As the ions become more complex, the strength of the electrostatic interaction decreases as the charge is either protected by steric bulk or delocalized over a larger volume. This principle is capitalized upon in the growing field of ionic liquids, whose properties rely on the complexity of the component ions to lower the melting points of the resulting salts closer to room temperature.

b. Hydrogen bonding interactions

Hydrogen bonds, an interaction between a hydrogen atom typically bound to an electronegative atom such as oxygen or nitrogen and a Lewis-basic site on another molecule (typically oxygen or nitrogen as well), are fairly strong interactions, however,

Table 1. Representative energy ranges for various supramolecular interactions. Ranges are taken from Steed and Atwood,[2] except for the anion-π range, which is taken from Gamez *et al.*[3]

Interaction	Energy Range, kJ mol^{-1}
Ion-Ion	100 – 350
Ion-dipole	20 – 200
Dipole-dipole	5 – 50
Hydrogen Bonding	4 – 120
Cation-π interactions	5 – 80
Anion-π interactions	20 – 70
π-π stacking	0 – 50
Van der Waals forces	< 5

their strength depends on the electropositive nature of the hydrogen atom and the electronegativity of the donor site on the other molecule(s) between which the interactions occur. In fact, there are systems in which the donor is sufficiently Lewis basic to engage in hydrogen bonds with a H atom bound to a carbon atom, known as a C-H hydrogen bond. Hydrogen bonds are typically classified into three categories, based on the degree of covalency exhibited and, by extension, the strength of the interaction (the more covalent, the stronger). Strong (primarily covalent) hydrogen bonds are in the range of 60-120 kJ mol^{-1}, an example being complexes with HF or proton sponges. Moderate hydrogen bonds, such as those exhibited by alcohols and biological molecules, are in the range of 16-60 kJ mol^{-1} and are mostly electrostatic in nature. Weak hydrogen bonds (such as C-H and O-H···π hydrogen bonds) are typically < 12 kJ mol^{-1} and are considered to be purely electrostatic interactions (Figure 2a). Due to the directional nature of these interactions, they are excellent candidates for use in the design of supramolecular assemblies.[2]

c. π-π interactions

Interactions between aromatic species, or π-π interactions, involve a displaced parallel, T-shaped or stacked arrangement of aromatic moieties (Figure 2b-d). The displaced parallel arrangement (Figure 2b) minimizes quadrupolar repulsion while maximizing dispersion interactions, while the T-shaped arrangement (Figure 2c) maximizes quadrupolar attraction to compensate for diminished dispersion interactions at the longer intermolecular distance. A stacked arrangement (Figure 2d) increases the quadrupolar repulsion and thus is less stable as compared to the displaced parallel

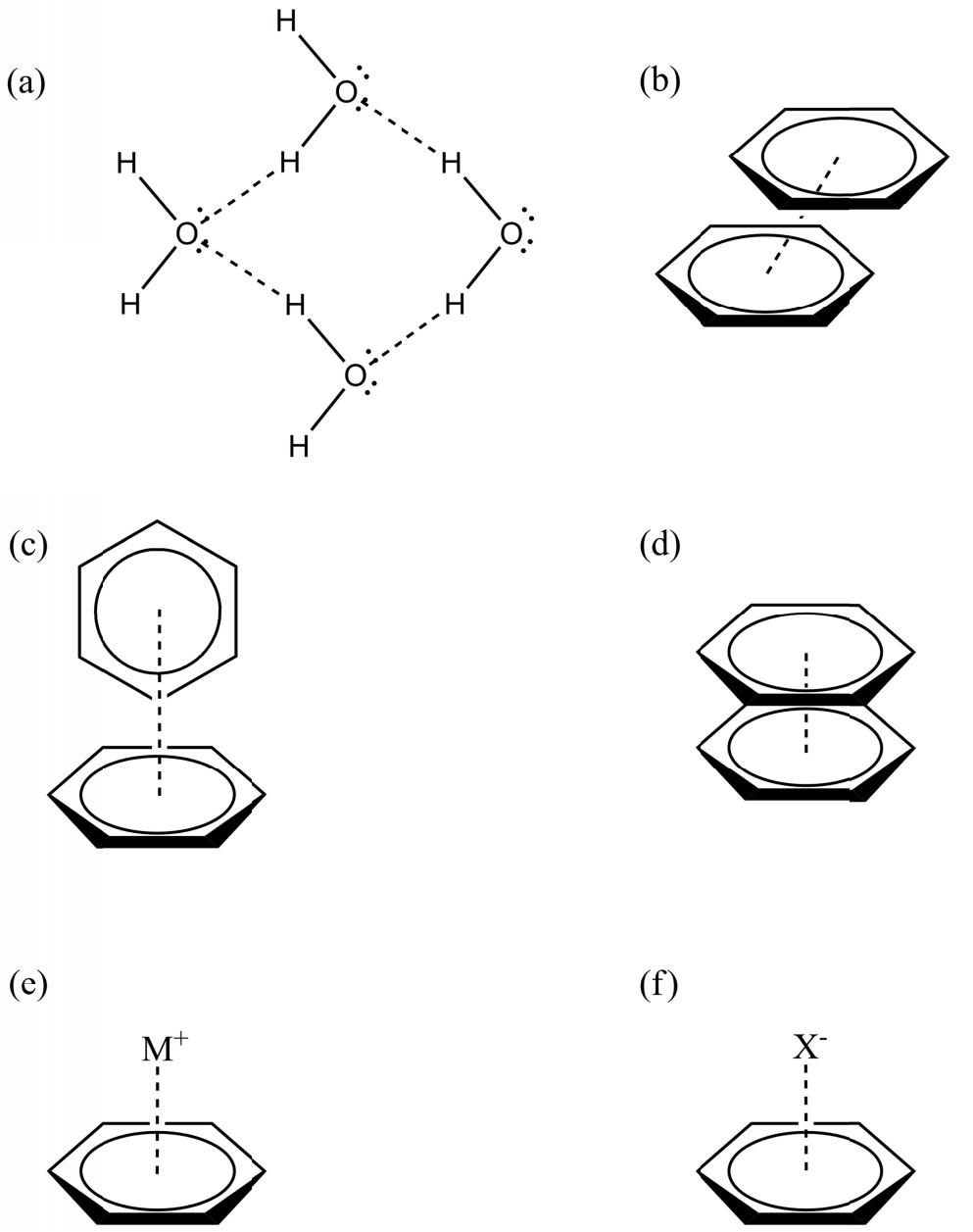

Figure 2. Scheme of (a) hydrogen bonding, (b) displaced parallel π-π, (c) T-shaped π-π, (d) stacked π-π, (e) cation-π, and (f) anion-π interactions.

arrangement, although if two aromatic rings of differing quadrupolarities are involved, this could actually become attractive. The T-shaped π-π interaction is found in the crystal structure of benzene, whereas face-to-face (typically displaced) interactions are observed in many systems involving intercalation and other parallel-type arrangement of aromatic moieties.[2]

d. Ion-dipole interactions

Ion-dipole interactions arise from the interaction of charged ions and polar neutral molecules. These interactions are quite strong (*ca*. 50-200 kJ mol^{-1}), as in the coordination of cations such as $[Na]^+$ with H_2O in aqueous solution or, in an example more pertinent to this discussion, the interaction of a crown ether (typically 18-crown-6) with $[Na]^+$ or $[K]^+$. It is one of the primary interactions responsible for the solubility of salts in highly polar media such as water. The coordination bond is typically considered to be an ion-dipole interaction, but can border on true covalency (as in the case of $[Ru(bpy)_3]^{3+}$) and as such, this classification becomes a point of contention. Nevertheless, coordination bonds, as mentioned earlier, are an important aspect of supramolecular assembly when transition metal ions are involved, and are certainly indicative of the fine, and often blurred, line between supramolecular and molecular species.[2]

e. Cation-π interactions

Cation-π interactions (Figure 2e) are characterized by a close (within the sum of the van der Waals radii) contact between a cation and the π-face of the olefinic/aromatic molecule. Although these contacts are often considered to be a purely electrostatic effect

(especially considering that it makes logical sense that the electrons in the π orbitals would be attractive to a positive charge), it is more complicated, with significant contributions related to the polarizability of the olefinic/aromatic group and other contributions from donor/acceptor, charge transfer and dispersion effects as well. The electrostatic contribution, however, is an excellent predictor of the strength of cation binding, as the other energetic components contribute only small changes to the energy across a range of aromatic molecules. A purely electrostatic (ion-quadrupole) model of the cation-π interaction does not, however, adequately model the short contact distances (as the energy of ion-quadrupole interactions scale with distance as $1/r^3$, while cation-π interactions scale as $1/r^n$, with n>2 in most cases). The strength of this interaction varies, but can, in fact, rival that of ion-dipole interactions. Surprisingly, the $[Na]^+\cdots H_2O$ interaction (75 kJ mol^{-1}) is weaker than the $[Na]^+\cdots C_6H_6$ (80 kJ mol^{-1}) interaction by ~5 kJ mol^{-1}. The directionality of these interactions along with their relative strength make them good candidates for the design of supermolecules.[4] A later discussion regarding the complementary anion-π interaction (Figure 2f) will explore the research in this newly recognized field.

f. Dipole-dipole interactions

Dipole-dipole attractions, such as those found in HCl (g) and SO_2 (g), are similar in concept to ion-ion interactions in that they are primarily electrostatic, but they are much weaker. Unlike ion-ion interactions, dipole-dipole interactions involve neutral molecules that have atoms with partial charges due to differences in electronegativity, which creates a permanent dipole and a slight attraction to neighboring molecules. This

attraction aids in the condensation of gaseous polar molecules, but at fairly low temperatures (-10^{o}C for SO_2), a fact that illustrates the weak nature of this interaction. The crystal structure at -135$\pm$5^{o}C shows the alignment of the SO_2 molecules along their dipoles.[5] The interactions are directional (as demonstrated by the SO_2 crystal structure), so they can be incorporated into the design of a supramolecular complex with predictable results.

g. Debye and London dispersion forces

Molecules that are highly polarizable undergo interactions with other molecules that either have a permanent dipole (dipole-induced dipole, or Debye, forces) or other highly polarizable molecules (induced dipole-induced dipole, or London dispersion, forces). These interactions, which fall under the category of van der Waals interactions, are extremely weak and, as they are generally non-directional, are difficult to use as a design element in supramolecular chemistry. They are, nevertheless, important to take into consideration as they often result in the inclusion of molecules (often solvent) into cavities of molecules or voids created by the crystal packing of molecules. Van der Waals forces are, as described by A. I. Kitaigorodsky,[6] maximized in the solid state, leading to so-called crystal packing forces that reduce the void space in the crystal structure (and in turn, lend credence to the idea that 'Nature abhors a vacuum').[2]

h. Additional remarks

Collectively, these interactions comprise the 'bonding' component of supramolecular chemistry. It is these interactions that form the larger-scale assemblies from molecular units as well as affording the wide range of functionality that these

assemblies can exhibit. The wide range of strengths of the interactions also allow for tuning of the species to allow for greater selectivity or for structural annealing in solution, often leading to single products in supramolecular, one-pot self-assembly reactions.

iii. Selected examples of supramolecular ensembles

The literature is replete with examples of supramolecular assemblies, too numerous for a thorough review here; a brief highlight of some interesting examples, however, is certainly in order. There are many examples of systems that use one primary interaction to achieve their goal, but most are a combination of several design elements, especially those that are device assemblies. A wide range of functionality, from sensing, sequestration and membrane transport to catalysis and models of biological phenomena, are achievable with supramolecular complexes.

a. Bis-corannulene 'buckycatcher'

An interesting example of a supramolecular ensemble with π-π interactions is the so-called 'buckycatcher' of Sygula *et al.* This bis-corannulene molecular clip (Figure 3) accommodates a full C_{60} molecule when in the concave-concave conformation, with close contacts between the corannulene groups and C_{60} as short as 3.128 Å in the solid state. This interaction also occurs in solution, as evidenced by systematic downfield shifts of the corannulene proton resonances, with a binding constant $K_a = 8600 \pm 500\ M^{-1}$. Free corannulene does not exhibit similar binding behavior in solution according to NMR studies, a fact that suggests that the individual π-π interactions of corannulene with C_{60} are too weak to overcome solvation in toluene of each species without linking two

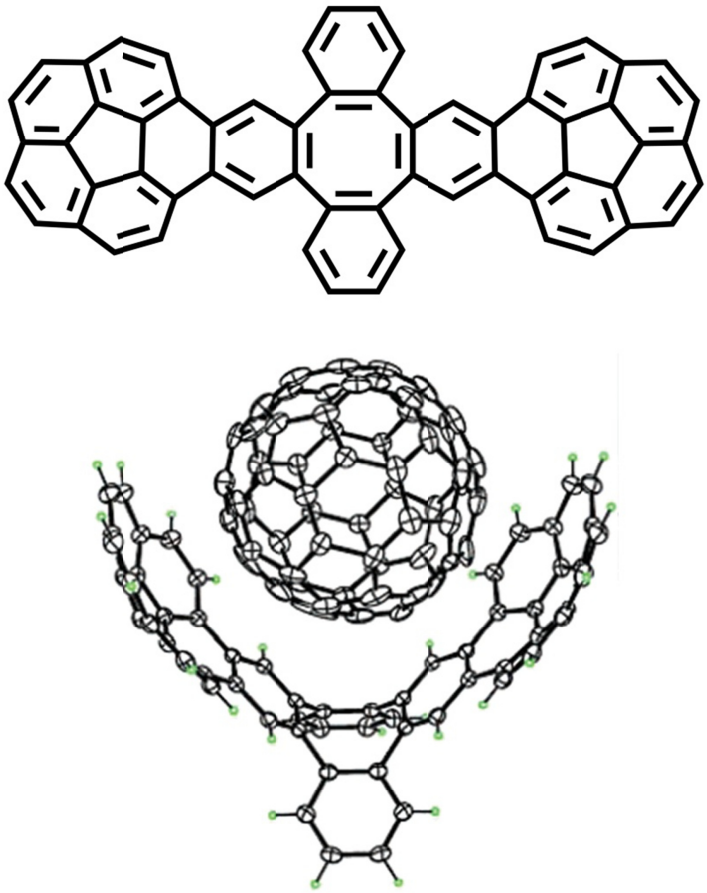

Figure 3. Bis-corannulene molecular clip scheme (top) and a thermal ellipsoid plot of C_{60} encapsulated by the molecular clip. Figure adapted from Sygula *et al.*[7]

corannulene units together in a conformation that allows for cooperative interactions.[7]

b. Effect of supramolecular interactions on chemomechanical polymers

Schneider and Strongin have described the nature of various supramolecular interactions and their effects on chemomechanical polymers which expand and contract based on external chemical stimuli. For example, in the methylanthracenylimino derivative of chitosan (Figure 4a), π-π interactions are implicated in the larger volume expansion of the polymer gel upon uptake of phenylalanine and tryptophan amino acid esters due to the interactions between the aromatic moieties of these esters and the anthracenyl unit of the polymer itself. Cation-π interactions are implicated in the chiral recognition of L- and D-dibenzoyltartaric acid with the same chitosan derivative. Magic-angle spinning ^{1}H NMR (Figure 4b) of the polymer with D-dibenzoyltartaric acid shows an upfield shift of the axial glucosamine protons, indicative of shielding by the phenyl substituent of D-dibenzoyltartaric acid, which suggests that the phenyl group is in a favorable orientation to interact *via* cation-π interaction with the protonated amine group of the glucosamine unit of chitosan. The L-dibenzoyltartaric acid derivative, however, does not undergo similar shielding of the axial glucosamine protons and therefore the phenyl substituent positioning is unfavorable for cation-π interactions between the protonated amine of chitosan and the phenyl substituent of L-dibenzoyltartaric acid. The D-dibenzoyltartaric acid molecule exhibits greater activity (polymer volume expansion) than does L-dibenzoyltartaric acid. Neither tartaric acid nor its *t*-butoxy derivative has any activity, further supporting the notion that the phenyl group is essential for activity. This information, taken together with the NMR data gathered with respect to the

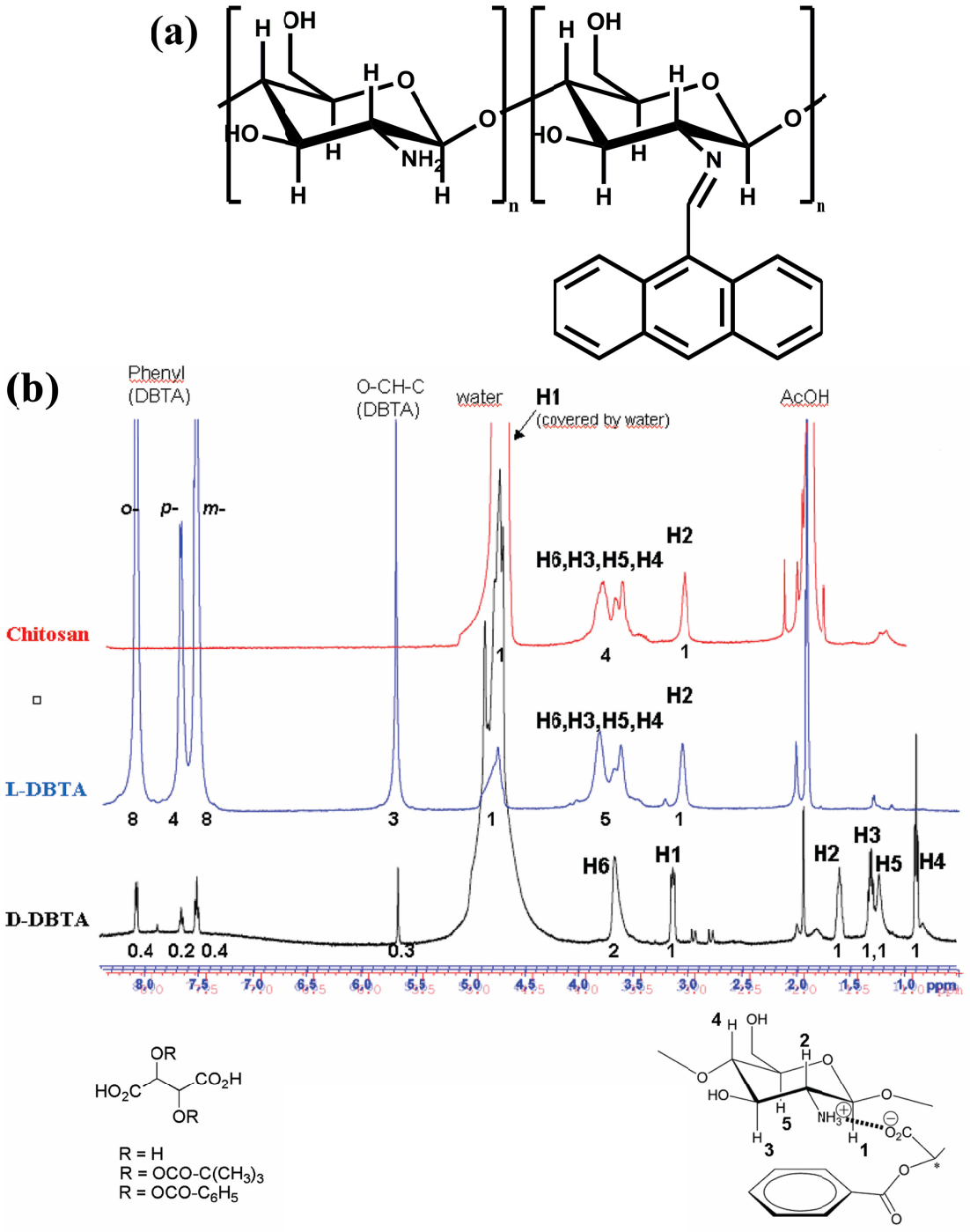

Figure 4. (a) Scheme of chitosan derivative, (b) ^{1}H MAS NMR of the chitosan derivative alone (red trace), with L-dibenzoyltartaric acid (blue trace) and with D-dibenzoyltartaric acid (black trace), demonstrating the shift of H1, H3 and H5 upon uptake of D-dibenzoyltartaric acid into the chitosan-based chemomechanical polymer. Figure adapted from Schneider and Strongin.[8]

favorable phenyl group positioning of D-dibenzoyltartaric acid, led Schneider and Strongin to conclude that cation-π interactions are operative in the chiral selectivity of the chitosan derivative. This chiral recognition plays a role in developing biodegradable drug delivery agents selective for the effective enantiomer of a drug, helping to reduce side effects as well as increase potency.[8]

c. Vapor-phase sensing of small-chain alcohols

A recent report by Dalcanale *et al.* highlights the use of hydrogen bonding and CH···π interactions in the selective vapor-phase sensing of small-chain alcohols. A monophosphonate cavitand, coupled *via* the phosphonate to a fluorophore based on 2-anilinonaphthalene-6-sulfonic acid, exhibits a bathochromic shift in its fluorescence spectrum upon exposure to the vapors of small-chain alcohols (methanol to 2-butanol). C-H···π interactions between the π-basic cavitand cavity and the terminal methyl groups of the alcohols and hydrogen bonding of the alcohol proton to the open P=O site (which is directed inward towards the cavity in the active cavitand) binds the molecule to the cavitand. The hydrogen bond to the P=O group, however, reduces the electron density on the phosphorus atom, leading to a lowering of the fluorophore's excited state and subsequent energy reduction of the charge transfer between the aniline and naphthalene groups, thus lowering the energy of the fluorescent emission. This effect is observed for the isomer with the P=O group facing outwards since, though the alcohol will still be bound to the cavitand, the alcohol proton cannot interact with the P=O group of the fluorophore. The ratio between the fluorophore's normal emission and the shifted emission is useful for tracking the concentration of alcohol in nitrogen stream. Longer

chain alcohols (such as 1-butanol, 1-pentanol, *etc*.) engage in weaker –OH···O=P interactions due to the increased length of the alkyl chain, which pushes the –OH group further out of the cavity and away from the O=P group. These types of vapochromic sensors hold great promise for the in-line detection of molecules (in this case alcohols) in gas streams for several applications, including industrial pollution monitoring.[9]

d. Additional remarks

The aforementioned examples are just a fraction of the numerous reports of supramolecular chemistry and its applications. Clearly, supramolecular chemistry is not only a continuing field, but a growing one as well. The applicability of these interactions and design paradigms is only limited by the imagination of the researchers in the field. As a testament to the expanding nature of the field, a 'new' interaction, the anion-π interaction, has only been fully recognized within the last decade. The interaction is, perhaps upon first consideration, a counterintuitive one, but, as described in the next section, one that is gaining momentum in the design of supramolecular entities.

B. Anion-π Interactions

i. Defining the anion-π interaction

Anion-directed processes are more complicated than those directed by cations due to their higher solvation energies, coordinative saturation and wide range of geometries and sizes.[10] As a consequence, the supramolecular chemistry of anions has lagged behind that of cations by a significant margin,[10] despite the nearly concurrent reports of cation complexation by crown ethers by Pedersen[11] and anion-binding katapinates (macrobicyclic ammonium molecules anion hosts) by Park and Simmons[12]

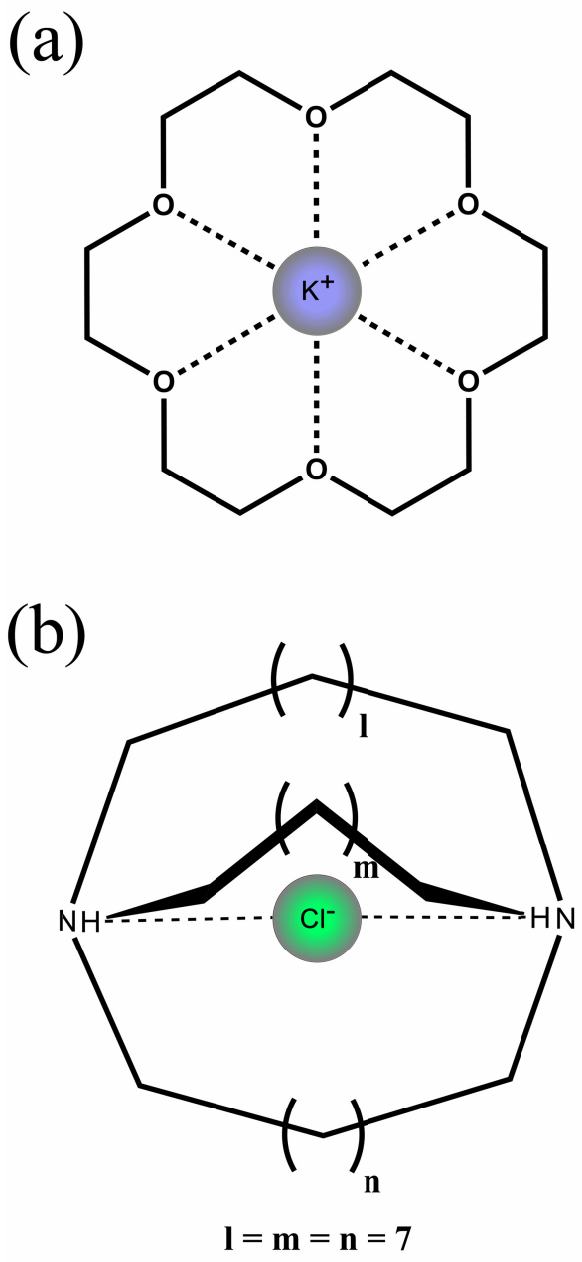

Figure 5. Schemes of (a) crown ether complexation of K^+ (Pedersen[11]) and (b) katapinate complexation of Cl^- (Park and Simmons[12]).

in 1967 and 1968, respectively (Figure 5a and b, respectively). This lag naturally led to the delay of the recognition of anion-π interactions, as well as their mainstream acceptance as design elements for supramolecular constructs.

a. Initial reports of anion-π interactions

The first recognition of anion-π interactions in solid-state and solution-phase systems was a report in 1993 by H.-J. Schneider, *et al.* detailing ^{1}H NMR complexation induced shift studies and molecular mechanics modeling of various anions with calixarenes.[13] Despite no explicit mention of 'anion-π', Schneider's study supported the conclusion that anions interact favorably with arenes, even in solution (with interaction energies on the order of ~2 kJ mol^{-1}).[13] Hiraoka, Mizuse and Yamabe also performed gas-phase reactions of $[F]^-$, $[Cl]^-$, $[Br]^-$ and $[I]^-$ with C_6F_6 and showed that $[F]^-$ covalently binds to C_6F_6 to form $C_6F_7^-$, while $[Cl]^-$, $[Br]^-$ and $[I]^-$ interacted *via* electrostatic interactions, with gas-phase binding energies of -73.6, -58.2 and -49.8 kJ mol^{-1}, with no specific mention of 'anion-π' interactions being made.[14] It was not, however, until three seminal theoretical studies published in 2002 in rapid succession by Alkorta *et al.*,[15] Mascal *et al.*[16] and Deyà *et al.*[17] confirming that anions can interact favorably with π-acidic arenes (with energies akin to hydrogen bonding) that mainstream acceptance of anion-π interactions began to take hold.[18]

b. Properties governing anion-π interactions

Like cation-π interactions, a canonical definition of an anion-π interaction is one that describes the effect of electrostatic and polarization components. The electrostatic component relies on the quadrupole moment (Q_{zz}, the measure of the charge distribution

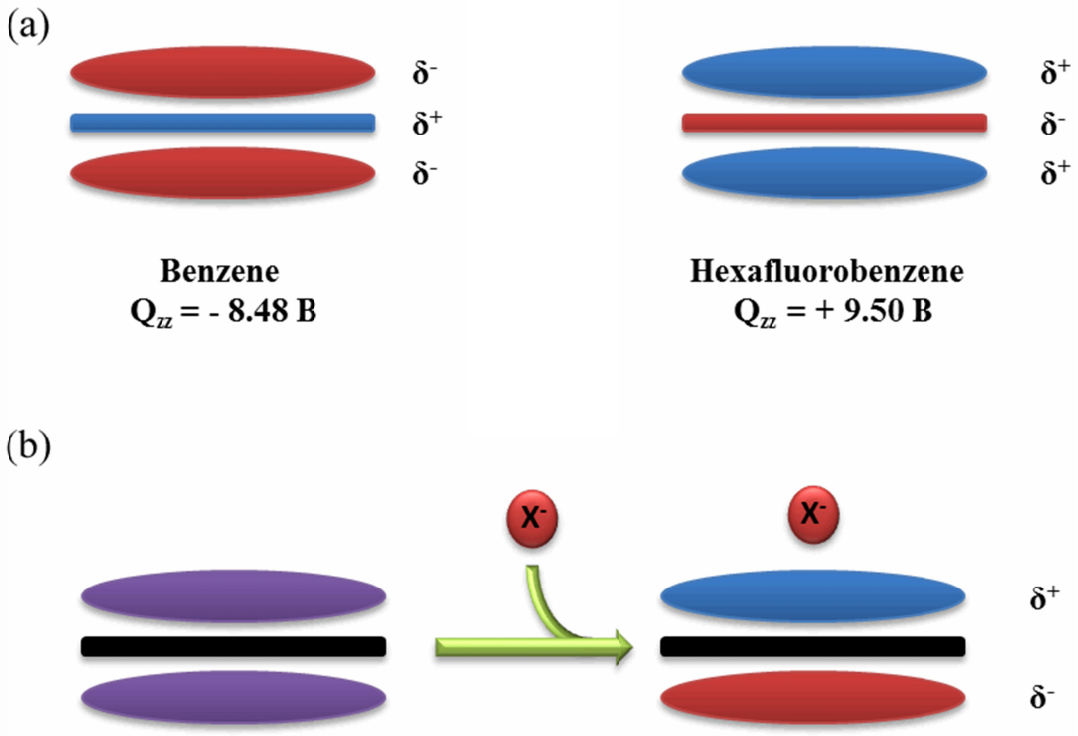

Figure 6. Diagrams of (a) the quadrupole moments of benzene (left) and hexafluorobenzene (right, red represents regions of greater electronegativity and blue represents regions of lower electronegativity) and (b) polarization of an arene upon interacting with an anion (purple represents an even electronic distribution).

of a molecule with respect to a particular axis, Figure 6a) of the π system (usually an arene, though olefins can undergo these interactions as well).[18] In contrast to cation-π interactions, however, positive rather than negative quadrupole moments are more amenable to anion-π interactions. As such, hexafluorobenzene (Q_{zz} = + 9.50 B; 1 B = 3.336 X 10^{-40} C m^2) should interact better than unsubstituted benzene (Q_{zz} = - 8.48 B), which gas-phase computations have shown to be true for Cl^--arene interactions.[15] As the interaction between the π-cloud and an anionic species is a generally repulsive one due to electron-electron repulsion, polarization of the electron density tends to strengthen the interaction (Figure 6b). Deyà and coworkers demonstrated this point through gas-phase computation of benzene interacting with $[Na]^+$ on one face and $[F]^-$ interacting on the opposite face. The polarization of the electron density of benzene induced by $[Na]^+$ allows for a favorable interaction between various anions and benzene despite benzene's largely negative quadrupole moment.[19]

c. σ-dipole effects as a possible source of anion interactions with arenes

Recently, Wheeler and Houk have pointed out that, even if benzene derivatives with electron withdrawing groups interact favorably with anions, the source of the interaction may be due to a combined effect of the individual σ-dipoles created between the electron withdrawing group and the phenyl C atoms.[20,21] As such, these authors claim that the positioning of the anion and increased strength of the interaction is not due to substituent-induced π-system charge redistribution but rather the additive effect of the σ-dipoles The claim was supported by the results of computational studies of $[Cl]^-$ with both monocyanobenzene and monocyanocyclohexane. Both of these systems show an

appreciable interaction with $[Cl]^-$ as compared to their unsubstituted counterparts despite the lack of a polarizable π system on cyclohexane, leading Wheeler and Houk to conclude that current arguments based on substituent-induced polarization effects require reassessment. They point out, however, that their findings only hold for substituted benzene molecules (substituents such as cyanide with bonding π-systems may be able to affect the benzene π-system) and that anion binding by heterocycles, *e. g.*, pyridine "remains an open question."[20] In these cases, the presence of an atom (N or O) more electronegative that C could in fact withdraw π electron density away from the C atoms, inducing π electron localization within the arene π system, leaving the C atoms a more attractive target for directional anion-π interactions (qualitatively demonstrated by Mascal *et al.* through ESP map computations using 1,3,5-triazine and its derivatives[16]).

d. Additional remarks

Despite much work on the subject, the nature of the anion-π interaction is still a topic of debate. The definition that guides the work presented in this dissertation is a more general one – that an anion interacting with an arene π system, whether purely electrostatic or not, is considered to be an anion-π interaction. Initial research into anion-π interactions was primarily computational, but recently there are many more experimental examples of anion-π interactions appearing in the literature. A brief survey of the research in the field follows, starting with computational efforts.

ii. Computational evidence of anion-π interactions

a. Initial computational evidence of anion-π interactions

The independent seminal work of Alkorta, *et al.*,[15] Mascal, *et al.*[16] and Deyà *et al.*[17] incited a flurry of computational work on the subject of anion-π interactions. Initially, research was limited to simple halides, linear (*e.g.* $[CN]^-$ and $[N_3]^-$) and planar anions (*e.g.* $[NO_3]^-$ and $[CO_3]^{2-}$).[18] The MP2 computational study of Mascal *et al.*[16] demonstrated that trifluoro-*s*-triazine (Q_{zz} = +8.23 B) exhibits stronger interactions and a shorter non-covalent bond distance (r, defined as the distance between the anion and the arene centroid) with $[Cl]^-$ than does *s*-triazine (Q_{zz} = +0.90 B) due to the difference in the quadrupole moment (E_{MP2} = -14.8 kcal mol^{-1}, r = 3.0 Å and E_{MP2} = -4.8 kcal mol^{-1}, r = 3.2 Å, respectively).[16] Similar results are found when $[Cl]^-$ is replaced by $[F]^-$ and $[N_3]^-$, but the lowest energy structure for $[F]^-$ is a Meisenheimer complex and $[N_3]^-$ has a π-π stacking structure in addition to the over-centroid arrangement typically regarded as anion-π (Figure 7).[16]

Alkorta *et al.* performed both MP2 and DFT computations on hexafluorobenzene, octafluoronaphthalene and pentafluoropyridine with a variety of anions. In addition to showing that the anions interact favorably with the arenes, the results indicate that DFT (with the hybrid functional B3LYP, a less computationally expensive method than the previously used MP2 theory) works well as a qualitative assessment of anion-π interactions, although the interaction distances are longer than in the corresponding MP2 case and the interactions are consistently weaker.[15] Also noted in these computations was the tendency for the anion position in the pentafluoropyridine

Figure 7. Geometry optimized structures of $[F]^-$ (top) and $[N_3]^-$ (bottom) with 1,3,5-triazine. The $[F]^-$ result shows the anion bonding to one of the carbon atoms in a Meisenheimer complex, whereas the $[N_3]^-$, in addition to a 'normal' anion-π interaction (not shown), exhibits a π-π stacking interaction between the $[N_3]^-$ π-system and the 1,3,5-triazine π-system. Figure adapted from Mascal *et al.*[16]

systems to be biased slightly towards the C atom opposite the N atom, lending support to the idea of localization of π-electron density on the N site.[15]

b. Additivity of anion-π interactions

Further work by Deyà and coworkers demonstrated that anion-π interactions are additive. Computations using MP2 theory revealed that the interaction of two and three substituted *s*-triazine molecules with $[Cl]^-$ and $[Br]^-$ were approximately two and three times more stable than the corresponding system with one ring (Figure 8, top row).[22] In other work, Deyà and coworkers demonstrate that anion-π, cation-π and π-π stacking interactions are cooperative, such that anions can interact with arenes that have negative quadrupole moments as long as that arene simultaneously interacts with an arene of a positive quadrupole moment (which can, in turn, interact with a cation, Figure 8, bottom row).[23]

c. Induction effects in cation-π-anion complexes

Studies of the importance of induction effects in cation-π-anion interactions by Kim *et al.* concluded that, although the ideal geometry of the system involves the formation of a close ion pair between the anion and the cation (and subsequent reduction of the cation-π interaction), induction effects can work to enhance the cation-π interaction when the anion is on the opposite face of the arene. This increases the anion-π interaction as well, despite the fact that the anion-π interaction is not the dominant force in these interactions.[24] Induction effects can also overcome the electrostatic repulsion of arenes with largely negative quadrupole moments to allow for anion-π interactions with even these arenes.[25] Evidence put forth by Clement and

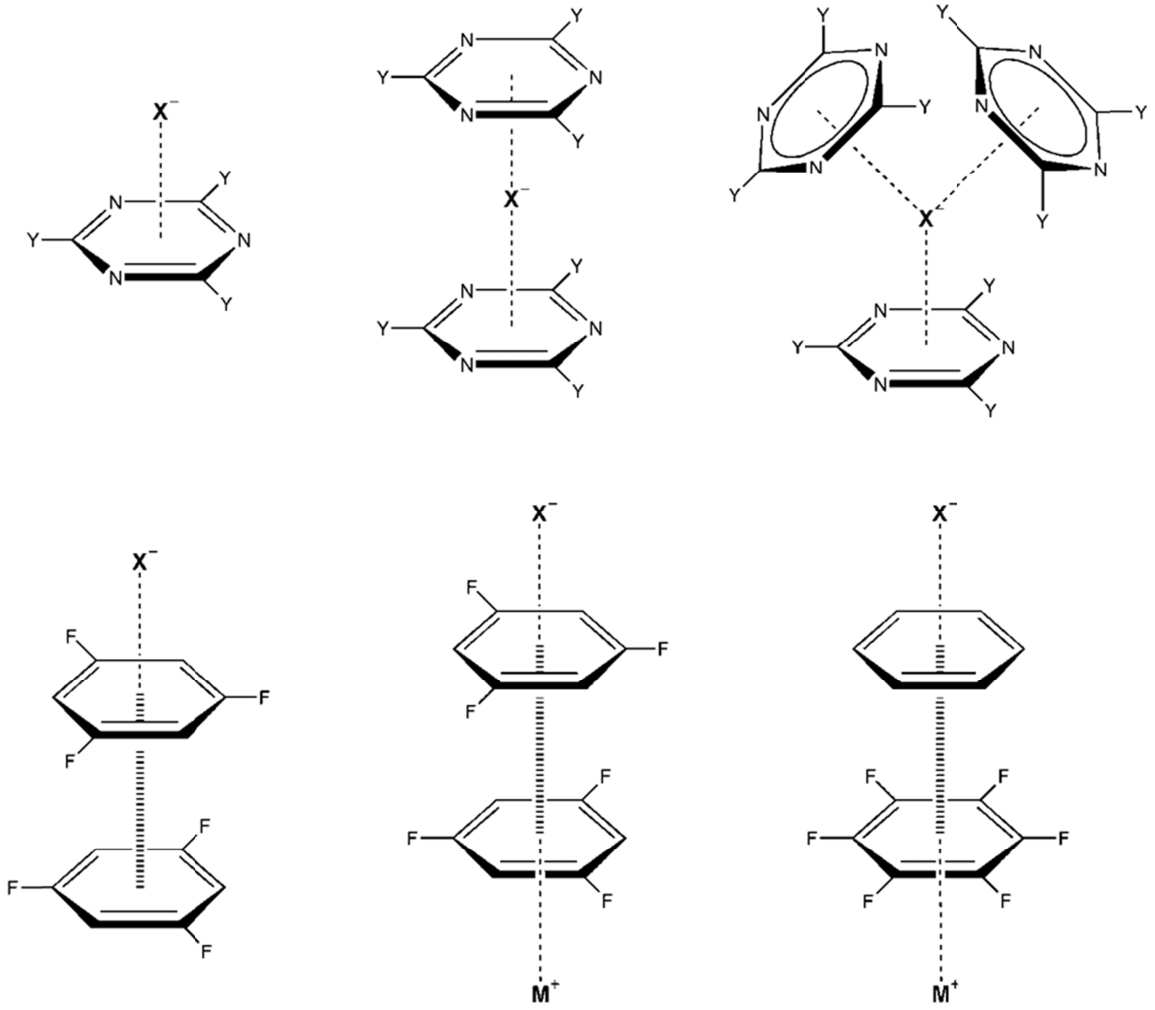

Figure 8. Schemes of anion-arene models shown to exhibit anion-π interactions in gas-phase geometry optimization computations by Deyà *et al.*[22,23,26]

coworkers in 2006 suggested that, while a correlation to arene quadrupole moment exists for cation-π interactions, there is no such correlation with anion-phenyl bonding.[27] Their work suggests that the polarizability of the arene is the dominant force in anion-phenyl bonding, and, in an argument similar to Wheeler and Houk,[20] they maintain it is the polarizability of the aromatic substituents, not the arene π electron density, that plays a role in the strength of the interaction.[27]

d. Anion-π interactions of polyatomic anions

Deyà and coworkers soon extended their computational studies to complex, three-dimensional anions, starting with $[BH_4]^-$, $[BF_4]^-$ and $[PF_6]^-$, studying their interaction with trifluoro-*s*-triazine.[28] As expected, these anions showed a favorable interaction with the arenes, but, due to the increased complexity afforded by the tetrahedral and octahedral anions, multiple conformations were found to be stable and only small differences in interaction energy separated the conformers (Figure 9).[28] The most stable conformer in all cases (and the conformation with the most examples in the CSD) is the one that with three F atoms of the anion interacting with the carbon atoms of trifluoro-*s*-triazine (as expected based on the idea of π-electron localization), forming a three-fold symmetric complex.[28] The same authors report that 1,2,4,5-tetrazine interacts favorably with halides, with some distortion of the tetrazine planarity.[29]

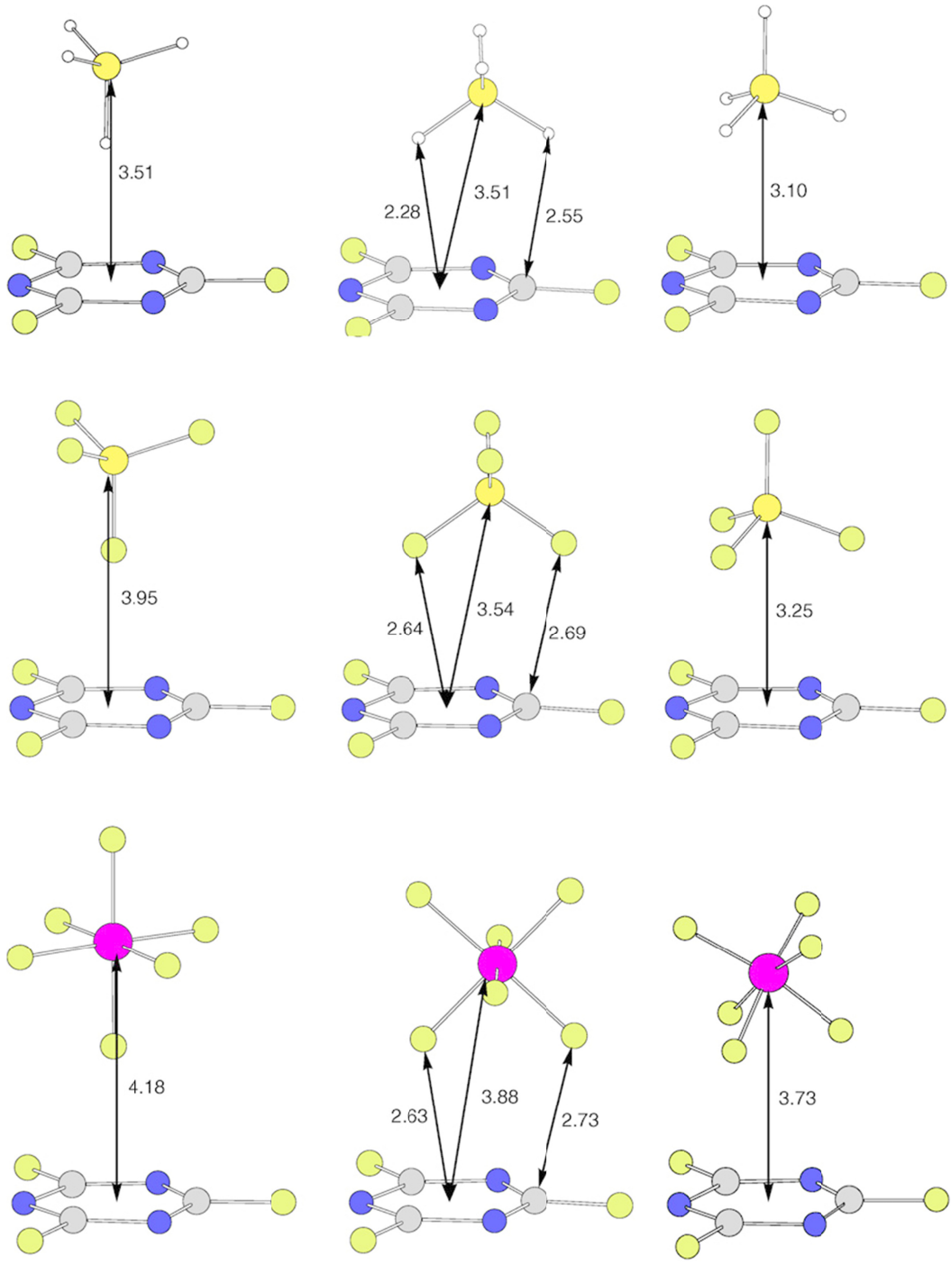

Figure 9. Local minimum energy geometries (MP2 geometry optimizations) of 1,3,5-trifluoro-1,3,5-triazine with $[BH_4]^-$ (top row), $[BF_4^-]$ (middle row) and $[PF_6]^-$ (bottom row). In all three cases, it can be seen that the anions interact either with the arene centroid or the carbon atoms of triazine. Figure reproduced from Deyà *et al.*[28]

e. Additional remarks

Although the computational work constitute seminal contributions to the recognition and explanation of anion-π interactions, the practical application of anion-π interactions to the design of functional supramolecular ensembles represents the next step in the development of anion-π interactions. As presented in the next subsection, much effort has been expended on the study of structural examples of anion-π interactions as well as on the design of supramolecular assemblies incorporating anion-π based receptors for anion interactions, with results that corroborate the findings of the computational work which inspired some of the experiments.

iii. Experimental evidence of anion-π interactions

Less than a decade has passed since the computational work of Alkorta *et al.*,[15] Mascal *et al.*[16] and Deyà *et al.*,[17] and in the ensuing time, numerous examples of anion-π interactions in both the solid and solution state have been reported. Several reviews and perspective articles have been written which detail the substantial progress in the field.[3,18,30-36] A few of the many experimental examples demonstrating anion-π interactions and their use in the design of supramolecular assemblies are highlighted in the following section.

a. Cocrystallization and titration studies of halides with π-acceptors

An excellent example of anion-π interactions in both solution and solid state is found in the study involving the titration and cocrystallization of various $[R_4N][X]$ salts ($R = {}^{n}Bu, {}^{n}Pr, Et$; $X = Cl^-, Br^-, I^-$) with tetracyanopyrazine, tetracyanoethylene (TCNE) and tetrachloro-*o*-benzoquinone performed by the late J. K. Kochi and coworkers.[37] The

chloride ion interacts closely with four tetracyanopyrazine units in the solid-state (3.07 Å, Σ_{vdW} for Cl^- and C = 3.45 Å, Figure 10) with the alkylammonium cation outside of the cavity.[37] Similar close contacts occur for the other salts, albeit with different molar ratios of anion to tetracyanopyrazine. Electronic absorption spectroscopy revealed a new band at 400 nm upon titration of tetracyanopyrazine with $[^nPr_4N][Br]$, where both the isolated bromide salt and tetracyanopyrazine exhibit absorbance in the ultraviolet only.[37] Other research by Kochi *et al.* demonstrated the formation of one dimensional chains of complex anions (*e.g.* $[NO_3]^-$, $[SCN]^-$, $[HSO_4]_2^{2-}$, $[ZnBr_4]^-$, *etc.*) with tetracyanopyrazine and 1,3,5-trinitrobenzene exhibiting anion-π interactions.[38]

b. Halide receptor enhanced by anion-π interactions

Johnson *et al.* provided an elegant study of the use of anion-π interactions in the design of an anion receptor to enhance the association of halides in solution.[39] Two receptors were designed and synthesized, one incorporating a phenyl substituent (the control) and the other a pentafluorophenyl substituent combined with a hydrogen-bond donating sulfonamide group (Figure 11a and b, respectively); the authors mention that, based on computational evidence, the anion-π interactions were expected to be too weak to bind anions in solution without the aid of other cooperative interactions).[39] ^1H NMR titration data with $[Et_4N]^+$ salts of $[Cl]^-$, $[Br]^-$ and $[I]^-$ show modest K_a values (in the range of 20 – 34 M^{-1}) for the anion-π receptor, while no appreciable K_a could be determined for the control receptor, providing strong evidence of anion-π interactions in solution.[39] Additionally, the trend in association constant did not follow the same one as for a sulfonamide receptor without any phenyl substituents (for which only the hydrogen

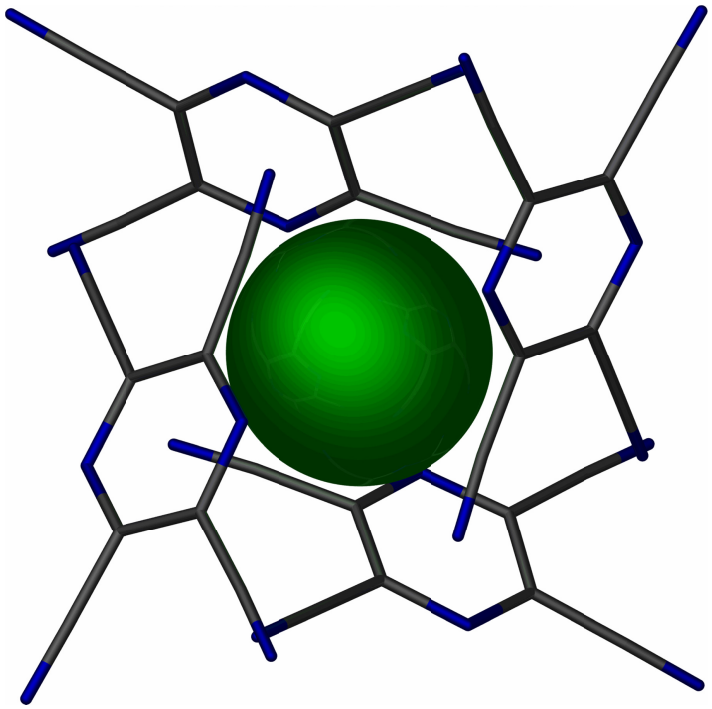

Figure 10. Structure of tetracyanopyrazine cocrystallized with $[Et_4N][Cl]$ (the cation is omitted for the sake of clarity). Four pyrazine groups surround the chloride ion, engaging in anion-π interactions with all four rings. Figure generated from CCDC 236242, submitted by Kochi *et al.*[37]

bonding interaction was available); in fact, $[Cl]^-$ and $[I]^-$ exhibit similar association constants, which is explained by the more polarizable $[I]^-$ forming a stronger interaction with the pentafluorophenyl group, compensating for the decreased hydrogen bonding.[39] Solid-state structural data demonstrating the anion-π interaction in the receptor, however, were more difficult to obtain. In an attempt to gain some insight into the possible structure of the anion-bound receptors, HF geometry minimizations were performed with both receptors. The control receptor showed two energy-minimized geometries, neither of which positioned the chloride ion over the phenyl group (Figure 11c).The anion-π receptor also showed two energy-minimized geometries, one with the chloride positioned over the pentafluorophenyl group (Figure 11d) and the other to the side of the pentafluorophenyl group.[39] These computations, coupled with the titration studies, led Johnson *et al.* to conclude that the binding enhancement in solution was a result of anion-π interactions.[39]

c. Anion-π interactions in Cu^{II} complexes of the polyheterocycle dpatta

Reedijk *et al.* have published work that reports structural evidence for anion-π interactions in compounds of first-row transition and main group elements with ligands containing heteroaromatic moieties such as pyridine, pyrimidine and 1,3,5-triazine.[34,40-48] Among the examples is an interesting complex resulting from the reaction of $Cu(NO_3)_2 \cdot 3H_2O$ with the polyheterocyclic ligand dpatta (Figure 12a, b) nitrate-triazine anion-π interaction that exhibits an unexpected alignment of one nitrate oxygen atom with the an electron-rich nitrogen atom of the triazine group (Figure 12c).[43] The authors postulate that this situation is the result of a second π-π interaction between the triazine

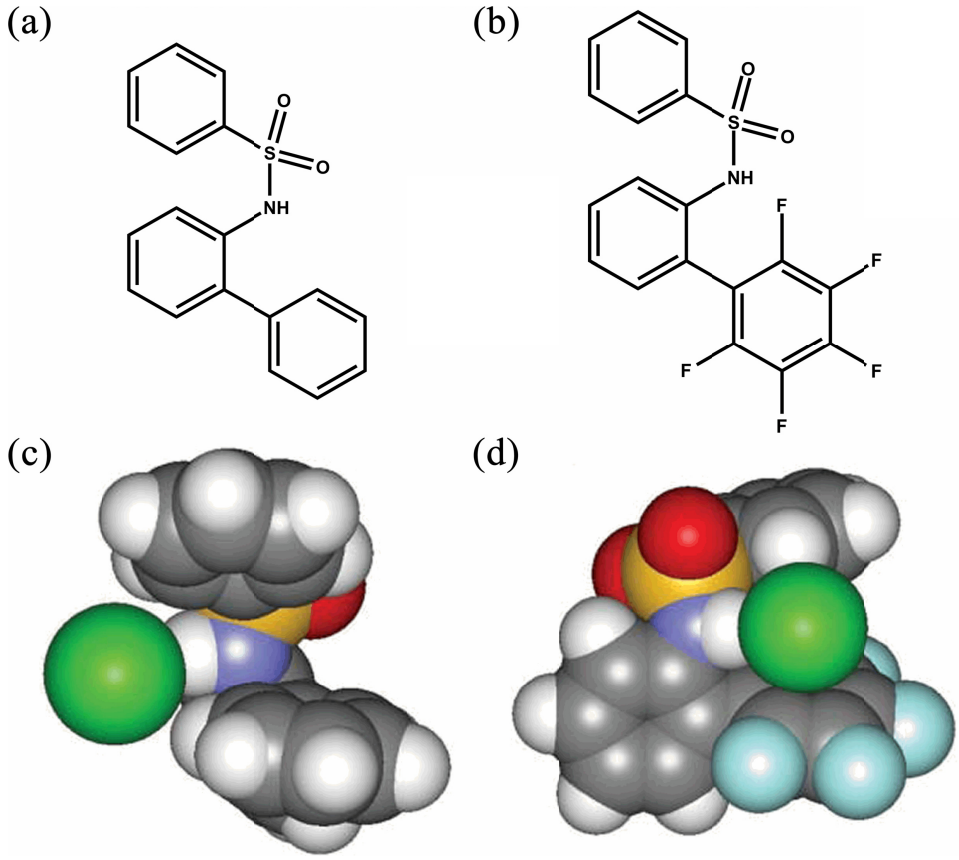

Figure 11. Schematic representations of (a) the control receptor and (b) the receptor incorporating an anion-π receptor arene. Local minimum structures from geometry optimization computations showing the (c) hydrogen bond interaction between the control receptor and $[Cl]^-$ with no anion-π interactions and (d) hydrogen bonding and anion-π interactions of the receptor with the (C_6F_5) substituent. Figure adapted from Johnson *et al.*[39]

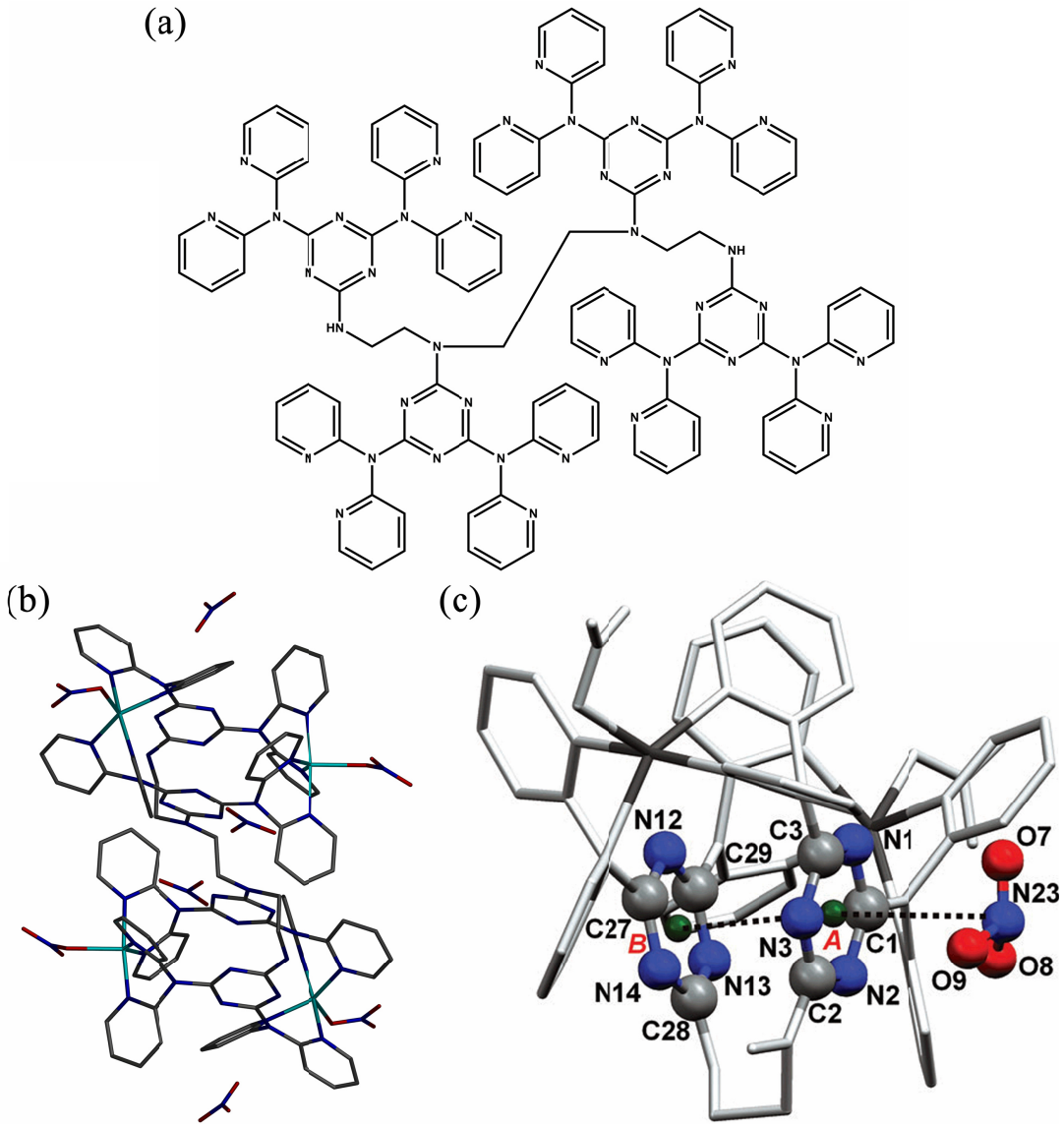

Figure 12. (a) Scheme of the dpatta ligand. (b) Structure of the tetranuclear Cu^{II} complex with dpatta, generated from the CIF of CCDC 615306 (atom colors: C grey, N blue, O red, Cu teal, H is omitted for the sake of clarity). (c) Enlarged view of the $[NO_3]^-$ ···triazine···triazine interaction (adapted from Reedijk *et al.*).[43]

and another neighboring triazine. DFT computations performed using ADF at the BLYP level of theory with the ET-pVQZ basis set, however, were inconclusive in determining whether the π-π stacking interaction is indeed the cause. A local geometry minimum did correspond to the arrangement seen in the crystal structure.[43]

d. Evidence of anion-π interactions from the CSD

Several CSD data mining assessments of anion-π interactions in the solid state have been reported, with varying degrees of success being highly dependent on the criteria used for the realization of a 'hit' from the database.[17,19,23,33,34,49-52] Hay and Custelcean purport that, based on severely restrictive criteria, that the CSD has few or no examples of anion-π interactions. Their criteria excluded any crystal structure that exhibited disorder or $R \geq 0.10$, a common occurrence in crystal structures of complex, three-dimensional anions such as $[BF_4]^-$ and $[SbF_6]^-$ (in fact, $[BF_4]^-$ is notorious for exhibiting disorder in crystal structures), which effectively eliminated any cases including these more complex anions. In addition, the restriction of the arene to C_6X_6 and C_5NX_5 systems precluded the inclusion many interesting heterocycles (which are expected to be better anion-π receptors). These restrictions, coupled with the rejection of any arene bound to a metal cation (understandably, $\eta^{5,6}$-bound arenes are excluded, however, this also rejects coordination complexes), severely limit the number of 'hits' returned. Naturally, the authors of this study concluded that anion-π interactions are quite uncommon in the CSD.[33] A similar, but somewhat less restrictive (namely in the inclusion of nitrogen heterocycles), analysis by Reedijk *et al.* revealed that, as the arene became more and more π-acidic, anions tended to cluster above the plane of the ring in a

fashion more akin to the expected anion-π configuration in the order $C_6 < C_5N <$ *o,m,p*-$C_4N_2 <$ *s*-C_3N_3.[36]

e. Anion-π based transmembrane anion transporters

In a very important example of the application of anion-π contacts in the design of new functional materials, Matile and coworkers published a number of reports regarding transmembrane anion transporters (or 'anion-π slides') based on various substituted oligonaphthalenediimides (NDIs) and perylenediimides (PDIs) that use anion-π interactions as their primary mode of anion transport.[31,53-59] NDIs were chosen for their known electron-acceptor properties, and with a Q_{zz} of +14.7 B, rigid structure and tunable π-acidity, they constitute a convenient platform for such transmembrane anion slides.[53] The prototypical anion-π slide studied by Matile and coworkers consists of three NDI units joined through 2,3,5,6-tetramethylphenyl linkers, with terminal ethylamines (Figure 13a).[53] When installed in a membrane, anion-π slides based on NDIs allow for translocation of anions *via* a multi-ion hopping mechanism. According to this mechanism, anions are attracted to the first NDI unit by anion-π interactions and partially desolvated, then pushed along by repulsion from subsequent anions binding to the first NDI unit until all NDI sites are occupied, at which point the next anion to bind at the start of the channel ejects the anion at the channel terminus with the aid of solvation by the cellular media (Figure 13b).[53] Evidence of the importance of anion-π interactions for the activity of these slides was obtained by performing ESI-FTICR-MS-MS experiments which detected the gas-phase formation of fragile dimers between NDI monomers and various halides and demonstrated the preference of $[Cl]^-$ for NDI

monomers with higher π-acidities and less steric crowding of the binding site through competition studies.[31] The slides were also installed in large unilamellar vesicles where it was found that the NDI slide resulting in the most activity contains a dicyano-substituted naphthalene core with phenyl linkers, maximizing the π-acidity while minimizing the steric bulk around the binding site as predicted by the mass spectrometric data (Figure 13c).[31] These remarkable systems demonstrate the viability of using anion-π interactions in biomimetic (and general supramolecular) design as controllable and tunable elements.

f. Additional remarks

Interest in anion-π interactions has increased significantly over the past decade. Numerous accounts have appeared that cite their presence and use in supramolecular assemblies, work that has helped to demonstrate their utility as a non-covalent bonding force. Debates on the strict definition of an anion-π interaction notwithstanding, there is little doubt that these interactions are viable design elements in supramolecular ensembles. As neutral ligands bearing π-systems (*e.g.* aromatic ligands such as 2,2-bipyridine, phenanthroline, *etc.* and non-aromatic ligands such as tetracyanoethylene, tetracyanoquinonedimethane, *etc.*) are common synthons in structural inorganic chemistry, there is ample opportunity for the occurrence of interactions between the ligands of the metal complex and its counteranions in both solution and solid-state. Supramolecular self-assembly between such ligands and metal ions results in a wide variety of shapes and sizes, including grid-type structures which are the most common, and numerous examples of cation templation in such architectures. Anions, with their

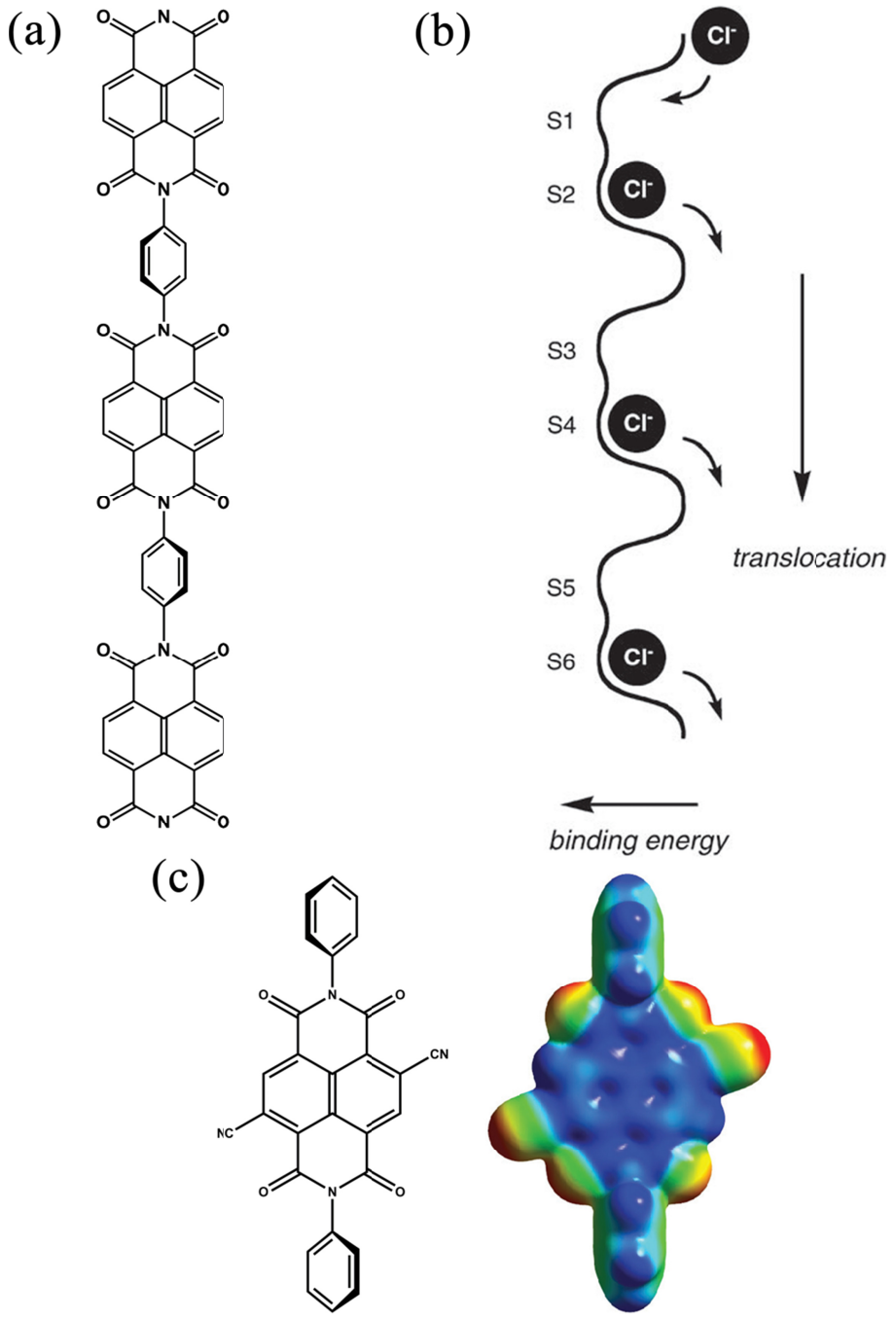

Figure 13. (a) Scheme of a typical oligo-naphthalenediimide (oNDI) anion-π slide of Matile *et al.* (b) Scheme of the ion-hopping mechanism for ion transport along oNDIs, showing the translocation of the anion along the slide due to the increased binding energy at the naphthalenediimide core. (c) Scheme (left) and ESP (right) of the NDI unit most active transporter of $[Cl]^-$ across a membrane, incorporating two electron-withdrawing cyanide substituents on the naphthalenediimide core. Figures adapted from Matile *et al.*[31,53]

wide variety of shapes and sizes, provide an intriguing platform for the self-assembly of more exotic polygons through interactions with flexible aromatic linkers.

C. Supramolecular Self-Assembly and Templation

i. Principles of self-assembly

One of the defining concepts in supramolecular chemistry is the idea of self-assembly, or the ability of molecules to spontaneously and reversibly associate with one another according to 'pre-programmed' molecular information to form larger, more complex assemblies. Such a process is critical to life, and one that Nature has perfected over eons.[2] Self-assembly relies on interactions weaker than covalent bonds to allow for kinetic reversibility, enabling an annealing process to occur which allows the molecular components to engage in associative/dissociative events such that they reach their thermodynamic minimum structure. In this manner there is a natural correction of structural 'errors' along the way even in one step, multicomponent reactions (so-called 'one-pot' reactions).[2] There are several design strategies being employed in an attempt to control self-assembly of molecules into preplanned structural motifs, which, according to Stang *et al.*, the most widely adopted of which are: directional bonding, symmetry interaction, molecular paneling, weak link and dimetallic building block approaches (Figure 14a-e, respectively).[60]

ii. Design strategies for supramolecular ensembles

The directional bonding approach was pioneered by Fujita *et al.*[61,62] and Stang *et al.*[63] with their work on molecular squares of Pt^{II} and Pd^{II} and requires building blocks with pre-defined coordination angles and rigid structures; in this case, the stoichiometry

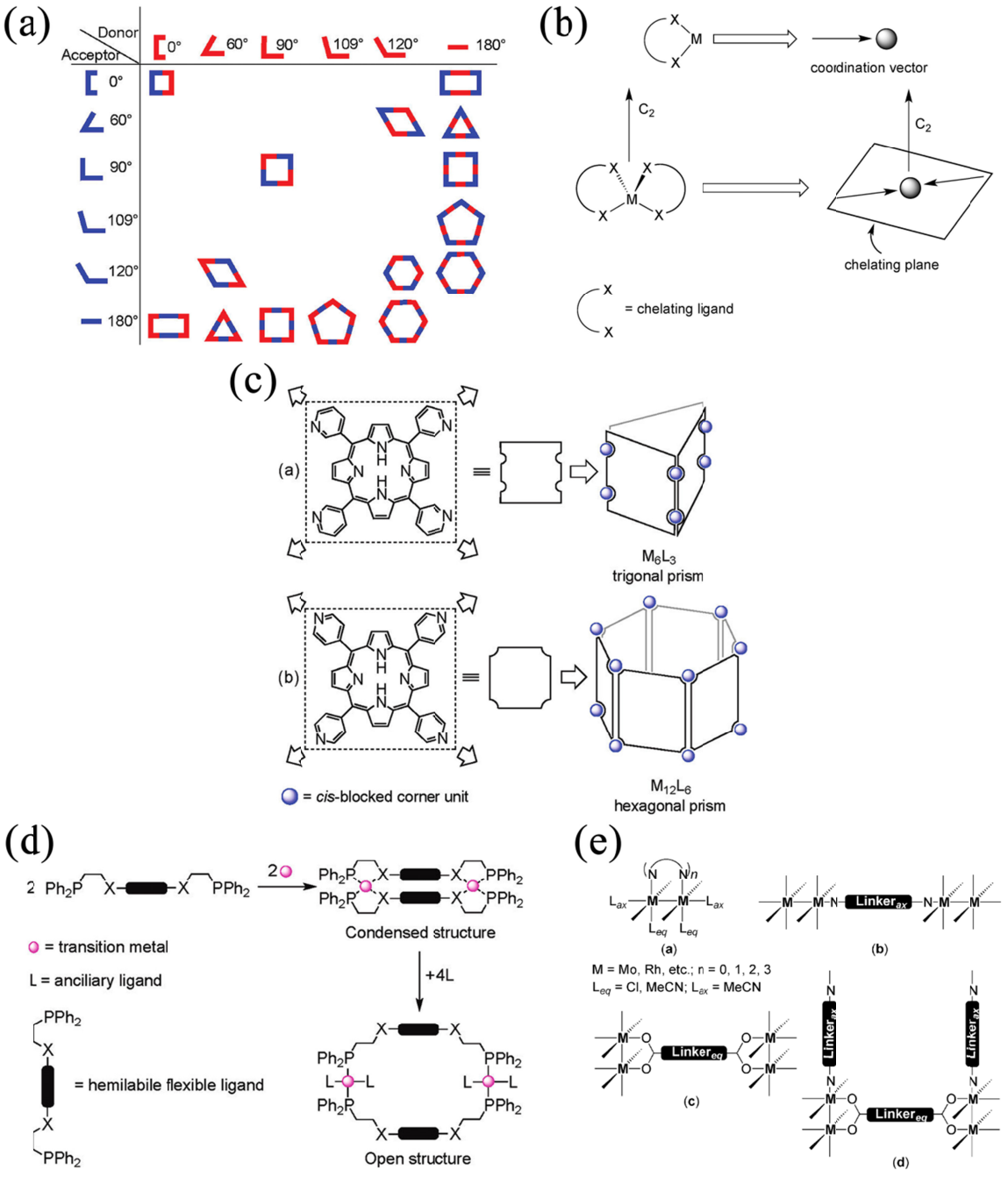

Figure 14. Schemes of (a) combinations of synthons for directional binding; (b) the use of symmetry interactions between ligands and metals to direct binding; (c) porphyrins for paneling supramolecular prisms; (d) hemilabile ligands for forming adjustable supramolecular structures responsive towards new ligands; and (e) dimetallic binding units with different linker ligands for the design of a wide variety of supramolecular structures. Figure adapted from Stang *et al.*[60]

of the building units determines the final structure (Figure 14a). The symmetry interaction approach, as developed by Raymond *et al.*,[64] involves using the binding symmetry of the ligands and the expected coordination geometries of the metal centers to direct the synthesis of the final structure (Figure 14b). The paneling approach, pioneered also by Fujita *et al.*,[65] involves taking two dimensional organic panels (such as tetra(4-pyridyl)porphyrin) and coordinating the panels to metal ions to build three-dimensional structures with the panels serving as the faces and the metal ions (or other suitable molecule) serving as the vertices. The result is the formation of a wide variety of molecular structures reminiscent of Platonic solids (Figure 14c). The "weak-link" approach of Mirkin and coworkers[66] involves the use of flexible ligands with two sets of coordinating atoms, one weaker than the other, to preorganize a compressed structure which can be expanded to the final structure by introducing an ancillary ligand that displaces one set of coordination bonds to the metal ion (Figure 14d). The dimetallic building block approach of Cotton and coworkers[67] uses paddlewheel complexes which can be linked together by the replacement of various combinations of labile axial and equatorial ligands to create extended or discrete complexes (Figure 14e).

iii. Self-assembled supramolecular polygons

While a wide variety of structures have been obtained by applying these design strategies, it is worth mentioning that most of the resulting structures are molecular squares and rectangles (or rectangular prisms and cubes if three dimensional) as the angles in these polygons are congruent with the typical octahedral and square-planar metal coordination angles of 90^{o} and 180^{o}. Less common are the higher-order regular

polygons such as pentagons and hexagons, with vertex angles of 108° and 120°, respectively. In fact, only a scant few metallosupramolecular pentagons exist.[60,68-72] Using dimolybdenum- or dicobaltbis(4-pyridyl)ethene donor units as the corners (Figure 15a) combined with diplatinum acceptor units as the edges, Stang and coworkers successfully obtained a mixture of hexagonal and pentagonal structures with the dicobalt species and pentagonal structures exclusively with the dimolybdenum species, as confirmed by $^{31}P\{^{1}H\}$ NMR and ESI-TOF-MS studies. Structural information was obtained from molecular force field modeling studies (Figure 15b).[68] The donor units were specifically designed such that the pyridyl groups are oriented at approximately 108°, allowing for the facile formation of the pentagonal unit while being close enough to 120° to accommodate the formation of a hexagonal moiety with the dicobalt species.[68] The pyridyl groups on the donor displace triflate ions on the Pt^{II} acceptor unit to link together, with 5 (for the pentagon) or 6 (for the hexagon) of each unit completing the cyclic structure. This is the only pentagonal structure to have been synthesized without the use of a template.[60]

iv. Anion-templated supramolecular pentagons

Both the pentagonal Fe^{II} helicate of Lehn *et al.*[71] and the pentagonal Ni^{II} metallacycle of Dunbar *et al.*[69,70] require the use of an anionic template and flexible ligands in order to accommodate a pentagonal structure. In both cases, nitrogen donor chelating ligands coordinate to the metal center with bite angles close to the ideal 90° angle adopted by octahedral metal ions while the flexibility in the ligands allows the M^{II}-M^{II}-M^{II} angle to adopt the ideal pentagonal angle of 108° in order to accommodate $[Cl]^-$

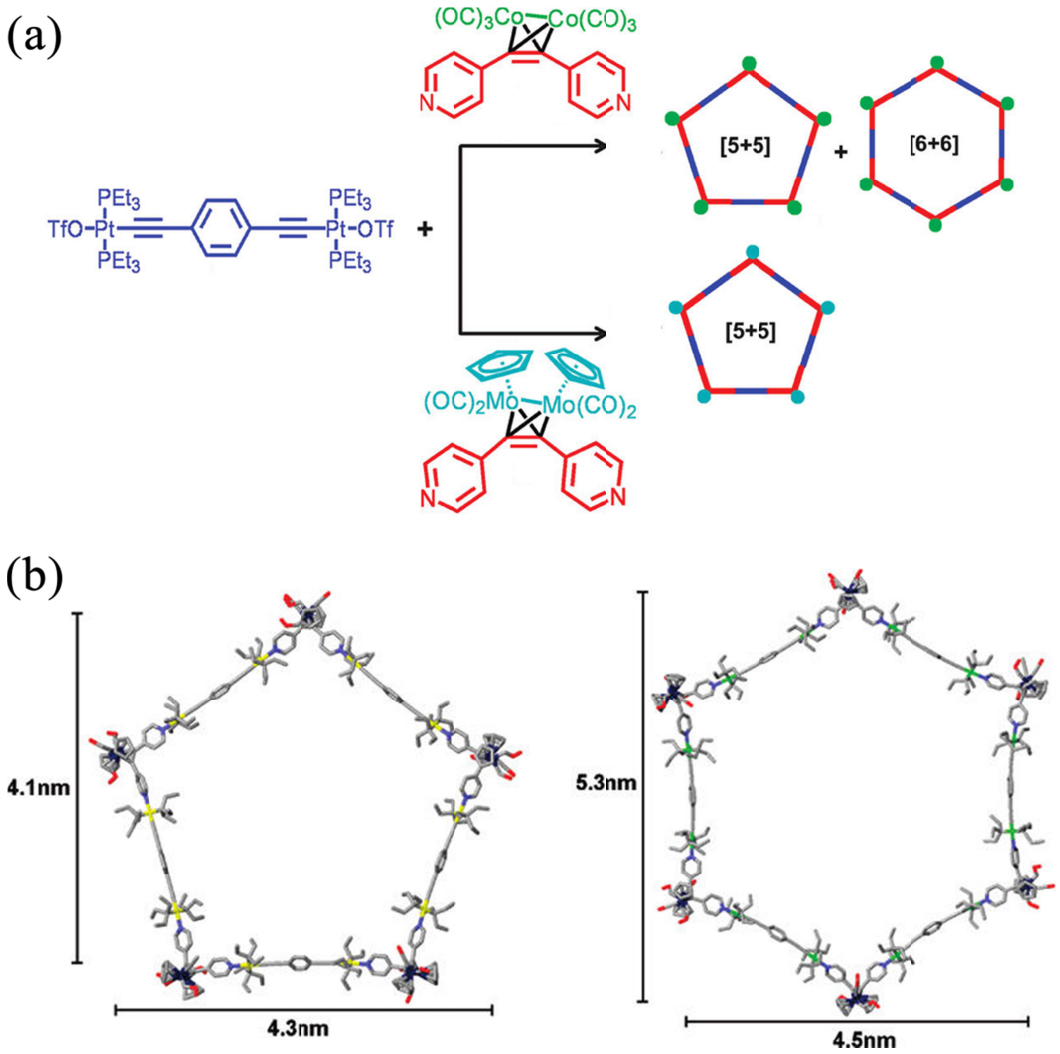

Figure 15. (a) Scheme of the directional binding units used for the synthesis of molecular pentagons and hexagons. The color of each building unit matches the color of its representative piece in the full polygon. (b) Molecular force field models of the structures of the pentagonal (left) and hexagonal (right) supramolecular structures based on the $[Co(CO)_3]_2(C_2(C_5H_4N)_2)$ building unit. Figures adapted from Stang *et al.*[68]

and $[SbF_6]^-$.[69-71] Templation in supramolecular chemistry is the use of a typically unbound molecule (such as solvent, cations or anions) around which a specific structure forms, much like the use of a frame to support an arch bridge while under construction. In the absence of the template (or in the presence of a different template), the structure fails to form. The template can either remain in the structure or, as in the example of the arch bridge, be removed upon completion of the structure. This templation effect is well known for cations and neutral species, however, due to the previously cited reasons of higher solvation energies, complex and varied structures, size and diffuse charge, anions have historically seen limited application in template-driven processes, though this has begun to change.[10,73-75]

As demonstrated by the Ni^{II} metallacycles of Dunbar *et al.*, anions can be effective templates, yielding two distinct structures depending on the anion present during their formation. In the case of the tetrahedral anions $[ClO_4]^-$ and $[BF_4]^-$, a tetranuclear square forms exclusively in high yield, whereas use of the octahedral (and larger) $[SbF_6]^-$ ion exclusively forms a pentanuclear pentagonal metallacycle (Figure 16a).[69,70,76] The Fe^{II} helicate of Lehn and coworkers consisting of tris-bipyridine ligands coordinated to Fe^{II} ions wrapping around a central chloride forms a closed double-helical pentagonal structure (Figure 16b). Identical reaction conditions with Ni^{II} result in a triple helical structure consisting of three Ni^{II} and three tris-bipyridyl ligands with little structural resemblance to the Fe^{II} case. Changing the anion from $[Cl]^-$ to $[BF_4]^-$ results in a hexameric structure, demonstrating the necessity of the $[Cl]^-$ ion for the formation of the pentagonal helicate.[71,77]

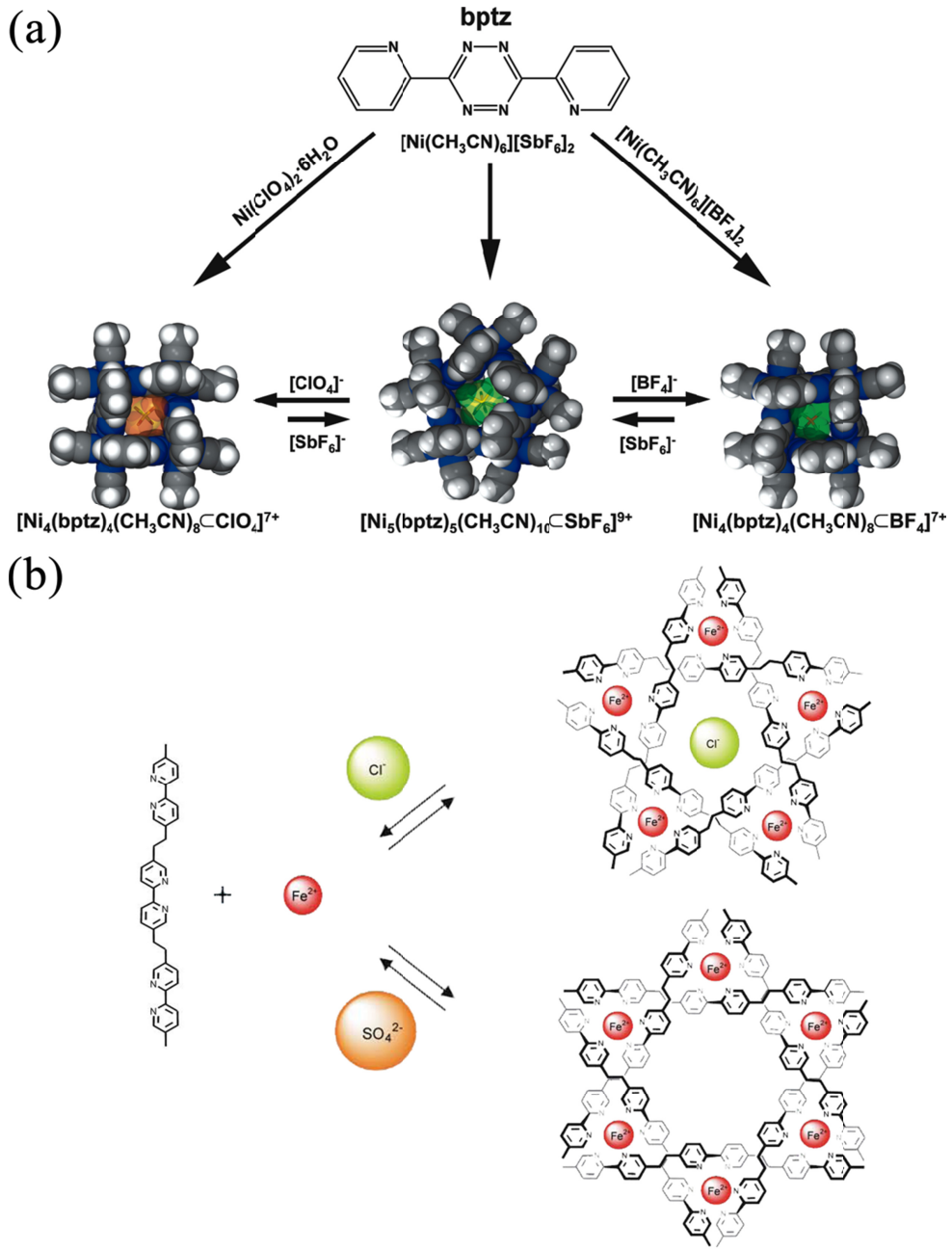

Figure 16. (a) Space-filling diagrams of the Ni^{II} squares with $[ClO_4]^-$ (left) and $[BF_4]^-$ (right), the Ni^{II} pentagon with $[SbF_6]^-$ (middle) with schemes of their interconversion and respective formation from bptz (figure reproduced from Dunbar *et al.*[70]). (b) Scheme of the synthesis of pentagonal (top) and hexagonal (bottom) helicates of Fe^{II} with the shown tris-bipyridine ligand, with the final nuclearity of the helices dependent on the counterion introduced ($[Cl]^-$ for the pentagonal helix and $[SO_4]^-$ for the hexagonal helix). In the petagonal helix, the counterion remains in the central cavity, while in the hexagonal helix, it does not (figure adapted from Lehn *et al.*[77]).

The aim of this dissertation research project was to assess the effect of changing the coordinating ligand, metal ion and counteranion on the supramolecular anion-π templation of square and pentagonal metallacycles based on N-heteroaromatic chelate ligands. The following chapters describe efforts to understand the factors, especially the role of anion-π interactions, that are operative in the self-assembly of these structures using a variety of techniques including computational modeling and structural analysis *via* NMR and XRD. It will be demonstrated that each of these parameters play a distinct role in the formation and stability of these fascinating metallacyclic structures.

CHAPTER II

THEORETICAL MODELING OF ANION-Π INTERACTIONS

A. Introduction

Computational research into anion-π interactions constituted the bulk of early research on the topic and sparked a wide investigation and general acceptance of anion-π interactions. Notable contributions in this area come from the independent and seminal works of Deyà *et al.*,[17] Mascal *et al.*,[16] and Alkorta *et al.*[15] in 2002. Initially, the computational efforts focused on halides with substituted benzene and triazine derivatives but has recently extended into studies involving complex anions such as $[BF_4]^-$ and $[PF_6]^-$ as well as tetrazine ring systems.[18,28,29,78] As discussed in Chapter I, these studies established that anion-π interactions are favorable and, coupled with experimental studies, aided in determining the extent to which the polarizability and quadrupole moments of the arenes affected the strength of the anion-π interaction. Since the anions studied in the Dunbar group with regards to the metallacycles and the complexes with Ag^I are polyatomic (for example, $[BF_4]^-$ and $[SbF_6]^-$), it is important to study these complex anions computationally with the expectation that the computational modeling can be used to predict the favorability of anion-π interactions with specific anions.

There are three principal metrics that are applied to the computational study of anion-π interactions: the distance from the anion to the arene centroid (r), the positioning of the anion above the arene (d, measured by the angle subtended by the anion-centroid-

arene edge), and the binding energy ($E_{binding}$, the total energy of the optimized complex minus the energies of the optimized geometries of isolated components) of the anion···arene complex (Figure 17). Anion-π interactions are typically considered to have anion-arene distances that are less than the sum of the van der Waals radii of the component atoms, negative binding energies which are indicative of favorable interactions, and configurations with the anion centered above the plane of the arene. Electrostatic potential (ESP) maps are often used as a qualitative predictor of the affinity of an arene for an anion in an anion-π interaction. These maps calculate the energy of attraction or repulsion between a positive point charge and the arene along a grid; attractive interactions have negative energies and indicate areas of negative electrostatic potential (indicated by red), while repulsive interactions have positive energies and indicate areas of positive electrostatic potential (indicated by blue). The more positive electrostatic potential an arene exhibits, the more likely it is to engage in anion-π interactions.[18]

These criteria were established based primarily on the studies of halides and other simple anions, but the study of polyatomic anions complicates the assessment of anion-π interactions. The anion-arene centroid distances are naturally elongated and the shapes of the anions introduce the possibility of directionality in the interaction. Complex anions can also become computationally prohibitive, especially when using *ab intio* MP2 theory to model them. In order to accurately model the anion-π interactions in these more complicated systems, the anion-arene distances can be defined between specific atoms on the anion and the arene, with the sum of the van der Waals radii

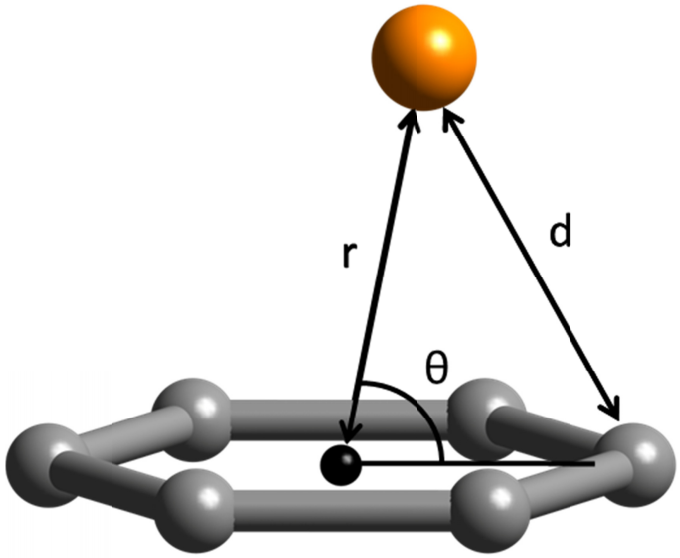

Figure 17. Metrics typically used in the definition of anion-π interactions. The distance, d, between an atom of the anion and an atom of the arene is typically used in the cases of polyatomic anions for which r, the distance between the central atom of the anion and the arene centroid, is often longer than the sum of the van der Waals radii. The angle from the anion to the arene centroid to an atom residing on the arene provides an estimate of anion positioning over the arene.

remaining an acceptable threshold. DFT computations using the B3LYP hybrid functional has been found to be less computationally prohibitive than MP2, yet they still yield reliable qualitative data regarding the strength of the interaction.

The Dunbar group has successfully employed computational work in the study of complexes between bptz and bppn with Ag^{I} as well as halide binding to $HAT(CN)_6$, primarily in the analysis of their ESP maps in an attempt to correlate the electrostatic potential of the arenes to the strength and positioning of the anion-π interactions observed in their respective supramolecular complexes.[79,80] $HAT(CN)_6$, for example, has regions of positive electrostatic potential at the center of the molecule, where one halide resides in the crystal structure (Figure 18, see Chapter V for an in depth discussion).[80] The ESP maps of the Ag^{I} complexes with bppn and bptz reveal shifts in the electrostatic potential maps that suggest polarization due to the close contact between the anion and the ligands in these complexes, especially the anion-templated complexes with bptz (Figure 19, see Chapter IV for an in depth discussion of these complexes).[79]

An extensive and systematic computational study in the Dunbar group established that anion-π interactions between $[BF_4]^-$ or $[PF_6]^-$ and tetrazine, pyridazine, triazine and benzene derivatives with F, Cl, Br, and CN substituents were favorable. The study also demonstrated that the smaller $[BF_4]^-$ anion established stronger interactions than $[PF_6]^-$ with all analyzed arenes, and that the complexes with polyatomic anions exhibited optimized structures that maximized contact between the F atoms of the anions and the electropositive carbon atoms of the arenes in question. Both MP2 and DFT methods were employed, with the MP2 results overestimating and the DFT results

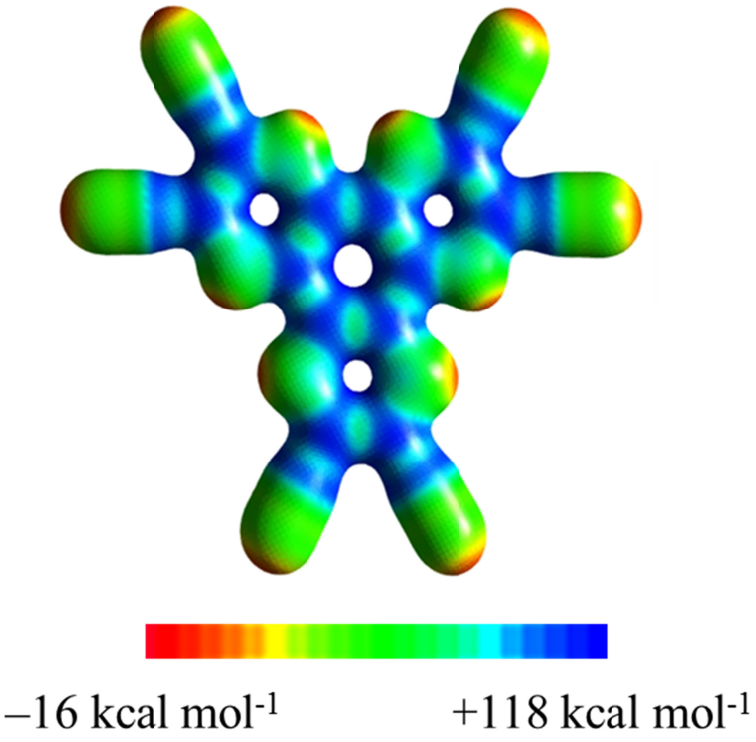

Figure 18. ESP map of $HAT(CN)_6$ at an isodensity value of 0.02 au with the electrostatic potential range as shown. The figure was adapted from Dunbar *et al.*[80]

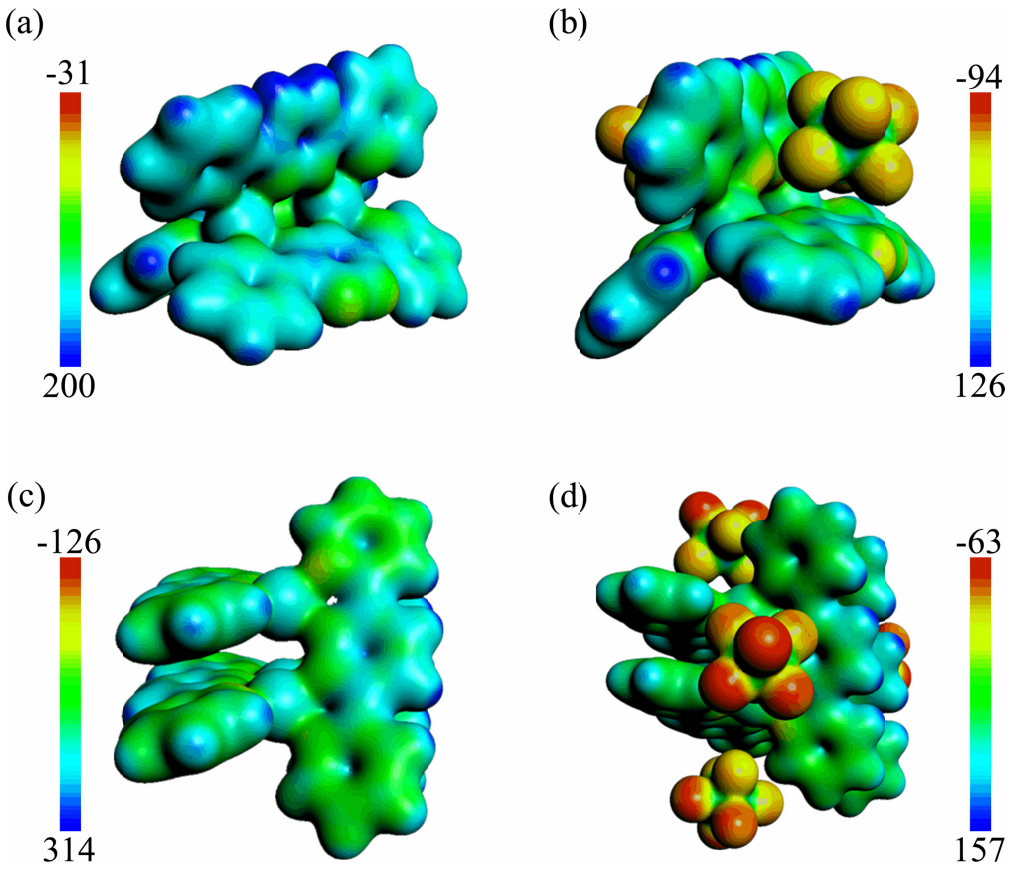

Figure 19. ESP maps of (a) $[Ag_2(bptz)_3]^{2+}$, (b) $[Ag_2(bptz)_3][AsF_6]_2$, (c) $[Ag_4(bppn)_4]^{4+}$, and (d) $[Ag_4(bppn)_4][SbF_6]_4$, with electrostatic potential color ranges as shown (values reported in kcal mol^{-1}) demonstrating the effect of the close proximity of the anion in each case. Figure adapted from Dunbar *et al.*[79]

underestimating the binding energies and the intermolecular distances. The positioning of the $[BF_4]^-$ anion over the tetrazine ring in the computation was shown to closely resemble that observed in the crystal structure of $[Ni_4(bptz)_4(NCCH_3)_8][BF_4]_8$, although the intermolecular distances calculated were shorter than those in the crystal structure, even for the "underestimated" DFT computation (Figure 20).[81]

This comprehensive study, however, only tested the interaction between one anion and one arene. This reasonably models the interaction geometries observed between the peripheral anions and the ligands in the Ag^I complexes, but the encapsulated anion interacts with four total tetrazine rings in the metallacycles, two of which align with the anion F atoms through close contact with the tetrazine C atoms (~2.8 Å). Each tetrazine ring in the square metallacycle of Ni^{II} and bptz also interacts with two anions in addition to the encapsulated anion. In order to more accurately model the interactions in the metallacycles, it is necessary to increase the complexity of the computations to complexes with two arenes and one anion and one arene with two anions. This also opens up the possibility of computational competition studies between two different anions and two different arenes.

This chapter details the computational study of the aforementioned complexes of $C_xN_{6-x}R_x\cdots[X]^-\cdots C_xN_{6-x}R_x$ and $[X]^-\cdots C_xN_{6-x}R_x\cdots[X]^-$ with F and CN substituted tetrazine and pyrazine derivatives with $[BF_4]^-$ and $[PF_6]^-$ (Figure 21). Pyrazine was chosen due to interest in using the ligand 3,6-bis(2′-pyridyl)pyrazine (bppz) to study the effect of ligand π-acidity on the formation of anion-templated metallacycles. The $C_xN_{6-x}R_x\cdots[X]^-$ complexes were also studied for pyrazine and repeated for tetrazine on account of the

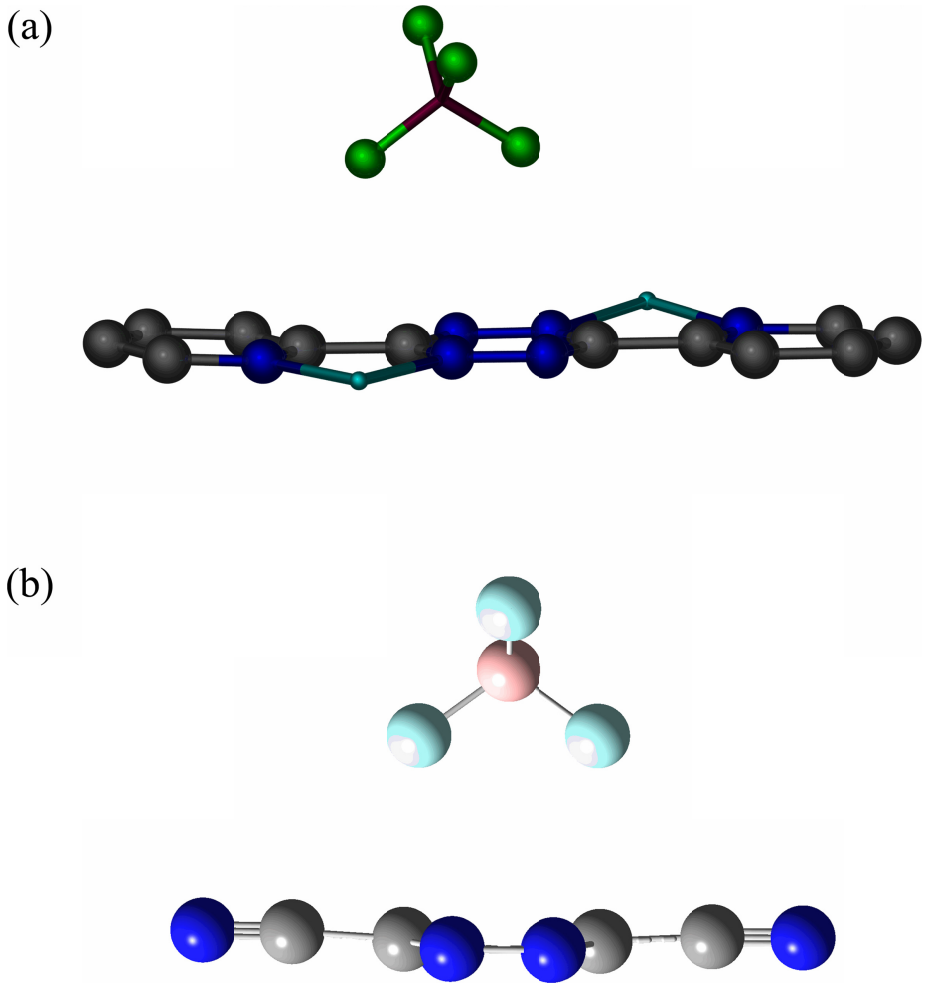

Figure 20. (a) Local environment of $[BF_4]^-$ with one of the bptz ligands of $[Ni(bptz)_4(NCCH_3)_8][BF_4]_8$, showing the alignment of $[BF_4]^-$ with the tetrazine ring of bptz. Atom colors: carbon (grey), nitrogen (blue), nickel (teal), boron (maroon), and fluorine (green). Hydrogen atoms and the rest of the structure are omitted for the sake of clarity. (b) Geometry optimized model complex $[BF_4]^-\cdots C_2N_4(CN)_2$, exhibiting the same alignment of $[BF_4]^-$ with the tetrazine molecule. Atom colors: carbon (grey), nitrogen (blue), boron (pink), and fluorine (light blue).

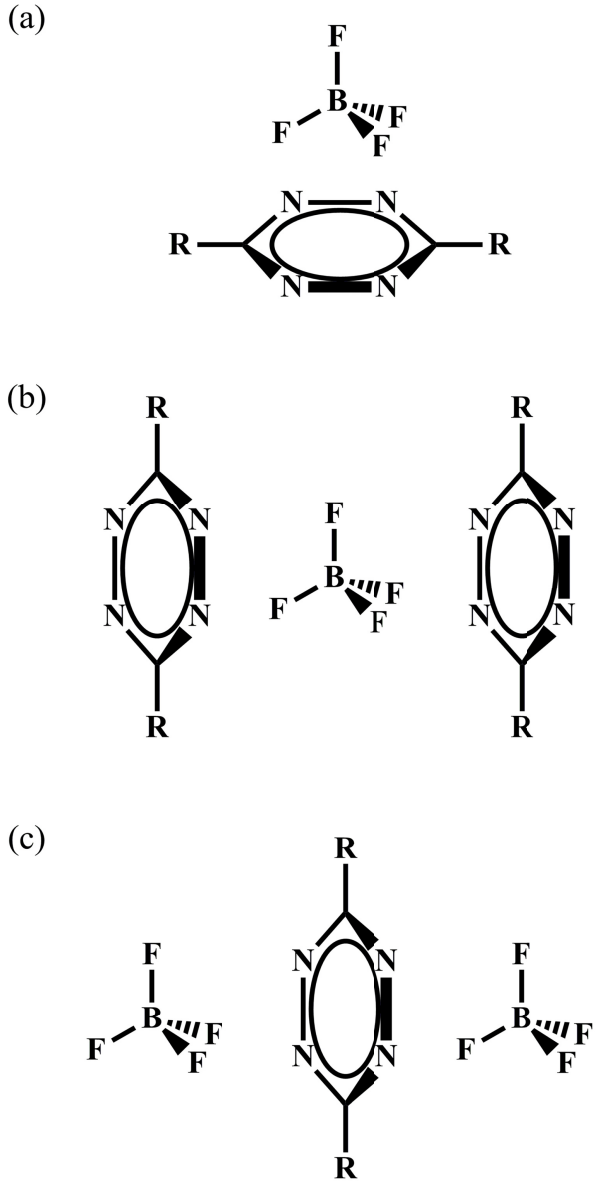

Figure 21. Schematic representations of the model complex geometries explored computationally, using $[BF_4]^-$ and tetrazine as examples (R = F and CN). They include (a) one anion with one arene, (b) one anion with two arenes, and (c) two anions with one arene. Pyrazine and $[PF_6]^-$ were used in the models as well, and mixed arene and mixed anion models for (b) and (c) orientations were also explored.

upgrade of Gaussian 03 to Gaussian 09. Isolated anion and arene computations were also performed in order to assess their ESP maps as well as to calculate the binding energies of the anion-π systems. The isolation and XRD structural analysis of metallacycles with low-spin Fe^{II}, as well as technological advances regarding supercomputers, have made it possible to perform computations on the full metallacycles due to the simplification of the modeling of the metal center, which can be treated as a closed-shell ion due to its d^6 electronic configuration. The results presented in this chapter demonstrate that the interaction between two arenes and one anion is favorable and approximately additive, as expected based on previous work with substituted benzene derivatives and halides,[22] whereas the interaction between two anions and one arene is not an additive one. The $C_4N_2F_4$ arene was also found to favorably interact with both $[BF_4]^-$ and $[PF_6]^-$, at longer F-C distances and lower binding energies than the corresponding interactions with $C_2N_4F_2$. Surprisingly, the complexes of $C_4N_2(CN)_4$ exhibit stronger binding energies despite longer F-C contacts as compared to the corresponding complexes with $C_2N_4(CN)_2$.

B. Computational Methods

DFT computations were performed in Gaussian 09, Revision B.01[82] with the B3LYP hybrid functional incorporating the Becke three-parameter (B3) exchange functional[83] and the correlation functional of Lee, Yang and Parr (LYP)[84] with the Pople-type basis set 6-31+G(d),[85,86] incorporating diffuse orbital and polarization functions on non-hydrogen atoms. Unrestricted geometry optimizations of two arenes with one anion and one arene with two anions were performed on an IBM iDataplex

Cluster comprising 372 nodes based on Intel's 64-bit Nehalem and Westmere processor architecture. Unrestricted geometry optimizations of one arene with one anion as well as the individual anions and arenes were performed on a 128-processor Altix 3700 with Itanium2 Madison processors. Frequency computations were performed on all of the final geometry optimized structures to ensure that a minimum had been reached, as determined by the absence of imaginary frequencies. Results were analyzed and images were generated using the Agui graphical user interface.[87]

C. Results and Discussion

All geometry optimization and frequency computations converged for (a) the individual anions and arenes, (b) the complexes of one arene with one anion, and (c) the complexes of two arenes with one anion. For the systems comprising two anions with one arene, only those involving tetracyanopyrazine converged to a stable minimum. In all cases, the frequency calculations exhibited no imaginary frequencies, unless otherwise noted. For all but the computations comprising two anions with one arene, the binding energies were negative, indicative of favorable interactions. A comprehensive discussion of each set of computations follows.

i. Individual arenes and anions

The individual anions and arenes were examined computationally, with the primary goal of extracting optimized minimum energies for calculation of the binding energies in the anion-π complexes. ESP maps were also generated for the arenes to assess the π-acidity of each and to help rationalize the positioning of the anions relative to the arenes. The ESP maps of the cyano and fluoro derivatives of pyrazine and

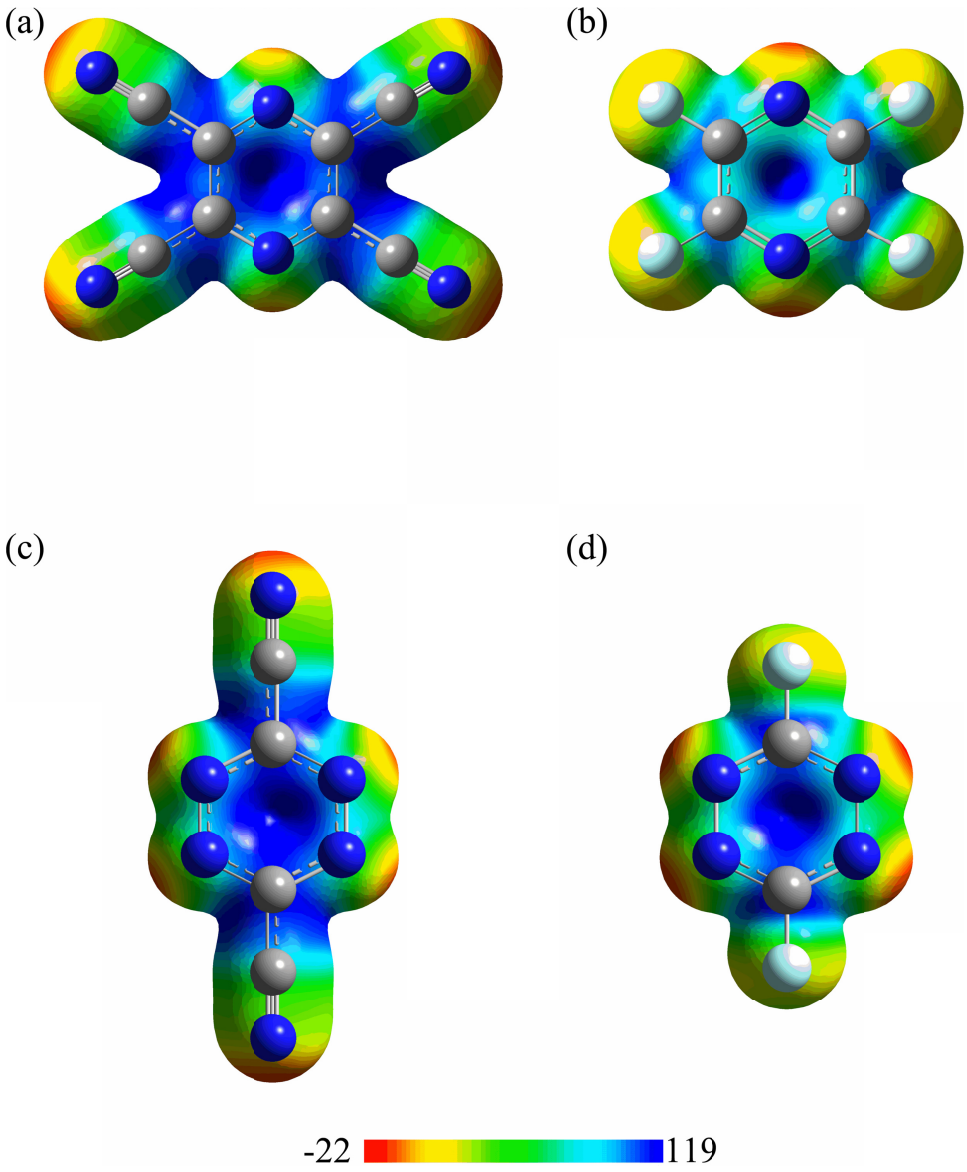

Figure 22. ESP maps of (a) tetracyanopyrazine ($C_4N_2(CN)_4$), (b) tetrafluoropyrazine ($C_4N_2F_4$), (c) dicyanotetrazine ($C_2N_4(CN)_2$), and (d) difluorotetrazine ($C_2N_4F_2$), overlaid with their respective ball and stick representations. Electrostatic potential color range values reported in kcal mol^{-1}. Atom colors: carbon (grey), nitrogen (blue), and fluorine (pale blue). ESP maps generated at an isodensity value of 0.02 a.u. from DFT geometry optimizations performed as indicated prior.

tetrazine reveal localization of positive electrostatic potential over the carbon atoms of the arenes (Figure 22a-d). The cyano derivatives of the arenes are more electropositive than the fluoro derivatives, suggesting that the cyano derivatives should engage in stronger anion-π interactions. Tetracyanopyrazine ($C_4N_2(CN)_4$) has a calculated quadrupole moment (Q_{zz}) of 19.5 B (1 B (Buckingham) = 3.34 X 10^{-40} C m^2), with C_{pyr}-N_{pyr} and C_{pyr}-C_{pyr} distances of 1.34 and 1.42 Å, respectively, and a calculated polarizability $\alpha_{||}$ = 8.4 $Å^3$. Tetrafluoropyrazine ($C_4N_2F_4$) has a calculated Q_{zz} = 6.3 B, with C_{pyr}-N_{pyr} and C_{pyr}-C_{pyr} distances of 1.31 and 1.40 Å, respectively, and a calculated polarizability $\alpha_{||}$ = 4.8 $Å^3$. Dicyanotetrazine ($C_2N_4(CN)_2$) has a calculated quadrupole moment Q_{zz} =12.5 B, with C_{tet}-N_{tet} and N_{tet}-N_{tet} distances of 1.35 and 1.31 Å, respectively, and a calculated polarizability $\alpha_{||}$ = 6.3 $Å^3$. Difluorotetrazine ($C_2N_4F_2$) has a calculated quadrupole moment Q_{zz} = 6.0 B, with C_{tet}-N_{tet} and N_{tet}-N_{tet} distances of 1.33 and 1.32 Å, respectively, and a calculated polarizability $\alpha_{||}$ = 4.4 $Å^3$. These data are summarized in Table 2. There are only small changes in the arene bond distances upon changing the substituent. Interestingly, the quadrupole moments, Q_{zz}, are more positive in the case of the pyrazine derivatives, with a much greater difference between pyrazine and tetrazine revealed in the cyano substituted arenes (7.0 B) as opposed to the fluoro derivatives (0.3 B). The molecular polarizability is greater in the pyrazine derivatives as well. This would suggest that pyrazine should, based on both Q_{zz} and $\alpha_{||}$, be more amenable to anion-π interactions than the tetrazine derivatives.

Table 2. Quadrupole moments (Q_{zz}), molecular polarizabilities parallel to the principle molecular axis ($\alpha_{\|}$) and arene bond distances for $C_2N_4F_2$, $C_2N_4(CN)_2$, $C_4N_2F_4$, and $C_4N_2(CN)_2$ calculated using DFT with the hybrid functional B3LYP and the Pople-type 6-31+g(d) basis set.

Arene	Q_{zz} (B)	$\alpha_{\|}$ (Å^3)	Arene Bond Distances (Å)
$C_2N_4F_2$	6.0	4.4	N-N: 1.32 C-N: 1.33
$C_2N_4(CN)_2$	12.5	6.3	N-N: 1.31 C-N: 1.35
$C_4N_2F_4$	6.3	4.8	C-C: 1.40 C-N: 1.31
$C_4N_2(CN)_2$	19.5	8.4	C-C: 1.42 C-N: 1.34

ii. Complexes of one arene and one anion

In order to benchmark the computations, $C_6F_6\cdots[Cl]^-$ was used as a standard since its gas-phase binding energy has been experimentally determined by Hiraoka, Mizuse, and Yamabe.[14] The computationally derived value for the $C_6F_6\cdots[Cl]^-$ gas-phase cluster, -11.7 kcal mol^{-1}, is approximately 33% weaker than the experimentally determined binding energy of -17.6 kcal mol^{-1}. It is not expected that the calculated binding energies will be experimentally accurate, but the comparison to the benchmark standard demonstrates an underestimation of the strength of the anion-π interaction by DFT using B3LYP, and suggests that if an interaction is considered favorable by the DFT methods, it should be expected to be experimentally feasible.

a. $C_2N_4R_2\cdots[X]^-$ complexes (R = CN, F; X = $[BF_4]^-$, $[PF_6]^-$)

The geometry-optimized complexes of the tetrazine molecules all exhibit close contacts between the tetrazine carbon atoms and the anion fluorine atoms along with favorable binding energies. The $[BF_4]^-$ anion aligns with tetrazine such that the anion fluorine atoms are directly above the electropositive carbon atoms of tetrazine (Figure 23). The F-C distances (Table 3) are well within the sum of the F and C atom van der Waals radii. It is noted that the $C_2N_4(CN)_2\cdots[BF_4]^-$ complex exhibited one imaginary frequency of minimal energy (<5 cm^{-1}). The $[PF_6]^-$ anion exhibits a similar alignment with F-C distances indicative of close contacts, however, they are longer than those between $[BF_4]^-$ and tetrazine (Figure 24, Table 3). The binding energies are also lower in magnitude with $[PF_6]^-$ than $[BF_4]^-$, suggesting that $[BF_4]^-$ undergoes stronger anion-π interactions than the more diffuse $[PF_6]^-$. Another notable trend is the lengthening of the

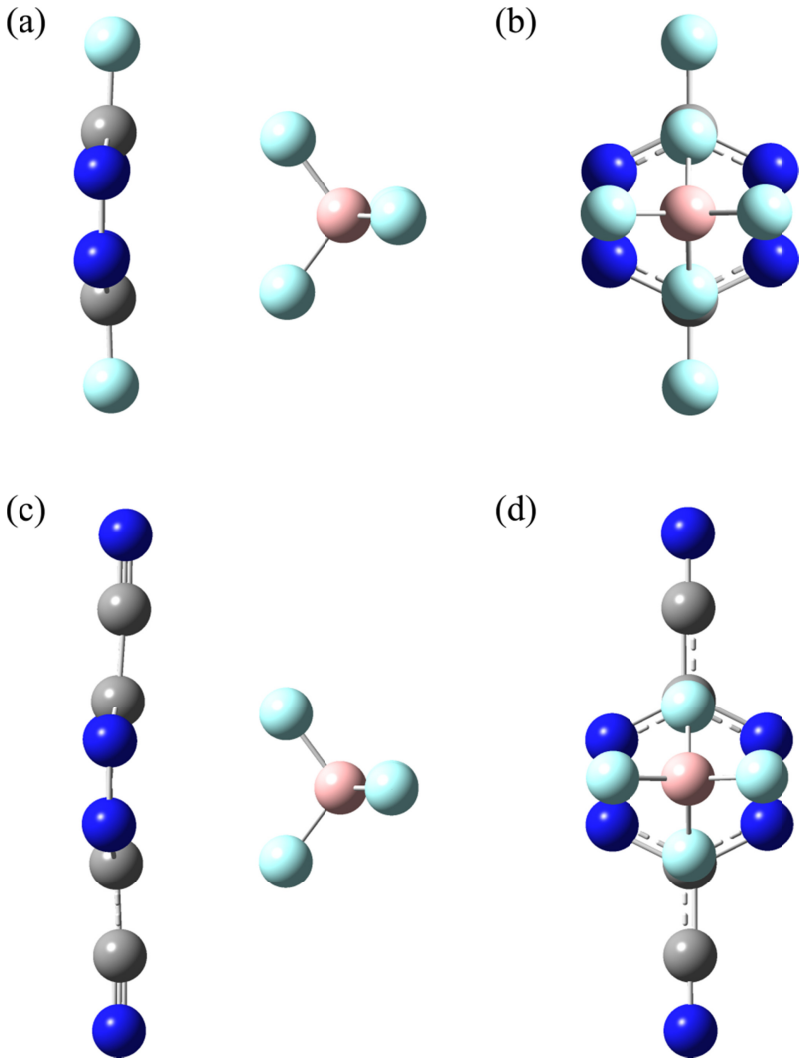

Figure 23. Geometry optimized structures of the tetrazine derivatives with $[BF_4]^-$. (a) Side-view and (b) top-view of a ball and stick representation of the $C_2N_4F_2\cdots[BF_4]^-$ complex. (c) Side-view and (d) top-view of a ball and stick representation of the $C_2N_4(CN)_2\cdots[BF_4]^-$ complex. Atom colors: carbon (grey), nitrogen (blue), fluorine (light blue), and boron (pink).

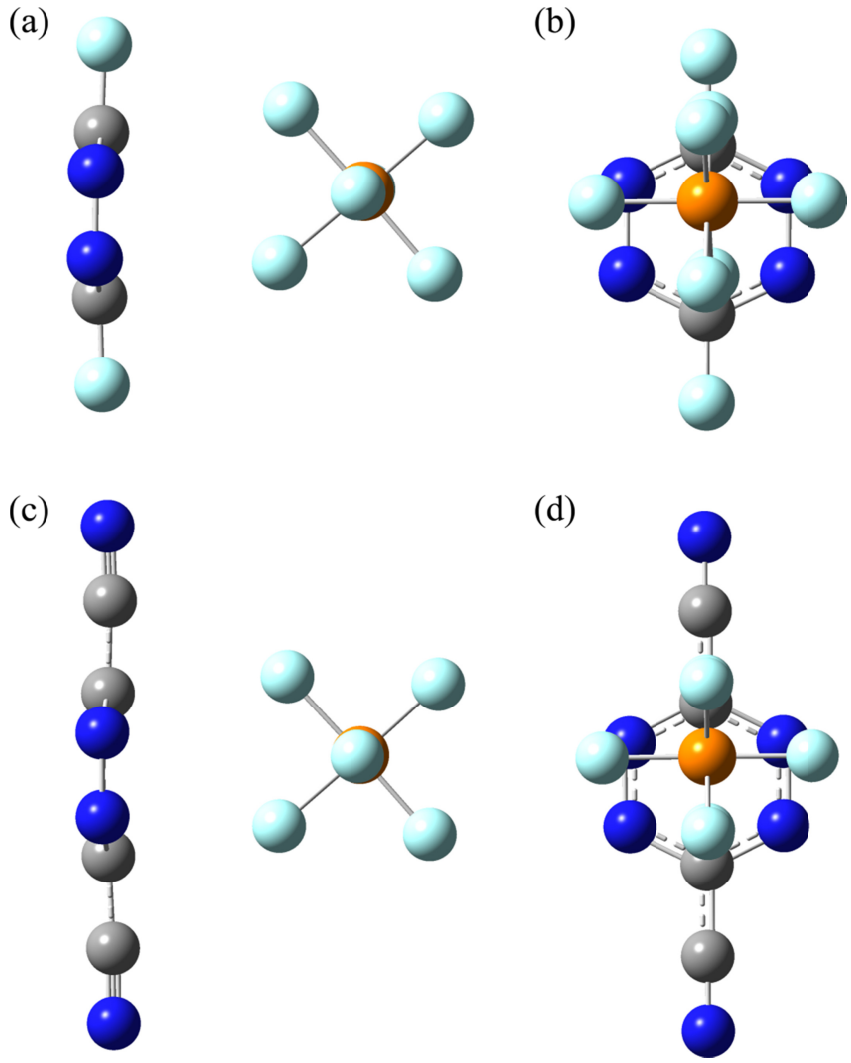

Figure 24. Geometry optimized structures of the tetrazine derivatives with $[PF_6]^-$. (a) Side-view and (b) top-view of a ball and stick representation of the $C_2N_4F_2\cdots[PF_6]^-$ complex. (c) Side-view and (d) top-view of a ball and stick representation of the $C_2N_4(CN)_2\cdots[PF_6]^-$ complex. Atom colors: carbon (grey), nitrogen (blue), fluorine (light blue), and phosphorus (orange).

Table 3. F-C contact distances (Å) and binding energies (kcal mol^{-1}) for the geometry-optimized $C_2N_4R_2\cdots[X]$ complexes (R = F, CN; X = $[BF_4]^-$, $[PF_6]^-$).

	$d_{F\text{-}C,}$ Å	$E_{binding}$, kcal mol^{-1}
$C_2N_4F_2\cdots[BF_4]^-$	2.69 2.69	-12.3
$C_2N_4(CN)_2\cdots[BF_4]^-$	2.63 2.64	-18.4
$C_2N_4F_2\cdots[PF_6]^-$	2.88 2.78	-9.6
$C_2N_4(CN)_2\cdots[PF_6]^-$	2.80 2.70	-14.6

F-C contact distances upon changing the tetrazine substituent from CN to F, indicating that the CN substituent renders the arene more amenable to anion-π interactions. The trend in binding energy also supports this conclusion. No appreciable changes in the bond distances within the tetrazine were exhibited for any of the complexes.

b. $C_4N_2R_4\cdots[X]^-$ complexes (R = CN, F; X = $[BF_4]^-$, $[PF_6]^-$)

The $C_4N_2R_4\cdots[X]^-$ complexes also exhibited short F-C distances and favorable binding energies. It is noted that the $C_4N_2F_4\cdots[PF_6]^-$ complex exhibited one imaginary frequency of minimal energy (< 5 cm^{-1}). The $[BF_4]^-$ anion aligned with both derivatives of pyrazine such that each F atom of the anion resides over one of the C-C bonds of pyrazine, sharing contact equally with each electropositive carbon atom in the bond (Figure 25, Table 4). The alignment of $[PF_6]^-$ with the pyrazine derivatives, however, differs from that of $[BF_4]^-$ in that three F atoms are aligned with pyrazine (Figure 26). Two of the anion F atoms align directly with pyrazine C atoms on one side while the third anion F atom resides over the C-C bond on the other side of the molecule, with F-C distances again indicative of close contacts due to anion-π interactions (Table 4). The $[BF_4]^-$ anion engages in stronger anion-π interactions with pyrazine than $[PF_6]^-$ as in the case of the tetrazine complexes. The relative difference in binding energies between the F and CN derivatives, however, is much greater with pyrazine than with tetrazine, possibly due to the greater difference in Q_{zz} and $\alpha_{||}$ seen in the pyrazine derivatives as opposed to the tetrazine derivatives. No appreciable changes to the pyrazine bond distances were observed.

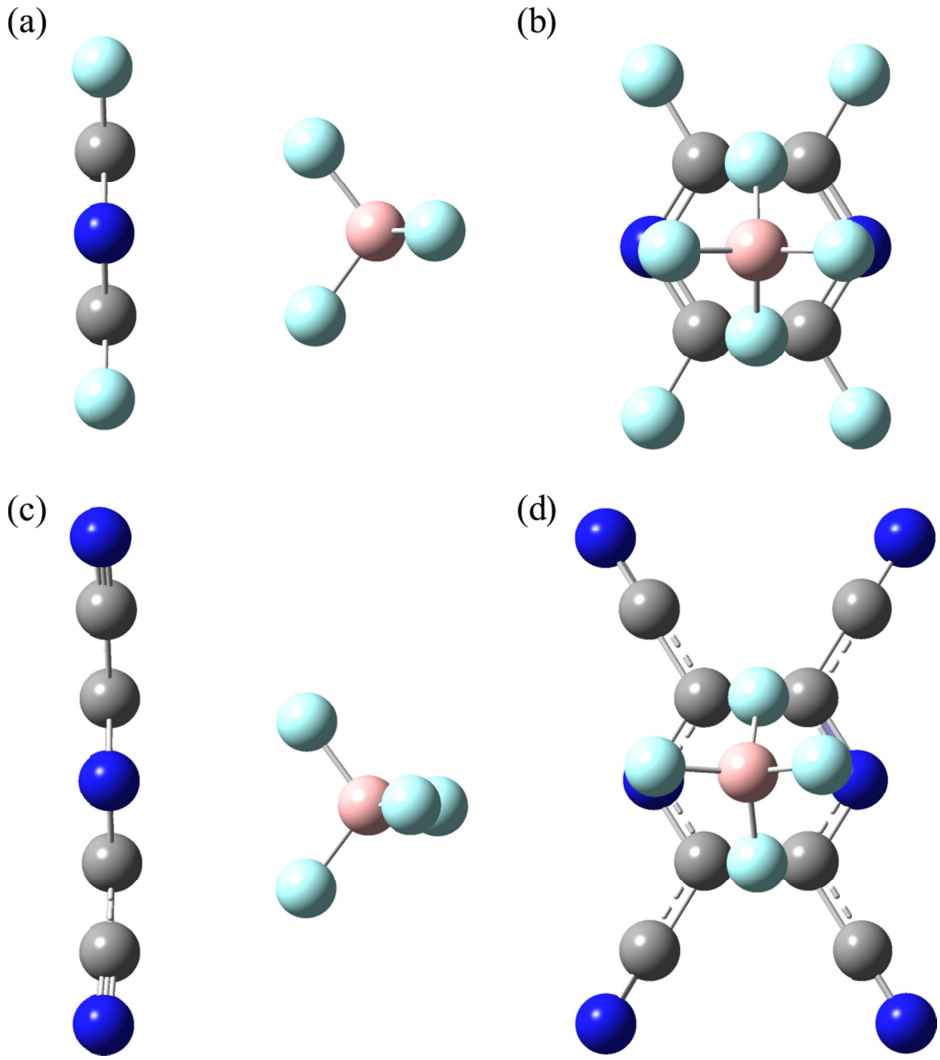

Figure 25. Geometry optimized structures of the pyrazine derivatives with $[BF_4]^-$. (a) Side-view and (b) top-view of a ball and stick representation of the $C_4N_2F_4\cdots[BF_4]^-$ complex. (c) Side-view and (d) top-view of a ball and stick representation of the $C_4N_2(CN)_4\cdots[BF_4]^-$ complex. Atom colors: carbon (grey), nitrogen (blue), fluorine (light blue), and boron (pink).

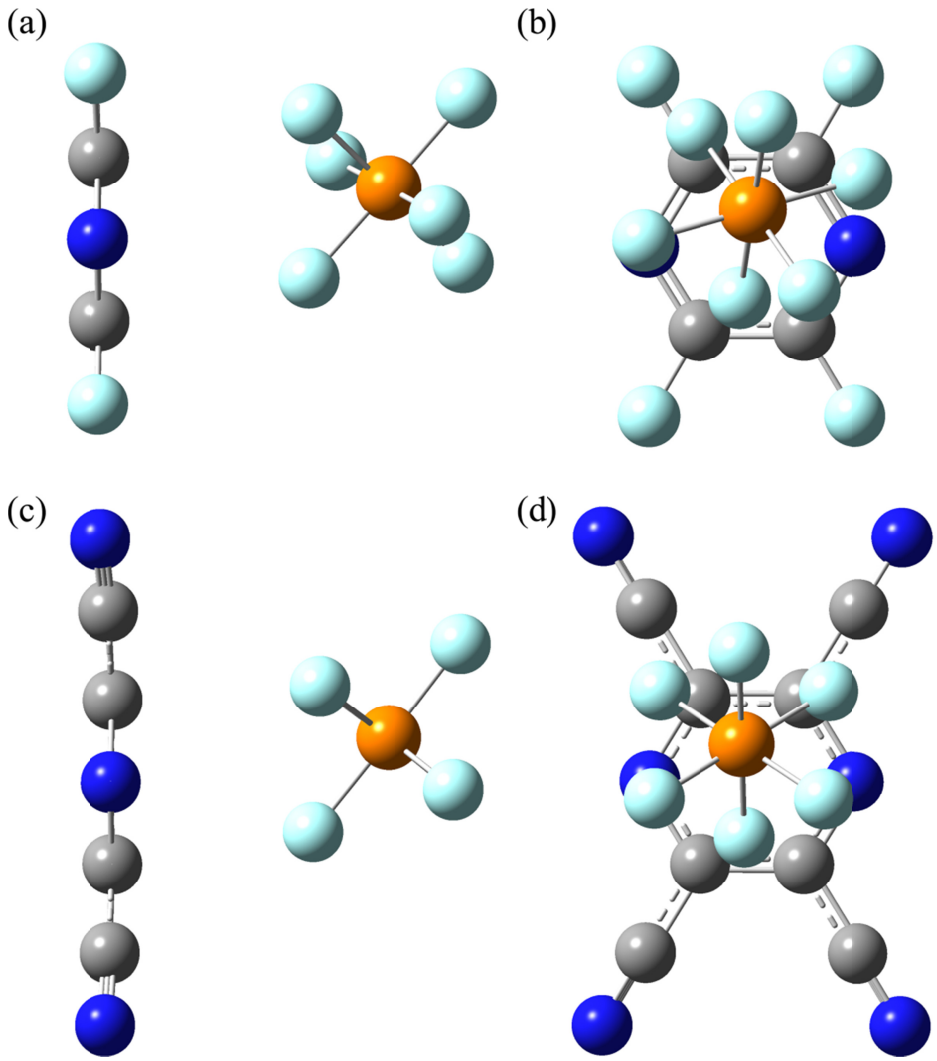

Figure 26. Geometry optimized structures of the pyrazine derivatives with $[PF_6]^-$. (a) Side-view and (b) top-view of a ball and stick representation of the $C_4N_2F_4\cdots[PF_6]^-$ complex. (c) Side-view and (d) top-view of a ball and stick representation of the $C_4N_2(CN)_4\cdots[PF_6]^-$ complex. Atom colors: carbon (grey), nitrogen (blue), fluorine (light blue), and phosphorus (orange).

Table 4. F-C contact distances (Å) and binding energies (kcal mol^{-1}) for the geometry-optimized $C_4N_2R_4\cdots[X]$ complexes (R = F, CN; X = $[BF_4]^-$, $[PF_6]^-$). Distances on the same line are from the same anion F atom to a different arene C atom.

	$d_{F-C,}$ Å	$E_{binding}$, kcal mol^{-1}
$C_4N_2F_4\cdots[BF_4]^-$	2.94, 2.94 2.94, 2.94	-10.8
$C_4N_2(CN)_4\cdots[BF_4]^-$	2.84, 2.82 2.80, 2.79	-22.7
$C_4N_2F_4\cdots[PF_6]^-$	3.01, 3.04 3.00 3.37	-8.7
$C_4N_2(CN)_4\cdots[PF_6]^-$	2.91, 2.91 2.92 2.92	-19.1

c. Comparison between the $C_2N_4R_2$ and $C_4N_2R_4$ complexes

In general, the tetrazine complexes showed shorter F-C contacts between the anion and the arene than the pyrazine derivatives. The binding energies, however, imply a different situation. For the F derivatives of pyrazine and tetrazine, the $C_2N_4F_2\cdots[X]^-$ complexes form stronger anion-π interactions with both $[BF_4]^-$ and $[PF_6]^-$. For the CN derivatives, however, an increase in binding energy is observed for pyrazine as compared to tetrazine. This situation may be a result of the increased Q_{zz} and $\alpha_{||}$ observed for $C_4N_2(CN)_4$ as compared to $C_2N_4(CN)_2$. The increased number of CN groups compensates for the fewer N atoms in pyrazine to allow for stronger anion-π binding energies. It is interesting to note that, while the $[PF_6]^-$ anion establishes three close F-C contacts with both pyrazine derivatives, the $[BF_4]^-$ anion retains the same geometry in the complexes with pyrazine as it does in the complexes with tetrazine, namely with two F atoms directed towards the arene.

iii. Complexes of two arenes and one anion

In order to gain a more realistic picture of the interactions occurring in the square metallacycles, the complexity of the models examined using DFT was increased to incorporate two arenes surrounding one anion in a stacked arrangement. This arrangement mimics part of the environment surrounding the encapsulated ligand, namely the two ligand tetrazine rings that align with the $[BF_4]^-$ in the cavity (Figure 27). Also, complexes incorporating both pyrazine and tetrazine derivatives were examined to determine whether there would be a preference for one arene over the other.

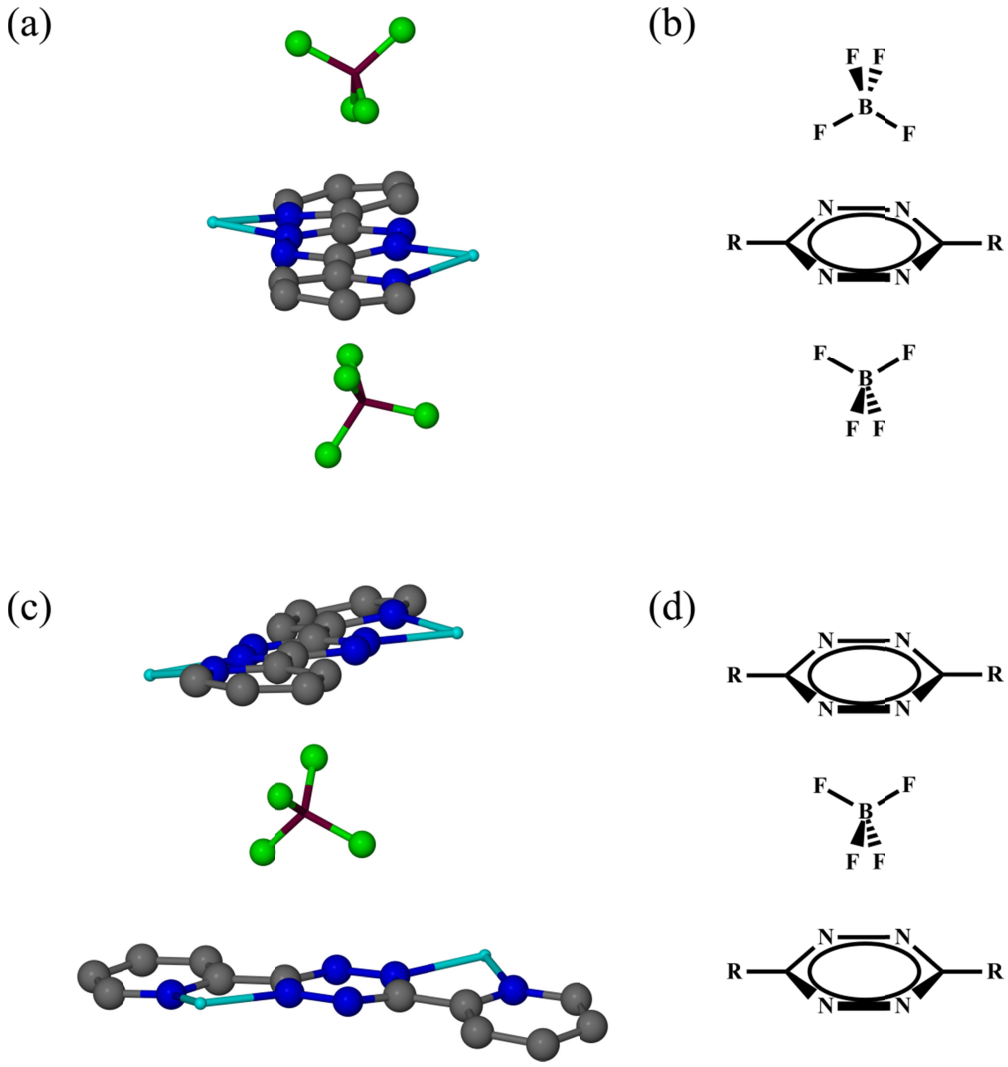

Figure 27. (a) The anion-arene-anion interaction in $[Ni_4(bptz)_4(NCCH_3)_8][BF_4]_8$ and (b) the corresponding computational model examined. (c) Ball and stick representation of the arene-anion-arene interaction in $[Ni_4(bptz)_4(NCCH_3)_8][BF_4]_8$ and (b) the corresponding computational model. Tetrazine and $[BF_4]^-$ are used as examples. Atom colors: carbon (grey), nitrogen (blue), fluorine (green), boron (maroon), and nickel (teal). R = F and CN. Figures (a) and (c) were generated from data presented in Dunbar *et al.*[70]

a. $C_2N_4R_2\cdots[BF_4]^-\cdots C_2N_4R_2$ complexes (R = CN, F)

The $C_2N_4R_2\cdots[BF_4]^-\cdots C_2N_4R_2$ complexes display an optimized geometry in which the tetrazine molecules are rotated 90° with respect to one another, maximizing F-C contacts with the $[BF_4]^-$ anion and both arenes (Figure 28). The F-C contacts (Table 5) are short (2.74 and 2.71 Å on average for R = F and CN, respectively), but longer than those in the corresponding $C_2N_4R_2\cdots[BF_4]^-$ complexes (2.69 Å and 2.63 Å for R = F and CN, respectively). This arrangement is reminiscent of the proximity of the ligand tetrazine rings with respect to the encapsulated $[BF_4]^-$ in the $[M_4(bptz)_4(NCCH_3)_8][BF_4]_8$ metallacycles of Zn^{II}, Ni^{II}, Co^{II}, and Fe^{II} (in which the bptz ligands are rotated only 60° with respect to one another due to structural constraints imposed by chelation to the metal centers). The computationally-derived F-C distances are only slightly shorter than the F-C distances observed in $[Fe_4(bptz)_4(NCCH_3)_8][BF_4]_8$ (2.74 – 2.88 Å, refer to Chapter III for a more detailed discussion), the metallacycle with the smallest cavity. The binding energies are favorable and approximately twice the binding energies of the complexes with only one tetrazine molecule and $[BF_4]^-$ anion, as expected based on research by Deyà and coworkers regarding the additivity of the anion-π interactions between halides and halide derivatives of 1,3,5-triazine.[22] The energies and F-C distances in the $C_2N_4R_2\cdots[BF_4]^-\cdots C_2N_4R_2$ complexes of follow the same trends with regard to arene substituents as seen in the complexes with one arene and one anion, namely closer distances and greater binding energies for the CN derivative as opposed to the F derivative. The tetrazine molecules exhibit no bond length changes.

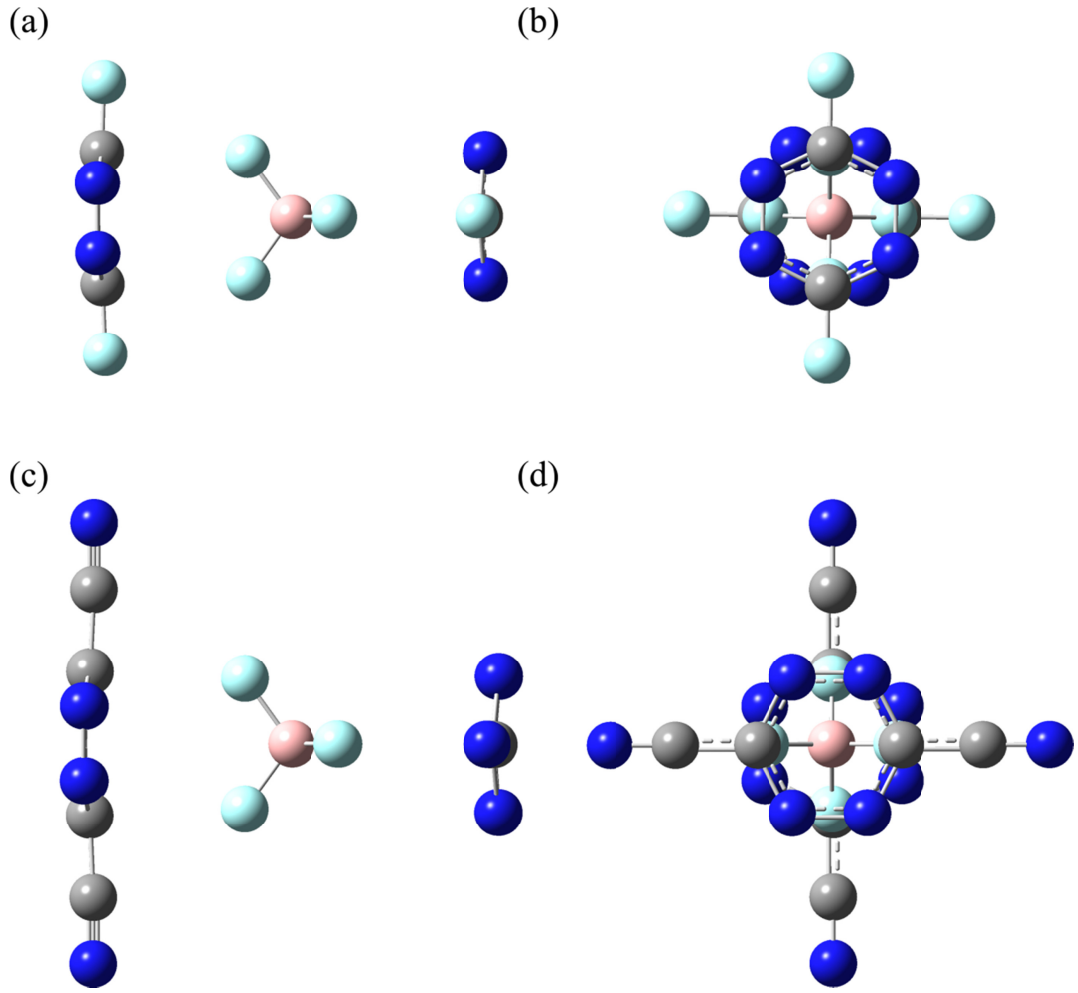

Figure 28. Geometry optimized structures of the complexes with two tetrazine derivatives and $[BF_4]^-$. (a) Side-view and (b) top-view of a ball and stick representation of the $C_2N_4F_2\cdots[BF_4]^-\cdots C_2N_4F_2$ complex. (c) Side-view and (d) top-view of a ball and stick representation of the $C_2N_4(CN)_2\cdots[BF_4]^-\cdots C_2N_4(CN)_2$ complex. Atom colors: carbon (grey), nitrogen (blue), fluorine (light blue), and boron (pink).

Table 5. F-C contact distances (Å) and binding energies (kcal mol^{-1}) for the geometry-optimized $C_2N_4R_2\cdots[X]^-\cdots C_2N_4R_2$, $C_4N_2R_4\cdots[X]^-\cdots C_4N_2R_4$, and $C_4N_2R_4\cdots[X]^-\cdots C_2N_4R_2$ complexes ($X = [BF_4]^-$; R = F, CN). Distances on the same line are from the same anion F atom to a different arene C atom. Rings defined as follows based on the complex identification in the first column: Arene 1···$[X]^-$···Arene 2.

	Arene 1 $d_{F\text{-}C,}$ Å	Arene 2 $d_{F\text{-}C,}$ Å	$E_{binding,}$ kcal mol^{-1}
$C_2N_4F_2\cdots[BF_4]^-\cdots C_2N_4F_2$	2.74 2.74	2.74 2.74	-23.0
$C_2N_4(CN)_2\cdots[BF_4]^-\cdots C_2N_4(CN)_2$	2.71 2.71	2.71 2.71	-33.2
$C_4N_2F_4\cdots[BF_4]^-\cdots C_4N_2F_4$	2.97, 2.97 2.99, 2.98	2.97, 2.98 2.99, 2.98	-20.5
$C_4N_2(CN)_4\cdots[BF_4]^-\cdots C_4N_2(CN)_4$	2.89, 2.89 2.88, 2.88	2.88, 2.98 2.89, 2.88	-40.3
$C_4N_2F_4\cdots[BF_4]^-\cdots C_2N_4F_2$	2.97, 2.99 2.99, 2.98	2.74 2.76	-21.7
$C_4N_2(CN)_4\cdots[BF_4]^-\cdots C_2N_4(CN)_2$	2.88, 2.87 2.86, 2.87	2.75 2.72	-36.8

b. $C_4N_2R_4\cdots[BF_4]^-\cdots C_4N_2R_4$ complexes (R = CN, F)

The $C_4N_2R_4\cdots[BF_4]^-\cdots C_4N_2R_4$ complexes exhibit an optimized geometry in which the pyrazine molecules are rotated 90^o with respect to one another, with each pyrazine molecule engaged in two contacts between the anion F atoms and the C-C bond of pyrazine, a total of four such contacts (Figure 29). The F-C contacts are short (2.98 Å and 2.88 Å on average for R = F and CN , respectively, Table 5) but longer than those in the corresponding $C_4N_2R_4\cdots[BF_4]^-$ complexes (2.94 Å and 2.84 Å for R = F and CN, respectively). The binding energies are favorable and, as in the aforementioned tetrazine case, they are approximately twice that of the corresponding $C_4N_2R_4\cdots[BF_4]^-$ complex. The F-C distances and binding energies also follow the trend of shorter F-C distances and greater binding energies for the CN derivative as opposed to the F derivative. No changes in the pyrazine C-C or C-N bond lengths were observed for these complexes.

c. $C_4N_2R_4\cdots[BF_4]^-\cdots C_2N_4R_2$ complexes (R = CN, F)

The $C_4N_2R_4\cdots[BF_4]^-\cdots C_2N_4R_2$ complexes optimize to a geometry in which the pyrazine and tetrazine molecules are arranged such that the N atoms of pyrazine are aligned with the C atoms of tetrazine, with each arene participating in anion-π interactions mirroring those in their respective $C_4N_2R_4\cdots[BF_4]^-$ or $C_2N_4R_2\cdots[BF_4]^-$ complexes (that is, F-C contacts with tetrazine and F to C-C bond contacts with pyrazine, Figure 30). The F-C contacts are short (2.98 and 2.88 Å on average for R = F and CN for pyrazine, respectively, and 2.75 and 2.73Å on average for R = F and CN for tetrazine, respectively), similar to those observed in their corresponding two arene with one $[BF_4]^-$ complexes (Table 5). The binding energies are favorable and

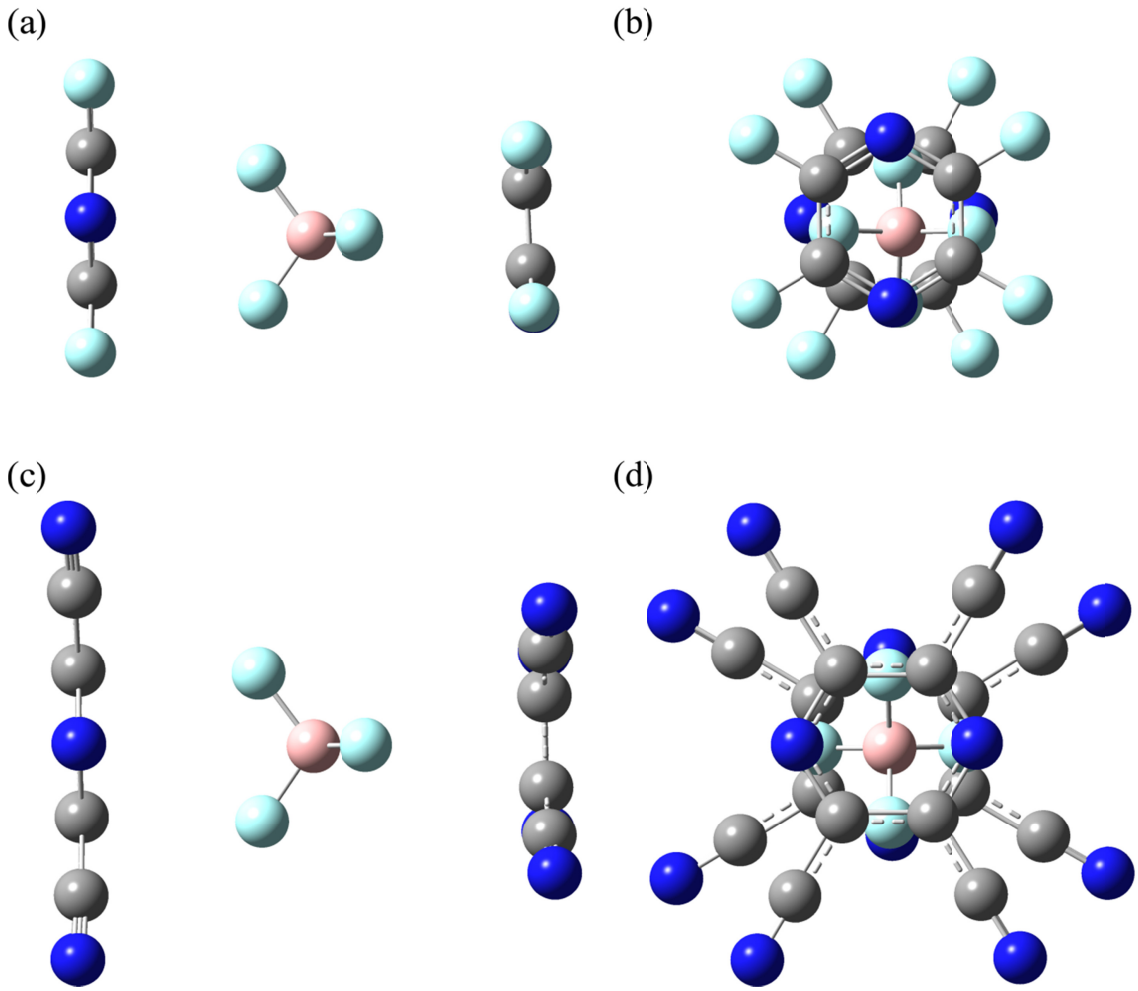

Figure 29. Geometry optimized structures of the complexes with two pyrazine derivatives and $[BF_4]^-$. (a) Side-view and (b) top-view of a ball and stick representation of the $C_4N_2F_4\cdots[BF_4]^-\cdots C_4N_2F_4$ complex. (c) Side-view and (d) top-view of a ball and stick representation of the $C_4N_2(CN)_4\cdots[BF_4]^-\cdots C_4N_2(CN)_4$ complex. Atom colors: carbon (grey), nitrogen (blue), fluorine (light blue), and boron (pink).

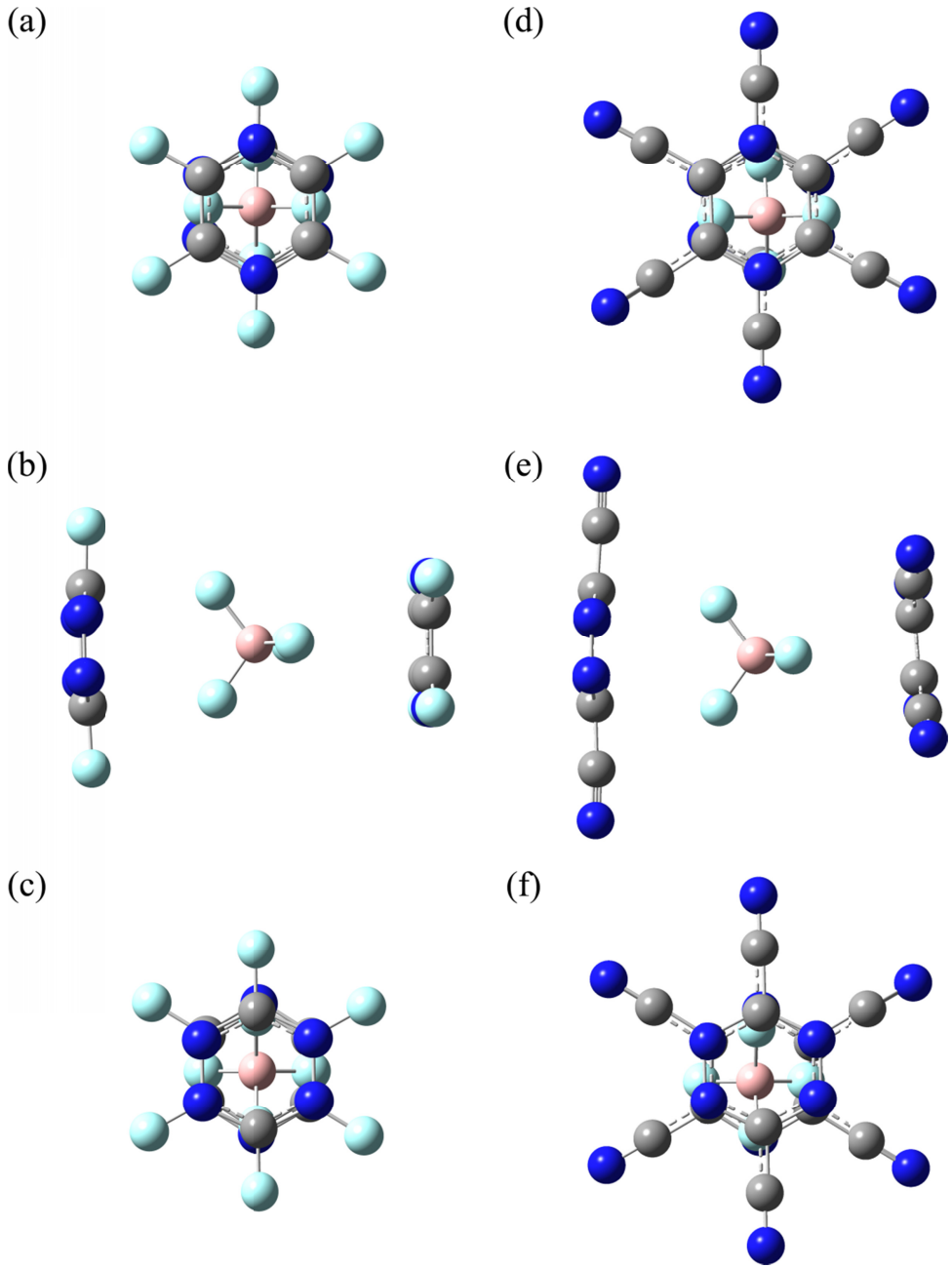

Figure 30. Geometry optimized structures of the complexes with one pyrazine and one tetrazine derivative and $[BF_4]^-$. (a) View down principle axis through $C_4N_2F_4$, (b) side-view and (c) view down principle axis through $C_2N_4F_2$ of a ball and stick representation of the $C_4N_2F_4\cdots[BF_4]^-\cdots C_2N_4F_2$ complex. (d) View down principle axis through $C_4N_2(CN)_4$, (b) side-view and (c) view down principle axis through $C_2N_4(CN)_2$ of a ball and stick representation of the $C_4N_2(CN)_4\cdots[BF_4]^-\cdots C_2N_4(CN)_2$ complex. Atom colors: carbon (grey), nitrogen (blue), fluorine (light blue), and boron (pink).

are approximately equal to the sum of the component $C_2N_4R_2\cdots[BF_4]^-$ and $C_4N_2R_4\cdots[BF_4]^-$ complex binding energies, as predicted based on the additivity of anion-π interactions. The F-C distances and binding energies also follow the trend of shorter F-C distances and greater binding energies for the complexes containing the CN derivative as opposed to the F derivative of the arenes. No changes in the pyrazine C-C and C-N or the tetrazine N-N and C-N bond lengths were observed for these complexes.

d. $C_2N_4R_2\cdots[PF_6]^-\cdots C_2N_4R_2$ complexes (R = CN, F)

The $C_2N_4R_2\cdots[PF_6]^-\cdots C_2N_4R_2$ complexes display an optimized geometry in which the tetrazine molecules are aligned with one another, thereby maximizing F-C contacts between the $[PF_6]^-$ anion and both tetrazine moieties, similar to the complexes with $[BF_4]^-$ (Figure 31). The F-C contacts (Table 6) are short (2.84 and 2.80 Å on average for R = F and CN, respectively), and are longer than those in the corresponding $C_2N_4R_2\cdots[PF_6]^-$ complexes (2.81 Å and 2.75 Å for R = F and CN, respectively). The binding energies are favorable and approximately twice the binding energies of the $C_2N_4R_2\cdots[PF_6]^-$ complexes. The energies and distances follow the trend of shorter distances and greater binding energies for the CN derivatives as opposed to the F derivatives. Also, no appreciable changes in the N-N and C-N bond distances were observed for tetrazine.

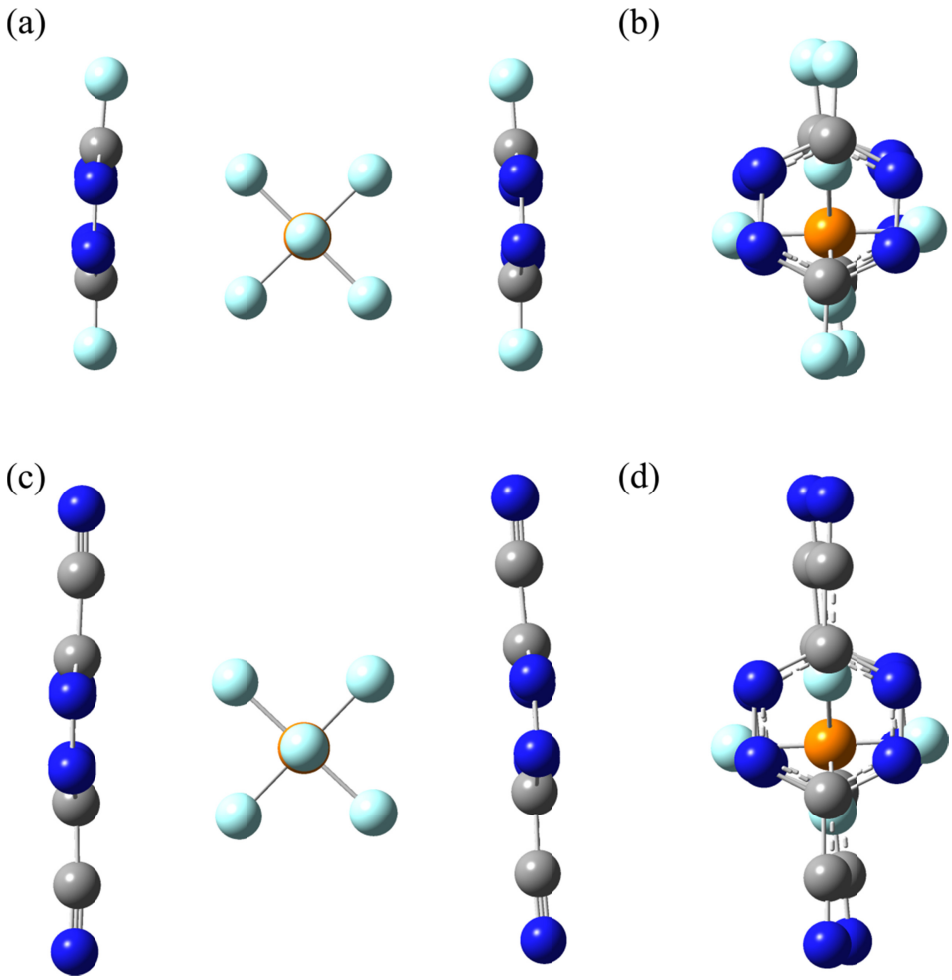

Figure 31. Geometry optimized structures of the complexes with two tetrazine derivatives and $[PF_6]^-$. (a) Side-view and (b) top-view of a ball and stick representation of the $C_2N_4F_2\cdots[PF_6]^-\cdots C_2N_4F_2$ complex. (c) Side-view and (d) top-view of a ball and stick representation of the $C_2N_4(CN)_2\cdots[PF_6]^-\cdots C_2N_4(CN)_2$ complex. Atom colors: carbon (grey), nitrogen (blue), fluorine (light blue), and phosphorus (orange).

Table 6. F-C contact distances (Å) and binding energies (kcal mol^{-1}) for the geometry-optimized $C_2N_4R_2\cdots[X]^-\cdots C_2N_4R_2$, $C_4N_2R_4\cdots[X]^-\cdots C_4N_2R_4$, and $C_4N_2R_4\cdots[X]^-\cdots C_2N_4R_2$ complexes (X = $[PF_6]^-$; R = F, CN). Distances on the same line are from the same anion F atom to a different arene C atom. Arenes defined as follows based on the complex identification in the first column: Arene 1···$[X]^-$···Arene 2.

	Ring 1 $d_{F\text{-}C,}$ Å	Ring 2 $d_{F\text{-}C,}$ Å	$E_{binding,}$ kcal mol^{-1}
$C_2N_4F_2\cdots[PF_6]^-\cdots C_2N_4F_2$	2.80 2.86	2.80 2.86	-18.1
$C_2N_4(CN)_2\cdots[PF_6]^-\cdots C_2N_4(CN)_2$	2.77 2.83	2.77 2.73	-26.7
$C_4N_2F_4\cdots[PF_6]^-\cdots C_4N_2F_4$	3.01, 3.02 3.07, 3.07	3.07, 3.07 3.02, 3.02	-16.5
$C_4N_2(CN)_4\cdots[PF_6]^-\cdots C_4N_2(CN)_4$	2.97 3.10 3.00, 3.44	3.01 3.00 2.96, 2.97	-34.0
$C_4N_2F_4\cdots[PF_6]^-\cdots C_2N_4F_2$	3.03 3.44 3.04, 3.05	2.82 2.82	-17.2
$C_4N_2(CN)_4\cdots[PF_6]^-\cdots C_2N_4(CN)_2$	3.00 2.97 2.95, 2.96	2.80 2.90	-30.5

e. $C_4N_2R_4\cdots[PF_6]^-\cdots C_4N_2R_4$ complexes (R = CN, F)

The $C_4N_2R_4\cdots[PF_6]^-\cdots C_4N_2R_4$ complexes are the only complexes in which the final optimized geometries differ between the F and CN derivatives (Figure 32). In the F derivative, the $[PF_6]^-$ engages in two contacts between the F atoms and the C-C bond of each tetrafluoropyrazine, unlike the $C_4N_2F_4\cdots[PF_6]^-$ complexes in which three F atoms are aligned with the pyrazine ring. The F-C distances average 3.05 Å (Table 6), slightly less than the sum of the van der Waals radii of C and F. The binding energy of this complex (-16.5 kcal mol^{-1}) is approximately twice that of the $C_4N_2F_4\cdots[PF_6]^-$ complex (-8.67 kcal mol^{-1}), despite the difference in the binding geometry.

The structure of the $C_4N_2(CN)_4\cdots[PF_6]^-\cdots C_4N_2(CN)_4$ complex exhibits an orientation of the $[PF_6]^-$ anion wherein three F-C contacts are made to the pyrazine, as in the $C_4N_2(CN)_4\cdots[PF_6]^-$ complex. The F-C distances are shorter than in the F derivative (Table 6), averaging 2.97 Å. The binding energy of the CN derivative is less than that of the F derivative complex and also approximately twice that of its corresponding $C_4N_2(CN)_4\cdots[PF_6]^-$ complex. Neither complex exhibits appreciable changes in the C-N or C-C bond distances of the pyrazine.

f. $C_4N_2R_4\cdots[PF_6]^-\cdots C_2N_4R_2$ complexes

In order for the $C_4N_2R_4\cdots[PF_6]^-\cdots C_2N_4R_2$ complex to maximize F-C contacts, the arenes are canted with respect to one another such that the $[PF_6]^-$ anion engages in 3 F-C contacts with $C_4N_2R_4$ and two F-C contacts with $C_2N_4R_2$ (Figure 33). The distances between the $[PF_6]^-$ anion and $C_2N_4R_2$ are shorter than those between the $[PF_6]^-$ anion and $C_4N_2R_4$ (Table 6, averages of 3.04 and 2.95 Å for R = F and CN, respectively, and 2.81

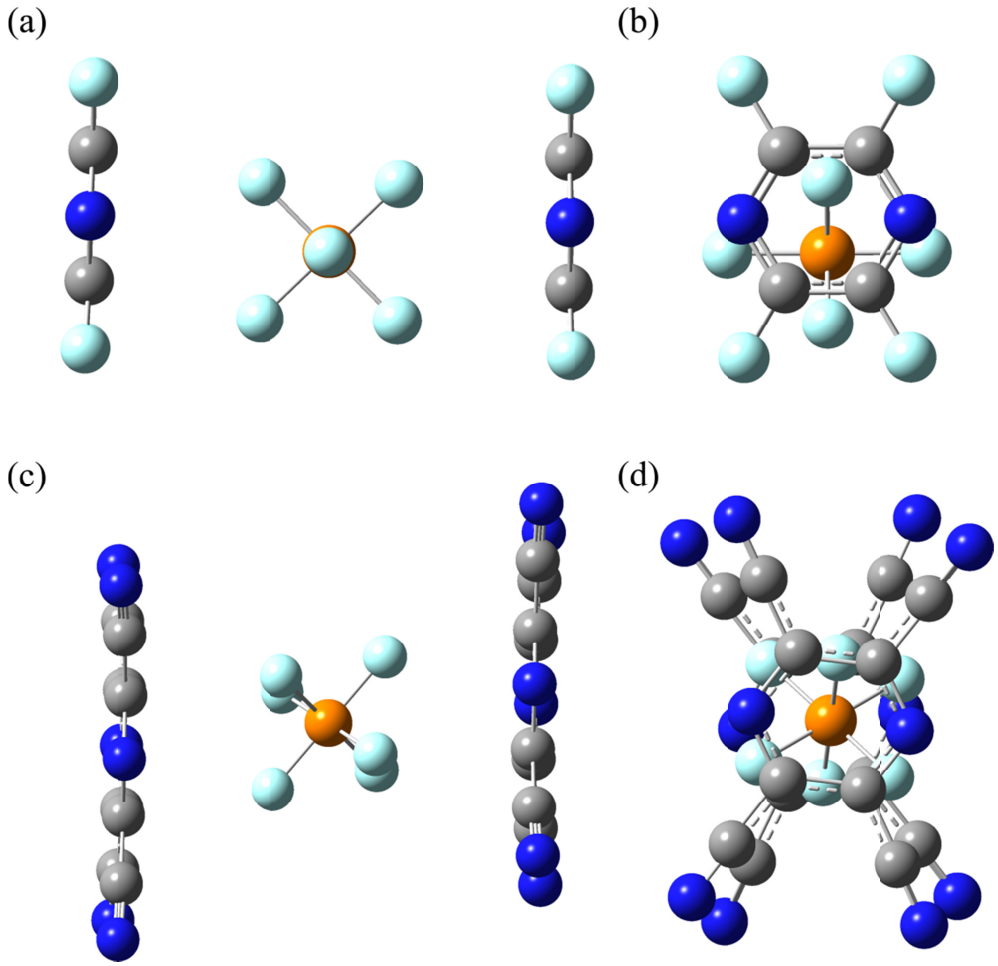

Figure 32. Geometry optimized structures of the complexes with two pyrazine derivatives and $[PF_6]^-$. (a) Side-view and (b) top-view of a ball and stick representation of the $C_4N_2F_4\cdots[PF_6]^-\cdots C_4N_2F_4$ complex. (c) Side-view and (d) top-view of a ball and stick representation of the $C_4N_2(CN)_4\cdots[PF_6]^-\cdots C_4N_2(CN)_4$ complex. Atom colors: carbon (grey), nitrogen (blue), fluorine (light blue), and phosphorus (orange).

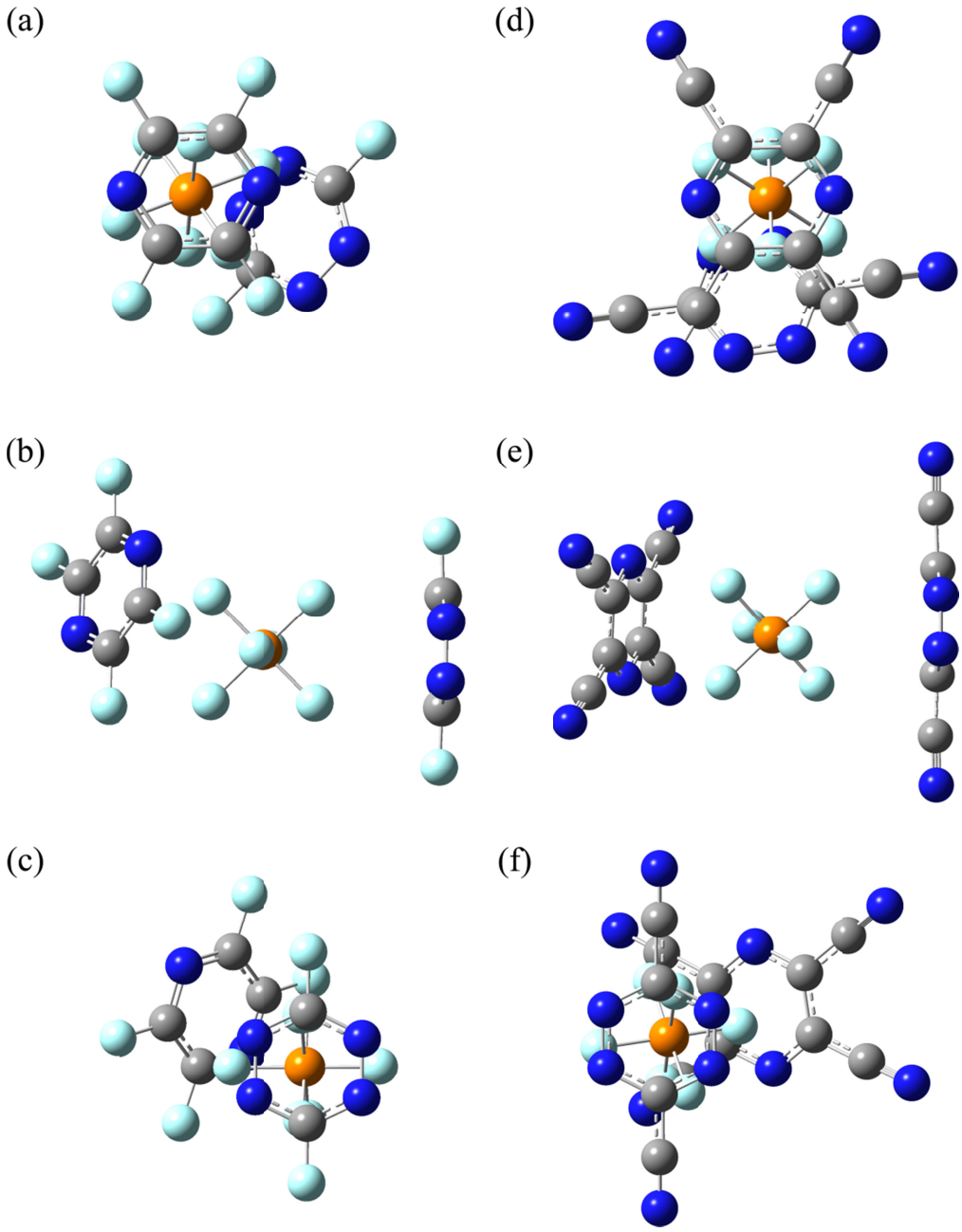

Figure 33. Geometry optimized structures of the complexes with one pyrazine and one tetrazine derivative and $[PF_6]^-$. (a) View down principle axis through $C_4N_2F_4$, (b) side-view and (c) view down principle axis through $C_2N_4F_2$ of a ball and stick representation of the $C_4N_2F_4\cdots[PF_6]^-\cdots C_2N_4F_2$ complex. (d) View down principle axis through $C_4N_2(CN)_4$, (b) side-view and (c) view down principle axis through $C_2N_4(CN)_2$ of a ball and stick representation of the $C_4N_2(CN)_4\cdots[PF_6]^-\cdots C_2N_4(CN)_2$ complex. Atom colors: carbon (grey), nitrogen (blue), fluorine (light blue), and phosphorus (orange).

and 2.80 Å for R = F and CN for tetrazine, respectively). The F derivative complex shows longer contact distances and weaker binding energies than the complex with the CN derivative. The binding energies of both complexes demonstrate the same additivity as the other $C_xN_{6-x}R_x\cdots[X]^-\cdots C_xN_{6-x}R_x$ complexes discussed thus far. In addition, no appreciable change in the C-C, C-N, or N-N bond distances of the arenes occurs upon complexation with $[PF_6]^-$.

g. Comparisons of the $C_xN_{6-x}R_x\cdots[X]^-\cdots C_xN_{6-x}R_x$ complexes

One of the key findings in the study of the $C_xN_{6-x}R_x\cdots[X]^-\cdots C_xN_{6-x}R_x$ complexes of tetrazine and pyrazine is the directionality of the anion-π interaction. In fact, the directionality exhibited in the $C_2N_4R_2\cdots[BF_4]^-\cdots C_2N_4R_2$ complexes suggests that the anion-π interactions can indeed direct the orientation of molecules in a supramolecular architecture, which is borne out in the metallacycles of bptz and divalent metal ions. The distances in the case of the $C_2N_4R_2\cdots[BF_4]^-\cdots C_2N_4R_2$ complex, the distances in the gas phase complex between the anion F and tetrazine C atoms is on the low end of the anion-ligand F-C distances observed in $[Fe_4(bptz)_4(NCCH_3)_8][BF_4]_8$. The binding energies of the mixed pyrazine/tetrazine complexes are approximately the average of the energies of the corresponding two tetrazine and two pyrazine complexes of the same substituent and anion. Also, the surprising results that the complexes of both $[BF_4]^-$ and $[PF_6]^-$ with two tetracyanopyrazine molecules are energetically more favorable despite exhibiting longer F-C contact distances suggest that the CN substituent can compensate electrostatically for the two N atoms that have been replaced for C atoms in pyrazine, as supported by the higher Q_{zz} of $C_4N_2(CN)_4$ with regards to $C_2N_4(CN)_2$. The favorable binding of

polyatomic anions to two pyrazine molecules also suggests that pyrazine-based ligands have the potential to anion-template metallacyclic structures, although the interaction distances may be too long for some of the metallacyclic cavities.

iv. Complexes of two anions with one arene

Of the complexes examined computationally involving one arene surrounded by two anions, only one set of complexes converged at a geometry optimized minimum: the $[X]^-\cdots C_4N_2(CN)_4\cdots[X']^-$ complexes (where X = $[BF_4]^-$, X′ = $[BF_4]^-$; X = $[PF_6]^-$, X′ = $[PF_6]^-$; X = $[BF_4]^-$, X′ = $[PF_6]^-$). The rest of the complexes failed to converge at an energy minimum. Closer inspection of the geometries of the calculations that did not converge reveals that, in all cases, the anions have moved well outside a reasonable anion-π interaction distance to the arene, suggesting that these types of interactions are generally unfavorable. This is not entirely unexpected, as two anionic species in close proximity separated only by an arene molecule would repel one another. The three converged complexes, however, do yield insight into anion-π interactions of this configuration.

The $[BF_4]^-\cdots C_4N_2(CN)_4\cdots[BF_4]^-$ complex exhibit the same binding orientation as observed in the modeled complexes of $C_4N_2(CN)_4\cdots[BF_4]^-$, namely that both $[BF_4]^-$ anions engage in two F to C-C bond contacts with the pyrazine moiety, with moderate distances that average ~3.06 Å (Figure 34, Table 7, just within the sum of the F and C van der Waals radii (3.17 Å)). The binding energy of this complex is positive, suggesting an unfavorable interaction, which is corroborated by the longer F-C distances. No appreciable change in C-C or C-N bond distances in pyrazine was observed.

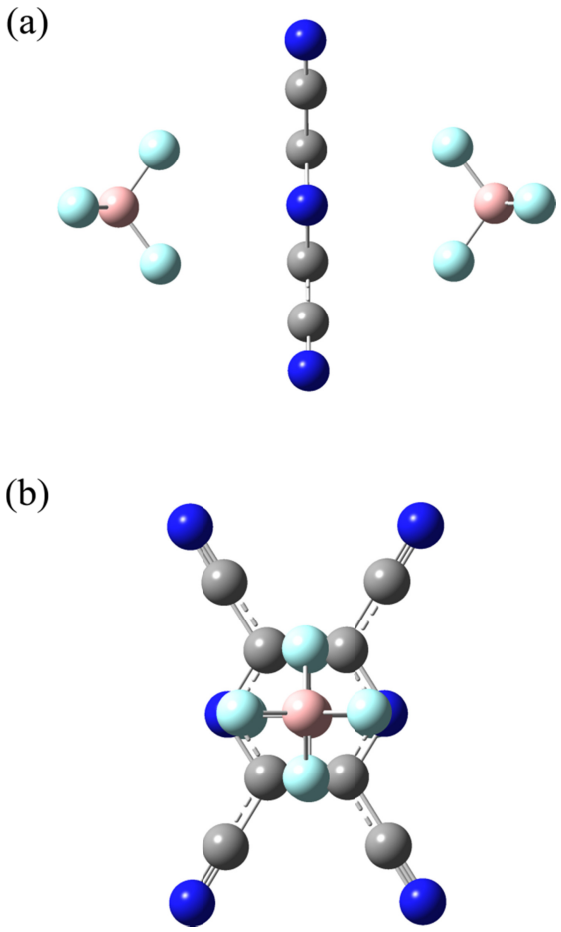

Figure 34. (a) Side-view and (b) top-view of a ball and stick representation of the geometry optimized $[BF_4]^-\cdots C_4N_2(CN)_4\cdots[BF_4]^-$ complex. Atom colors: carbon (grey), nitrogen (blue), fluorine (light blue), and boron (pink).

Table 7. F-C contact distances (Å) and binding energies (kcal mol^{-1}) for the geometry-optimized $[X]^-\cdots C_4N_3(CN)_4\cdots[X]^-$ (X = $[BF_4]^-$, $[PF_6]^-$). Distances on the same line are from the same anion F atom to a different arene C atom. Anions are defined as follows based on the complex identification in the first column: Anion 1$\cdots C_4N_2(CN)_4\cdots$Anion 2.

	Anion 1 $d_{F\text{-}C}$, Å	Anion 2 $d_{F\text{-}C}$, Å	$E_{binding}$, kcal mol^{-1}
$[BF_4]^-\cdots C_2N_4(CN)_2\cdots[BF_4]^-$	3.07, 3.07 3.07, 3.07	3.07, 3.07 3.07, 3.07	4.9
$[PF_6]^-\cdots C_4N_2(CN)_4\cdots[PF_6]^-$	3.14, 3.14 3.14, 3.14	3.14, 3.14 3.14, 3.14	7.7
$[BF_4]^-\cdots C_2N_4(CN)_2\cdots[PF_6]^-$	3.02, 3.02 3.02, 3.02	3.20, 3.20 3.20, 3.10	6.1

The $[PF_6]^-\cdots C_4N_2(CN)_4\cdots[PF_6]^-$ complex exhibits the same orientation as the complex with two $[BF_4]^-$, with longer F-C interaction distances of 3.14 Å, just within the threshold for anion-π interaction distances (Figure 35, Table 7). Again, the binding energy is positive (and greater than the complex with two $[BF_4]^-$), suggesting an unfavorable interaction, also corroborated by the elongated F-C contact distances. The bond distances in the C-C and C-N bonds of pyrazine did not change to an appreciable extent.

The $[BF_4]^-\cdots C_4N_2(CN)_4\cdots[PF_6]^-$ complex exhibited an orientation geometry similar to the previously discussed $[X]^-\cdots C_xN_{6-x}R_x\cdots[X]^-$ complexes (Figure 36). The F-C contact distances for $[BF_4]^-$ to pyrazine (3.02 Å, on average) are shorter than those for the $[PF_6]^-$ anion in the same complex (3.17 Å, on average). The $[PF_6]^-$ F-C distances are longer in the mixed anion complex than in the complex with two $[PF_6]^-$ anions, but the $[BF_4]^-$ F-C distances are actually shorter in the mixed anion complex. The binding energy is approximately the average of the binding energies of the $[BF_4]^-\cdots C_4N_2(CN)_4\cdots[BF_4]^-$ and $[PF_6]^-\cdots C_4N_2(CN)_4\cdots[PF_6]^-$ complexes. Again, there is no appreciable lengthening or shortening of the C-N or C-C bonds of the pyrazine molecule observed for this complex.

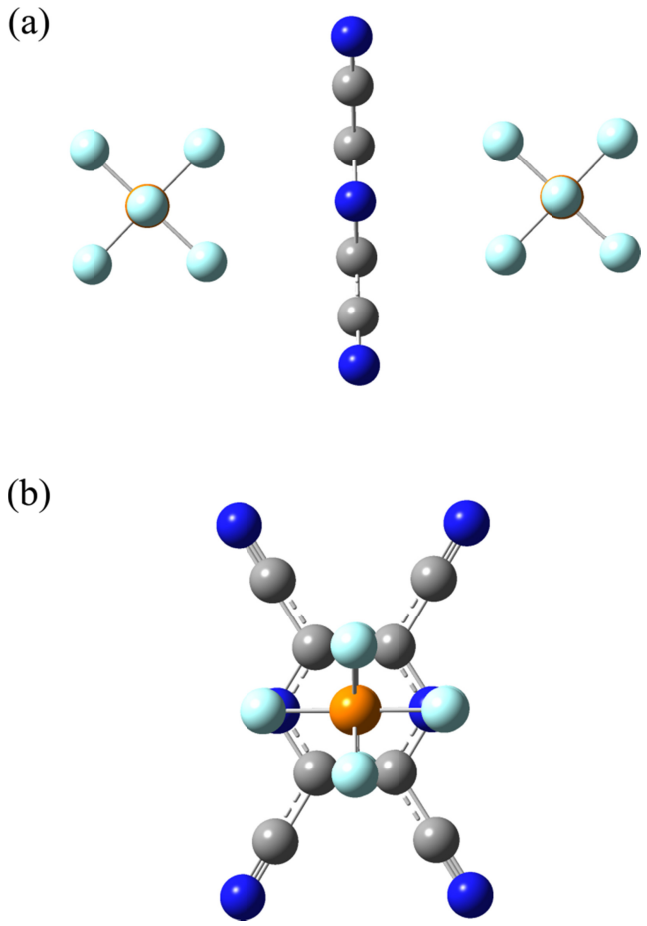

Figure 35. (a) Side-view and (b) top-view of a ball and stick representation of the geometry optimized $[PF_6]^-\cdots C_4N_2(CN)_4\cdots[PF_6]^-$ complex. Atom colors: carbon (grey), nitrogen (blue), fluorine (light blue), and phosphorus (orange).

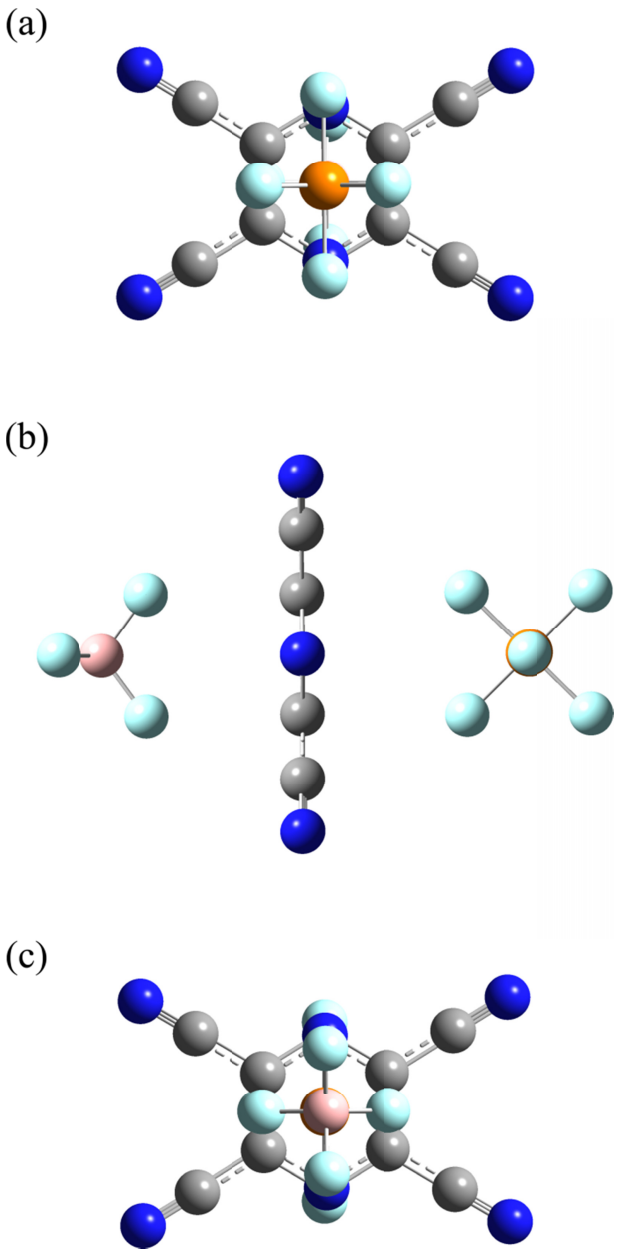

Figure 36. (a) View down principle axis through $[PF_6]^-$, (b) side-view, and (c) view down principle axis through $[BF_4]^-$ of a ball and stick representation of the geometry optimized $[BF_4]^-\cdots C_4N_2(CN)_4\cdots[PF_6]^-$ complex. Atom colors: carbon (grey), nitrogen (blue), fluorine (light blue), boron (pink), and phosphorus (orange).

Considering the positive binding energies for all of the $[X]^-\cdots C_4N_2(CN)_4\cdots[X]^-$ complexes, it is clear that the additivity of the anion-π interaction binding energy only holds for introducing multiple arenes, not multiple anions. Multiple anions interacting with one arene serve to destabilize the complex, resulting predominantly in the repulsion of the anion from the arene and one another, except in the case of an arene with a large Q_{zz} (tetracyanopyrazine). In the square metallacycles, since there are anions residing in close contact with the ligands on the periphery of the metallacycle, the interactions of the arenes with the ligands can divided into two anion-arene-anion interactions and one arene-anion-arene interaction (without taking into account the metal cations), which, when summed, should still retain a favorable total binding energy, assuming negligible contributions from interactions between the arenes themselves (as they are over 6 Å apart in the modeled complexes as well as the metallacycles) and with the metal ions in the metallacycle. Since $[X]^-\cdots C_2N_4R_2\cdots[X]^-$ complexes did not converge, the corresponding $[X]^-\cdots C_4N_2(CN)_4\cdots[X]^-$ complexes will be used to demonstrate this principle. Two $[BF_4]^-\cdots C_4N_2(CN)_4\cdots[BF_4]^-$ binding energies summed together (2 X +4.87 kcal mol^{-1} = +9.74 kcal mol^{-1}) and one $C_4N_2(CN)_4\cdots[BF_4]^-\cdots C_4N_2(CN)_4$ binding energy (-40.27 kcal mol^{-1}) yields a net binding energy of -30.53 kcal mol^{-1}, suggesting that this arrangement for pyrazine should be favorable. This also suggests that pyrazine may be able to interact with anions through anion-π interactions to template metallacyclic structures, assuming the F-C distances are sufficiently flexible.

v. Single-point energy computation of the Fe^{II} metallacycles

Over the years, the computing power at the disposal of researchers has reached the point that the computational modeling of $[Fe_4(bptz)_5(NCCH_3)_8 \subset BF_4]^{7+}$ through Gaussian 09 rather than Amsterdam Density Functional theory is possible (which was necessary in 2006 to model the Ag^I structures of bppn and bptz[79]). A single point energy computation on the fixed crystallographic structures of $[Fe_4(bptz)_5(NCCH_3)_8 \subset BF_4]^{7+}$ and $[Fe_5(bptz)_5(NCCH_3)_{10} \subset 2SbF_6]^{8+}$ were performed using the B3LYP hybrid functional and the Pople-type basis set 6-31g(d′) for C, H, N, F, and B, and SDD for the Fe^{II} ions, incorporating ECPs (diffuse functions were removed to aid convergence). For the Sb atoms, a LANL2DZdp basis set with ECPs was used.[88-91] It was necessary to perform successive stepwise SCF convergence computations to achieve convergence.

a. $[Fe_4(bptz)_4(NCCH_3)_8 \subset BF_4]^{7+}$

Single point energy computations of the $[Fe_4(bptz)_5(NCCH_3)_8]^{8+}$ cationic unit and $[BF_4]^-$ anion were also completed in order to calculate a binding energy for the anion. The binding energy is very large, -417.6 kcal mol^{-1}, suggesting that the anion is strongly bound within the cavity of the metallacycle, although much of this energy is attributable to the electrostatic attraction of the anion to the 8+ cage. ESP maps of $[Fe_4(bptz)_5(NCCH_3)_8 \subset BF_4]^{7+}$ and the $[Fe_4(bptz)_5(NCCH_3)_8]^{8+}$ cages (Figure 37) reveal behavior similar to the Ag^I complexes discussed earlier. The interior faces of the tetrazine rings of the bptz ligands bear a higher electrostatic potential than the exterior faces as the close proximity of the anion causes the electrostatic potential to decrease, also evident from comparison with the free $[Fe_4(bptz)_4(NCCH_3)_8]^{8+}$ cage. The presence

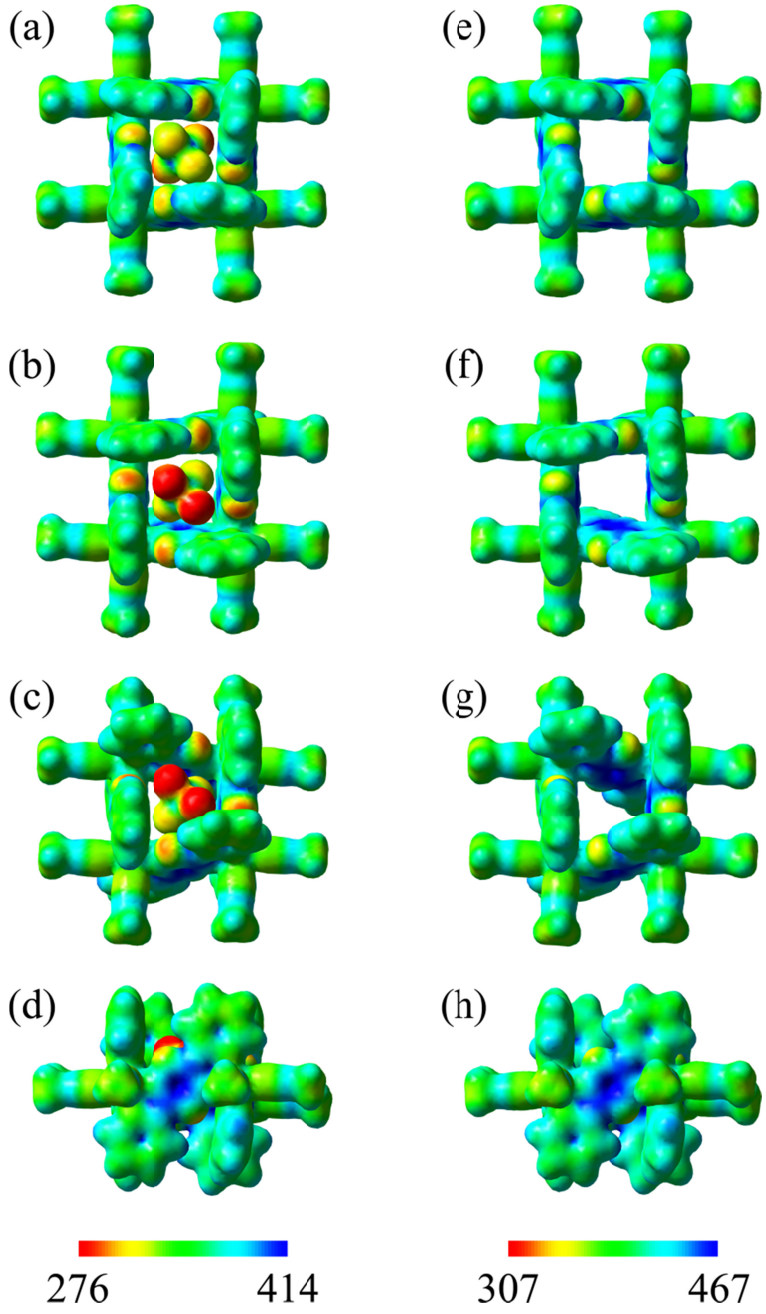

Figure 37. ESP maps of the $[Fe_4(bptz)_4(NCCH_3)_8 \subset BF_4]^{7+}$ (a-d) and the $[Fe_4(bptz)_4(NCCH_3)_8]^{8+}$ cages (e-h) mapped at an isodensity value of 0.02 a.u. The colors of the outer pyridyl rings and CH_3CN solvent molecules were matched in order to allow comparison between the 7+ and 8+ cages. Color ranges reported in kcal mol^{-1}. Views are as follows (the second letter denotes the corresponding view in the cage without the anion): (a, e) view of the interior side of $[BF_4]^-$, (b, f) view of the exterior side of $[BF_4]^-$, (c, g) same view as (b, f) slightly tilted to show the exterior face of bptz, and (d, h) full view of the exposed face of bptz shown in (c, g).

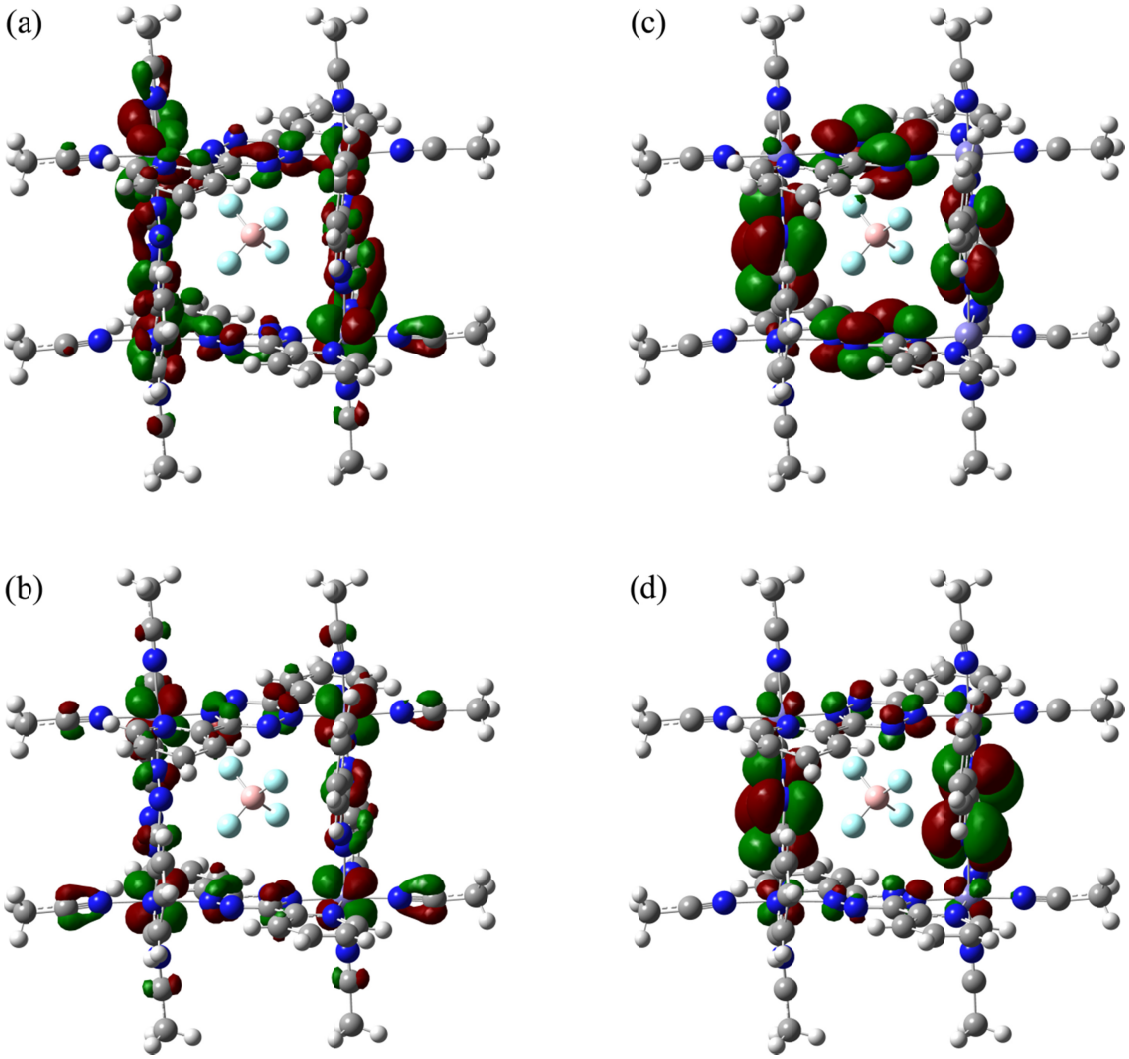

Figure 38. (a) HOMO-1, (b) HOMO, (c) LUMO, and (d) LUMO+1 of $[Fe_4(bptz)_4(NCCH_3)_8 \subset BF_4]^{7+}$ at an isodensity value of 0.02 a.u.

of the anion also increases the electrostatic potential of the exterior face of the ligand. The anion also has a lower electrostatic potential on the F atoms that are closer to the exterior of the cavity. Considering the lack of bond length changes in the simplified models, it is unlikely that there is any net flow of electrons to the ligand in the metallacycle (or in any of the computational models presented earlier).

An analysis of the molecular orbitals reveals that the HOMO-1 and HOMO are situated principally on the Fe^{II} ions of the square metallacycle whereas the LUMO and LUMO+1 are situated almost exclusively on the tetrazine rings of the bptz ligands (Figure 38). Both the HOMO-1 and HOMO have character from both the bptz ligands and d-orbitals of all four of the metal ions. The orbital contributions from the metal ion and the bptz ligands are antibonding with respect to each other. The LUMO and LUMO+1 are both comprised of antibonding orbitals on the tetrazine rings. The character of the LUMO and LUMO+1 supports the notion that the reduction of the complex occurs on the bptz ligands and could lead to destabilization of the anion-π interactions in the complex and the subsequent decomposition resulting in an irreversible reduction wave in the cyclic voltammogram of the complex (see Chapter III for further discussion).

b. $[Fe_5(bptz)_5(NCCH_3)_{10}\subset 2SbF_6]^{8+}$

The single-point energy computations of $[Fe_5(bptz)_5(NCCH_3)_{10}\subset 2SbF_6]^{8+}$, its corresponding 10+ cation and the two $[SbF_6]^-$ anions reveal a binding energy of -926.2 kcal mol^{-1}, the strength of which is due chiefly to the electrostatic attraction of the 10+ cationic unit and the anions, as in the $[Fe_4(bptz)_4(NCCH_3)_8\subset BF_4]^{7+}$ case. ESP maps

reveal similar differences in the electrostatic potential between the $[Fe_5(bptz)_5(NCCH_3)_{10}]^{10+}$ cationic unit and $[Fe_5(bptz)_5(NCCH_3)_{10}\subset 2SbF_6]^{8+}$ as seen in $[Fe_4(bptz)_4(NCCH_3)_8\subset BF_4]^{7+}$, which are again due to proximity of the anion rather than any net electron flow from the anion to the ligand (Figure 39). Analysis of the molecular orbitals of $[Fe_5(bptz)_5(NCCH_3)_{10}\subset 2SbF_6]^{8+}$ reveals that the HOMO and HOMO-1 are composed of d orbitals on four and five Fe^{II} ions, respectively, with additional orbital character residing on the ligands in an antibonding configuration with respect to the Fe^{II} orbitals (Figure 40). The LUMO and LUMO+1 comprise orbitals that reside almost exclusively on the tetrazine moiety of three and four neighboring bptz ligands, respectively. The tetrazine contribution to the LUMO and LUMO+1 again support the notion that the reduction of the complex occurs on the tetrazine ring of the bptz ligands which could lead to destabilization of anion-π interactions and the decomposition of the complex resulting in the irreversible reduction wave observed for this complex (see Chapter III for further discussion).

D. Conclusions

It is clear from the computational models investigated in this work that anion-π interactions are directional. This directionality can be used to design and template supramolecular structures, especially those incorporating N-heterocyclic ligands and polyatomic anions. The anion-π interaction is clearly additive in terms of multiple arenes, even for polyatomic anions. Multiple anions, however, serve only to destabilize the complexes due to increased electrostatic repulsion forces on account of the close proximity of the anions. Surprisingly, tetracyanopyrazine exhibited the strongest anion-π

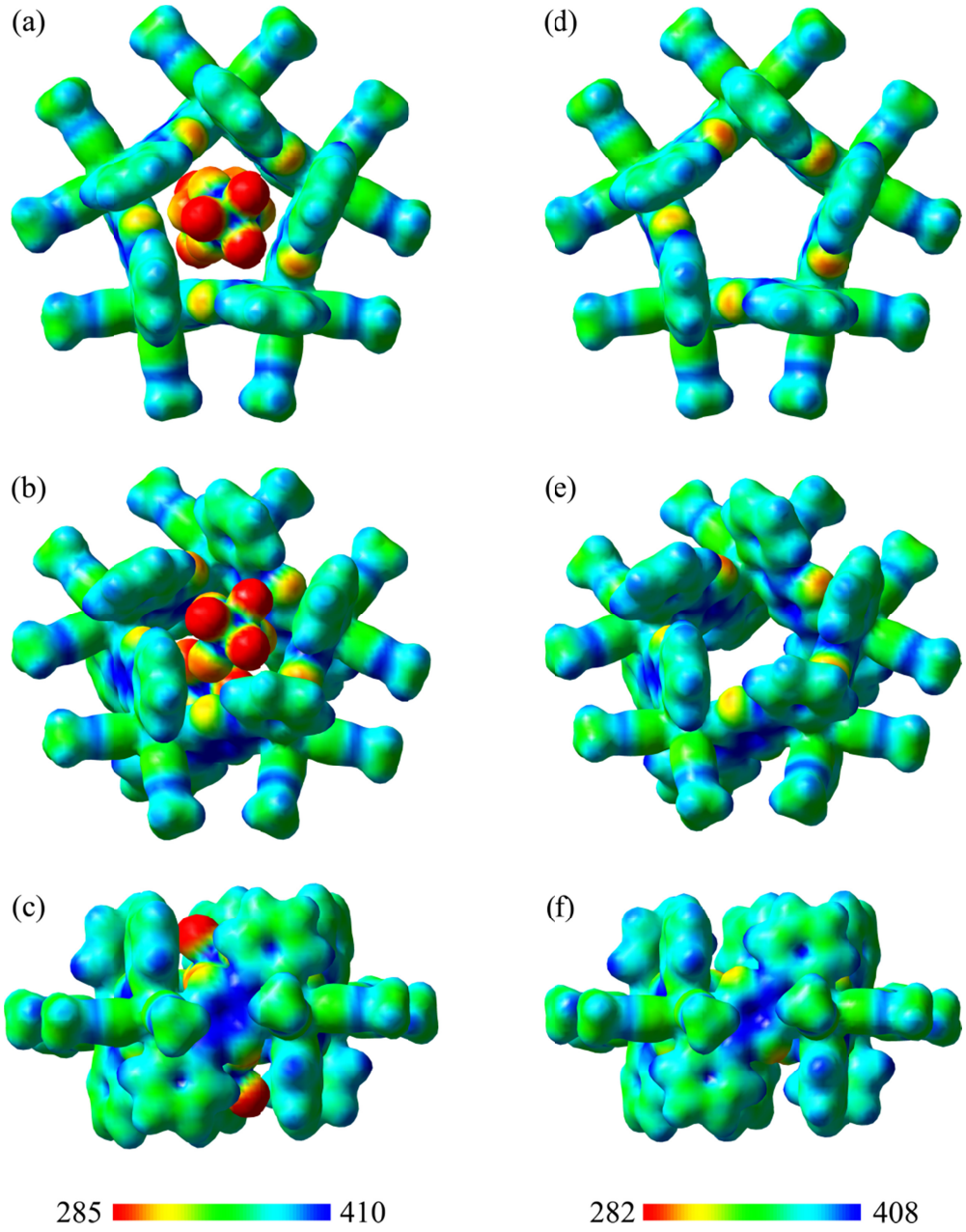

Figure 39. ESP maps of the $[Fe_5(bptz)_5(NCCH_3)_{10}\subset 2SbF_6]^{8+}$ (a-c) and the $[Fe_5(bptz)_5(NCCH_3)_{10}]^{10+}$ cages (d-f) mapped at an isodensity value of 0.02 a.u. The colors of the outer pyridyl rings and CH_3CN solvent molecules were matched in order to allow comparison between the 8+ and 10+ cages. Color ranges reported in kcal mol^{-1}. Views are as follows (the second letter denotes the corresponding view in the cage without the anion): (a, d) front-view, (b, e) same view as (a, d) slightly tilted to show the exterior face of bptz, and (c, e) full view of the exposed face of bptz shown in (b, e).

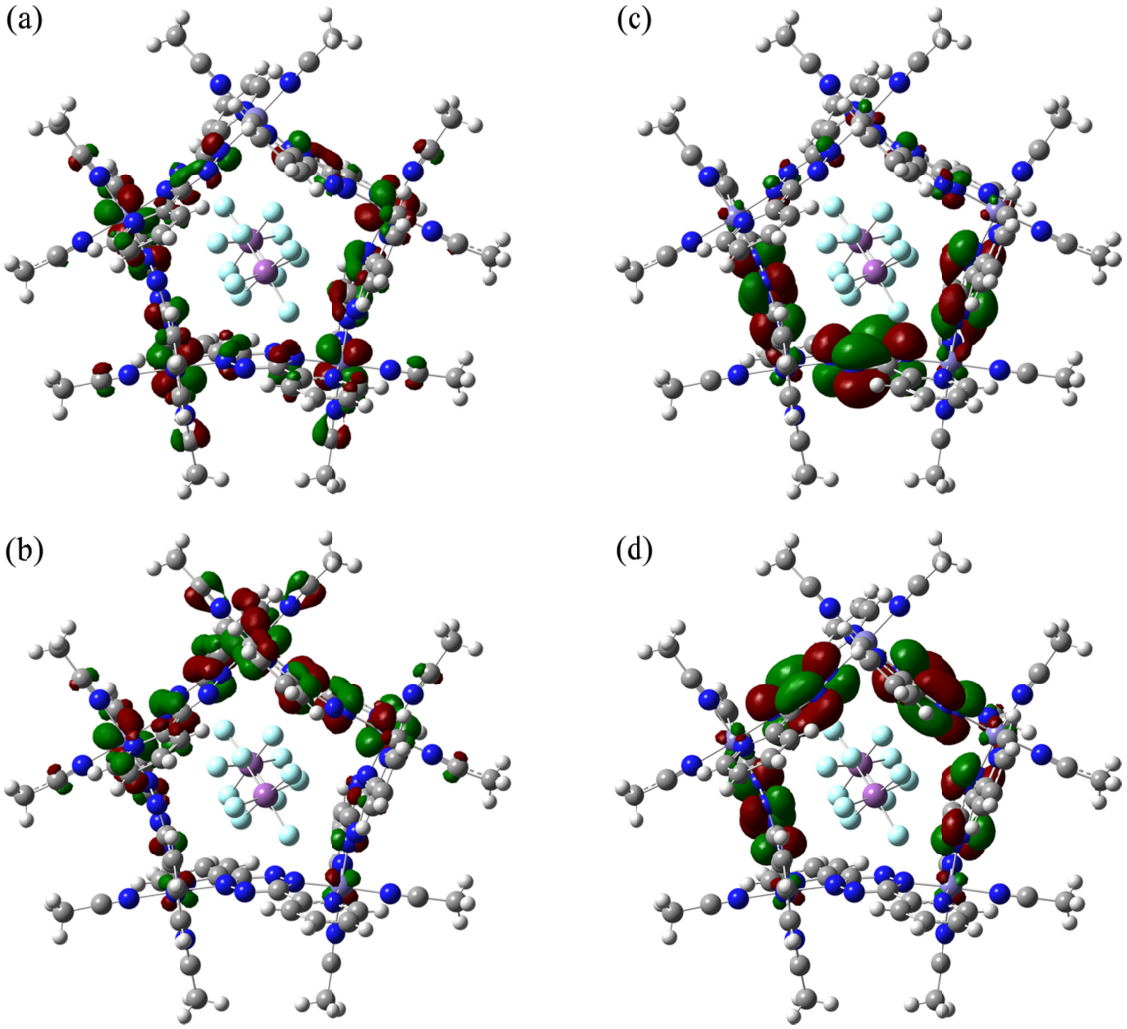

Figure 40. (a) HOMO-1, (b) HOMO, (c) LUMO, and (d) LUMO+1 of $[Fe_5(bptz)_5(NCCH_3)_{10}\subset 2SbF_6]^{8+}$ at an isodensity value of 0.02 a.u.

interactions, despite longer F-C contact distances compared to dicyanotetrazine. This can be attributed to the higher Q_{zz} and $\alpha_{\|}$ of tetracyanopyrazine versus dicyanotetrazine. In addition to the simplified computational models, the full $[Fe_4(bptz)_4(NCCH_3)_8 \subset BF_4]^{7+}$ metallacycle was studied computationally, revealing a high binding energy for the anion and ESP maps exhibiting behavior similar to the Ag^I complexes of bptz and bppn.

The next step in the computational modeling of anion-π interactions is to increase the complexity of the simple models by incorporating four and five arenes arranged in a configuration similar to that observed in the square and pentagonal metallacycles, respectively, as well as to study the square and pentagonal metallacycles with all of their respective anions. With the improved computational power currently available (and expectations of future improvements based on current trends), it may be possible to study a wide variety of anions within the cavities of square and pentagonal metallacycles through geometry optimization studies in order to target specific anions for experimental studies.

CHAPTER III

THE EFFECT OF CHANGING THE METAL ION IDENTITY ON THE STRUCTURE OF DIVALENT FIRST-ROW TRANSITION METAL POLYGONAL ARCHITECTURES WITH BPTZ*

A. Introduction

In the search for ligands capable of communicating spin information between metal ions in multinuclear metal complexes a number of years ago, the Dunbar group investigated the N-heterocyclic ligand 3,6-bis(2′-pyridyl)-1,2,4,5-tetrazine (bptz) and its corresponding Ni^{II} complexes. The ligand was found to be a poor mediator for magnetic coupling, but it was found to exhibit an intriguing property not observed in other coordination complexes to date – depending on the counterion used in the synthesis of the Ni^{II} complexes, different nuclearities (and different polygons) were obtained. Reactions of bptz with $[Ni(NCCH_3)_6][BF_4]_2$ exclusively yield the tetranuclear square complex $[Ni_4(bptz)_4(NCCH_3)_8][BF_4]_8$, whereas the corresponding reaction with $[Ni(NCCH_3)_6][SbF_6]_2$ results in the formation of the pentanuclear pentagonal complex $[Ni_5(bptz)_5(NCCH_3)_{10}][SbF_6]_{10}$. In both cases, a polynuclear tetrahedral ($[BF_4]^-$) or octahedral ($[SbF_6]^-$) anions resides in the central cavity of the respective square or pentagonal structures.[69,70,76] Magnetic studies of both square and pentagonal complexes revealed no appreciable coupling of the Ni^{II} centers and the paramagnetism of the

* Portions of this chapter are reprinted with permission from "Anion-templated self-assembly of highly stable Fe(II) pentagonal metallacycles with short anion-π contacts" Giles, I. D.; Chifotides, H. T., Shatruk, M.; Dunbar, K. R. *Chem. Commun.* **2011**, *47*, 12604-12606.

complexes prevented any reliable assessment of their solution behavior by either ^{1}H or ^{19}F NMR spectroscopy.

Studies of the stability of the Ni^{II} square and pentagon uncovered their ability to interconvert in solution upon addition of an excess of the appropriate anion. Addition of $[^{n}Bu_4N][BF_4]$ to a solution of the Ni^{II} pentagon converts it to the square, which can be crystallized even in the presence of the original $[SbF_6]^-$ ions. The resulting square contains $[BF_4]^-$ in the cavity, with $[SbF_6]^-$ ions surrounding the square. The reverse process, however, is not as facile; upon addition of a large excess of $[^{n}Bu_4N][SbF_6]$ to a solution of the square and reflux in CH_3CN, only the pentagon was be detected by ESI-MS. These results support the conclusion that the square structure is more stable than its pentagonal counterpart, as expected based on geometrical considerations.[70]

An inspection of the crystal structure (Figure 41), reveals the obvious source of the greater stability of the square. In both cases, the coordination environment of each Ni^{II} consists of two bidentate bptz ligands and two *cis*-coordinated CH_3CN molecules in an octahedral environment. The N-Ni-N angles are close to 90^{o} (the bptz bite angle is ~80^{o}) in both cases as well, but whereas the Ni-Ni-Ni angle in the square is 90^{o} (and well-suited for octahedrally coordinated ligands), the Ni-Ni-Ni angle in the pentagon is required to be 108^{o}. The bptz ligand in the pentagon is forced to bend to accommodate the incongruent coordination and polygon angles, thereby introducing strain into the ligand-metal bonds. In the case of the Ni^{II} square, the F atoms of $[BF_4]^-$ align with the electropositive carbon atoms of the central tetrazine rings of two opposing bptz ligands. No such alignment is observed in the Ni^{II} pentagon, but, the F atoms of

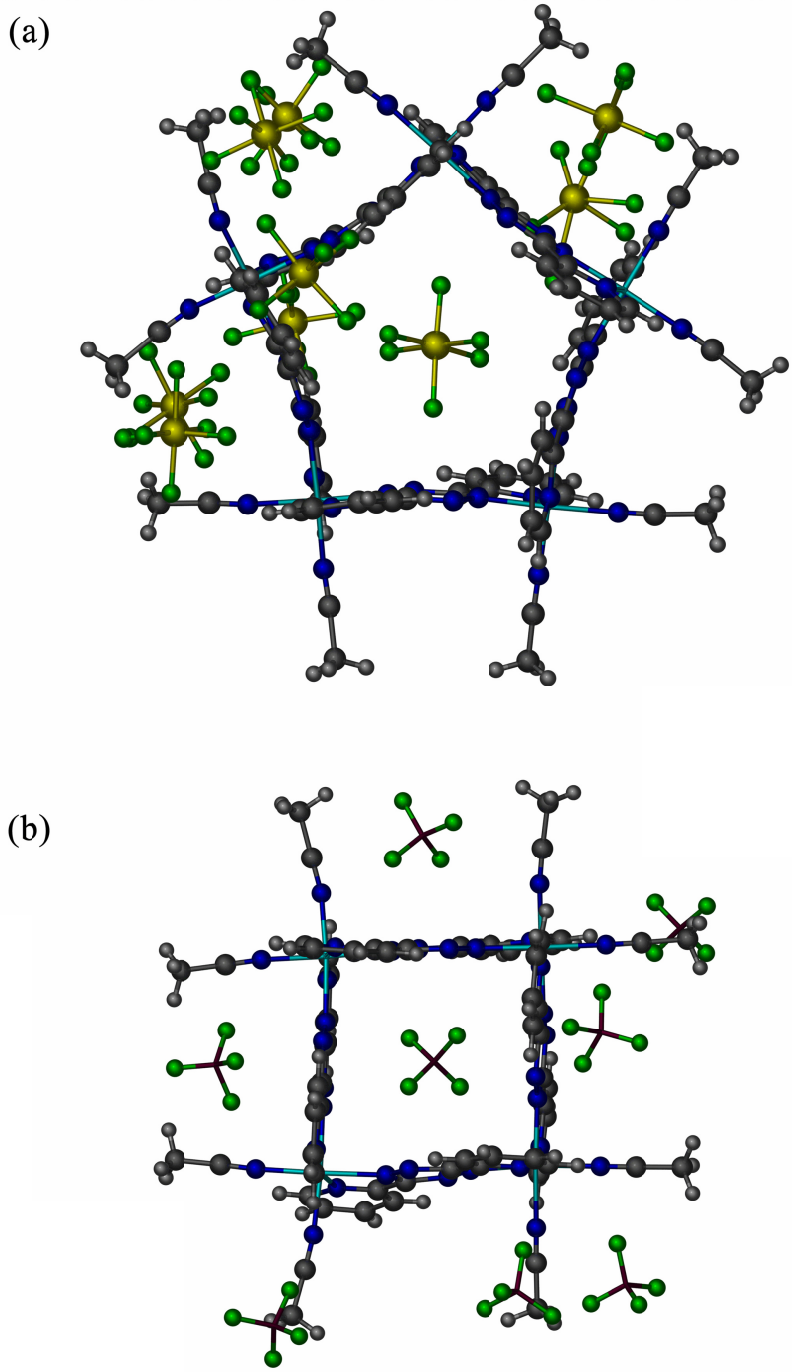

Figure 41. Ball and stick representations of (a) $[Ni_5(bptz)_5(NCCH_3)_{10}][SbF_6]_{10}$ (Ni^{II} pentagon) and (b) $[Ni_4(bptz)_4(NCCH_3)_8][BF_4]_8$ (Ni^{II} square). Atom colors: C (grey), N (blue), H (light grey), F (green), Ni (teal), B (maroon), Sb (yellow). Interstitial solvent molecules are omitted for the sake of clarity. Models generated from CCDC 275033 and 252137, respectively.[70]

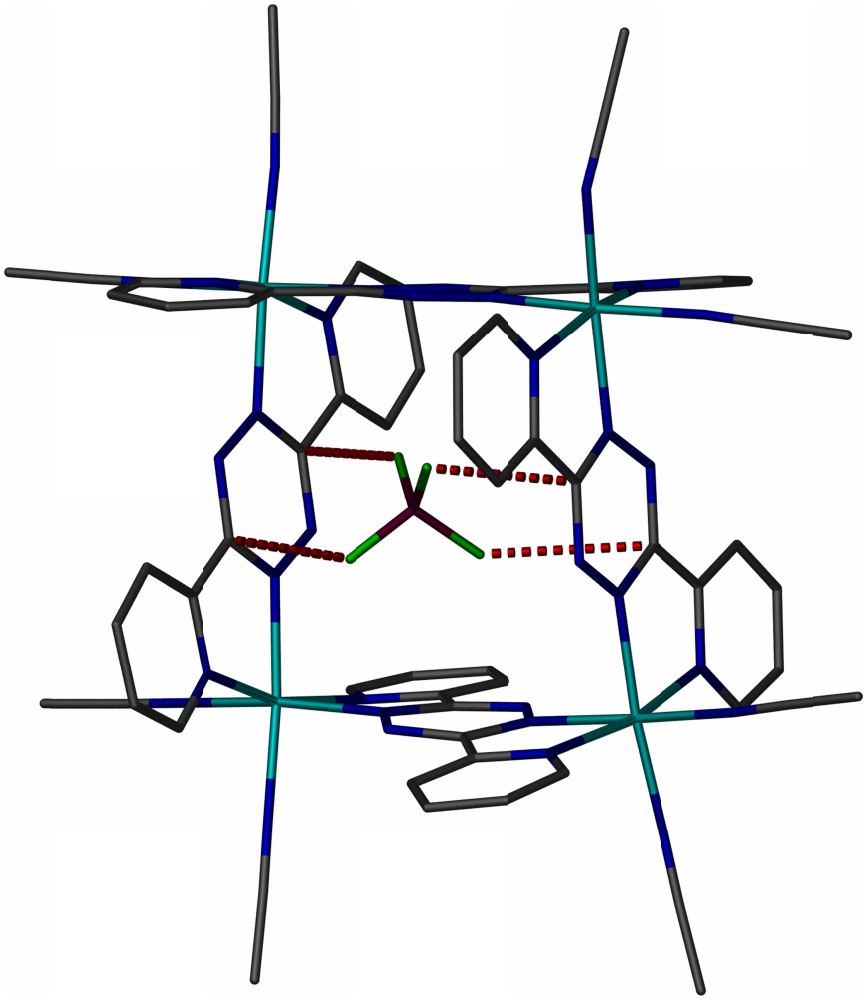

Figure 42. Stick representation of the cationic unit of the Ni^{II} square ($[Ni_4(bptz)_4(NCCH_3)_8BF_4]^{7+}$, highlighting the alignment of the encapsulated $[BF_4]^-$ anion with the central tetrazine rings of two bptz ligands. Atom colors: C (grey), N (blue), Ni (teal), F (green), B (maroon). Hydrogen atoms and interstitial solvent molecules are omitted for the sake of clarity. Figure generated from CCDC 252137.[70]

$[SbF_6]^-$ are directed at the tetrazine rings and the disordered anion resides in the center of the pentagon cavity (Figure 42).[69,70,76]

Further investigation of the role of the anion in the templation of the square and pentagon involved the synthesis of the isostructural Zn^{II} square, $[Zn_4(bptz)_4(NCCH_3)_8][BF_4]_8$, which could be explored by NMR spectroscopy due to the fact that d^{10} Zn^{II} ions are diamagnetic. This same ion, however, could not be incorporated into a pentagonal structure, as the closed-shell d^{10} configuration that leads to its diamagnetism evidently introduces sufficient instability in the N-Zn coordination bonds between the ligand and the metal ion to prevent the stable formation of the inherently strained pentagon (a theory supported by the slow decomposition of the Zn^{II} square in CH_3CN). Indeed, ^1H NMR spectra of the Zn^{II} square contain significant resonance shifts of the bptz protons from the free ligand (Figure 43). Mass spectral studies of the Ni^{II} square and pentagon indicate that these polygonal complexes are stable in solution and remain intact even in the gas phase, with anions remaining associated with the polygonal cations. Similar stability in mass spectral studies of Zn^{II} complex is observed, however, the Zn^{II} square decomposes into an insoluble material when left in CH_3CN for more than a week.[70] A chiral Zn^{II} square of bptz with encapsulated $[ClO_4]^-$ has also been reported by Shionoya *et al.*, but in this case, four of the coordinated CH_3CN molecules are replaced by adventitious water from the $ZnClO_4 \cdot 6H_2O$ starting material.[92]

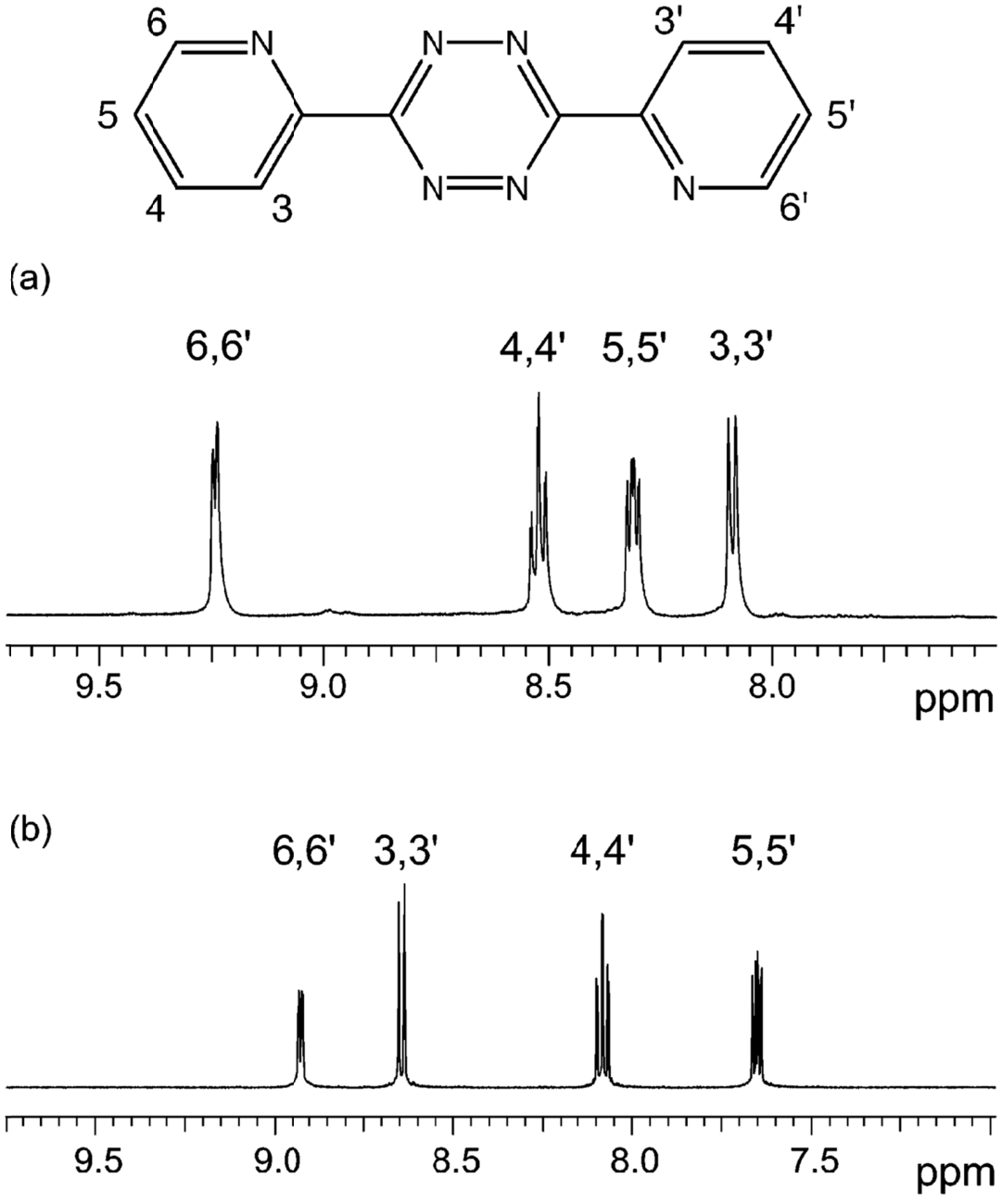

Figure 43. Aromatic region of the ^{1}H NMR spectrum of (a) $[Zn_4(bptz)_4(NCCH_3)_8][BF_4]_8$ and (b) free bptz at room temperature in CD_3CN. Figure reproduced from Dunbar *et al.*[70]

Initial efforts to extend these complexes to divalent first-row transition elements such as Cu^{II}, Fe^{II} and Mn^{II} met with only limited success. Wet $[ClO_4]^-$ salts of Cu^{II}, Fe^{II} and Mn^{II} mixed with bptz in CH_3CN all exhibited m/z signals corresponding to a square in solution, but only on freshly prepared samples (due to decomposition involving the water present in the starting materials). Reactions of $[Co(NCCH_3)_6][BF_4]_2$ with bptz in CH_3CN yielded only mononuclear Co^{II} complexes containing the transformed ligand 2,5-bis(2′-pyridyl)-1,3,4-oxadiazole (Figure 44) due to a Co^{II}-assisted decomposition of bptz in the presence of trace H_2O.[93] At the time, these results suggested that the bptz polygons of more active metal ions such as Co^{II} and Fe^{II} were too unstable to isolate or structurally characterize, although this was later found not to be the case, as the following discussion will describe.

Efforts to extend both the square and pentagonal metallacycles of bptz to Co^{II} and Fe^{II} are discussed in this chapter. It was expected that the Fe^{II} metallacycles may be low-spin and hence diamagnetic, which would allow for NMR studies to be performed, and, in fact, properties of the Fe^{II} complexes in solution are discussed according to their NMR and electrochemical behavior. Under scrupulously dry conditions, the partially solvated Fe^{II} pentagon and square, along with the Co^{II} square, were isolated and structurally characterized by single-crystal X-ray crystallography. These results demonstrate that polygons of Fe^{II} with bptz are stable, including the anion-templated pentagonal complexes. These data reveal that the pentagons are not limited to Ni^{II}, as once previously thought.

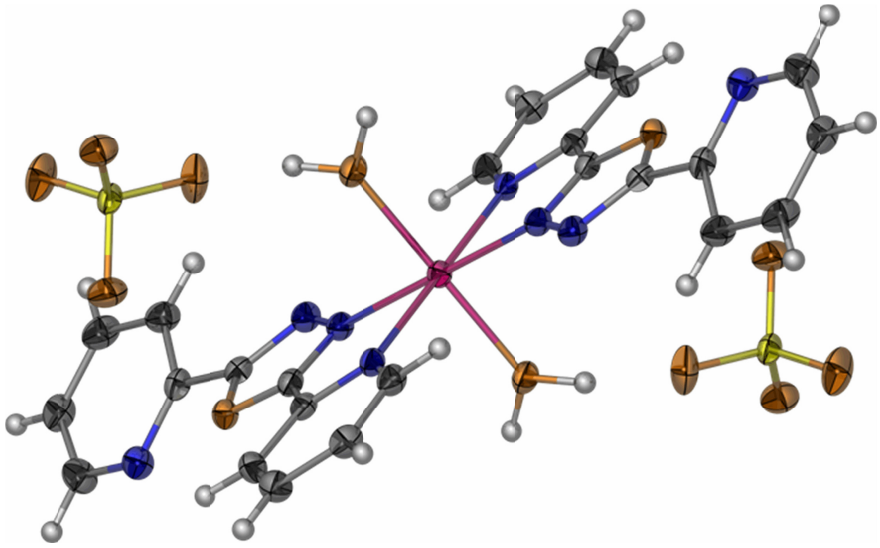

Figure 44. Thermal ellipsoid plot of $[Co(bpod)_2(H_2O)_2][ClO_4]_2$ generated at the 50% probability level (bpod = 2,5-bis(2′-pyridyl)oxadiazole). Atom colors: Co (pink), C (grey), O (orange), Cl (yellow), H (white). Figure reproduced from structural data presented in the dissertation of Cristian Saul Campos-Fernández.[93]

B. Experimental

i. General methods and starting materials

All reactions were performed under nitrogen using standard Schlenk techniques or in an MBraun inert atmosphere glovebox. All glassware was oven-dried prior to use. Acetonitrile was dried over 3 Å molecular sieves and distilled under nitrogen. Toluene was dried and dispensed under nitrogen using an MBraun Solvent Purification System. Dichloromethane was dried over P_2O_5 and distilled under nitrogen. The fully-solvated metal salts $[Co(NCCH_3)_6][BF_4]_2$, $[Co(NCCH_3)_6][SbF_6]_2$, $[Fe(NCCH_3)_6][BF_4]_2$, and $[Fe(NCCH_3)_6][SbF_6]_2$ were synthesized by literature methods.[94] The bptz ligand (magenta) was synthesized by reported methods, recrystallized from benzene, and dried *in vacuo* prior to use.[95]

ii. X-ray crystallography

For a typical experiment, the selected single crystal was isolated, mounted on a cryoloop with Paratone oil, and placed in a dry nitrogen cryostream set at 110 K on a three-circle goniometer. Reflection data were collected using either a Brüker SMART CCD detector ($[Co_4(bptz)_4(NCCH_3)_8][BF_4]_8$) or APEXII CCD detector (all others) as ω scans with 0.3^o step widths. Data were integrated with SAINT (either standalone or within the APEXII software suite[96]), with absorption corrections performed by fitting a function to the empirical transmission surface as sampled by multiple equivalent measurements using SADABS.[97,98] The SHELX[99] suite of programs was used to solve and refine the crystal structures within either the XSEED[100] or ShelXle[101] graphical user interfaces. The direct methods solution was used for all structures, which resolved the

positions of most non-hydrogen atoms. Least-squares refinement and difference Fourier maps were used to locate remaining non-hydrogen atoms. Hydrogen atoms were placed at calculated positions and refined using a riding model. Highly disordered solvent was removed using the PLATON[102] utility SQUEEZE[103]. Final refinements were carried out using anisotropic thermal parameters for all non-hydrogen atoms unless otherwise noted.

iii. Physical property measurements

IR spectra were obtained on a Nicolet 740 FT-IR Spectrometer as Nujol mulls on KBr plates (or CsI for far-IR spectra). Magnetic susceptibility measurements were obtained using a Quantum Design SQUID MPMS-XL magnetometer on dried powder samples in the DC mode from 2-300 K in an applied field of 0.1 T. ESI-MS were obtained on a Sciex API QStar Pulsar mass spectrometer with an electrospray ionization source; ESI-FT-ICR-MS data were obtained on a Brüker 9.4 T FTICR. ^{1}H NMR spectra were obtained on either a 300 MHz Mercury spectrometer or a 500 MHz Inova spectrometer at 20 ^{o}C in CD_3CN, unless otherwise noted. ^{19}F NMR spectra were obtained on a 300 MHz Inova spectrometer equipped with a Quad probe. Electrochemical data were obtained on a CH Instruments 620a Electrochemical Analyzer in a three-electrode configuration using a Pt working electrode, Ag/AgCl reference electrode, and Pt wire counterelectrode. Elemental analyses were performed by Atlantic Microlab.

iv. Syntheses of compounds

a. $[Co_4(bptz)_4(NCCH_3)_8][BF_4]_8$

A magenta solution of bptz (0.074 g, 0.31 mmol) in 25 mL CH_3CN was added slowly to an orange solution of $[Co(NCCH_3)_6][BF_4]_2$ (0.150 g, 0.313 mmol) in 25 mL of CH_3CN (orange solution) with stirring, resulting in the immediate formation of a green-brown solution. After stirring overnight, the reaction solution was layered over toluene in a 100-mL screw-top jar, precipitating a brown powder. Yield: 0.136 g (79%).

b. $[Fe_4(bptz)_4(NCCH_3)_8][BF_4]_8$

The addition of a magenta solution of bptz (0.126 g, 0.523 mmol) in CH_3CN (35 mL) to a colorless solution of $[Fe(NCCH_3)_6][BF_4]_2$ (0.249 g, 0.523 mmol) in CH_3CN (15 mL) induces an immediate color change of the solution to dark blue. After overnight stirring, a blue solid was obtained by filtration after layering the acetonitrile solution of $[Fe_4(bptz)_4(NCCH_3)_8][BF_4]_8$ over toluene or dichloromethane in a 100-mL screw-top jar, under anaerobic conditions. Yield: 0.233 g, 81%. Elemental Analysis: Calculated for $Fe_4C_{64}N_{32}H_{54}B_8F_{32}\cdot 4CH_2Cl_2\cdot CH_3CN$: C, 32.65; N, 17.96; H, 2.60%. Found: C, 32.69; N, 18.14; H, 2.63%. ^{1}H NMR, δ, ppm (CD_3CN): 7.61 (d; 3, 3′), 8.05 (td; 5,5′), 8.29 (td; 4,4′), 8.89 (d; 6,6′) ppm, and 1.95 (s, CH_3CN). EAS: $\lambda_{max}(CH_3CN)$/nm, (ε/L mol^{-1} cm^{-1}): 797 (19,000). CV (CH_3CN, vs. Ag/AgCl): $E_{1/2}$(ox): -0.094, +0.046, +0.32, +0.52 V (reversible), -1.07, -1.61 V (irreversible). ESI-FT-ICR-MS (submitted in CD_3CN): m/z 2154.19 for $[Fe_4(bptz)_4(CH_3CN)_6(CD_3CN)(BF_4)_8+H^+]^+$.

c. $[Fe_5(bptz)_5(NCCH_3)_{10}][SbF_6]_{10}$

The addition of a magenta solution of bptz (0.169 g, 0.716 mmol) in CH_3CN (10 mL) to a colorless solution of $[Fe(CH_3CN)_6][SbF_6]_2$ (0.554 g, 0.716 mmol) in CH_3CN (10 mL) induces an immediate color change of the solution to dark blue. After overnight stirring, pure blue solid was obtained by filtration after layering the acetonitrile solution of over toluene in a 100-mL screw-top jar under anaerobic conditions. Yield: 0.555 g, 90%. Elemental Analysis: Calculated for $Fe_5C_{80}N_{40}H_{70}Sb_{10}F_{60}\cdot C_7H_8$: C, 24.18; N, 12.96; H, 1.84%. Found: C, 24.40; N, 13.28; H, 1.96%. ^{1}H NMR, δ, ppm (CD_3CN): 7.52 (10H, d, 3,3′-H), 8.07 (10H, td, 5,5′-H), 8.31 (10H, td, 4,4′-H), 8.82 (10H, d, 6,6′-H), 1.95 (30H, s, CH_3CN). EAS: $\lambda_{max}(CH_3CN)$/nm, (ε/L mol^{-1} cm^{-1}): 802 (30,000). CV (CH_3CN, vs. Ag/AgCl): $E_{1/2}$(ox): -0.027, +0.034, +0.372, +0.560 V (reversible), -1.22, -1.54 V (irreversible). ESI-FT-ICR-MS: m/z 1774.83 for $[Fe_5(bptz)_5(CH_3CN)_5(SbF_6)_8–2H]^{2+}$.

d. $[Co(NCCH_3)_6][SbF_6]_2$ + bptz

In a representative synthesis, $[Co(NCCH_3)_6][SbF_6]_2$ (0.245 g, 0.315 mmol) in 10 mL of CH_3CN (orange solution) was treated dropwise with a solution of bptz (0.0745 g, 0.315 mmol) in 50 mL of CH_3CN (magenta solution, no undissolved bptz), with the instantaneous formation of a brown solution, which was stirred overnight. Upon treatment with approximately 5 mL of toluene, a brown powder precipitated which was found to be insoluble in CH_3CN upon further attempts to recrystallize the material. The remaining filtrate was orange, hinting at the presence of unreacted $[Co(NCCH_3)_6][SbF_6]_2$. Yield: 0.178g. IR (cm^{-1}): 2323, 2289 (ν CN, CH_3CN); 1581, 1568 (ν C=C, C=N pyridyl); 660 (ν Sb-F).

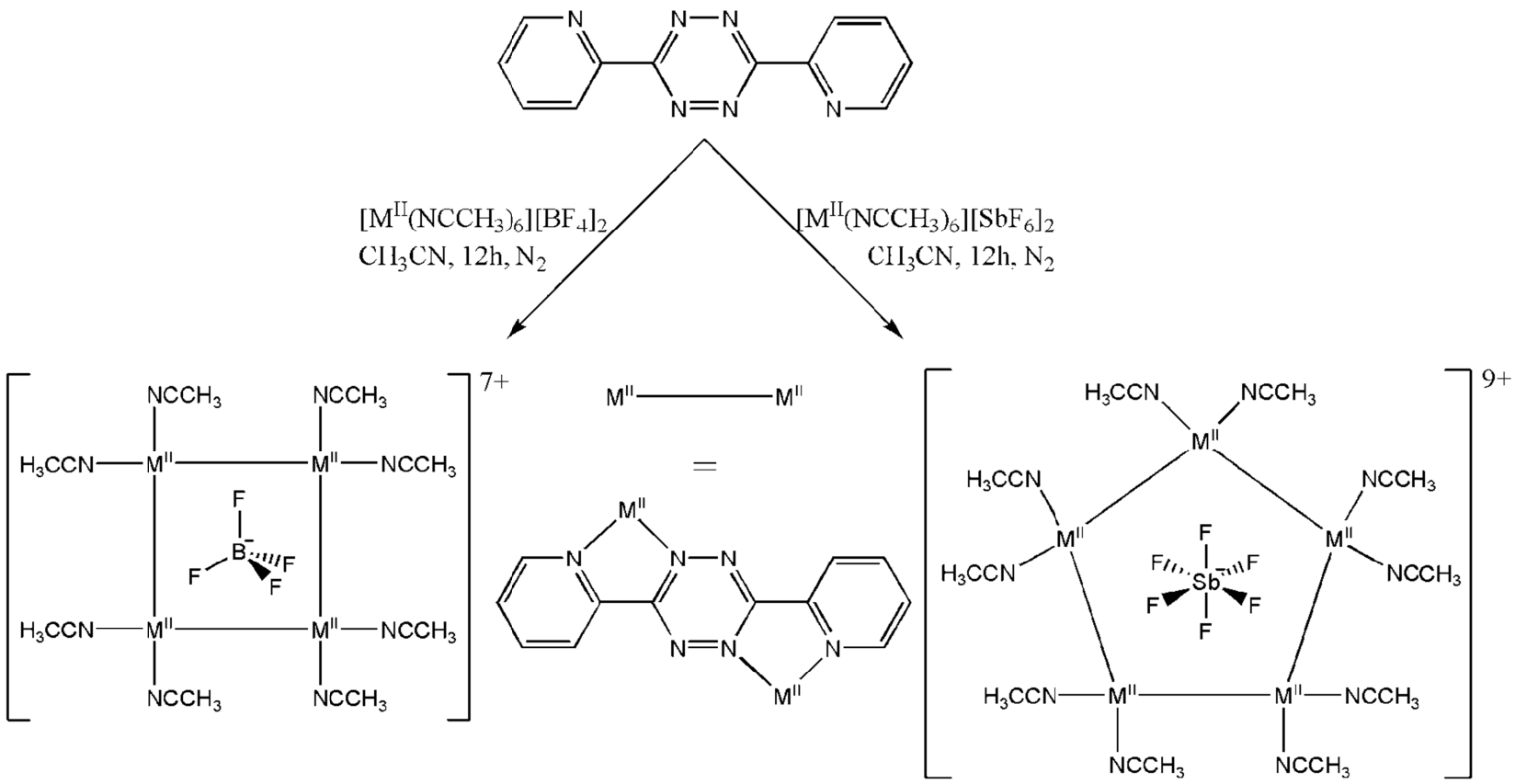

Figure 45. Schematic representation of the synthesis of the square and pentagonal metallacycles (square, bottom left; pentagon, bottom right) from their $[M(NCCH_3)_6][X]_2$ (M = Zn^{II}, Ni^{II}, Co^{II}, and Fe^{II}; X = BF_4^- and SbF_6^-) salts and bptz (top) in CH_3CN. The binding of bptz in the *anti* orientation is also shown (bottom center).

C. Results and Discussion

i. Syntheses

The syntheses of the Co^{II} and Fe^{II} squares and the Fe^{II} pentagon with bptz were carried out in a similar manner to their Ni^{II} congeners (Figure 45). The reactions proceed rapidly upon combination of the metal and ligand solutions as indicated by their immediate color changes. Overnight stirring is carried out, but no heating is required for the full formation of these species, as the metal and ligands self-assemble into the resulting polygonal architectures. Although the Ni^{II} and Co^{II} reactions were carried out with a slight excess of metal precursor, the Fe^{II} polygons were synthesized with strict stoichiometric equivalents due to concerns regarding contamination of paramagnetic $[Fe(NCCH_3)_6][X]_2$ in the final products. A mixture of crystals and powder results from treating the resulting reaction solutions by layering them over toluene.

Attempts to synthesize the pentagonal Co^{II} metallacycle with bptz and $[SbF_6]^-$ using the same procedure as the Ni^{II} and Fe^{II} pentagons yielded a brown solution that precipitated a brown powder upon treatment with toluene, leaving an orange filtrate that contains unreacted $[Co(NCCH_3)_6][SbF_6]_2$. The resulting brown powder is insoluble in CH_3CN, unlike the Ni^{II} and Fe^{II} pentagonal metallacycles. An extended network solid consisting of Co^{II} ions linked by bptz ligands with no coordinated CH_3CN solvent may form rather than the expected pentagonal metallacycle. Infrared spectroscopy reveals the presence of coordinated CH_3CN (ν_{CN} = 2323 and 2295 cm^{-1}) and bptz, along with the characteristic $\nu_{Sb\text{-}F}$ vibrational mode at 660 cm^{-1}. From these data, it is obvious that the product incorporates both bptz and $[SbF_6]^-$ and retains the coordinated CH_3CN,

suggesting an octahedral environment for Co^{II} but the insolubility of the product in CH_3CN makes it unlikely that a discrete compound is being formed The synthesis of such coordination polymers with bptz is precedented.[70,79]

ii. Single crystal X-ray crystallographic analyses

a. $[Co_4(bptz)_4(NCCH_3)_8][BF_4]_8$

Structural analysis of a green-brown single crystal of $[Co_4(bptz)_4(NCCH_3)_8][BF_4]_8$ obtained by layering an acetonitrile solution of $[Co_4(bptz)_4(NCCH_3)_8][BF_4]_8$ over toluene revealed a tetranuclear, distorted square metallacycle of Co^{II} ions linked by chelating bptz ligands in an *anti* orientation and capped by coordinated CH_3CN molecules (See Table 8 for crystallographic parameters). One $[BF_4]^-$ anion resides within the cavity of the square in close contact with the ligand, with the rest of the anions occupying the periphery of the square cage, four of which are also in close contact with the ligands (Figure 46). The $[BF_4]^-$ anions exhibit slight disorder as evidenced by large thermal parameters for the F atoms as compared with the rest of the non-hydrogen atoms. The encapsulated $[BF_4]^-$ is tightly packed (Figure 47) within the center of the cavity, with short F···C contact distances to the central tetrazine ring of the bptz ligand. $[BF_4]^-\cdots C_{tetrazine}$ distances are as follows: F1···C6 2.890(7); F2···C7 2.733(8); F3···C30 2.879 (6); F4···C31 2.794(8) Å (Figure 48a). The Co^{II}-N distances range from 2.03 – 2.18 Å. The N-Co^{II}-N angles range from 75.6 – 102.6^o, with the bptz-Co^{II} bite angles on the lower end of the range and the CH_3CN-Co^{II}-$NCCH_3$ angles all close to 90^o (Table 9). The Co^{II}-Co^{II}-Co^{II} angles vary between 86.1^o and 93.4^o, deviating from an ideal square geometry. Distances between the Co^{II} ions across the

Table 8. Crystallographic parameters for $[Co_4(bptz)_4(NCCH_3)_8][BF_4]_8$, $[Fe_4(bptz)_4(NCCH_3)_8][BF_4]_8 \cdot 9CH_3CN$, and $[Fe_5(bptz)_5(NCCH_3)_{10}][SbF_6]_{10} \cdot 8.5CH_3CN$.

	$[Co_4(bptz)_4(NCCH_3)_8][BF_4]_8$	$[Fe_4(bptz)_4(NCCH_3)_8][BF_4]_8 \cdot 9CH_3CN$	$[Fe_5(bptz)_5(NCCH_3)_{10}][SbF_6]_{10} \cdot 8.5CH_3CN$
Formula	$C_{128}H_{112}B_{16}Co_8F_{64}N_{64}$	$C_{82}H_{83}B_8F_{32}Fe_4N_{41} \cdot 9CH_3CN$	$Sb_{10}Fe_5F_{60}N_{48.5}C_{97}H_{95.5}$
Temp (K)	110	110	110
Space group	$P\bar{1}$ (no. 2)	$P\bar{1}$ (no. 2)	Pbcn (no. 60)
a (Å)	13.9339(17)	14.678(3)	11.82(1)
b (Å)	16.985(2)	18.363(4)	37.92(4)
c (Å)	21.816(2)	20.780(5)	34.12(3)
α (°)	94.357(2)	85.364(3)	90.00
β (°)	91.873(2)	84.223(3)	90.00
γ (°)	97.297(2)	76.651(3)	90.00
V (Å^3)	5101.8(10)	5412(2)	15299(25)
Z	2	2	4
Color	green-brown	dark blue	dark blue
ρ_{calc}(g/cm^3)	1.434	1.345	1.836
μ (mm^{-1})	0.750	0.630	2.314
θ range (°)	0.94-27.45	1.14-24.71	1.19-26.46
Reflections collected	23,305	50,883	30,355
Unique reflections	23,305	18,430	15,658
Parameters/restraints	0/1269	0/1306	912/21
R_1,[a] wR_2[b] [$I > 2\sigma(I)$]	0.0859, 0.2363	0.0971, 0.2478	0.0863, 0.1971
R_1,[a] wR_2[b] (all data)	0.0859, 0.2363	0.1748, 0.2813	0.2414, 0.2419
Goodness-of-fit[c] (F^2)	1.201	0.899	0.719
Largest diff. peak, hole (e Å^{-3})	4.084, -1.065	1.441, -0.466	1.42, -1.16

[a] $R = \Sigma \| \|F_o\| - \|F_c\| \| / \Sigma |F_o|$. [b] $wR = \{\Sigma[w(F_o^2 - F_c^2)^2] / \Sigma w(F_o^2)^2]\}^{1/2}$. [c] Goodness-of-fit = $\{\Sigma[w(F_o^2 - F_c^2)^2]/(n-p)\}^{1/2}$, where n is the number of reflections and p is the total number of parameters refined.

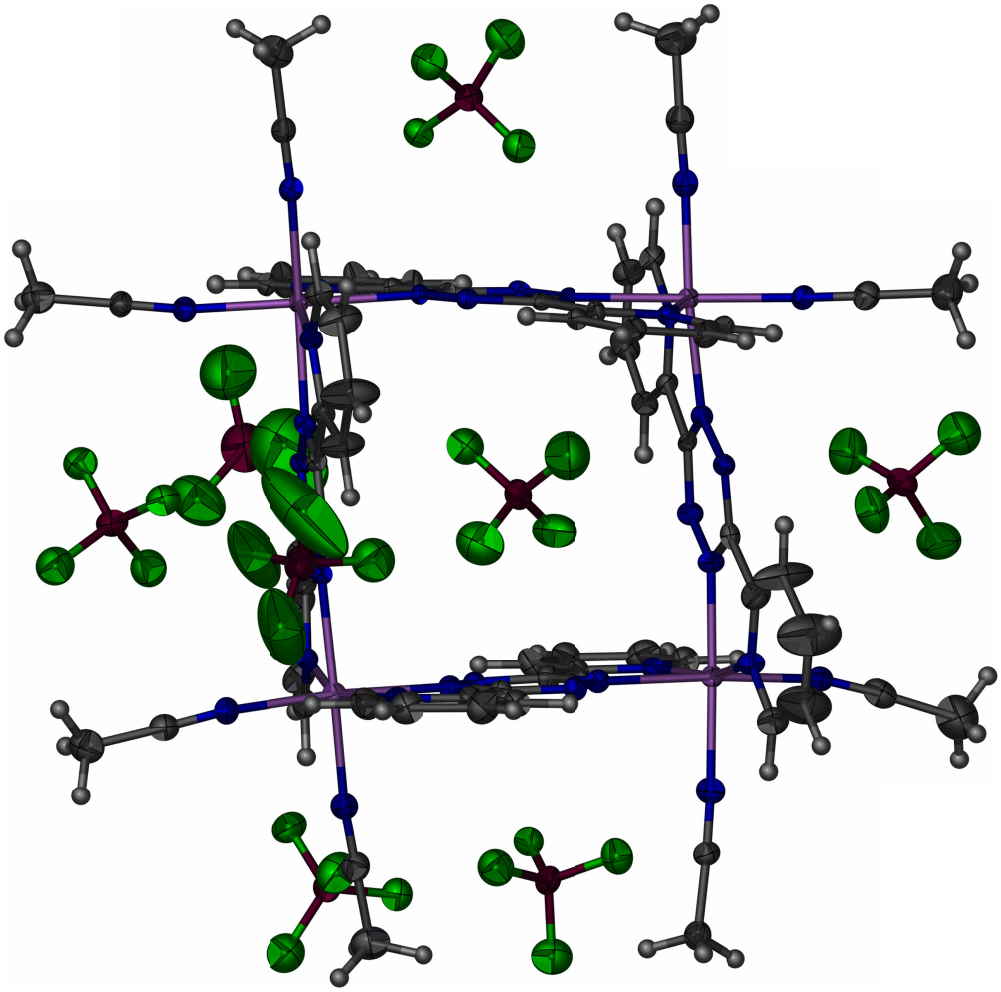

Figure 46. Thermal ellipsoid plot of $[Co_4(bptz)_4(NCCH_3)_8][BF_4]_8$ drawn at the 50% probability level. Atom colors: Co (purple), C (dark grey), N (blue), B (maroon), F (green), H (light grey).

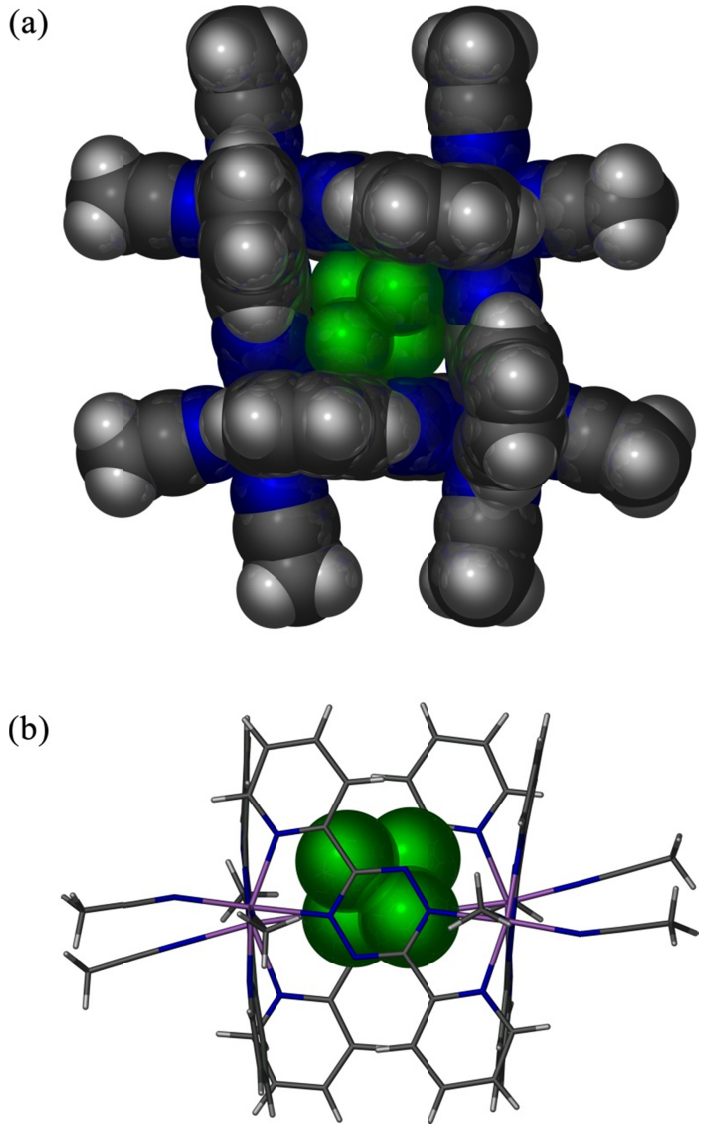

Figure 47. (a) Space-filling front view of the $[BF_4]^-$ anion in the cavity of $[Co_4(bptz)_4(NCCH_3)_8 \subset BF_4]^{7+}$ showing the tight packing of the anion within the cavity. (b) Side view emphasizing the alignment of the anion (space-filling) with the bptz ligands of the Co^{II} square (stick). Atom colors: Co (purple), C (dark grey), N (blue), B (maroon), F (green), H (light grey). Non-encapsulated anions are omitted for the sake of clarity.

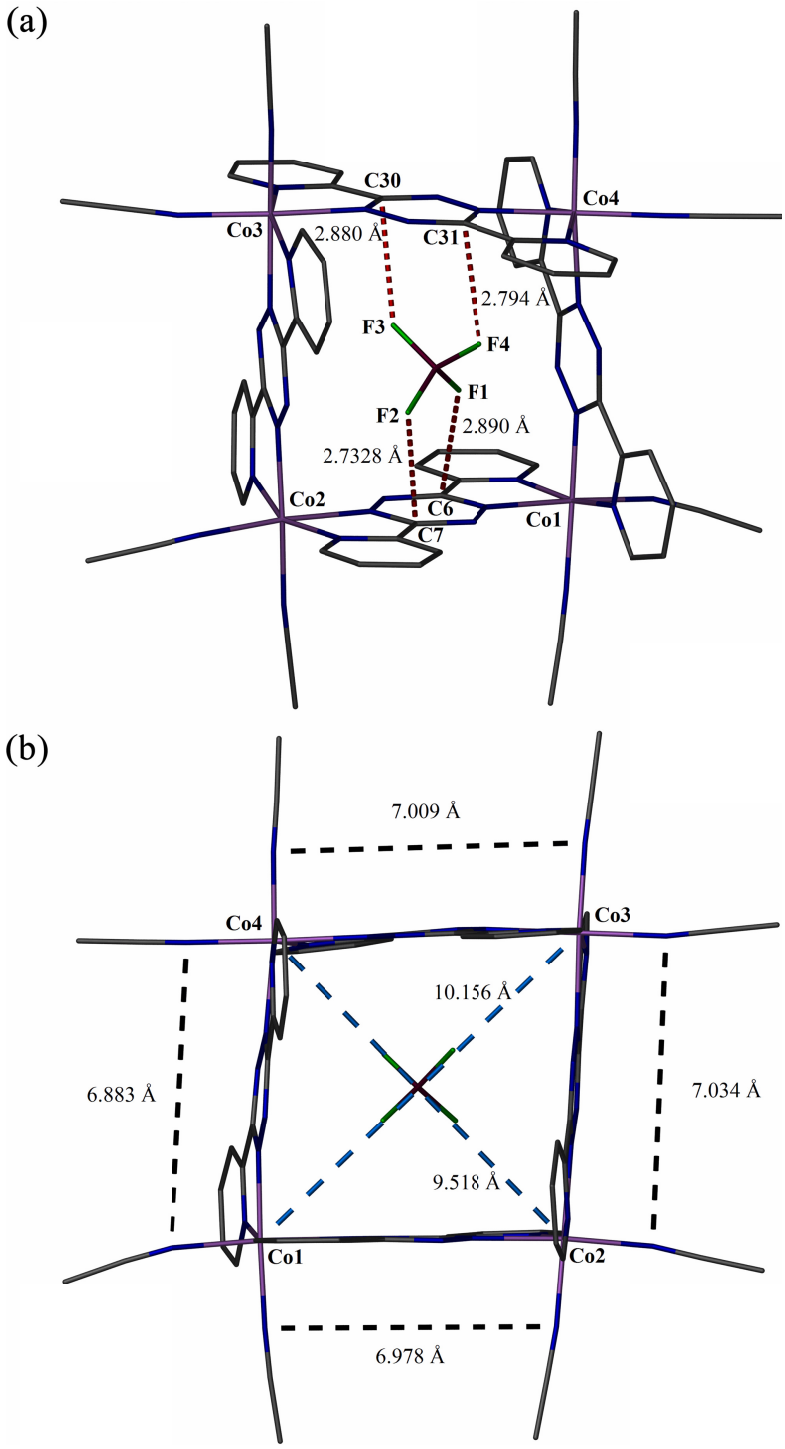

Figure 48. Side-view stick representations of $[Co_4(bptz)_4(NCCH_3)_8 \subset BF_4]^{7+}$ with (a) F-C distances and (b) cross-ligand and cross-cavity distances indicated. Atom colors: Co (purple), C (dark grey), N (blue), B (maroon), F (green). Non-encapsulated anions and H atoms are omitted for the sake of clarity.

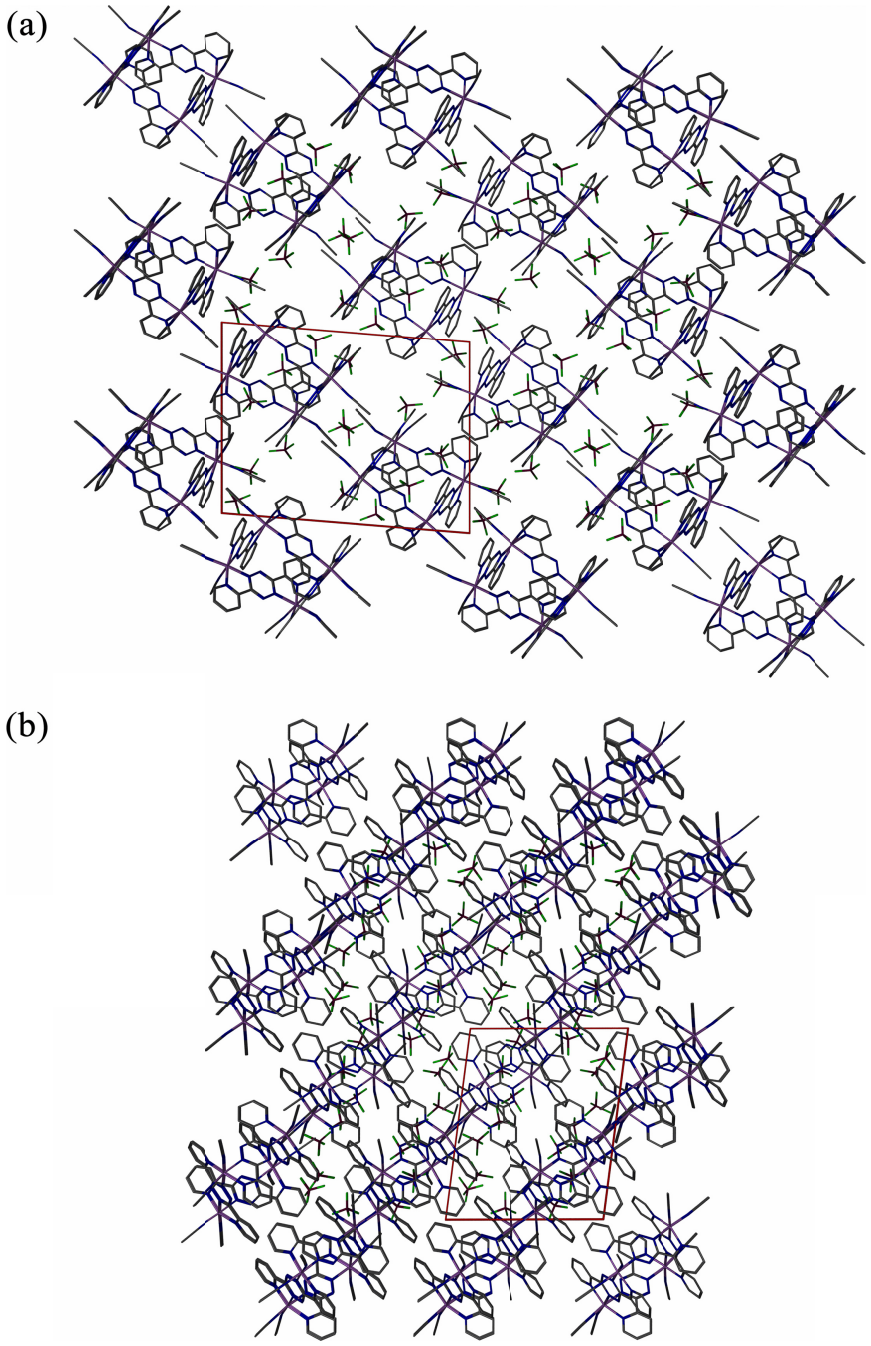

Figure 49. Crystal packing diagrams of $[Co_4(bptz)_4(NCCH_3)_8][BF_4]_8$ along the (a) *a* and (b) *c* axis of the unit cell (inscribed in red) highlighting the layered packing of the squares.

Table 9. Co^{II}-N bond distances in Å (top) and N-Co^{II}-N angles in degrees (bottom) for $[Co_4(bptz)_4(NCCH_3)_8][BF_4]_8$.

Atoms	Distance	Atoms	Distance	Atoms	Distance
Co1-N22	2.026(4)	Co1-N26	2.032(5)	Co1-N1	2.038(4)
Co1-N23	2.058(4)	Co1-N25	2.089(5)	Co1-N2	2.141(4)
Co2-N27	2.048(5)	Co2-N28	2.070(5)	Co2-N7	2.090(4)
Co2-N4	2.102(4)	Co2-N5	2.169(4)	Co2-N(8	2.178(4)
Co3-N29	2.061(4)	Co3-N30	2.080(4)	Co3-N10	2.102(4)
Co3-N13	2.105(4)	Co3-N14	2.160(4)	Co3-N11	2.180(4)
Co4-N31	2.041(5)	Co4-N32	2.049(4)	Co4-N16	2.084(4)
Co4-N19	2.096(4)	Co4-N20	2.146(4)	Co4-N17	2.175(4)

Atoms	Angle	Atoms	Angle	Atoms	Angle
N22-Co1-N26	98.40(18)	N1-Co1-N23	89.89(16)	N22-Co1-N2	91.81(17)
N22-Co1-N1	165.01(17)	N22-Co1-N25	91.91(17)	N26-Co1-N2	87.54(17)
N26-Co1-N1	92.52(18)	N26-Co1-N25	88.92(18)	N1-Co1-N2	78.37(16)
N22-Co1-N23	78.72(17)	N1-Co1-N25	98.56(17)	N23-Co1-N2	90.13(16)
N26-Co1-N23	176.25(18)	N23-Co1-N25	93.56(17)	N25-Co1-N2	175.20(16)
N27-Co2-N28	90.59(19)	N7-Co2-N4	156.73(16)	N27-Co2-N8	172.79(18)
N27-Co2-N7	96.62(18)	N27-Co2-N5	84.87(17)	N28-Co2-N8	90.74(17)
N28-Co2-N7	96.94(17)	N28-Co2-N5	175.06(17)	N7-Co2-N8	76.18(15)
N27-Co2-N4	95.72(18)	N7-Co2-N5	85.54(16)	N4-Co2-N8	90.91(15)
N28-Co2-N4	102.58(18)	N4-Co2-N5	76.00(16)	N5-Co2-N8	94.00(15)
N29-Co3-N30	90.62(17)	N10-Co3-N13	160.23(15)	N29-Co3-N11	89.43(16)
N29-Co3-N10	99.24(16)	N29-Co3-N14	172.54(16)	N30-Co3-N11	170.55(16)
N30-Co3-N10	94.85(16)	N30-Co3-N14	90.58(15)	N10-Co3-N11	75.83(15)
N29-Co3-N13	95.80(16)	N10-Co3-N14	88.00(15)	N13-Co3-N11	91.63(14)
N30-Co3-N13	97.76(15)	N13-Co3-N14	76.74(15)	N14-Co3-N11	90.60(14)
N31-Co4-N32	91.31(17)	N16-Co4-N19	154.61(15)	N31-Co4-N17	87.68(16)
N31-Co4-N16	96.18(16)	N31-Co4-N20	172.87(16)	N32-Co4-N17	172.97(16)
N32-Co4-N16	97.60(16)	N32-Co4-N20	84.34(16)	N16-Co4-N17	75.61(15)
N31-Co4-N19	99.86(16)	N16-Co4-N20	90.00(15)	N19-Co4-N17	85.47(14)
N32-Co4-N19	101.55(16)	N19-Co4-N20	75.59(15)	N20-Co4-N17	97.32(14)

ligands (henceforth referred to as the "cross-ligand" distance) are all close to 7.0 Å, with diagonal Co^{II}-Co^{II} distances across the cavity (henceforth referred to as the "cross-cavity" distance) of 9.5 and 10.16 Å (Figure 48b), also indicative of distortion from an ideal square geometry. The Co^{II} squares pack in sheets with anions occupying void spaces as can be seen in views down the *a* (Figure 49a) and *c* (Figure 49b) axes of the crystal structure.

b. $[Fe_4(bptz)_4(NCCH_3)_8][BF_4]_8 \cdot 9CH_3CN$

The X-ray crystal structure analysis of a dark blue platelet of $[Fe_4(bptz)_4(NCCH_3)_8][BF_4]_8 \cdot 9CH_3CN$ grown by layering an acetonitrile solution of $[Fe_4(bptz)_4(NCCH_3)_8][BF_4]_8$ over toluene revealed a tetranuclear Fe^{II} unit linked by chelating bptz N-donor ligands in an *anti* orientation with seven $[BF_4]^-$ anions located around the periphery of the square metallacycle in close proximity to the ligands and a fully encapsulated $[BF_4]^-$ anion (Figure 50, Figure 51, see Table 8 for crystallographic parameters). The encapsulated anion is disordered equally over two positions and is in close contact with electropositive C atoms of the bptz tetrazine rings: F1A···C6 2.923(9), F2A···C7 2.861(9), F3A···C30 2.883(9), F4A···C31 2.835(9), F1B···C43 2.742(2), F2B···C18 2.951(16), F3B···C19 2.780(2), and F4B···C42 2.798(2) (Figure 52a). Unlike the Co^{II} metallacycle, the Fe^{II} metallacycle templated by $[BF_4]^-$ is much closer to an ideal square due to the increased stability of the Fe^{II}-N bond as compared to the Co^{II}-N bond. The Fe^{II}-Fe^{II} cross-ligand distances are all 6.45 Å (within 0.01 Å) and the Fe^{II}-Fe^{II} cross-cavity distances (9.23 and 9.02 Å) are in closer agreement than in the Co^{II} metallacycle (Figure 52b). Further evidence of the almost ideal square structure are the Fe^{II}-Fe^{II}-Fe^{II}

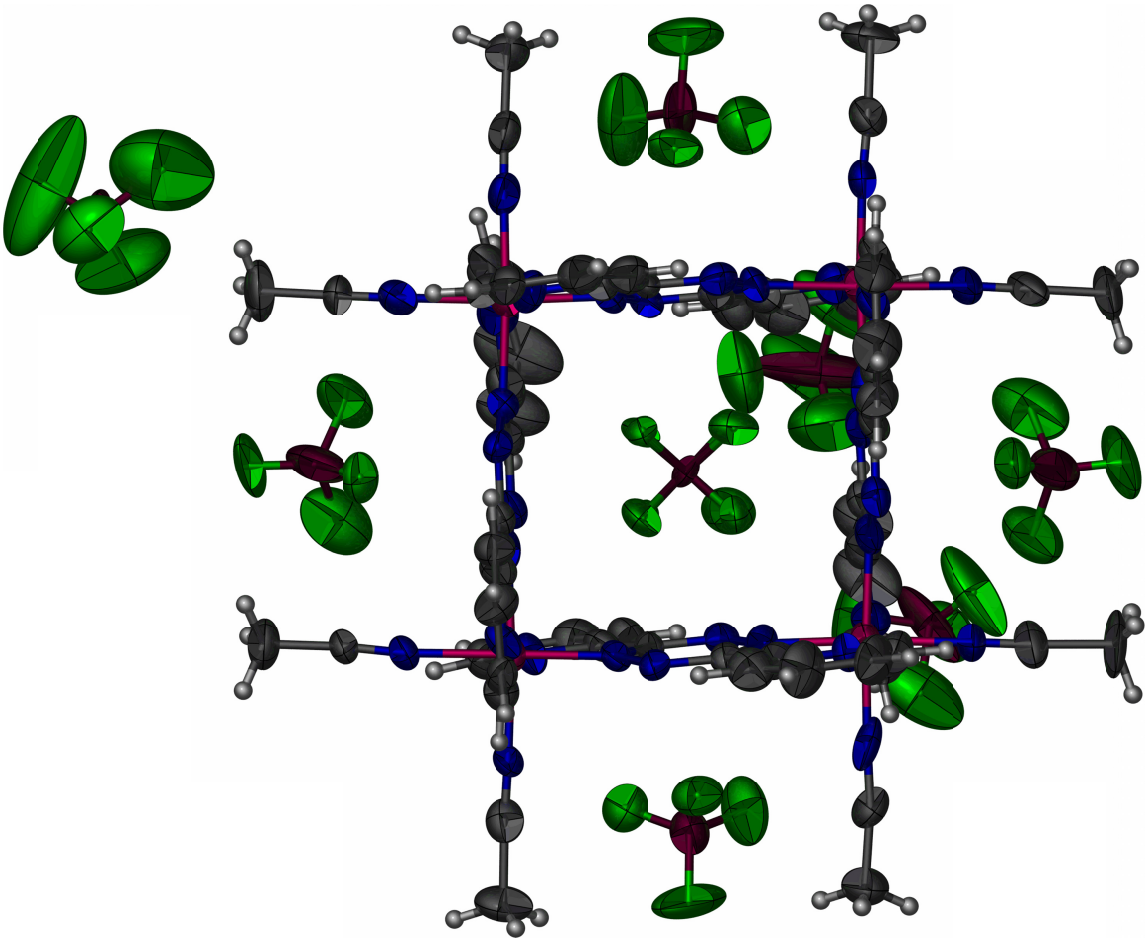

Figure 50. Thermal ellipsoid plot of $[Fe_4(bptz)_4(NCCH_3)_8][BF_4]_8$ drawn at the 50% probability level. Atom colors: Fe (pink), C (dark grey), N (blue), B (maroon), F (green), H (light grey). The encapsulated $[BF_4]^-$ anion is disordered over two positions, only one of which is shown.

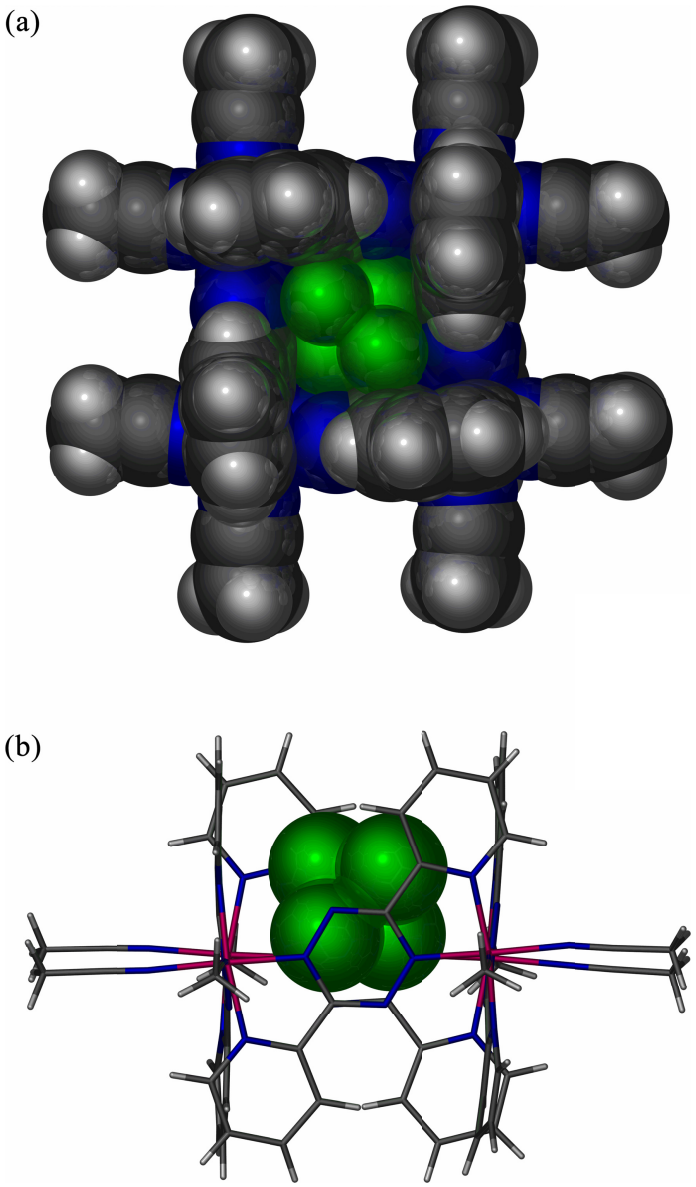

Figure 51. (a) Space-filling front view of the $[BF_4]^-$ anion in the cavity of $[Fe_4(bptz)_4(NCCH_3)_8 \subset BF_4]^{7+}$ showing the tight packing of the anion within the cavity. (b) Side view emphasizing the alignment of the anion (space-filling) with the bptz ligands of the Fe^{II} square (stick). Atom colors: Fe (pink), C (dark grey), N (blue), B (maroon), F (green), H (light grey). Non-encapsulated anions are omitted for the sake of clarity.

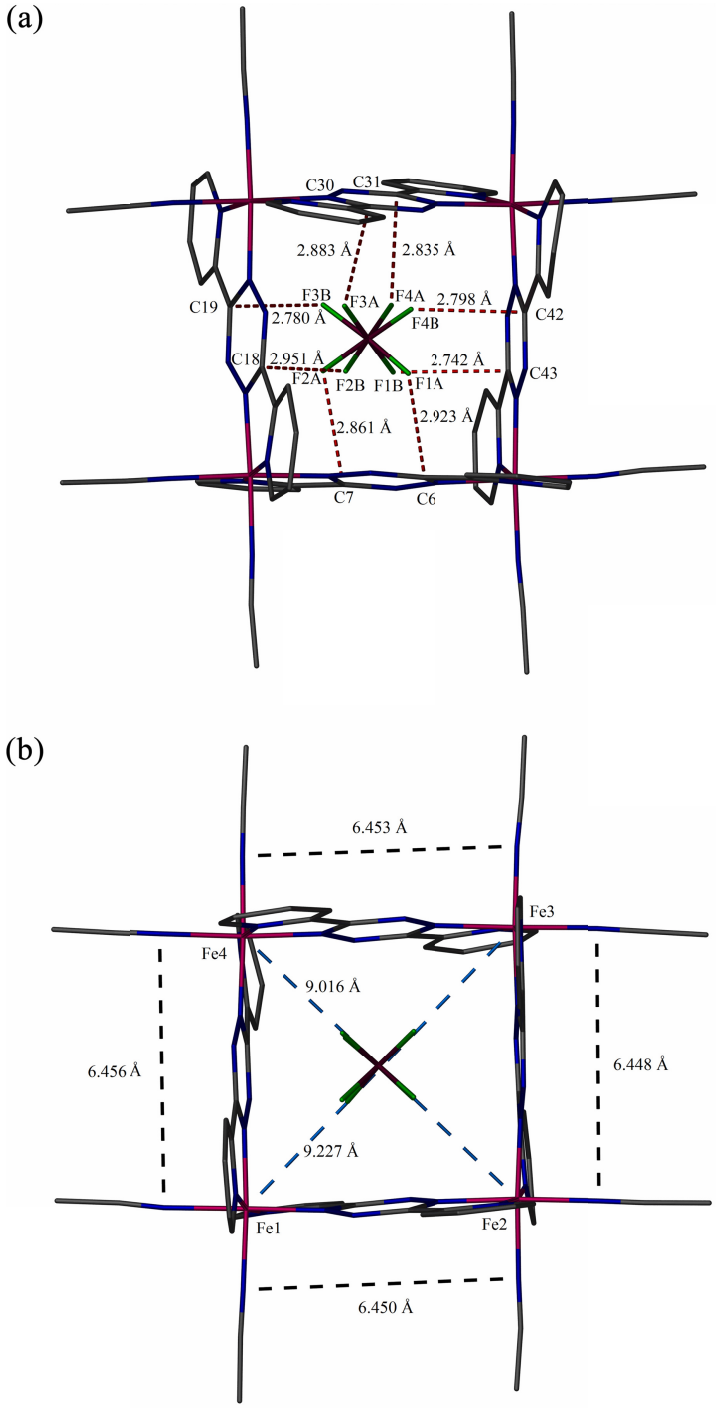

Figure 52. Side-view stick representations of $[Fe_4(bptz)_4(NCCH_3)_8 \subset BF_4]^{7+}$ with (a) F-C distances for both anion positions and (b) cross-ligand and cross-cavity distances indicated. Atom colors: Fe (pink), C (dark grey), N (blue), B (maroon), F (green). Non-encapsulated anions and H atoms are omitted for the sake of clarity.

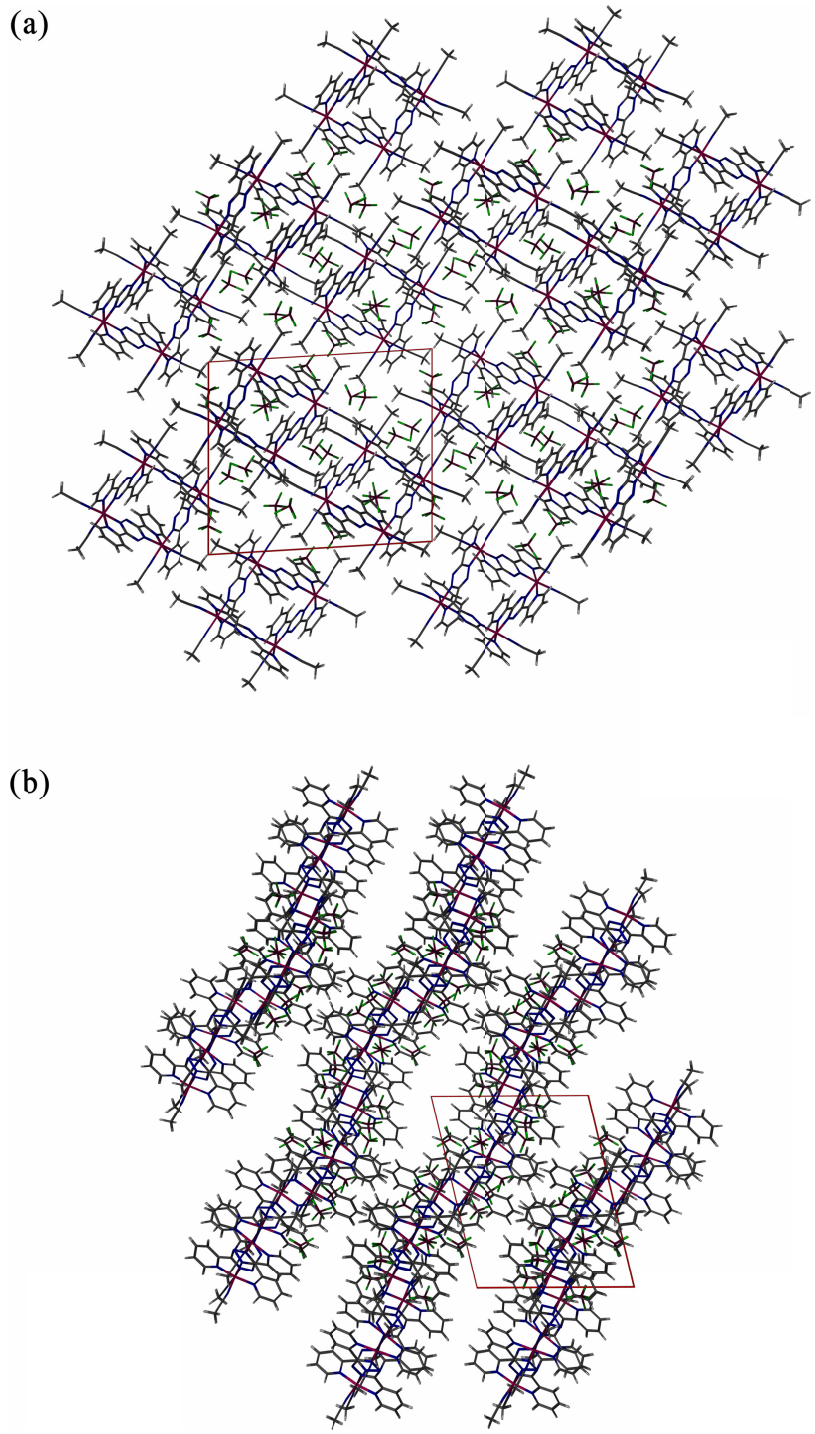

Figure 53. Crystal packing diagrams of $[Fe_4(bptz)_4(NCCH_3)_8][BF_4]_8$ along the (a) *a* and (b) *c* axis of the unit cell (inscribed in red) highlighting the layered packing of the squares.

Table 10. The Fe^{II}-N bond distances in Å (top) and N-Fe^{II}-N angles in degrees (bottom) for $[Fe_4(bptz)_4(NCCH_3)_8][BF_4]_8 \cdot 9CH_3CN$.

Atoms	Distance	Atoms	Distance	Atoms	Distance
Fe1-N2	1.893(5)	Fe1-N26	1.936(6)	Fe1-N25	1.954(6)
Fe1-N23	1.901(6)	Fe1-N3	1.951(6)	Fe1-N24	1.969(6)
Fe2-N27	1.888(9)	Fe2-N8	1.924(6)	Fe2-N28	1.946(6)
Fe2-N5	1.900(6)	Fe2-N6	1.940(7)	Fe2-N9	1.963(7)
Fe3 -N11	1.860(7)	Fe3-N14	1.926(5)	Fe3-N29	1.948(7)
Fe3-N12	1.953(7)	Fe3-N15	1.960(8)	Fe3-N30	1.944(7)
Fe4-N17	1.887(6)	Fe4-N21	1.922(7)	Fe4-N18	1.950(7)
Fe4-N20	1.899(6)	Fe4-N31	1.931(8)	Fe4-N32	1.971(7)

Atoms	Angle	Atoms	Angle	Atoms	Angle
N2-Fe1-N23	92.7(2)	N26-Fe1-N3	91.3(3)	N2-Fe1-N24	92.8(3)
N2-Fe1-N26	90.7(2)	N2-Fe1-N25	177.1(3)	N23-Fe1-N24	82.1(3)
N23-Fe1-N26	176.2(2)	N23-Fe1-N25	87.7(2)	N26-Fe1-N24	96.0(3)
N2-Fe1-N3	81.3(3)	N26-Fe1-N25	89.0(2)	N3-Fe1-N24	170.7(2)
N23-Fe1-N3	90.9(3)	N3-Fe1-N25	95.8(2)	N25-Fe1-N24	90.1(2)
N27-Fe2-N5	88.8(3)	N8-Fe2-N6	94.3(3)	N27-Fe2-N9	96.2(3)
N27-Fe2-N8	176.1(3)	N27-Fe2-N28	88.4(3)	N5-Fe2-N9	91.6(3)
N5-Fe2-N8	93.9(2)	N5-Fe2-N28	176.3(3)	N8-Fe2-N9	80.9(3)
N27-Fe2-N6	88.9(3)	N8-Fe2-N28	89.0(2)	N6-Fe2-N9	171.3(3)
N5-Fe2-N6	81.4(3)	N6-Fe2-N28	96.1(3)	N28-Fe2-N9	91.1(3)
N11-Fe3-N14	93.2(2)	N30-Fe3-N29	88.7(2)	N11-Fe3-N15	90.1(3)
N11-Fe3-N30	176.6(2)	N11-Fe3-N12	83.1(3)	N14-Fe3-N15	81.1(3)
N14-Fe3-N30	90.1(2)	N14-Fe3-N12	92.0(3)	N30-Fe3-N15	90.8(3)
N11-Fe3-N29	87.9(2)	N30-Fe3-N12	96.4(3)	N29-Fe3-N15	97.0(3)
N14-Fe3-N29	177.8(3)	N29-Fe3-N12	90.0(3)	N12-Fe3-N15	170.1(3)
N17-Fe4-N20	93.9(2)	N21-Fe4-N31	93.9(3)	N17-Fe4-N32	176.1(3)
N17-Fe4-N21	90.3(3)	N17-Fe4-N18	81.7(3)	N20-Fe4-N32	89.5(2)
N20-Fe4-N21	82.6(3)	N20-Fe4-N18	94.4(3)	N21-Fe4-N32	92.0(3)
N17-Fe4-N31	88.6(2)	N21-Fe4-N18	171.3(3)	N31-Fe4-N32	88.2(3)
N20-Fe4-N31	175.7(3)	N31-Fe4-N18	89.4(3)	N18-Fe4-N32	96.1(3)
N17-Fe4-N20	93.9(2)	N21-Fe4-N31	93.9(3)	N17-Fe4-N32	176.1(3)

angles of 88.6 and 91.3°, both of which are only minor deviations from the 90° angles subtended by the edges of an ideal square. The cationic square molecule packs in space group P-1 as layers of squares with interstitial anions and solvent (electron density equivalent to nine highly disordered CH_3CN molecules was removed using the SQUEEZE[103] routine in PLATON[102], Figure 53). The Fe^{II}-N distances range from 1.86 – 1.97 Å and the N-Fe^{II}-N angles range from 80.9 – 96.4° (Table 10), as expected for low-spin Fe^{II} ions bound to N, a fact that is further supported by their characteristic electronic absorption spectrum (see below).

c. $[Fe_5(bptz)_5(NCCH_3)_{10}][SbF_6]_{10}\cdot 8.5CH_3CN$

The crystal structure of $[Fe_5(bptz)_5(NCCH_3)_{10}][SbF_6]_{10}\cdot 8.5CH_3CN$ (measured on a dark blue platelet crystal grown by layering an acetonitrile solution of $[Fe_5(bptz)_5(NCCH_3)_{10}][SbF_6]_{10}$ over toluene (CCDC: 844757) consists of a molecular pentagon with Fe^{II} ions linked by chelating bptz entities in an *anti* orientation, as can be seen in the thermal ellipsoid plot (Figure 54, see Table 8 for crystallographic parameters). In the pentagon, the coordination geometry of the Fe^{II} ions is octahedral with four of the sites occupied by two different ligand chelate donors with the other two positions being capped by two CH_3CN molecules. The interatomic Fe^{II}–N distances are in the range 1.84 – 2.02 Å, indicative of low-spin Fe^{II} centers. The average Fe^{II}–Fe^{II}–Fe^{II} angle (108°) is that of an ideal pentagon (108°) in spite of the fact that the N–Fe^{II}–N angles at the vertices are close to 90° (Table 11). The fact that these two requisite geometrical preferences are met is due to the flexibility of the bridging ligands, which bend towards the encapsulated anions to alleviate angle strain (Figure 55).

Interestingly, there are two symmetry-related $[SbF_6]^-$ anions in close proximity in the cavity (Figure 56), a rare situation but not unprecedented for metallacyclic cages, *e. g.* the dodecanuclear Cu^{II} complex of J. M. Lehn, *et al.* which comprises twelve Cu^{II} ions and four bipyridine-pyridazine based ligands and encapsulates four $[PF_6]^-$ ions in close proximity.[104,105] The remaining eight $[SbF_6]^-$ anions are closely packed around the external ligand periphery of the cationic unit (Figure 54). The two encapsulated $[SbF_6]^-$ anions fit tightly within the cavity and each anion establishes three close F···C contacts between three F atoms and three tetrazine rings of the bptz entities (Figure 56, Figure 57a, each anion is disordered between two positions): $[SbF_6]^-\cdots C_{tetrazine}$: F10···C13 2.81(2), F12A···C12 2.83(3), F14A···C25 2.89(3), F14···C24 2.93(2), F10A···C13 2.96(3), F12···C12 3.03(2) Å, and longer ones, F10A···C6 3.35(3), F12···C6 3.37(2) Å. There are also close contacts of the external anions to the pyridyl groups of bptz, for example $[SbF_6]_{ext}^-\cdots C_{pyridyl}$: F3···C15 2.855, F5···C10 2.942 Å (shorter by up to 0.32 Å than R_{vdW} C···F = 3.1 Å) The cross-cavity and cross-ligand distances are also contracted compared to the Ni^{II} pentagon, as expected from the shorter M^{II}-N bond lengths (Figure 57b).

The Fe^{II} pentagon crystallizes in the *Pbcn* space group, exhibiting a corrugated packing of the pentagons along the *b* and *c* axes with interstitial anions and solvent occupying the intermolecular void (electron density equivalent to 8.5 highly disordered CH_3CN molecules was removed using the SQUEEZE[103] routine in PLATON[102], Figure 58a). A precise alignment of pentagonal metallacycles occurs along the *a* axis. Each column (along the *b* axis) of pentagons depicted in the view along the *a* axis contains

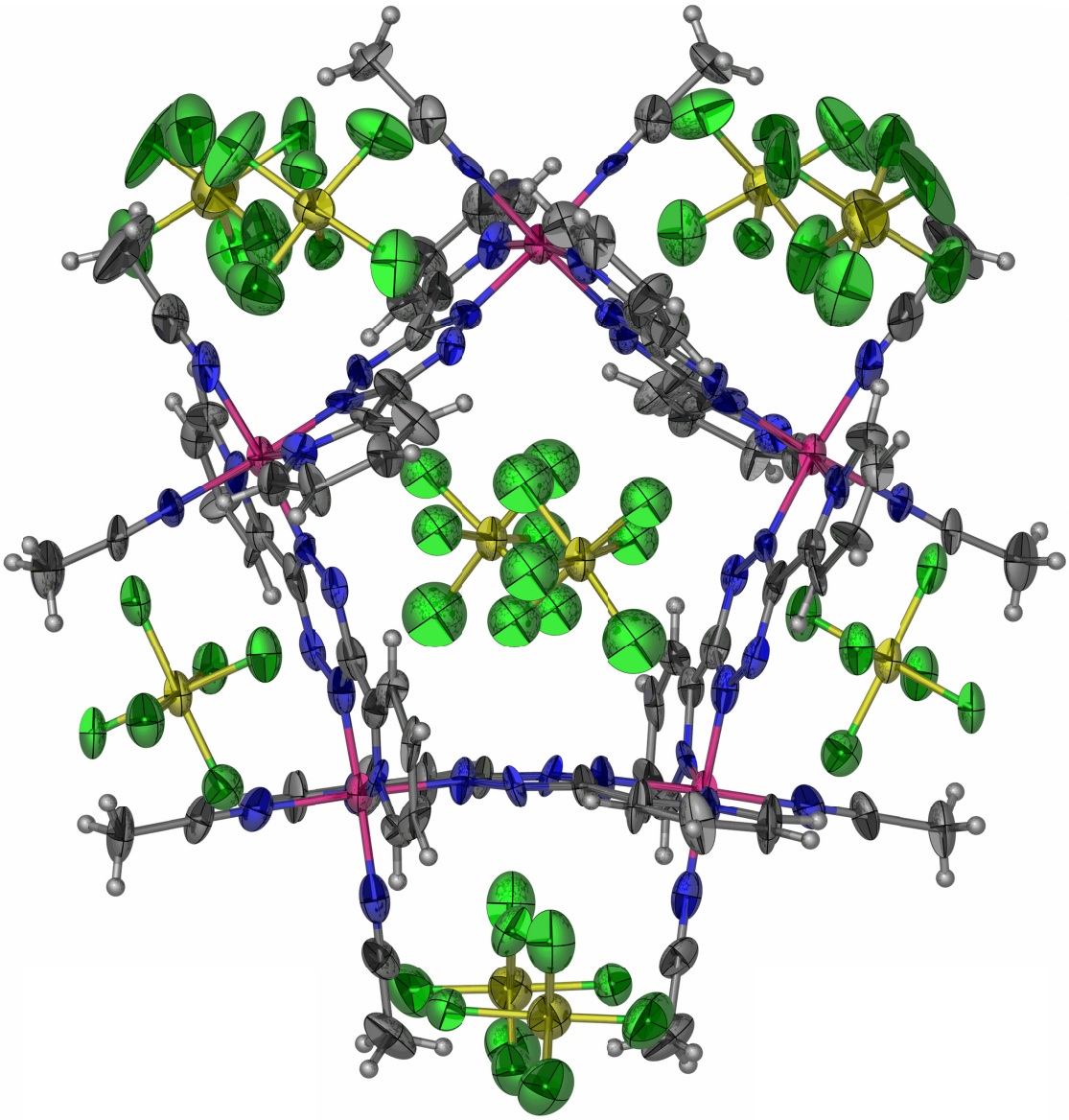

Figure 54. Thermal ellipsoid plot of $[Fe_5(bptz)_5(CH_3CN)_{10}\subset 2SbF_6][SbF_6]_8 \cdot 8.5CH_3CN$ drawn at the 50% probability level. Atom colors: Fe (pink), C (dark grey), N (blue), Sb (yellow), F (green), H (light grey). The encapsulated $[SbF_6]^-$ anions are disordered over two positions. Figure adapted from Dunbar *et al.*[106]

Table 11. The Fe^{II}-N bond distances in Å (top) and N-Fe^{II}-N angles in degrees (bottom) for $[Fe_5(bptz)_5(NCCH_3)_{10}][SbF_6]_{10}\cdot 8.5\ CH_3CN$.

Atoms	Distance	Atoms	Distance	Atoms	Distance
Fe1-N5	1.879(14)	Fe1-N16	1.931(17)	Fe1-N1	1.963(12)
Fe1-N2	1.897(11)	Fe1-N17	1.946(14)	Fe1-N4	1.967(13)
Fe2-N11	1.884(11)	Fe2-N18	1.953(12)	Fe2-N9	2.007(13)
Fe2-N19	1.906(17)	Fe2-N10	1.959(11)	Fe2-N8	1.872(12)
Fe3-N13	1.868(11)	Fe3-N20	1.971(14)	Fe3-N15	1.972(11)

Atoms	Angle	Atoms	Angle	Atoms	Angle
N5-Fe1-N2	93.9(5)	N16-Fe1-N17	89.3(5)	N5-Fe1-N4	80.6(6)
N5-Fe1-N16	177.4(5)	N5-Fe1-N1	92.9(5)	N2-Fe1-N4	90.0(5)
N2-Fe1-N16	88.3(5)	N2-Fe1-N1	81.7(5)	N16-Fe1-N4	98.2(6)
N5-Fe1-N17	88.4(5)	N16-Fe1-N1	88.6(5)	N17-Fe1-N4	91.4(5)
N2-Fe1-N17	177.4(6)	N17-Fe1-N1	97.2(5)	N1-Fe1-N4	169.1(5)
N8-Fe2-N11	95.4(5)	N19-Fe2-N18	87.2(6)	N8-Fe2-N9	81.4(6)
N8-Fe2-N19	174.7(5)	N8-Fe2-N10	89.2(5)	N11-Fe2-N9	92.5(5)
N11-Fe2-N19	89.8(6)	N11-Fe2-N10	83.7(5)	N19-Fe2-N9	97.4(6)
N8-Fe2-N18	87.6(5)	N19-Fe2-N10	92.3(6)	N18-Fe2-N9	91.1(5)
N11-Fe2-N18	175.6(5)	N18-Fe2-N10	93.2(5)	N10-Fe2-N9	169.5(5)
N13*-Fe3-N13	94.3(7)	N20*-Fe3-N20	86.9(6)	N13-Fe3-N15*	81.1(6)
N13-Fe3-N20	176.3(5)	N13-Fe3-N15	92.6(5)	N20*-Fe3-N15	99.3(6)
N13-Fe3-N20*	89.4(5)	N20-Fe3-N15	87.5(5)	N15*-Fe3-N15	170.7(9)

* Symmetry-related atoms with identical atom numbers.

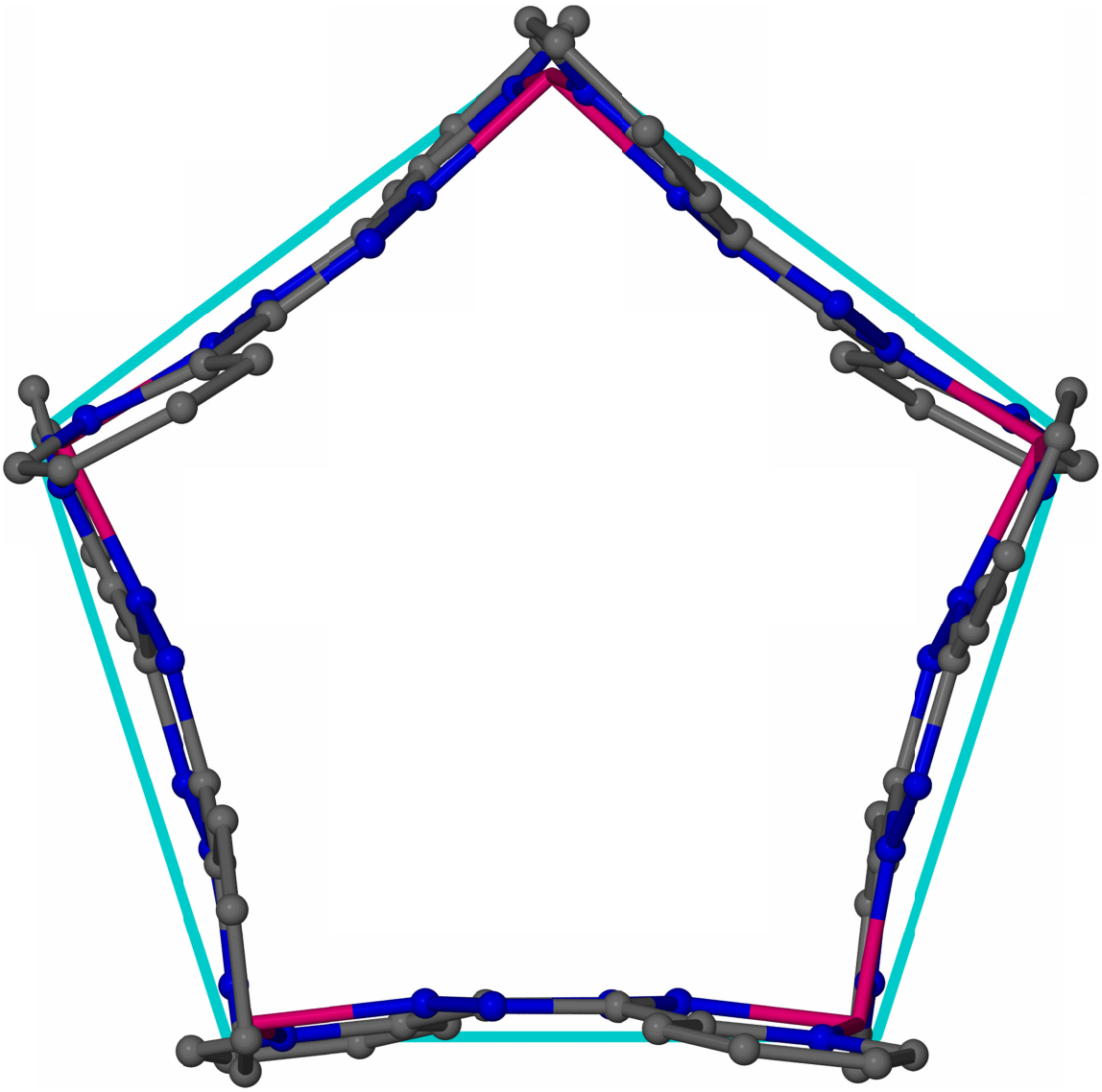

Figure 55. Ball and stick framework diagram of the cationic $[Fe_5(bptz)_5]^{10+}$ metallacycle with a regular pentagon circumscribed about it in teal, highlighting the significant inward bowing of the bptz ligands toward the anions in the central cavity. Atom colors: Fe (pink), C (grey), N (blue). Anion, H atoms and bound solvent are omitted for the sake of clarity. Figure reproduced from Dunbar *et al*.[106]

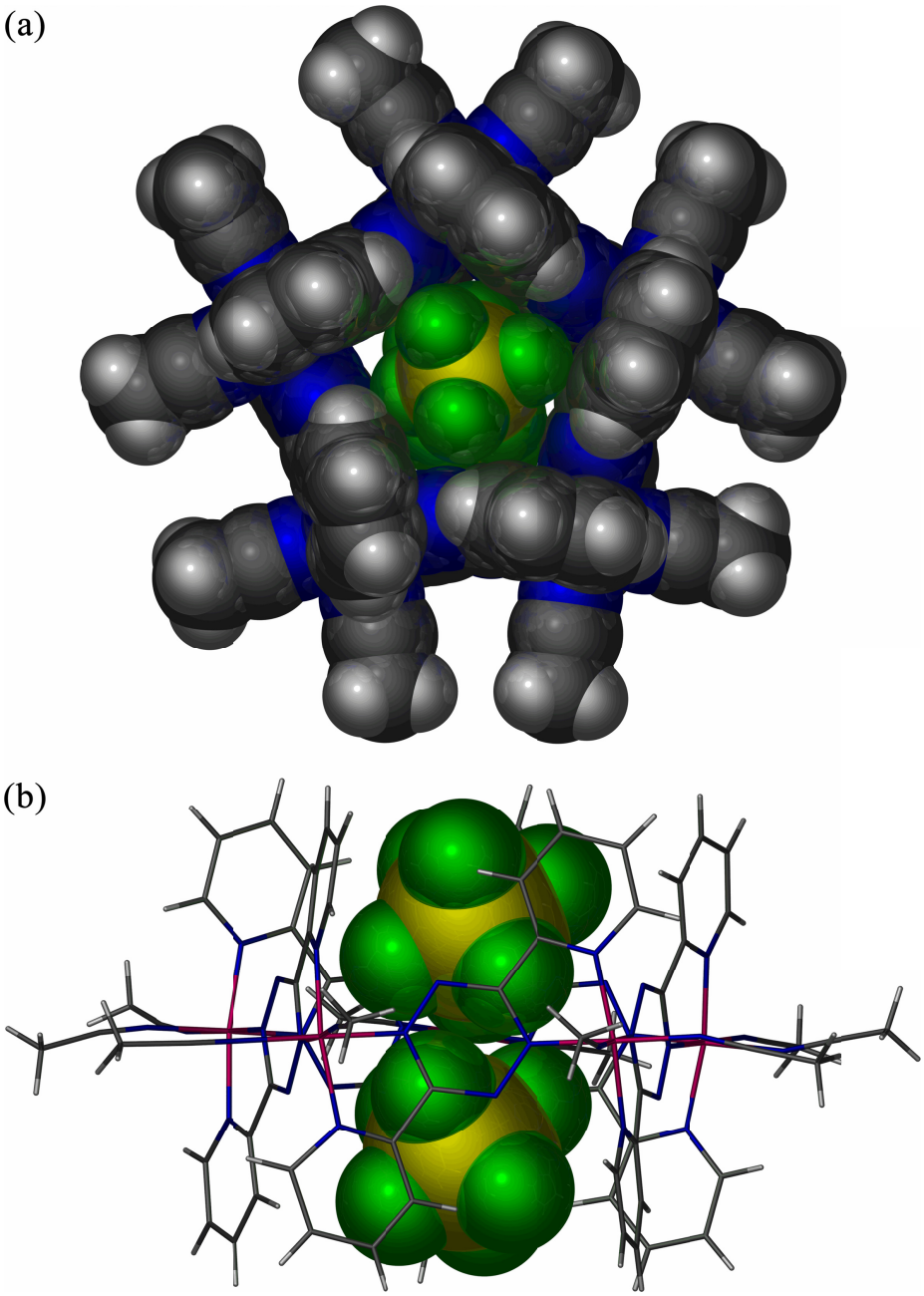

Figure 56. (a) Space-filling front view of the $[SbF_6]^-$ anions in the cavity of $[Fe_5(bptz)_5(NCCH_3)_{10}\subset 2SbF_6]^{8+}$ showing the tight packing of the anions within the cavity. (b) Side-view emphasizing the alignment of the anions (space-filling) with the bptz ligands of the Fe^{II} pentagon (stick). Atom colors: Fe (pink), C (dark grey), N (blue), Sb (yellow), F (green), H (light grey). Non-encapsulated anions are omitted for the sake of clarity.

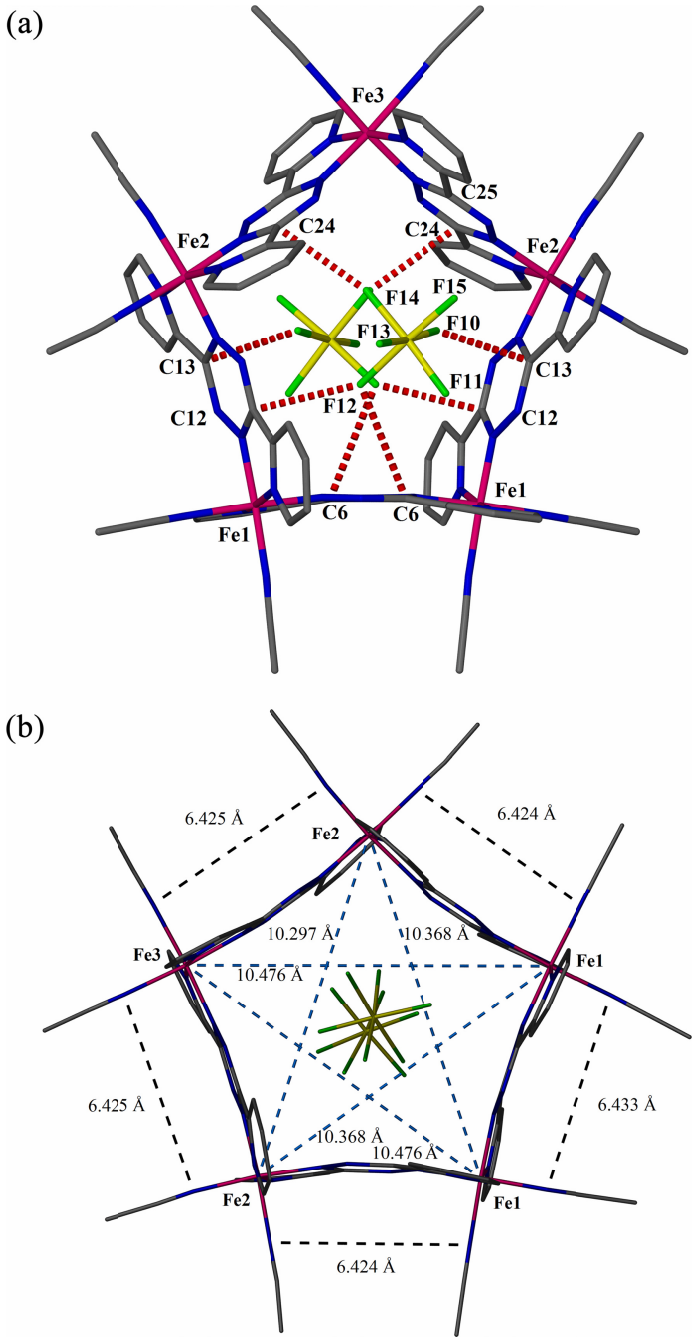

Figure 57. Side-view stick representations of $[Fe_5(bptz)_5(NCCH_3)_{10}\subset 2SbF_6]^{8+}$ with (a) F-C interactions highlighted for one of two anion positions and (b) cross-ligand and cross-cavity distances indicated. Atom colors: Fe (pink), C (dark grey), N (blue), B (yellow), F (green). Non-encapsulated anions and H atoms are omitted for the sake of clarity.

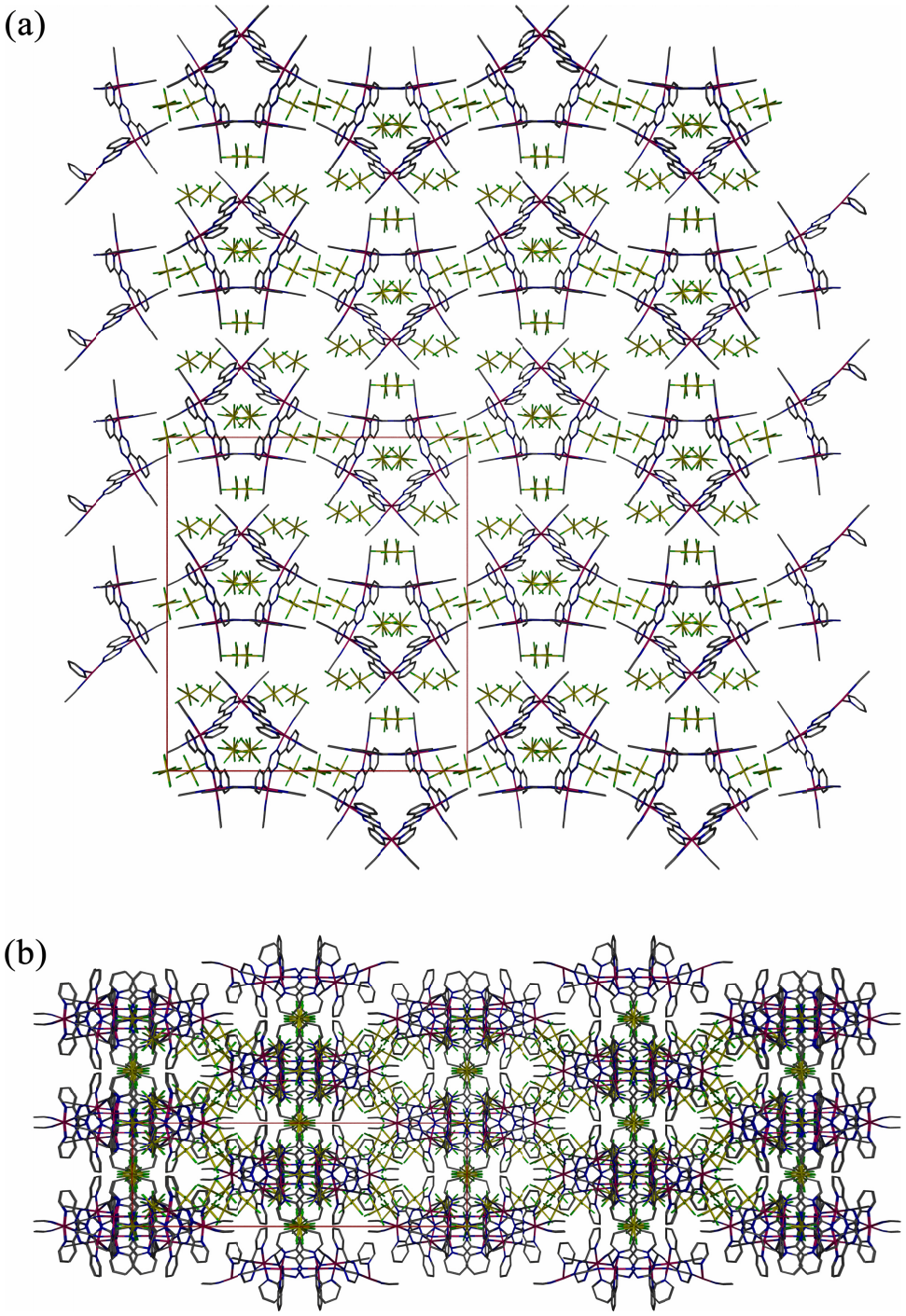

Figure 58. Crystal packing diagram of $[Fe_5(bptz)_5(NCCH_3)_{10}][SbF_6]_{10}$ along the (a) *a* and (b) *c* axis of the unit cell (inscribed in red) highlighting the corrugated packing of the pentagons.

pentagons arranged such that two neighboring columns have pentagons pointing in the opposite direction, with the rows of pentagons apparently alternating between pointing up and down along the *b* axis. As viewed from the *c* axis (looking down the rows, Figure 58b), however, each row contains pentagons pointing in the same direction along the *b* axis, with the rows displaced by ½ of the *a* and ½ of the *b* axis length from one another.

iii. Solution analyses

a. Mass spectrometry

Positive ion mode ESI-FT-ICR-MS of a powder sample of $[Fe_5(bptz)_5(NCCH_3)_{10}][SbF_6]_{10}$ dissolved in CH_3CN displays a characteristic parent ion signal at m/z = 1774.65 consistent with $[Fe_5(bptz)_5(CH_3CN)_5(SbF_6)_8–2H]^{2+}$ (Figure 59). Positive ion mode ESI-FT-ICR-MS of a sample of $[Fe_4(bptz)_4(NCCH_3)_8][BF_4]_8$ in CD_3CN displays a characteristic parent ion signal at m/z = 2155.01 consistent with $[Fe_4(bptz)_4(NCCH_3)_6(CD_3CN)(BF_4)_8+H^+]^+$ (Figure 60) The Fe^{II} pentagon required gentle ionization conditions to observe the full metallacycle, as expected due to the increased ligand strain from the distortions necessary to adopt an ideal pentagonal geometry. It is reasonable to assume that the anions lost are from the periphery of the pentagon rather than the central cavity.

b. Electrochemistry

Cyclic voltammetry and differential pulse voltammetry experiments were performed on a solution of $[Fe_4(bptz)_4(NCCH_3)_8][BF_4]_8$ dissolved in CH_3CN in 0.15 M $[^nBu_4N][BF_4]$ as the supporting electrolyte (to prevent any conversion in solution). In addition to the irreversible ligand reduction waves at -1.07 and -1.61 V vs. Ag/AgCl,

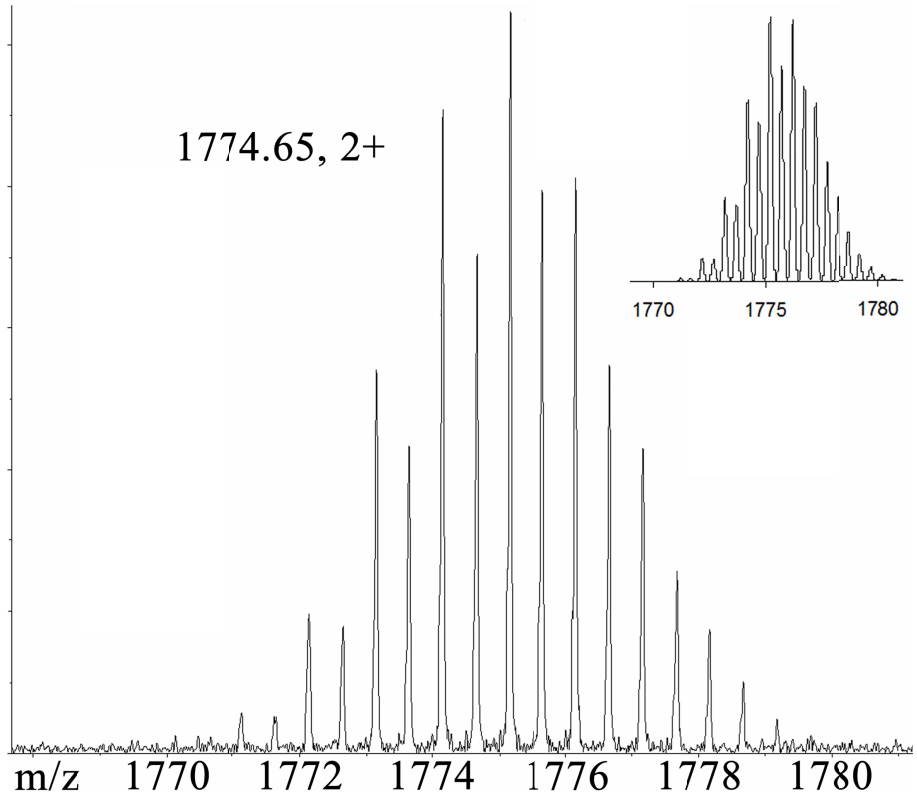

Figure 59. Parent ion signal consistent with $[Fe_5(bptz)_5(CH_3CN)_5(SbF_6)_8–2H]^{2+}$ in CH_3CN at m/z = 1774.65. Theoretical isotopic distribution is shown in the inset.

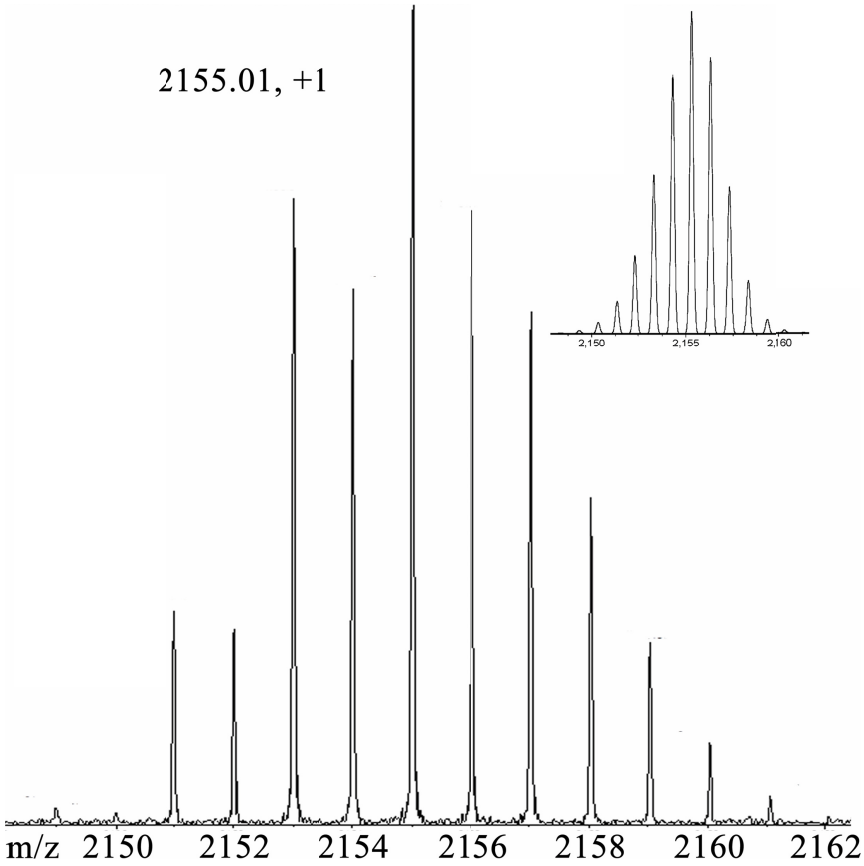

Figure 60. Parent ion signal consistent with $[Fe_4(bptz)_4(CH_3CN)_6(CD_3CN)(BF_4)_8+H^+]^+$ in CD_3CN at m/z = 2155.01. Theoretical isotopic distribution is shown in the inset.

there are four reversible oxidation events at $E_{1/2}$ = -0.094, 0.047, 0.323 and 0.517 V, corresponding to sequential oxidation of the four Fe^{II} ions in the square. These data further establish the stability of the Fe^{II} square metallacycle in solution, and also suggest that communication between the Fe^{II} centers occurs as subsequent oxidation events require higher potentials. The first two oxidation events closely overlap, a fact that is attributed to events occurring at Fe^{II} sites that occupy opposing vertices in the square metallacycle. The remaining Fe^{II} ions are influenced to a greater extent by the Fe^{III} ions that flank them on each side, thereby increasing the oxidation potential of the remaining ions and leading to more separation of the redox couples (Figure 61 and Figure 62).

Electrochemical studies (by cyclic voltammetry and differential pulse voltammetry) of a solution of $[Fe_5(bptz)_5(NCCH_3)_{10}][SbF_6]_{10}$ in a 0.15 M solution of $[^nBu_4N][SbF_6]$ in CH_3CN demonstrated the stability of the Fe^{II} pentagon with bptz in solution (Figure 63 and Figure 64). The oxidation behavior of the Fe^{II} pentagonal metallacycle is more complicated than the Fe^{II} square, with three overlapping oxidation couples followed by two clearly resolved events at higher potential. The oxidation potentials for the pentagon are comparable to those of the square, as expected for a metallacycle comprising the same building units and Fe^{II} coordination environment. In addition to the irreversible ligand reduction waves at -1.22 and -1.54 V vs. Ag/AgCl, there are four reversible oxidation events at $E_{1/2}$ = -0.027, +0.034, +0.37, +0.56 V, corresponding to sequential oxidation of four Fe^{II} ions in the pentagon. In the case of the pentagon, a possible mechanism for the oxidation of the Fe^{II} ions involves oxidation of the apical and two basal Fe^{II} ions at lower potential with minimal influence from the

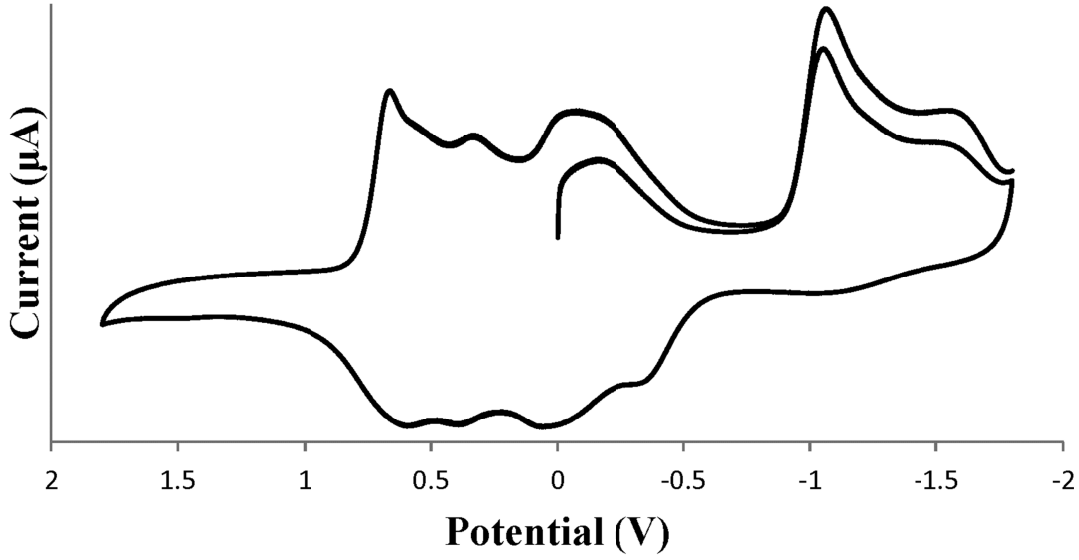

Figure 61. Cyclic voltammogram of $[Fe_4(bptz)_4(NCCH_3)_8][BF_4]_8$ in CH3CN with $[^nBu_4N][BF_4]$ as the supporting electrolyte referenced to Ag/AgCl at a scan rate of 0.2 V/s from 1.8 to -1.8 V.

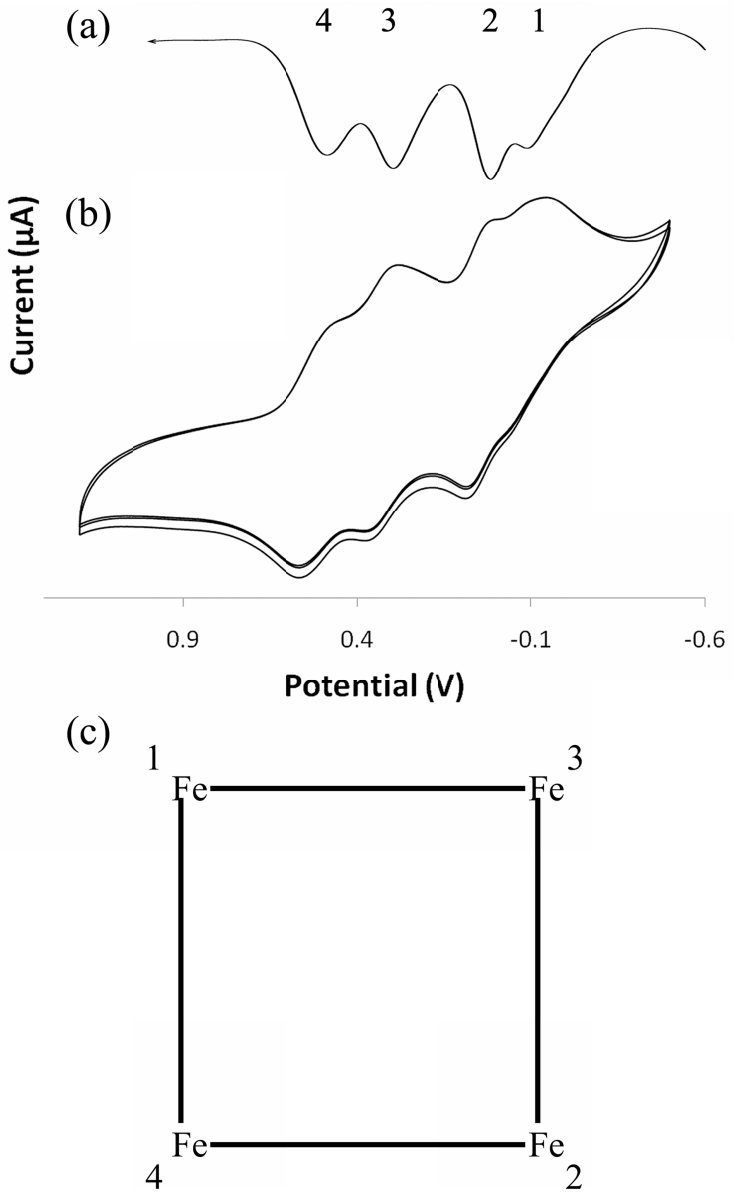

Figure 62. (a) Differential pulse voltammogram and (b) cyclic voltammogram of $[Fe_4(bptz)_4(NCCH_3)_8][BF_4]_8$ in CH_3CN with $[^nBu_4N][BF_4]$ as the supporting electrolyte referenced to Ag/AgCl at a scan rate of 0.2 V/s from 1.3 to -0.5 V. The numbers on the bottom scheme (c) correspond to the proposed order of oxidation events as shown in the voltammogram above.

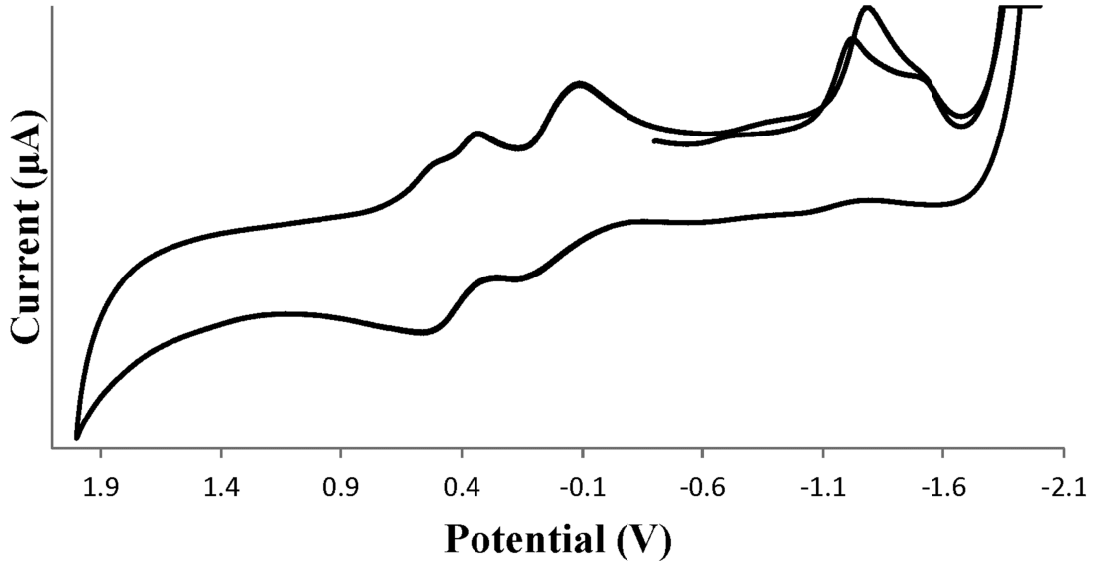

Figure 63. Cyclic voltammogram of $[Fe_5(bptz)_5(NCCH_3)_{10}][SbF_6]_{10}$ in CH3CN with $[^nBu_4N][SbF_6]$ as the supporting electrolyte referenced to Ag/AgCl at a scan rate of 0.1 V/s from 2.0 to -2.0 V.

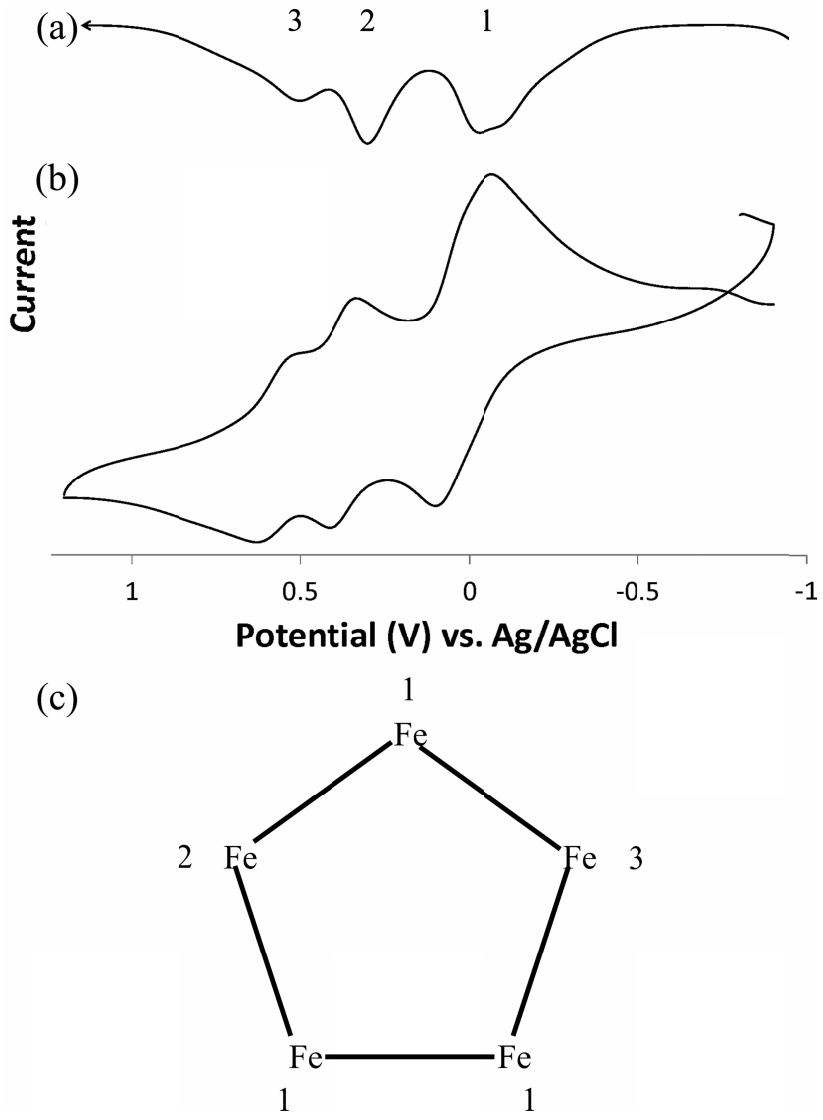

Figure 64. Differential pulse voltammogram (top) and cyclic voltammogram (middle) of $[Fe_5(bptz)_5(NCCH_3)_{10}][SbF_6]_{10}$ in CH_3CN with $[^nBu_4N][SbF_6]$ as the supporting electrolyte referenced to Ag/AgCl at a scan rate of 0.2 V/s from 1.2 to -0.9 V. The numbers on the bottom scheme correspond to the proposed order of oxidation events as shown in the voltammogram above.

other Fe^{II} ions, which subsequently oxidize at higher and more resolved potentials (Figure 64).

The distinct redox behavior of these two metallacycles renders it possible to distinguish between the two polygons in solution. As well-diffracting single crystals of these polygonal architectures often can be difficult to obtain, the electrochemicalbehavior may provide an initial insight into the general structure and stability of metallacycles when incorporating different anions. This is particularly helpful when using anions too large to fit within the square metallacycle cavity but too small to effectively support a pentagonal metallacycle. The stepwise oxidation observed for the Fe^{II} metallacycles is also quite different than the single oxidation observed in the cyclic voltammogram of the Ni^{II} species.[93] Once oxidized to Fe^{III}, the metal ion draws more electron density away from the ligand, diminishing the donation to neighboring Fe^{II} ions and making it harder to remove electrons from their t_{2g} orbitals. The effect is less pronounced in the oxidation of Ni^{II} as the electrons are easily removed from the slightly antibonding e_g orbitals.

The electrochemical studies demonstrate the solution stability of both $[Fe_4(bptz)_4(NCCH_3)_8][BF_4]_8$ and $[Fe_5(bptz)_5(NCCH_3)_{10}][SbF_6]_{10}$, even when the structure is perturbed by oxidation of the Fe^{II} centers. In fact, the electrochemical studies highlight the importance of the anion-π interaction to the stability of the structures, even in solution. Oxidation of the Fe^{II} ions to Fe^{III} increases the positive charge, thereby increasing the Coulombic attraction of the anions to the cationic metallacycle, leaving the structure intact. Reduction of the ligand, however, has the opposite effect. The

irreversibility of the ligand-based reduction indicates the decomposition of the metallacycle. Reducing the ligand decreases the π-acidity of the central arene, increasing repulsion of the anion and therefore destabilizing the structure, which subsequently decomposes

c. Electronic absorption spectroscopy

The electronic absorption spectra of both $[Fe_4(bptz)_4(NCCH_3)_8][BF_4]_8$ and $[Fe_5(bptz)_5(NCCH_3)_{10}][SbF_6]_{10}$ in CH_3CN exhibit ligand-to-metal charge-transfer (LMCT) absorption bands at 797 (19,000 $Lmol^{-1}cm^{-1}$) and 802 nm (30,000 $Lmol^{-1}cm^{-1}$), respectively; the extinction coefficients support the assignment of these transitions as LMCT bands. These transitions result in the characteristic dark blue color of these polygonal architectures with Fe^{II} ions, and are further support for the presence of diamagnetic low-spin d^6 Fe^{II}.[107,108]

d. Magnetic susceptibility

Magnetic susceptibility measurements performed on a powder sample of $[Fe_4(bptz)_4(NCCH_3)_8][BF_4]_8$ prepared under anaerobic conditions exhibits a χT value at room temperature of 1.4 emu K^{-1} mol^{-1} consistent with 52% of one H. S. S = 2 Fe^{II} ion. This fraction of paramagnetic Fe^{II} center undergoes a spin transition from high to low spin upon cooling the sample to 1.8 K, resulting in a χT value of 0.5 emu K^{-1} mol^{-1} corresponding to 33% of one S = 2 Fe^{II} ion. These data reveal that the majority of the solid sample contains molecules with diamagnetic low spin Fe^{II}, with a small fraction of Fe^{II} existing in the high spin S = 2 state.

Magnetic susceptibility measurements performed on a powder sample of $[Fe_5(bptz)_5(NCCH_3)_{10}][SbF_6]_{10}$ prepared under anaerobic conditions exhibits a χT value at room temperature of 0.67 emu K^{-1} mol^{-1} consistent with 24% of one H. S. S = 2 Fe^{II} ion. This fraction of paramagnetic Fe^{II} center undergoes a spin transition from high to low spin upon cooling the sample to 1.8 K, resulting in a χT value of 0.33 emu K^{-1} mol^{-1} corresponding to 18% of one S = 2 Fe^{II} ion. As in the case of the $[Fe_4(bptz)_4(NCCH)_3][BF_4]_8$ compound, these data indicate that the majority of the solid sample is diamagnetic with low spin Fe^{II} ions, and a small fraction of Fe^{II} ions in the high spin S = 2 state.

e. NMR spectroscopy

Previous work had established that the Zn^{II} square metallacycle with $[BF_4]^-$ anions is sufficiently stable in solution to allow for study by ^1H NMR spectroscopy. The Zn^{II} square exhibits resonance shifts of the aromatic bptz protons in CD_3CN of δ = 8.10 (d; 3, 3′), 8.31 (td; 5,5′), 8.52 (td; 4,4′) and 9.25 (d; 6,6′) ppm. The resonances are shifted from free bptz in CD_3CN; chemical shift values are δ = 8.64 (d; 3, 3′), 7.65 (td; 5,5′), 8.10 (td; 4,4′) and 8.93 (d; 6,6′) ppm.[70] The downfield shifts of the 6,6′-H, 4,4′-H, and 5,5′-H proton resonances are attributed to the inductive effect of the metal ion binding to the ligand; the upfield shift of the 3,3′-H protons is attributed to the shielding effect from the ring currents of the pyridyl groups on neighboring ligands.[70]

Unlike their Ni^{II} and Co^{II} congeners, the metallacycles of Fe^{II} are diamagnetic in solution, and thus were studied *via* ^1H NMR spectroscopy. The ^1H NMR spectrum of the Fe^{II} square is similar to that of the corresponding Zn^{II} square, demonstrating the stability

of the Fe^{II} square in solution. The proton resonance shifts of bptz in the Fe^{II} square are as follows: δ = 7.61 (d; 3, 3′), 8.05 (td; 5,5′), 8.29 (td; 4,4′) and 8.89 (d; 6,6′) ppm (Figure 65). One significant difference between the Zn^{II} and Fe^{II} squares is that the chemical shifts of the 6,6′-H protons are more shielded in the Fe^{II} than the Zn^{II} congener. In general, all of the aromatic bptz protons are shielded more in the Fe^{II} square, possibly due to the closer proximity of the ligands to each other as a result of the shorter Fe^{II}-N distances.

For the first time, ^{1}H NMR spectroscopy was used to examine the solution structure of a pentagonal metallacycle of bptz with $[SbF_6]^-$. Surprisingly, the chemical shifts of the aromatic bptz protons of the Fe^{II} pentagon differ slightly from the Fe^{II} square in the ^{1}H NMR spectrum. The chemical shifts of the Fe^{II} pentagon are as follows: 7.52 (d, 3,3′-H), 8.07 (td, 5,5′-H), 8.31 (td, 4,4′-H), 8.82 (d, 6,6′-H) (Figure 66). Most notable is the greater shielding of the 3,3′-H proton due to a better alignment of the proton to the face of a neighboring ligand pyridyl group (Figure 67). In the square, the proton-centroid distances are in range from 3.3 to 4.1 Å, whereas in the pentagon they are in the range of only from 3.4 to 3.8 Å. In the pentagon, the 3′ protons tend to point more consistently towards the neighboring ring centroid. It is this difference between the spectra of the square and pentagonal metallacycles that provides a handle for qualitatively tracking the relative amounts of each in solution when studying the interconversion of the two species.

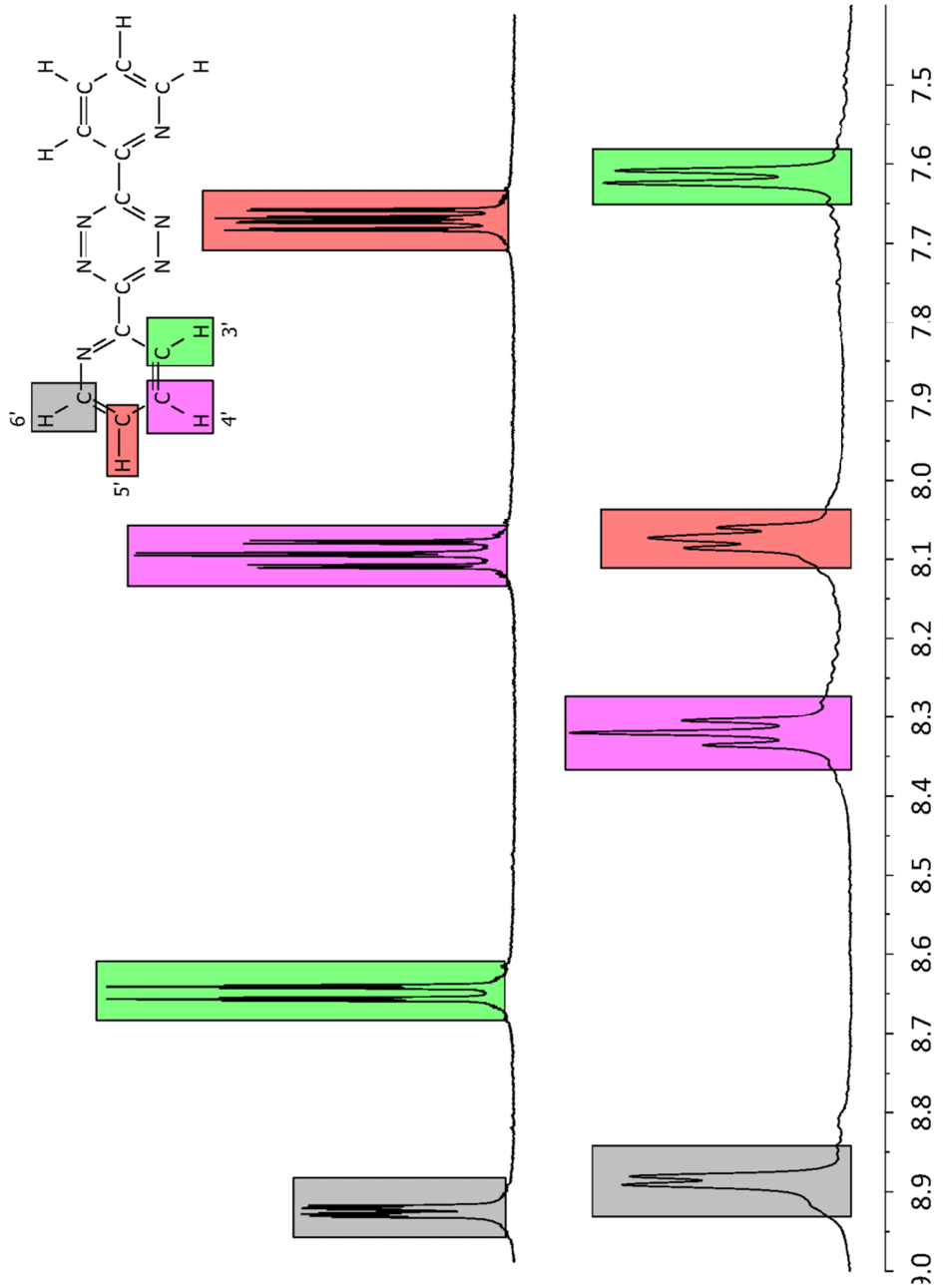

Figure 65. Aromatic region of the ^{1}H NMR spectrum of free bptz (top) and $[Fe_4(bptz)_4(NCCH_3)_8][BF_4]_8$ (bottom) in CD_3CN, referenced to CH_3CN impurities in the deuterated solvent. Proton resonances are color coded according to the inset scheme.

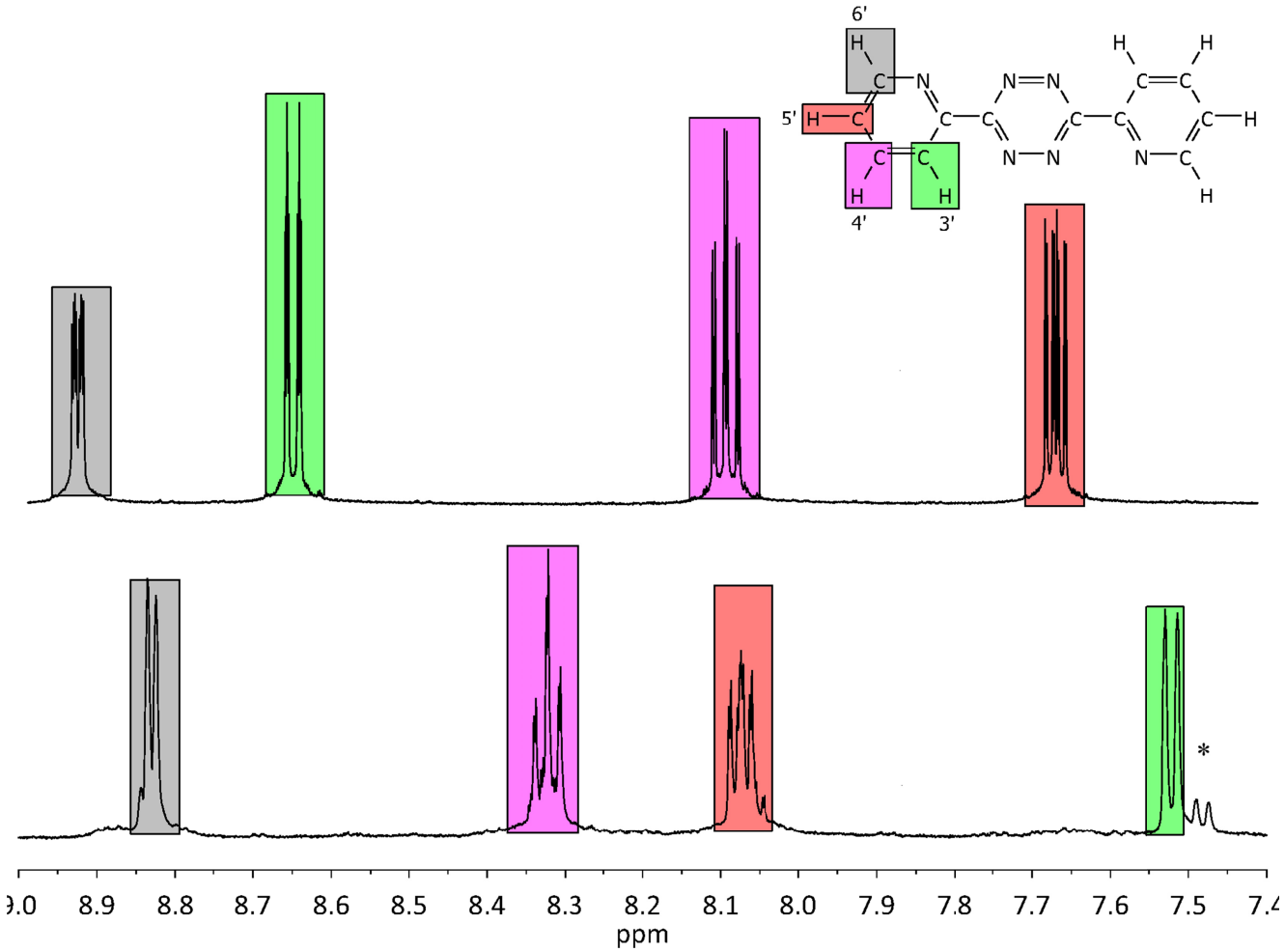

Figure 66. Aromatic region of the ^{1}H NMR spectrum of free bptz (top) and $[Fe_5(bptz)_5(NCCH_3)_{10}][SbF_6]_{10}$ (bottom) in CD_3CN, referenced to CH_3CN impurities in the deuterated solvent. Proton resonances are color coded according to the inset scheme. The resonance marked with an asterisk (*) is likely due to the movement of the 3′-H out of the pyridine ring current.

In order to follow the interconversion between the square and pentagonal metallacycles in solution, a sample of the Fe^{II} pentagon was dissolved in CD_3CN under a nitrogen environment, sealed in a J. Young air tight NMR tube and its ^1H NMR spectrum was measured. Under a nitrogen environment, an excess of $[^nBu_4N][BF_4]$ in CD_3CN was added and the spectrum was measured again. Despite some resonance broadening (likely due to opening and closing of the metallacyclic structures in solution), it is clear that the majority of the species in solution have converted to the square metallacycle (Figure 68). This demonstrates a clear preference for the $[BF_4]^-$ ion over the $[SbF_6]^-$ in the templation of these metallacycles and that the square metallacycle is more stable than the pentagonal one, a conclusion that coincides with that of the mass spectrometric interconversion studies of the Ni^{II} metallacycles. The study also demonstrates the importance of the anion templation processes in the formation and stability of the metallacycles in solution.

Attempts to observe both free and encapsulated anions in either of the metallacycles by ^{19}F NMR spectroscopy have not yielded definitive results. For the Fe^{II} square, only free $[BF_4]^-$ anions could be observed, which may be a consequence of the anion being closer to the edge of the cavity and thus more accessible for exchange with other anions in solution. Due to the presence of antimony in the $[SbF_6]^-$ anion, its ^{19}F NMR signal exhibited a complicated splitting pattern from the coupling to both ^{121}Sb (I = 5/2) and ^{123}Sb (I = 7/2), which occur in almost equal abundance, and further complicated by broadening from the influence of their quadrupole moments. Only one signal for $[SbF_6]^-$ is observed, but, owing to the reasons stated above, it is difficult to

`

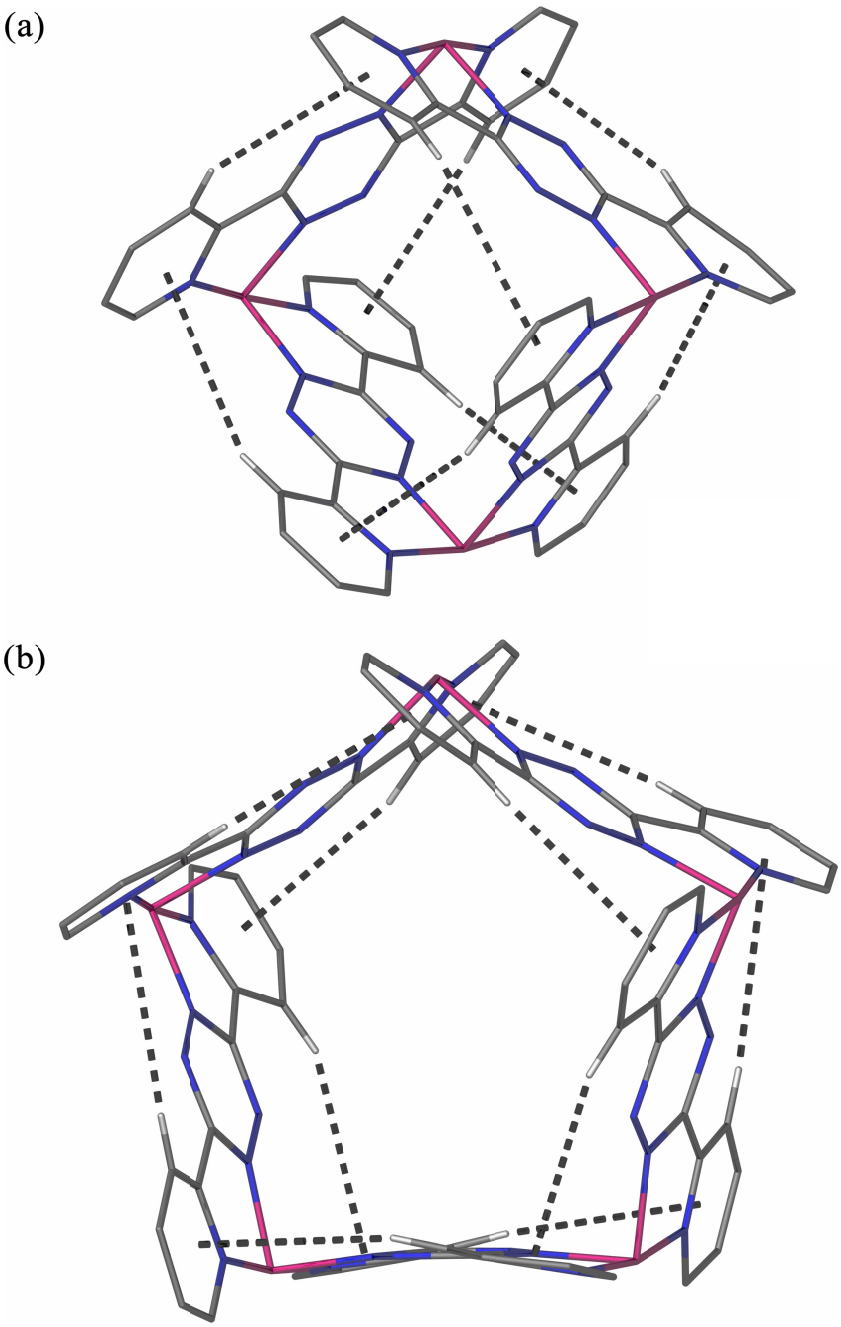

Figure 67. Stick representations of the (a) Fe^{II} square and (b) Fe^{II} pentagon highlighting the shielding of the 3′ proton of the pyridyl ring by the neighboring pyridyl ring, denoted by the grey dashed line between the 3′-H and the neighboring pyridyl centroid, which is more pronounced in the pentagon than in the square.

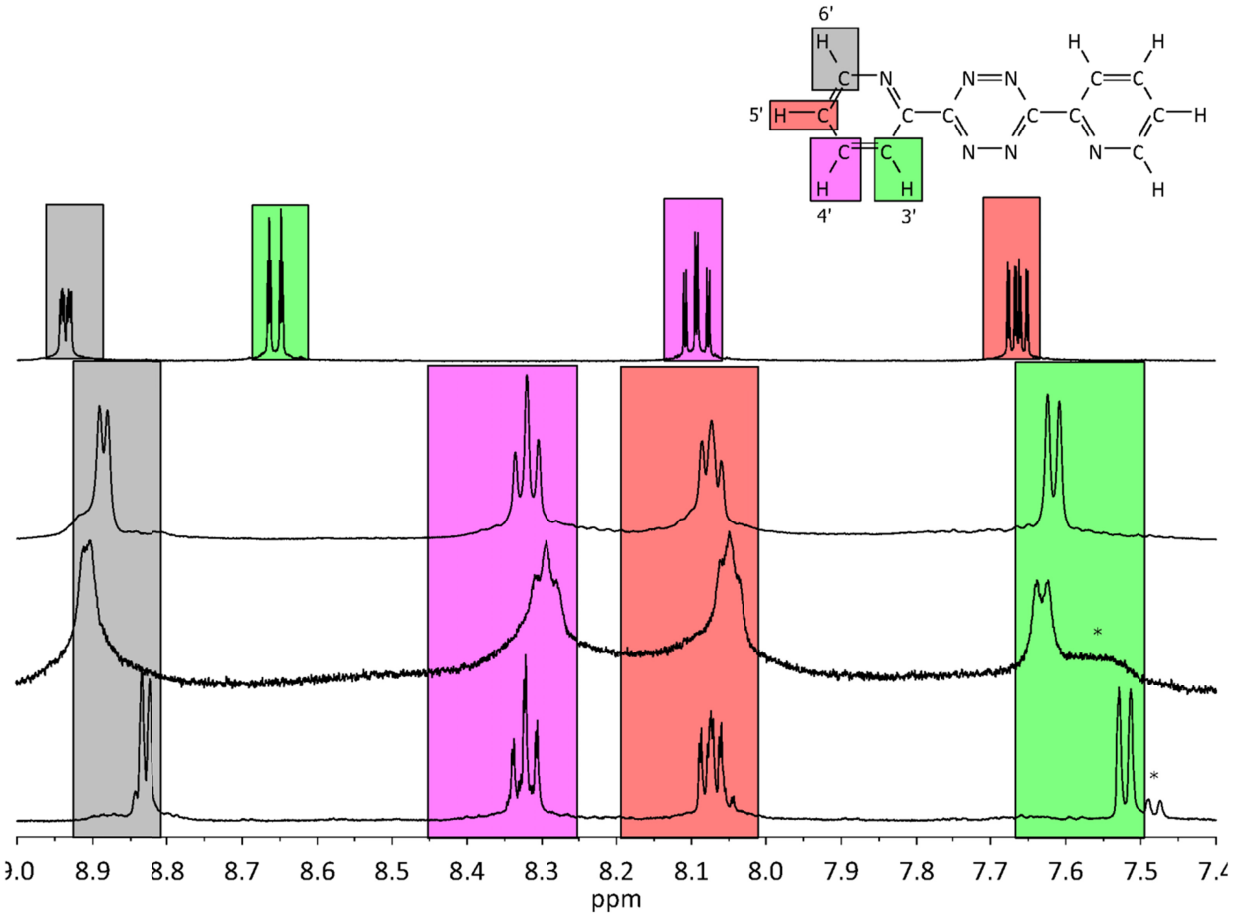

Figure 68. Aromatic region of the ^{1}H NMR of free bptz (top spectrum), synthesized $[Fe_4(bptz)_4(NCCH_3)_8][BF_4]_8$ (second spectrum from top), $[Fe_5(bptz)_5(NCCH_3)_{10}][SbF_6]_{10}$ (second spectrum from bottom), and a sample of $[Fe_5(bptz)_5(NCCH_3)_{10}][SbF_6]_{10}$ treated with excess $[^{n}Bu_4N][BF_4]$ (second spectrum from bottom), showing the interconversion of the pentagon to the square upon addition of an excess of $[BF_4]^-$. All spectra were measured in CD_3CN and referenced to CH_3CN impurities in the deuterated solvent. Resonances are color coded according to the provided ligand scheme (inset). Resonances marked with an asterisk (*) are likely due to the movement of the 3′-H out of the pyridine ring current.

detect whether or not there are two types of anions contributing to the observed resonance. Also, the proximity of the anions to the cavity openings in the Fe^{II} metallacycles makes the anions more accessible for exchange in solution. This situation has prompted attempts to synthesize pentagonal metallacycles of Fe^{II} with other anions such as $[PF_6]^-$ and $[AsF_6]^-$, with the expectation of simpler ^{19}F NMR spectra (Chapter V).

D. Conclusions

It is clear from the data presented in this chapter that the square and pentagonal metallacycles formed by the reaction of bptz with Ni^{II} or Zn^{II} salts of $[BF_4]^-$ (square, Ni^{II} and Zn^{II}) or $[SbF_6]^-$ (pentagon, Ni^{II}) are not limited to these metal ions. The synthesis that leads to the formation of the anion templated square in the Ni^{II} and Zn^{II} cases can be extrapolated to Co^{II} and Fe^{II} ions and the pentagon of Fe^{II} can be formed as well by a method similar to that of the Ni^{II} pentagon. The key to synthesizing the metallacycles of Co^{II} and Fe^{II} is the use of scrupulously dry and air-free conditions during their (and their starting materials') preparation and handling.

Key structural differences are observed with changes in the metal ion. The M^{II}-N bond distances contract in the order $Zn^{II} > Ni^{II} \sim Co^{II} >> Fe^{II}$ (Table 12), as expected considering the increasing occupation of the e_g orbitals as one moves from low-spin Fe^{II} (e_g^0) to high-spin Co^{II}/Ni^{II} (e_g^2) Zn^{II} (e_g^4). One consequence of the bond distance contraction is the reduction of the cavity size, most notably in the Fe^{II} metallacycles. Despite the decrease in cavity size, an anion is still tightly encapsulated in the square metallacycle of Fe^{II}. In the pentagonal metallacycle, the contraction leads to the encapsulation of two closely associated $[SbF_6]^-$ anions within the cavity. In order for

Table 12. Comparison of average distances (d_{avg}) for the square and pentagonal metallacycles, in Å. Values for the Ni^{II} and Zn^{II} metallacycles are from the dissertation of Cristian Saul Campos-Fernández, 2001.[93]

Metal Ion	Cross-ligand d_{avg}	Cross-cavity d_{avg}	M-N $d_{shortest} - d_{longest}$
		Square	
Fe^{II}	6.5	9.1	1.86 – 1.97
Co^{II}	7.0	9.9	2.03 – 2.18
Ni^{II}	6.9	9.7	2.04 – 2.11
Zn^{II}	7.2	10.1	2.07 – 2.29
		Pentagon	
Fe^{II}	6.4	10.4	1.87 – 2.01
Ni^{II}	6.7	10.9	2.04 – 2.09

these anions to be located in such close proximity and in tight contact with the metallacycles (and other anions), there must be some stabilizing force involved. Considering the close association of the anions with the electropositive carbon atoms of the tetrazine and pyridyl groups of bptz, it is reasonable to conclude that the stabilizing forces involved are anion-π interactions, a hypothesis supported by previous work in our group involving Ag^{I} structures of bptz and 3,6-bis(2′-pyridyl)pyridazine[79,109] (see Chapter IV) as well as computational work presented in this dissertation (see Chapter II).

Although they are often considered as a significant contributing factor in the close association of molecules in the solid state, crystal packing forces (London forces) alone do not fully account for the positioning of the anions in the cavities of these metallacycles. If crystal packing forces alone accounted for the encapsulation of the anion, the pentagonal metallacycle would not exist (especially not in solution). The formation of a pentagonal metallacycle over a square one is entropically disfavored since this would result in fewer particles for the same number of starting particles. From an enthalpy standpoint, the strain induced by the incongruence of the pentagonal and coordination angles makes the square a more favored structure as well. It would be reasonable to expect the square metallacycle to encapsulate solvent molecules rather than the $[BF_4]^-$ anion (or any anion) in the solid state as is often the case in Fujita's and Stang's work, for example, yet this is clearly not the case.[60,61,110] The anion-π interactions are sufficiently strong as to allow for the persistence of the square and pentagonal metallacycles in solution and their analyses by mass spectrometry, NMR, and even through multiple oxidation events.

Table 13. The metallacycles synthesized to date with the indicated anion and metal ion. Black mark indicates metallacycles synthesized prior to this work, those in blue indicate metallacycles synthesized during the course of this dissertation.

	Fe^{II}	Co^{II}	Ni^{II}	Zn^{II}
Square ($[BF_4]^-$)	✓	✓	✓	✓
Pentagon ($[SbF_6]^-$)	✓		✓	

The work presented in this chapter serves to extend the series of square and pentagonal metallacycles to earlier divalent transition metals and has allowed, for the first time, more detailed studies of the interconversion of these species by ^{1}H NMR spectroscopy (Table 13). Still, this is only a small fraction of the metal ions (and oxidation states) available for use in metallacycles of these types. It is of considerable interest to extend the syntheses to larger 4d and 5d metal ions, as well as oxidation states other than 2+. The metal ions with larger radii should allow for the encapsulation of larger anions, and the greater flexibility of the coordination environment may lead to new types of anion-templated structures. As the data presented herein attest, the metal ion plays a key role in the structure of the resulting metallacycle through changes in bond lengths which affects stabilities and can lead to surprising results such as the incorporation of two anions within the cavity of the Fe^{II} pentagon.

CHAPTER IV

THE EFFECT OF REPLACING BPTZ WITH LIGANDS OF DIFFERENT Π-ACIDITY

A. Introduction

Interest in the role of anion-π interactions in the anion templation of the metallacycles discussed in Chapter III prompted the Dunbar group to study the extent to which the difference in π-acidity between the bptz and 3,6-bis(2′-pyridyl)pyridazine (bppn) ligands affects their propensity for anion-templation with salts of Ag^{I}. The substitution of the central tetrazine ring with pyridazine in bppn decreases the π-acidity of the central arene, which is expected to weaken the anion-π interactions with a potentially templating anion (Figure 69). The other consequence of introducing pyridazine as the central ring is the limitation of the binding mode to *syn*-only, as opposed to the *syn* or *anti* coordination option provided by bptz (Figure 70). The Ag^{I} ion was chosen since it is adaptable with regards to its coordination number and geometry, a situation that provides a good platform to assess the self-annealing nature of structures formed with bptz or bppn.[79]

These studies revealed that the change in the central ring π-acidity between bppn and bptz is sufficient to affect the anion templation of their complexes with Ag^{I}. In the Ag^{I} compounds of bptz, the anion dictates the final structure. Variations of stoichiometry lead to different compounds, even with the same anion, with anion-π interactions being evident in all of them. The most notable of these compounds are the $[Ag_2(bptz)_3][X]_2$

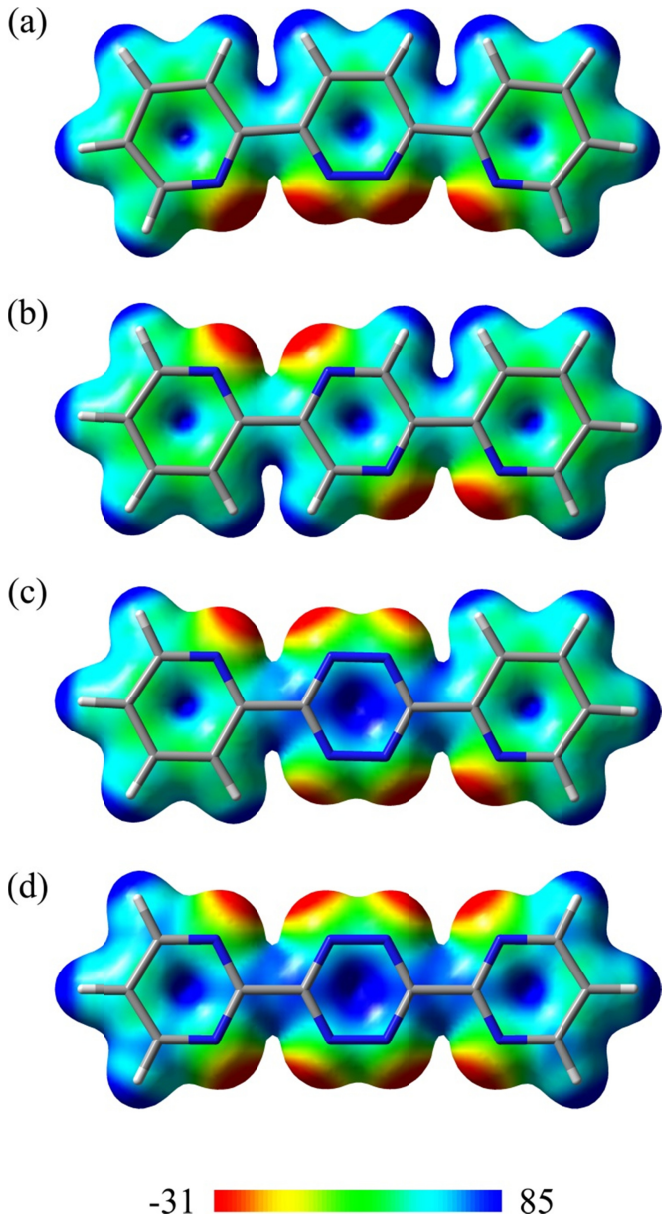

Figure 69. ESP maps of (a) 3,6-bis(2′-pyridyl)pyridazine (bppn), (b) 2,5-bis(2′-pyridyl)pyrazine (bppz), (c) 3,6-bis(2′-pyridyl)-1,2,4,5-tetrazine (bptz), and (d) 3,6-bis(2′-pyrimidyl)-1,2,4,5-tetrazine (bmtz) generated at an isodensity value of 0.02 a.u. from DFT geometry optimization computations using the B3LYP functional and 6-31+g(d, p) basis set. The dihedral angles between the outer and central arenes were fixed in each case to mimic the binding modes of the ligands (see Figure 70). A stick representation of the corresponding ligand is overlaid on the ESP map for reference. Atom colors: carbon (grey), nitrogen (blue), and hydrogen (white). The color range is depicted at the bottom, with values reported in kcal mol^{-1}.

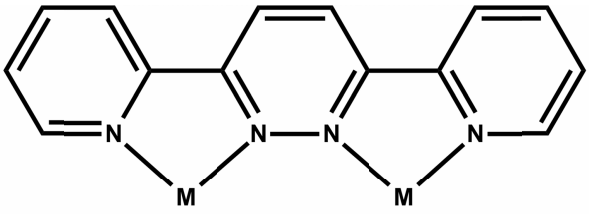

3,6-bis(2′-pyridyl)pyridazine (bppn)

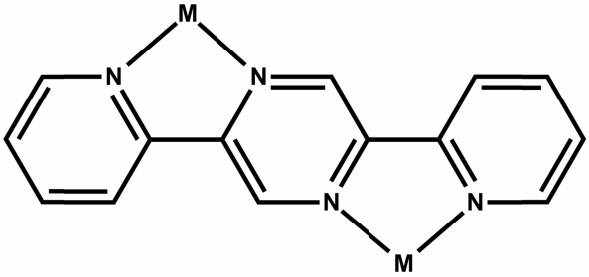

3,6-bis(2′-pyridyl)pyrazine (bppz)

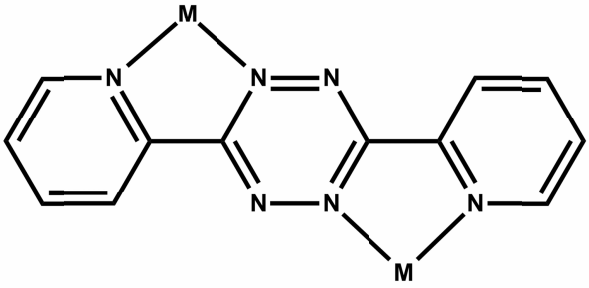

3,6-bis(2′-pyridyl)-1,2,4,5-tetrazine (bptz)

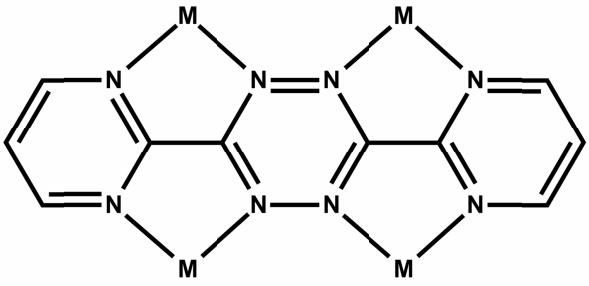

3,6-bis(2′-pyrimidyl)-1,2,4,5-tetrazine (bmtz)

Figure 70. Schematic depiction the binding modes for bppn, bppz, bptz, and bmtz, highlighting the *syn* binding of bppn observed in the structures with Ag^{I} and the *anti* binding observed with the metallacyclic structures of bptz.

trigonal prismatic structures formed when using the ratios 2:3 $AgAsF_6$:bptz and 1:1 or 2:3 $AgSbF_6$:bptz (Figure 71).[79,109] In both of these trigonal prismatic complexes, three bptz ligands are coordinated to two Ag^I ions in a *syn* fashion with each anion interacting with three tetrazine rings. The F atoms of the $[AsF_6]^-$ and $[SbF_6]^-$ anions exhibit close contacts with the tetrazine ring, with F···centroid distances of 2.91 Å for both cases. The $[Ag_2(bptz)_3][SbF_6]_2$ trigonal prismatic compound can also crystallize without interstitial solvent, with one $[SbF_6]^-$ anion participating in anion-π interactions with six tetrazine rings, albeit at a somewhat elongated F···centroid distance of 3.27 Å. Intermolecular π-π stacking interactions are also present, with the tetrazine rings of bptz 3.36 Å apart (Figure 72).[79]

When the $[PF_6]^-$ anion is used as the anion in reactions with bptz, both the infinite coordination polymer $\{[(Ag(bptz)][PF_6]\}_\infty$ and the dimer $[Ag_2(bptz)_2(CH_3CN)_2][PF_6]_2$ were synthesized from a 1:1 $AgPF_6$:bptz reaction, with the final product depending on the concentration of the reactants, the latter forming under more dilute conditions (Figure 73). Both of these structures involve the $[PF_6]^-$ anion interacting with two tetrazine rings, exhibiting close F···centroid interaction distances of 2.84 and 2.81 Å for the polymer and dimer, respectively. A 1:1 reaction of $AgAsF_6$:bptz also forms a dimeric species isostructural to that with $[PF_6]^-$, with an F···centroid distance of 2.78 Å (the shortest among all of the bptz structures incorporating Ag^I).[79]

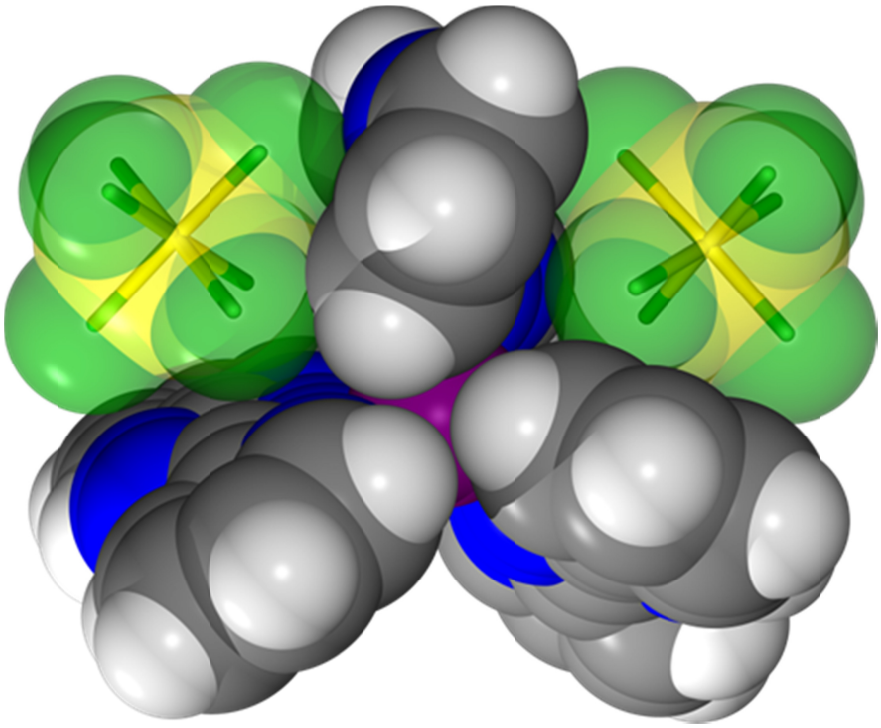

Figure 71. Space filling diagram of$[Ag_2(bptz)_3][SbF_6]_2$, showing the anion-π interactions between $[SbF_6]^-$ and the central tetrazine rings of bptz. Atom colors: Ag (pink), N (blue), C (grey), H (white), Sb (yellow), and F (green). Figure adapted from Dunbar *et al.*[79]

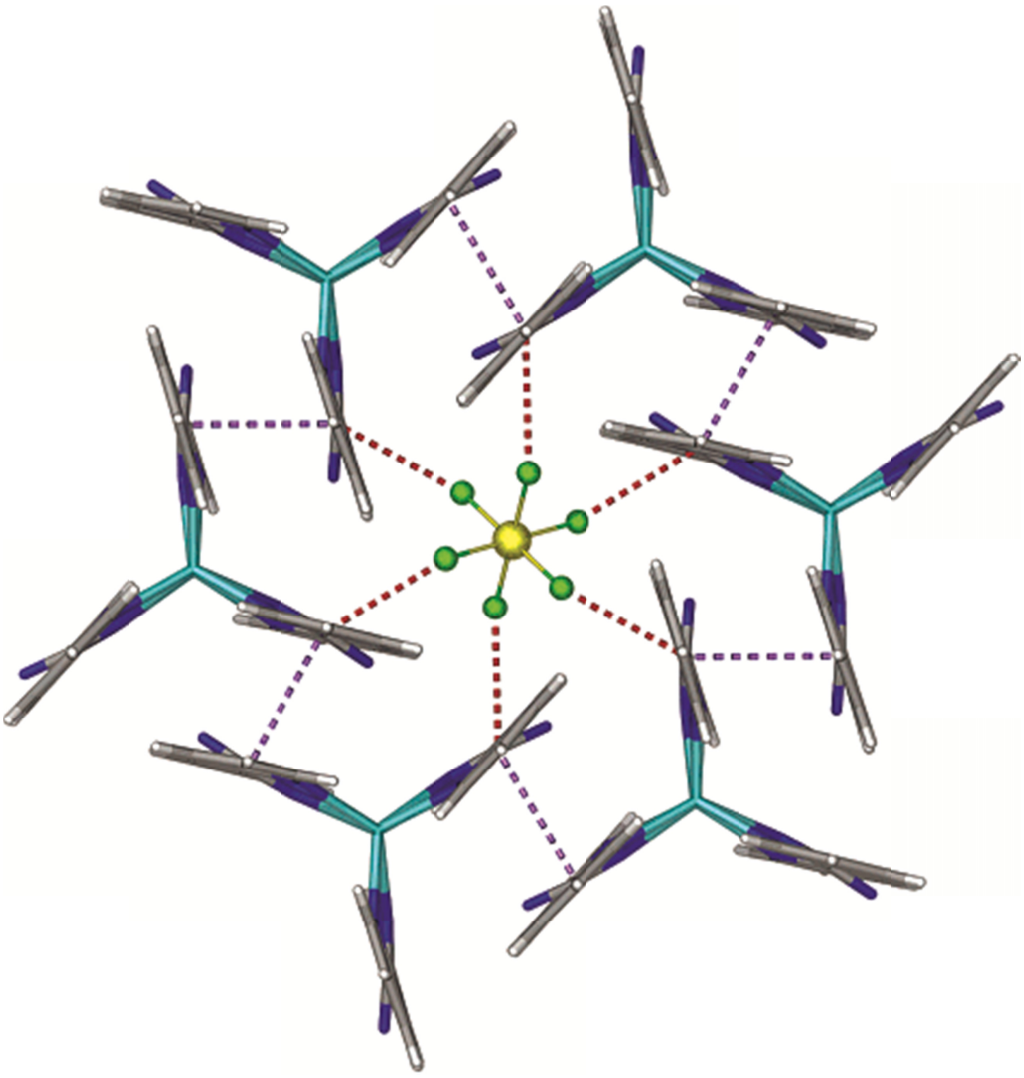

Figure 72. Alternate crystal packing of $[Ag_2(bptz)_3][SbF_6]_2$ showing one $[SbF_6]^-$ anion involved in anion-π interactions with six bptz tetrazine moieties, indicated by the red dashed lines. The $[Ag_2(bptz)_3]^{2+}$ units also participate in molecular π-π stacking interactions, as indicated by the purple dashed lines. Atom colors: Ag (teal), N (blue), C (grey), H (white), Sb (yellow), F (green). Figure reproduced from Dunbar *et al.*[79]

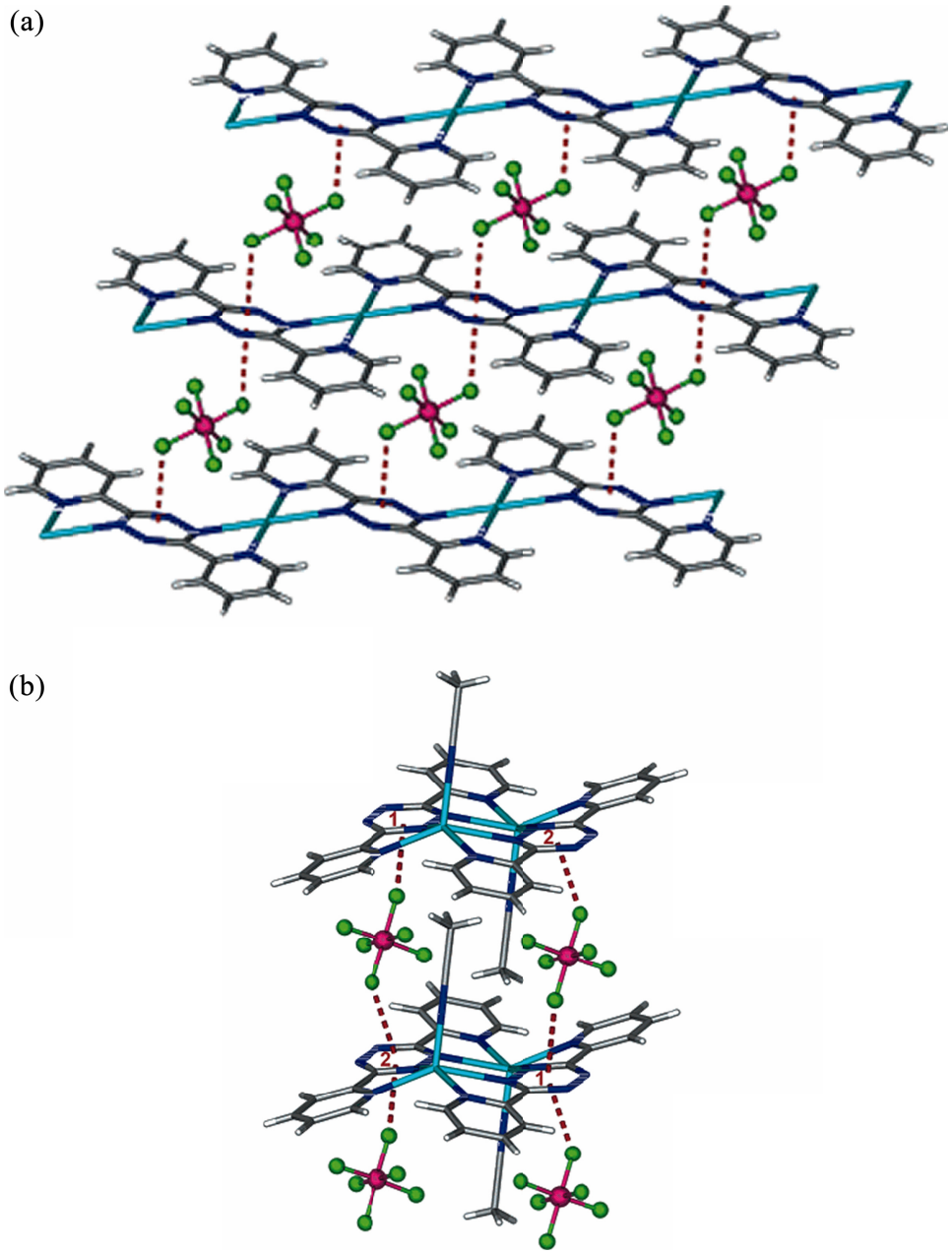

Figure 73. Structures of the (a) $\{[(Ag(bptz)][PF_6]\}_\infty$ polymer and (b) $[Ag_2(bptz)_2(CH_3CN)_2][PF_6]_2$ dimer formed by reaction of $AgPF_6$ with bptz under concentrated and dilute conditions, respectively. The anion-π interactions between the $[PF_6]^-$ and bptz tetrazine rings are indicated by red dashed lines in both. Atom colors: Ag (teal), N (blue), C (grey), H (white), P (pink), F (green). Figure adapted from Dunbar *et al.*[79]

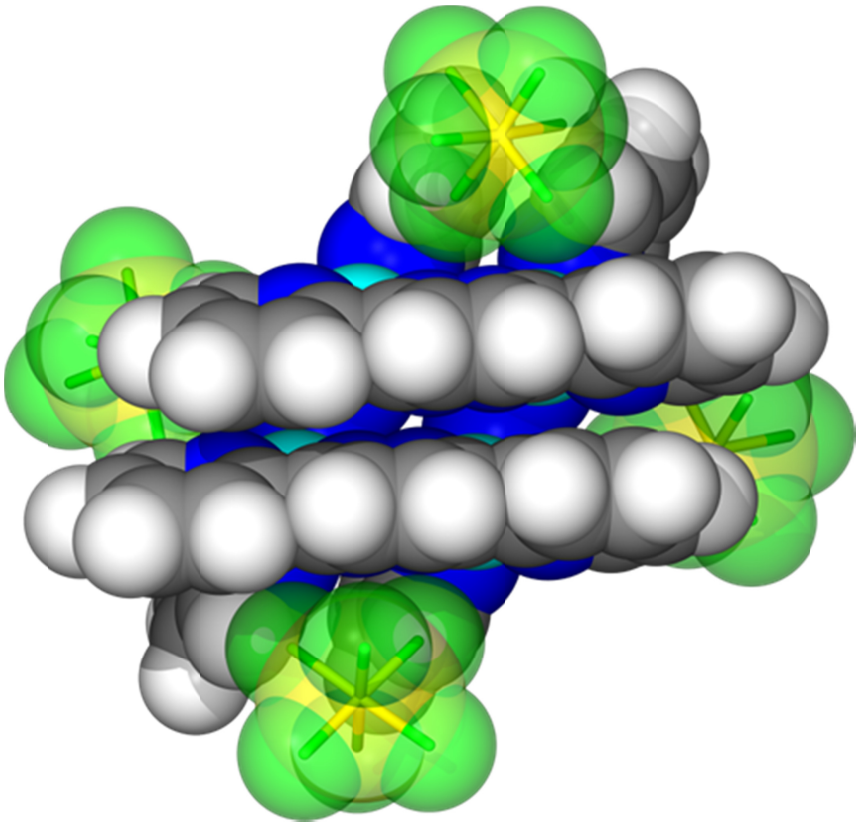

Figure 74. Space filling diagram of $[Ag_4(bppn)_4][SbF_6]_4$, representative of the grid structures formed between $AgBF_4$, $AgPF_6$, $AgAsF_6$, and $AgSbF_6$. Intramolecular π-π stacking interactions dominate the formation of the grid structure, with weak anion-π interactions between the $[SbF_6]^-$ anions and the bppn pyridazine rings about the periphery of the grid. Atoms colors: Ag (teal), N (blue), C (grey), H (white), Sb (yellow), F (green). Figure adapted from Dunbar *et al.*[79]

The Ag^{I} compounds with bppn, however, only form 4x4 grids regardless of the anion or stoichiometry between AgX and bppn (X = $[BF_4]^-$, $[PF_6]^-$, $[AsF_6]^-$, or $[SbF_6]^-$; Figure 74). In all cases, π-π stacking interactions dictate the formation of the grid structure. Anion-π interactions are present in each of the grid structures formed with the various AgX salts, but the distances are much longer than those in the corresponding bptz cases and clearly do not direct the final structure of the complex. The F···centroid distances increase in the order $[BF_4]^-$ > $[PF_6]^-$ ~ $[AsF_6]^-$ > $[SbF_6]^-$ (2.90, 3.10, 3.10, and 3.27 Å, respectively), following the expected trend as the anion charge becomes more diffuse. The π-π stacking interactions in these compounds are all in a staggered alignment, with inter-arene distances close to 3.4 Å for the $[PF_6]^-$, $[AsF_6]^-$, and $[SbF_6]^-$ species and 3.5 Å for the $[BF_4]^-$ species, which are all within expected distances. The differences between the Ag^{I} structures observed using bppn and bptz demonstrate the importance of the π-acidity of the central ring in dictating the extent of anion-templation in these molecules, as seen in the lack of templation by anion-π interactions in the structures with the less π-acidic bppn ligand.[79]

With similar studies in mind, the Dunbar group reacted 3,6-bis(2′-pyrimidyl)-1,2,4,5-tetrazine (bmtz, Figure 70 bottom) with $[Cu(NCCH_3)_4][BF_4]$, forming the octanuclear $[Cu_8(bmtz)_6][BF_4]_6 \cdot CH_3CN$ cluster (Figure 75). Anion-π interactions are present in the crystal packing of this compound; it is the π-π stacking interactions, however, that dictate the final structure. The Cu^{I} centers were oxidized to Cu^{II} (considering the tetrahedral coordination environment about Cu) by the bmtz ligands, which exhibited bond arene bond lengths characteristic for their reduced forms. The

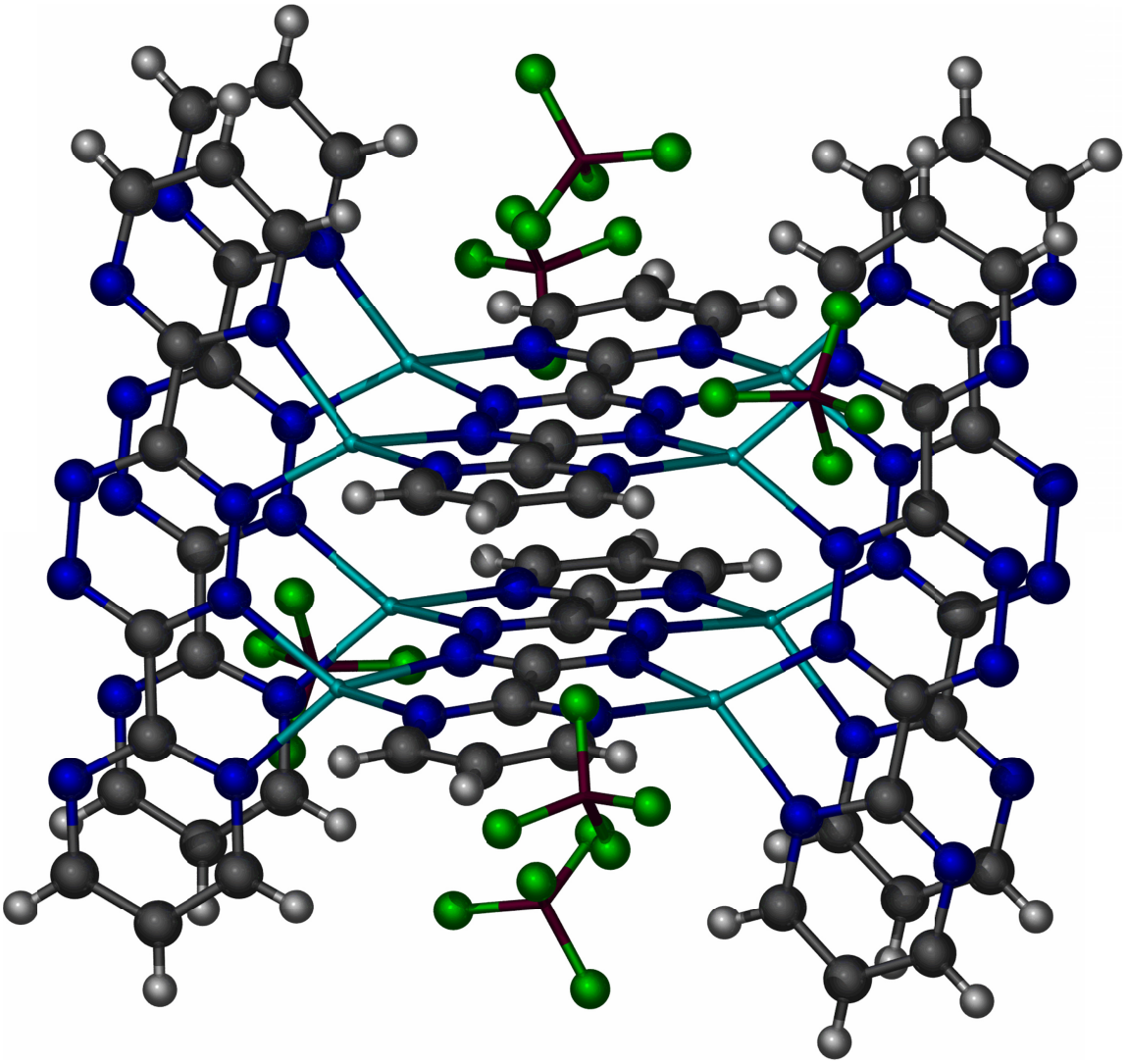

Figure 75. Ball and stick representation of $[Cu_8(bmtz)_6][BF_4]_6$. Atom colors: Cu (teal), C (grey), H (white), N (blue), B (maroon), F (green). Interstitial solvent omitted for the sake of clarity. Figure generated from data presented in the M. S. thesis of Edward S. Funck.[111]

structure highlights two important properties of bmtz: its lower reduction potential in comparison to bptz and its ability to adopt either a μ^2 *syn* or *anti* or a μ^4 bridging mode.[111]

The first electron reduction potential of bmtz in CH_3CN is at -0.70 V *vs*. Ag/AgCl, as compared to -0.79 V *vs*. Ag/AgCl for bptz. In both bptz and bmtz, the LUMO, as calculated by MO perturbation theory, is located solely on the tetrazine moiety,[112,113] meaning that any change in reduction potential is a measure of changes in the π-acidity of the central tetrazine ring, and thus should predict the relative propensity of each ligand to interact with anions through anion-π interactions (Figure 76). The substitution of the pyridyl groups in bptz with pyrimidyl groups in bmtz lowers the reduction potential, indicating that bmtz should be more amenable towards anion-π interactions than bptz. Comparison of the ESP maps (Figure 69) leads to a similar conclusion, showing higher electrostatic potentials for the bmtz tetrazine carbon atoms.

The ligand 2,5-bis(2′-pyridyl)pyrazine (bppz) is similar to the bppn ligand used in the Ag^I studies as it has a less π-acidic central ring than bptz (Figure 69), however, as the central ring is pyrazine rather than pyridazine, the ligand can adopt the same *anti* binding configuration as bptz in the anion-templated metallacycles discussed in Chapter III. Considering its decreased π-acidity with respect to bptz and the results of the bppn studies with Ag^I, bppz is not expected to form structures templated by anion-π interactions with metals such as Fe^{II}. The preference for an octahedral coordination environment for Fe^{II}, however, may support the formation of anion-templated structures despite the lower propensity of bppz to interact with anions.

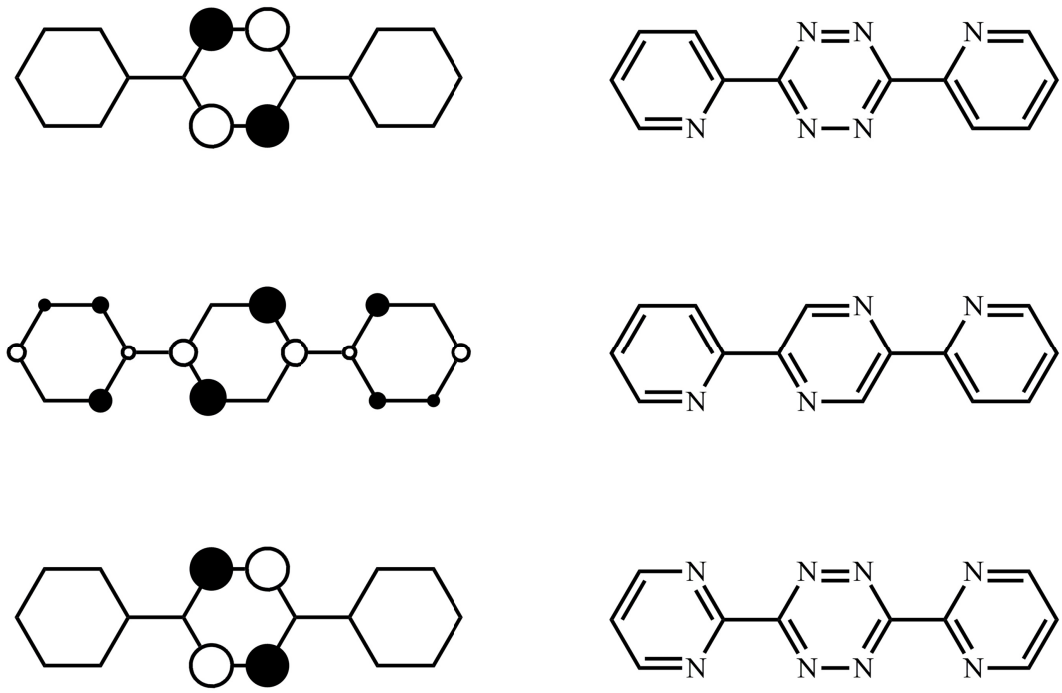

Figure 76. Schematic representation of the lowest unoccupied molecular orbitals (LUMOs) of bptz (top), bppz (middle), and bmtz (bottom) showing that the primary contribution to each LUMO is from the central N-heterocyclic ring. Orbitals were calculated using a perturbation approach to Hückel MO theory to estimate the effect of coordination to a metal center. The orbital diagrams for bptz and bppz were adapted from Kaim *et al*.[112] and for bmtz from Kaim *et al.*[113]

The work presented in this chapter details efforts to assess the effect of the π-acidity of the central ring (tetrazine and pyrazine) on the templation of metallacyclic structures of Fe^{II}. A new Fe^{II} pentagonal metallacycle with bmtz that encapsulates only one $[SbF_6]^-$ ion will be presented, along with efforts to react bmtz with $[Fe(NCCH_3)_6][BF_4]_2$ to form a square analog of $[Fe_4(bptz)_4(NCCH_3)_8][BF_4]_8$. Attempts to synthesize the bppz ligand and react it with Fe^{II} salts under conditions analogous to the metallacycles presented in Chapter III will be discussed as well, despite only limited success in the synthesis of bppz.

B. Experimental

i. General methods

All reactions were performed under nitrogen using standard Schlenk techniques or in an MBraun inert atmosphere glovebox. All glassware was oven-dried prior to use. Acetonitrile was dried over 3 Å molecular sieves and distilled under nitrogen. Toluene was dried by passing it through a column of a proprietary desiccant and dispensed under nitrogen using an MBraun Solvent Purification System. Ethanol was purified by distillation under nitrogen in the presence of magnesium ethoxide. The fully-solvated metal salts $[Fe(NCCH_3)_6][BF_4]_2$ and $[Fe(NCCH_3)_6][SbF_6]_2$ were synthesized by literature methods.[94] The ligand bmtz was synthesized using a modified literature preparation and dried under vacuum prior to use.[111,113] Physical properties measurements were performed as outlined in Chapter III.

ii. Syntheses

a. 2,5-bis(2′-pyridyl)pyrazine (bppz)

The ligand bppz was synthesized by a modified literature preparation from *p*-tosyl-2-acetylpyridineoxime (synthesized by reaction of 2-acetylpyridine with hydroxylamine hydrochloride to form methyl-2-pyridylketoxime, which is subsequently reacted with *p*-tosylchloride according to the preparation of Clemo *et al*.[114], forming the *p*-tosyl derivative in high yield).[115] Potassium metal (4.53 g, 116 mmol) was dissolved in dry EtOH under nitrogen. A slurry of *p*-tosyl-2-acetylpyridineoxime (23.98 g, 82.6 mmol) in dry EtOH (120 mL) was added and stirred overnight, resulting in an orange solution containing precipitated potassium tosylate. The precipitate was removed by filtration and the filtrate was treated with diethyl ether and refiltered to ensure the removal of the potassium tosylate. The orange solution was then extracted using HCl(aq), treated directly with NH_4OH (without isolating the HCl salt of 2-aminoacetylpyridine) and then treated with activated charcoal, which was removed by filtration. The solvent was removed by rotary evaporation, yielding an orange oil that, upon standing in air, precipitated red-orange bppz in low yield (0.512 g, 5%). The product was confirmed by ^{1}H NMR.

b. $[Fe_5(bmtz)_5(NCCH_3)_{10}][SbF_6]_{10}$

The addition of a pink suspension of bmtz (0.083 g, 0.348 mmol) in CH_3CN (10 mL) to a colorless solution of $[Fe(CH_3CN)_6][SbF_6]_2$ (0.269 g, 0.348 mmol) in CH_3CN (10 mL) under anaerobic conditions induces an immediate color change of the solution to dark purple/blue. After overnight stirring, a blue solid was obtained by filtration after

layering the acetonitrile solution over toluene under anaerobic conditions. Yield: 0.253 g, 86%. Elemental Analysis, calculated for $Fe_5C_{70}N_{50}H_{60}Sb_{10}F_{60}\cdot C_7H_8\cdot 3CH_3CN$: C, 22.38; N, 16.67; H, 1.76%; found: C, 22.36; N, 16.66; H, 1.95%. ^{1}H NMR, δ, ppm (CD_3CN): 8.00 (td, 5,5′-H), 8.77 (dd, 6,6′-H), 9.48 (dd, 4,4′-H), 1.96 (s, CH_3CN). ^{1}H NMR, bmtz, δ, ppm (CD_3CN): 7.70 (t, 5,5′-H), 9.13 (d, 4,4′,6,6′-H). EAS: $\lambda_{max}(CH_3CN)$/nm, (ε/L mol^{-1} cm^{-1}): 775 (19,603), 577 (15,562). CV (CH_3CN, vs. Ag/AgCl): $E_{1/2}$(ox): 0.032, 0.19, 0.50, 0.82 V (reversible), 1.41, -1.17, -1.67 V (irreversible). ESI-FT-ICR-MS: m/z 1466.7 for $[Fe_5(bmtz)_5(CH_3CN)_{10}(SbF_6)_{10} + 4(CH_3CN) - 3H^-]^{3+}$.

C. Results and Discussion

i. Syntheses

a. 2,5-bis(2′-pyridyl)pyrazine (bppz)

The synthesis of bppz (Figure 77) involves the conversion of 2-acetylpyridine to methyl-2-pyridylketoxime by refluxing with hydroxylamine hydrochloride in pyridine (~70% yield, purity confirmed by ^{1}H NMR). Treatment of a solution of methyl-2-pyridyl ketoxime in pyridine with *p*-toluenesulfonylchloride at 0^{o}C forms *p*-toluenesulfonyl-2-acetylpyridineoxime, which is purified by recrystallization from ethanol titrated with water at ~50% yield and confirmed by ^{1}H NMR. According to Neels and Stoeckli-Evans, treatment of *p*-toluenesulfonyl-2-acetylpyridineoxime with K(s) in ethanol, followed by treatment with HCl(aq) (following the method of Clemo, Leitch and Holmes[114]) should yield the solid 2-α-aminoacetylpyridine hydrochloride salt, which, upon treatment with NH_4OH, converts to a “red” solid of bppz after stirring in air for 3

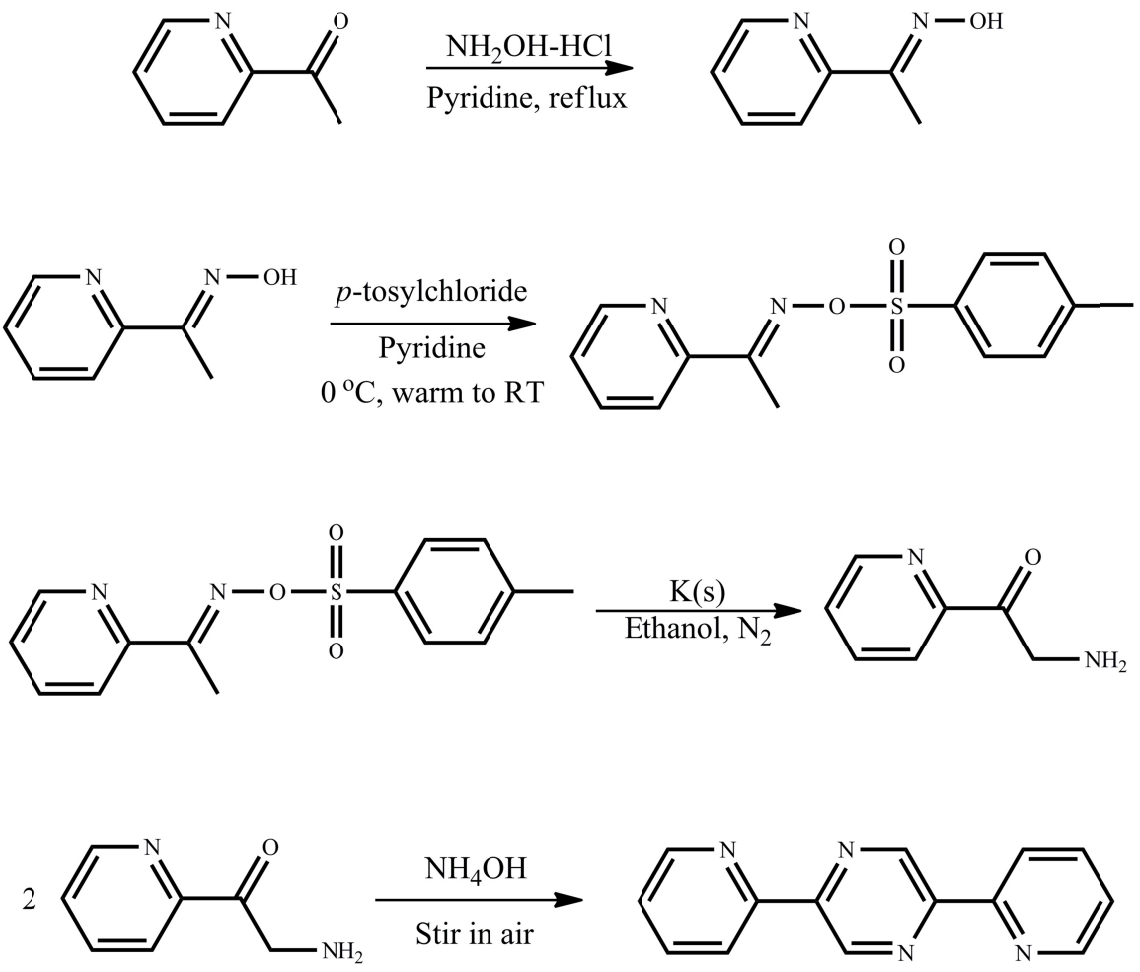

Figure 77. Schematic representation of the synthesis of bppz from 2-acetylpyridine. The first three steps are reported by Clemo, Leitch, and Holmes.[114] The final step is reported by Neels and Stoeckli-Evans.[115]

hours. It was found, however, that the ligand was not obtained as expected.

Upon further research into the synthesis of bppz, two other methods (Case and Koft[116] in 1959 and Armand *et al*.[117] in 1974) were found. The procedure of Case and Koft involves the treatment of an alkaline aqueous solution of 2-α-aminoacetylpyridine hydrochloride with H_2O_2 and Pd/C, but the yield is extremely low.[116] Armand *et al.* report the oxidation of an acetonitrile solution of 3,6-dihydro-2,5-bis(2′-pyridyl)pyrazine (formed from a deoxygenated aqueous solution of 2-α-aminoacetylpyridine hydrochloride treated with NH_4OH) in air, but again, with only a minimal reported yield.[117]

In an attempt to improve the synthesis of bppz (particularly the final pyrazine cyclization), the isolation of 2-α-aminoacetylpyridine hydrochloride was replaced with extraction with HCl(aq) and then direct reaction of the resulting solution with NH_4OH and purification by treatment with activated charcoal followed by removal of the solvent, which resulted in the isolation of pure bppz, albeit, in only a limited yield. Attempts to react the amine directly with NH_4OH (or NaOH) were unsuccessful in producing bppz. These efforts did not improve the yield or reproducibility of the synthesis of bppz but did successfully produce the ligand in useable quantities.

b. Reactions of bppz with $[M(NCCH_3)_6][X]_2$, M = Ni^{II}, Fe^{II} X = $[BF_4]^-$, $[SbF_6]^-$

These reactions were carried out in a method similar to the syntheses of the metallacycles of bptz. Addition of bppz in CH_3CN (yellow-orange) to pale lavender solutions of $[Ni(NCCH_3)_6][BF_4]_2$ or $[Ni(NCCH_3)_6][SbF_6]_2$ immediately produces a

brown solution similar to that formed using bptz as the chelating ligand. Work up of both reactions by layering the reaction solutions over diethyl ether, dichloromethane or toluene produces brown powder with no XRD quality single crystals. Similar reactions using colorless solutions of $[Fe(NCCH_3)_6][BF_4]_2$ or $[Fe(NCCH_3)_6][SbF_6]_2$ resulted in immediate color changes to green-blue. The reaction was stirred overnight and then layered over toluene and CH_2Cl_2, producing a blue-green powder and no XRD quality single crystals. In all cases the color changes are reminiscent to those observed in reactions with bptz, suggesting that similar compounds are being formed, however, the less intense green-blue color in the Fe^{II} reactions may indicate differences in the spin state of Fe^{II} in the product, especially considering that similar concentrations using bptz produce intense blue solutions and products.

c. Reactions of bmtz with $[Fe(NCCH_3)_6][X]_2$, X = $[BF_4]^-$, $[SbF_6]^-$

The bmtz ligand is less soluble in CH_3CN than bptz, forming pink solutions with remaining purple crystalline solid. As a result, suspensions of bmtz are added to the colorless solutions of $[Fe(NCCH_3)_6][BF_4]_2$ or $[Fe(NCCH_3)_6][SbF_6]_2$ while stirring. As in the reactions with bptz, immediate color changes are observed upon addition of the ligand to the metal ion solutions, in this case from pink (bmtz) and colorless (Fe^{II} salt) to dark violet blue. Treatment of the reaction solutions with toluene produces dark blue powder for both $[BF_4]^-$ and $[SbF_6]^-$. The intense colors indicate the presence of LMCT transitions characteristic of low spin Fe^{II} in an all N-ligand coordination environment.

ii. Single crystal X-ray crystallography

a. $[Fe_5(bmtz)_5(CH_3CN)_{10}\subset SbF_6][SbF_6]_9\cdot 6.5CH_3CN\cdot C_7H_8$

The structure of $[Fe_5(bmtz)_5(CH_3CN)_{10}\subset SbF_6][SbF_6]_9\cdot 6.5CH_3CN\cdot C_7H_8$ (measured on a dark blue platelet crystal grown by layering an acetonitrile solution of $[Fe_5(bmtz)_5(NCCH_3)_{10}][SbF_6]_{10}$ over toluene, CCDC: 844756, Table 14) consists of a molecular pentagon with Fe^{II} ions linked by chelating bmtz ligands, in an *anti* orientation. A thermal ellipsoid plot for the metallacycle and its counterions is depicted in Figure 78. The coordination geometry of the Fe^{II} ions in the pentagonal metallacycle with bmtz is octahedral with four coordination sites occupied by two different ligand chelate donors and the other two positions being capped by two CH_3CN molecules. The interatomic Fe^{II}–N distances are in the range 1.84–2.02 Å, which indicate low-spin Fe^{II} centers (Table 15). The average Fe^{II}–Fe^{II}–Fe^{II} angle (108^o) in each of 1 and 2 is that of an ideal pentagon (108^o) in spite of the fact that the N–Fe^{II}–N angles at the vertices are close to 90^o. These two requisite geometrical preferences are met only due to the flexibility of the bridging ligands, which bend to alleviate angle strain as in the Fe^{II} pentagon with bptz.

The metallacycle is structurally similar to the Ni^{II} and Fe^{II} pentagons with bptz. It is noteworthy that the encapsulated $[SbF_6]^-$ anion resides in the center of the pentagonal cavity (Figure 79) and participates in six short F···C anion–π contacts with five tetrazine rings of the bmtz entities (Figure 80): $[SbF_6]^-\cdots C_{tetrazine}$: F3···C35 2.79(3), F6···C6 2.81(2), F2···C26 2.94(3), F1···C15 2.93(3), F4···C36 3.00(2), F5···C45 3.09(3) Å. The Fe^{II} pentagonal cavity is smaller, since there is a significant contraction in the $M^{II}\cdots M^{II}$

Table 14. $[Fe_5(bmtz)_5(CH_3CN)_{10}][SbF_6]_{10}\cdot 6.5CH_3CN\cdot C_7H_8$ crystallographic parameters.

	$[Fe_5(bmtz)_5(CH_3CN)_{10}][SbF_6]_{10}\cdot 6.5CH_3CN\cdot C_7H_8$
Formula	$Sb_{10}Fe_5F_{60}N_{56.5}C_{90}H_{87.5}$
Temp (K)	110
Space group	*Pc* (no. 7)
a (Å)	16.180(3)
b (Å)	21.569(4)
c (Å)	23.123(4)
α (º)	90.00
β (º)	106.198(2)
γ (º)	90.00
V (Å^3)	7749(2)
Z	2
Color	dark blue
ρ_{calc}(g/cm^3)	1.970
μ (mm^{-1})	2.295
θ range (º)	1.31-26.41
Reflections collected	82,034
Unique reflections	31,659
Parameters/restraints	1,870/2
R_1,[a] wR_2[b] [$I>2\sigma(I)$]	0.0780, 0.1599
R_1,[a] wR_2[b] (all data)	0.1960, 0.2097
Goodness-of-fit[c] (F^2)	0.940
Largest diff. peak, hole (e Å^{-3})	1.54, –1.60

[a] $R = \Sigma \big| |F_o| - |F_c| \big| / \Sigma |F_o|$. [b] $wR = \{\Sigma[w(F_o^2 - F_c^2)^2] / \Sigma w(F_o^2)^2]\}^{1/2}$. [c] Goodness-of-fit = $\{\Sigma[w(F_o^2 - F_c^2)^2]/(n-p)\}^{1/2}$, where *n* is the number of reflections and *p* is the total number of parameters refined.

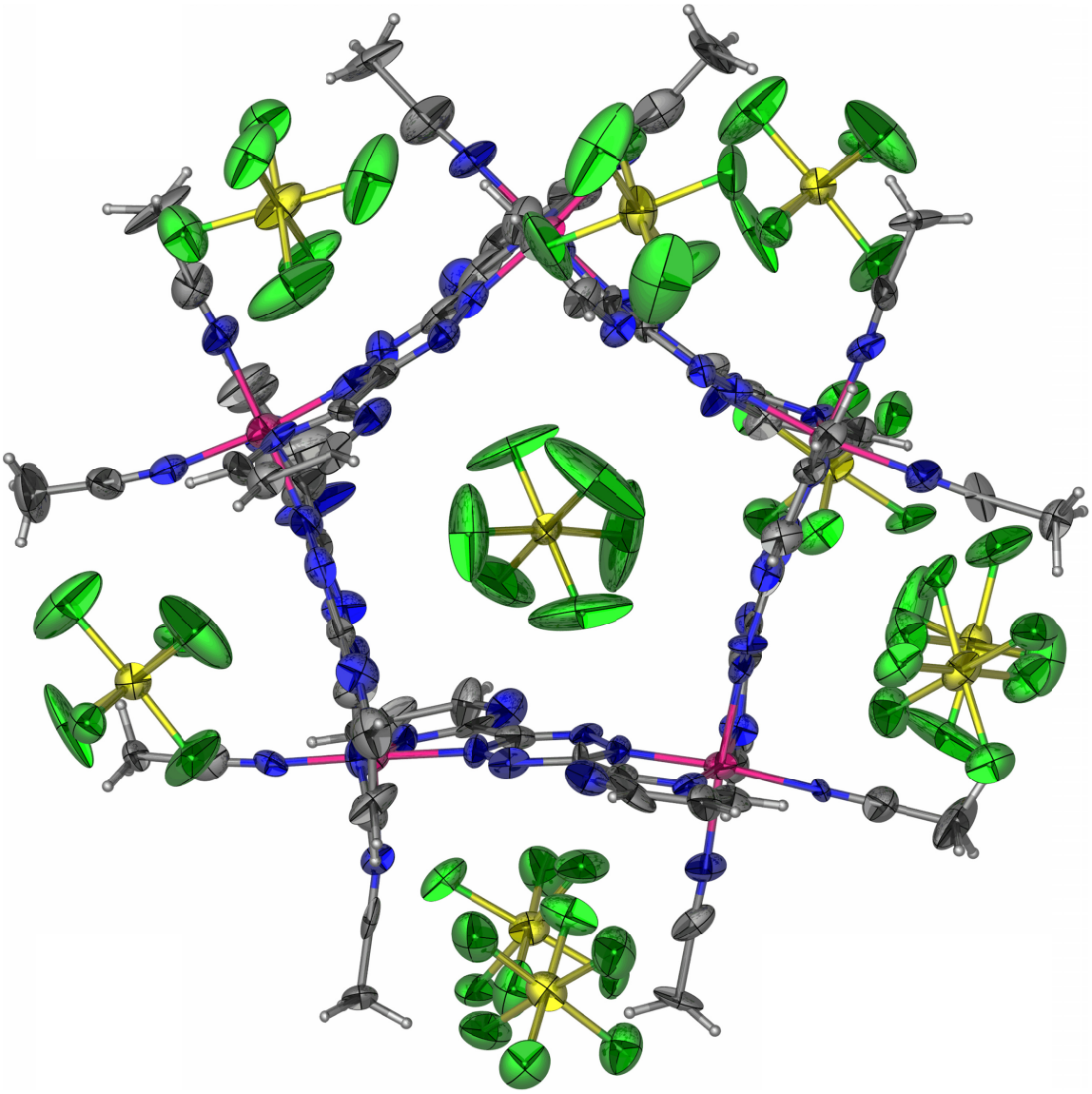

Figure 78. Thermal ellipsoid plot of $[Fe_5(bmtz)_5(CH_3CN)_{10}][SbF_6]_{10}\cdot 6.5CH_3CN\cdot C_7H_8$ drawn at the 50% probability level. Atom colors: Fe (pink), C (dark grey), N (blue), Sb (yellow), F (green), H (light grey). Interstitial solvent molecules are omitted for the sake of clarity. Figure adapted from Dunbar *et al.*[106]

Table 15. Fe^{II}-N bond distances in Å (top) and N-Fe^{II}-N angles in degrees (bottom) for $[Fe_5(bmtz)_5(CH_3CN)_{10}][SbF_6]_{10}\cdot 6.5CH_3CN\cdot C_7H_8$.

Atoms	Distance	Atoms	Distance	Atoms	Distance
Fe1-N2	1.844(18)	Fe1-N41	1.905(18)	Fe1-N1	1.960(15)
Fe1-N38	1.866(15)	Fe1-N42	1.943(17)	Fe1-N37	2.013(14)
Fe2-N6	1.856(16)	Fe2-N5	1.931(17)	Fe2-N44	1.94(2)
Fe2-N10	1.877(13)	Fe2-N43	1.938(17)	Fe2-N9	1.965(13)
Fe3-N14	1.883(13)	Fe3-N45	1.911(18)	Fe3-N17	1.958(13)
Fe3-N18	1.889(15)	Fe3-N46	1.948(17)	Fe3-N13	2.025(14)
Fe4-N22	1.886(15)	Fe4-N47	1.935(14)	Fe4-N48	1.975(16)
Fe4-N26	1.920(13)	Fe4-N25	1.956(14)	Fe4-N21	2.001(13)
Fe5-N49	1.918(17)	Fe5-N34	1.919(15)	Fe5-N50	1.946(16)
Fe5-N30	1.919(14)	Fe5-N33	1.940(15)	Fe5-N29	2.015(15)

Atoms	Angle	Atoms	Angle	Atoms	Angle
N2-Fe1-N38	94.5(6)	N41-Fe1-N42	87.4(7)	N2-Fe1-N37	91.2(7)
N2-Fe1-N41	173.3(6)	N2-Fe1-N1	83.7(7)	N38-Fe1-N37	81.5(7)
N38-Fe1-N41	91.9(6)	N38-Fe1-N1	89.8(6)	N41-Fe1-N37	91.7(7)
N2-Fe1-N42	86.3(7)	N41-Fe1-N1	94.5(7)	N42-Fe1-N37	96.7(6)
N38-Fe1-N42	178.0(7)	N42-Fe1-N1	92.0(6)	N1-Fe1-N37	169.5(6)
N6-Fe2-N10	93.9(6)	N5-Fe2-N43	91.6(6)	N6-Fe2-N9	92.8(6)
N6-Fe2-N5	83.0(6)	N6-Fe2-N44	174.8(7)	N10-Fe2-N9	82.7(6)
N10-Fe2-N5	91.4(6)	N10-Fe2-N44	90.5(6)	N5-Fe2-N9	172.5(6)
N6-Fe2-N43	87.1(7)	N5-Fe2-N44	94.2(7)	N43-Fe2-N9	94.4(6)
N10-Fe2-N43	177.0(7)	N43-Fe2-N44	88.6(7)	N44-Fe2-N9	90.4(6)
N14-Fe3-N18	95.6(6)	N45-Fe3-N46	87.7(6)	N14-Fe3-N13	81.8(5)
N14-Fe3-N45	85.7(6)	N14-Fe3-N17	92.5(5)	N18-Fe3-N13	88.4(6)
N18-Fe3-N45	175.1(6)	N18-Fe3-N17	82.9(6)	N45-Fe3-N13	96.5(6)
N14-Fe3-N46	172.8(6)	N45-Fe3-N17	92.3(6)	N46-Fe3-N13	96.1(6)
N18-Fe3-N46	91.2(6)	N46-Fe3-N17	90.7(5)	N17-Fe3-N13	169.1(6)
N22-Fe4-N26	95.2(5)	N47-Fe4-N25	94.0(6)	N22-Fe4-N21	82.3(6)
N22-Fe4-N47	89.6(5)	N22-Fe4-N48	175.8(6)	N26-Fe4-N21	90.6(6)
N26-Fe4-N47	173.3(6)	N26-Fe4-N48	88.1(6)	N47-Fe4-N21	94.8(6)
N22-Fe4-N25	90.7(6)	N47-Fe4-N48	87.4(6)	N25-Fe4-N21	168.7(6)
N26-Fe4-N25	81.2(6)	N25-Fe4-N48	92.3(6)	N48-Fe4-N21	95.1(6)
N49-Fe5-N30	90.9(6)	N34-Fe5-N33	81.4(7)	N49-Fe5-N29	92.7(6)
N49-Fe5-N34	172.3(7)	N49-Fe5-N50	88.0(6)	N30-Fe5-N29	81.3(6)
N30-Fe5-N34	95.7(6)	N30-Fe5-N50	176.7(6)	N34-Fe5-N29	92.3(6)
N49-Fe5-N33	94.6(7)	N34-Fe5-N50	85.7(6)	N33-Fe5-N29	168.3(6)
N30-Fe5-N33	89.5(6)	N33-Fe5-N50	93.7(6)	N50-Fe5-N29	95.7(6)

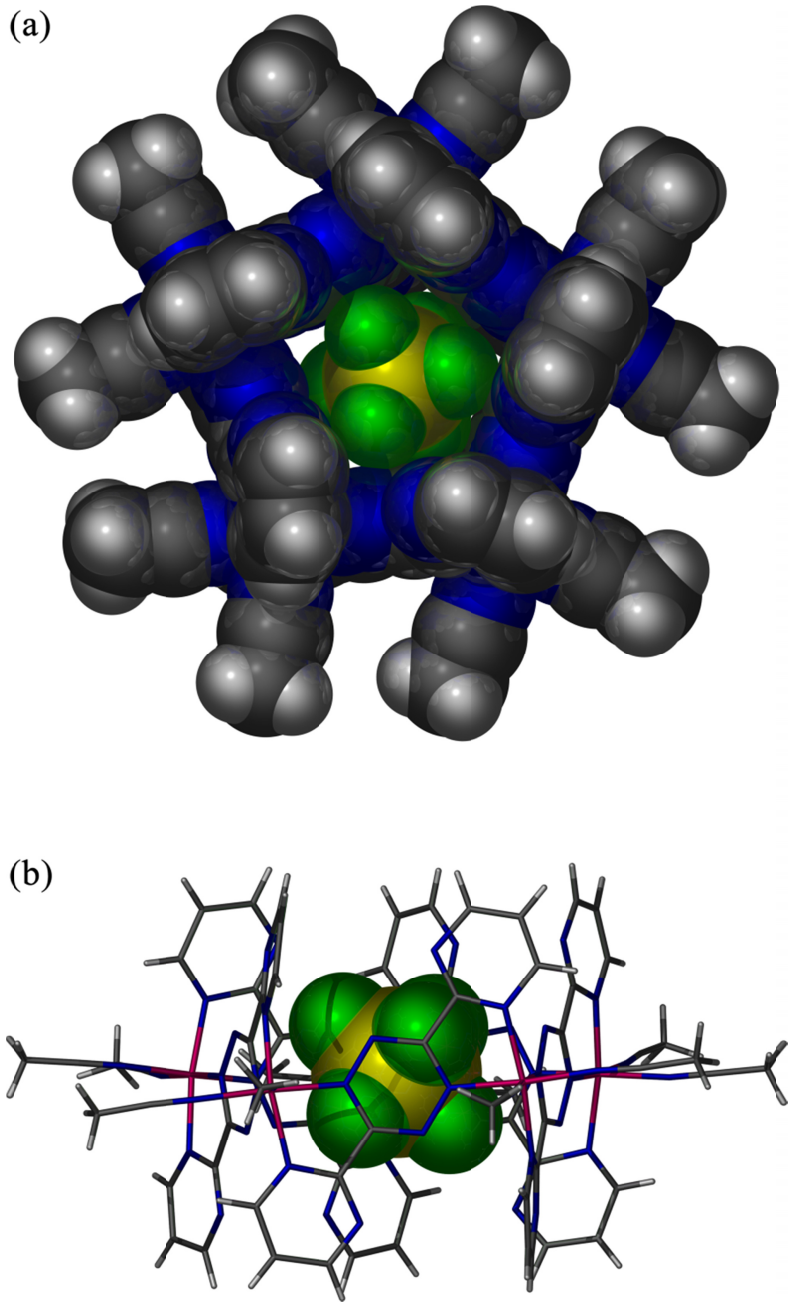

Figure 79. (a) Space-filling view of the $[SbF_6]^-$ anion in the cavity of $[Fe_5(bmtz)_5(NCCH_3)_{10}\subset SbF_6]^{9+}$ showing the tight packing of the anions within the cavity. (b) Side-view emphasizing the alignment of the anions (space-filling) with the bmtz ligands of the Fe^{II} pentagon (stick). Atom colors: Fe (pink), C (dark grey), N (blue), Sb (yellow), F (green), H (light grey). Non-encapsulated anions and interstitial solvent are omitted for the sake of clarity.

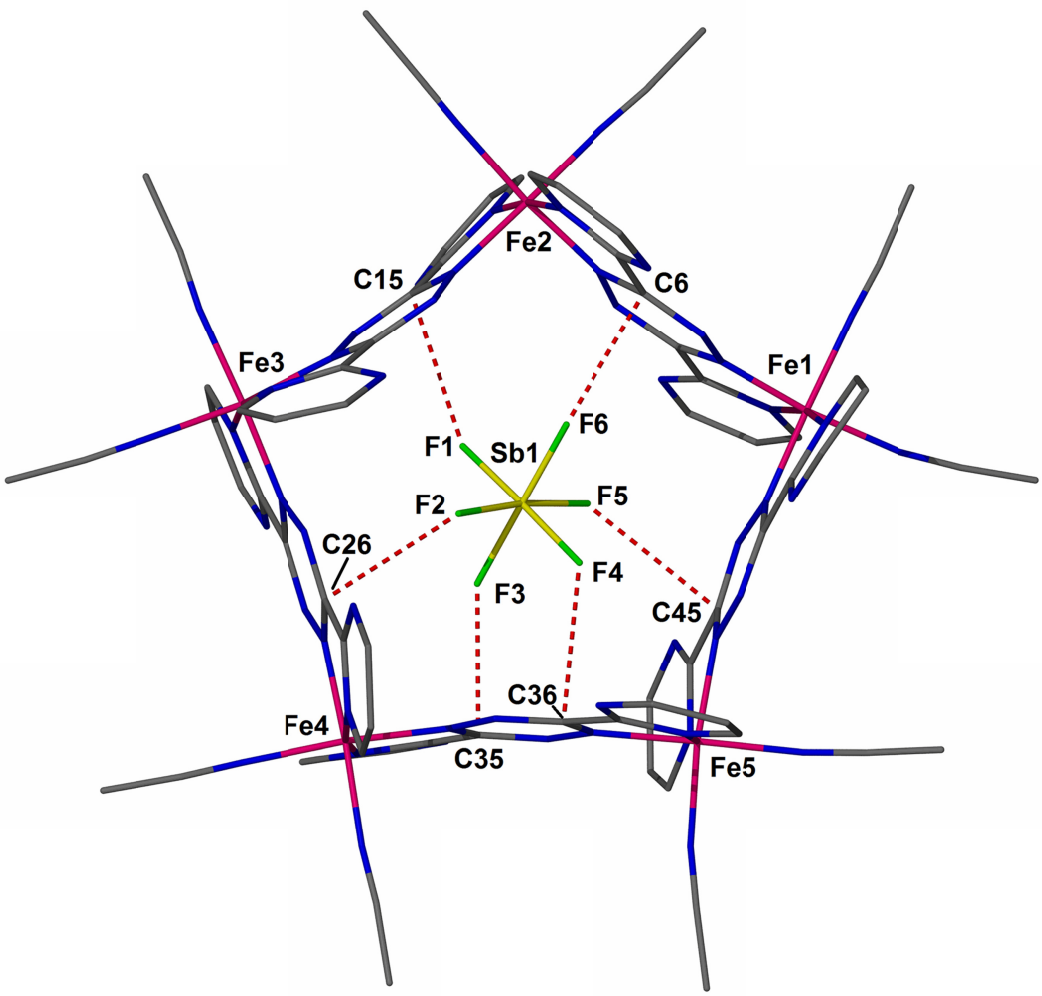

Figure 80. Side-view stick representations of $[Fe_5(bmtz)_5(NCCH_3)_{10}\subset SbF_6]^{9+}$ with F-C interactions between $[SbF_6]^-$ and the ligand tetrazine ring indicated by red dashed lines. Atom colors: Fe (pink), C (dark grey), N (blue), B (yellow), F (green). Non-encapsulated anions, interstitial solvent, and H atoms are omitted for the sake of clarity. Figure reproduced from Dunbar *et al.*[106]

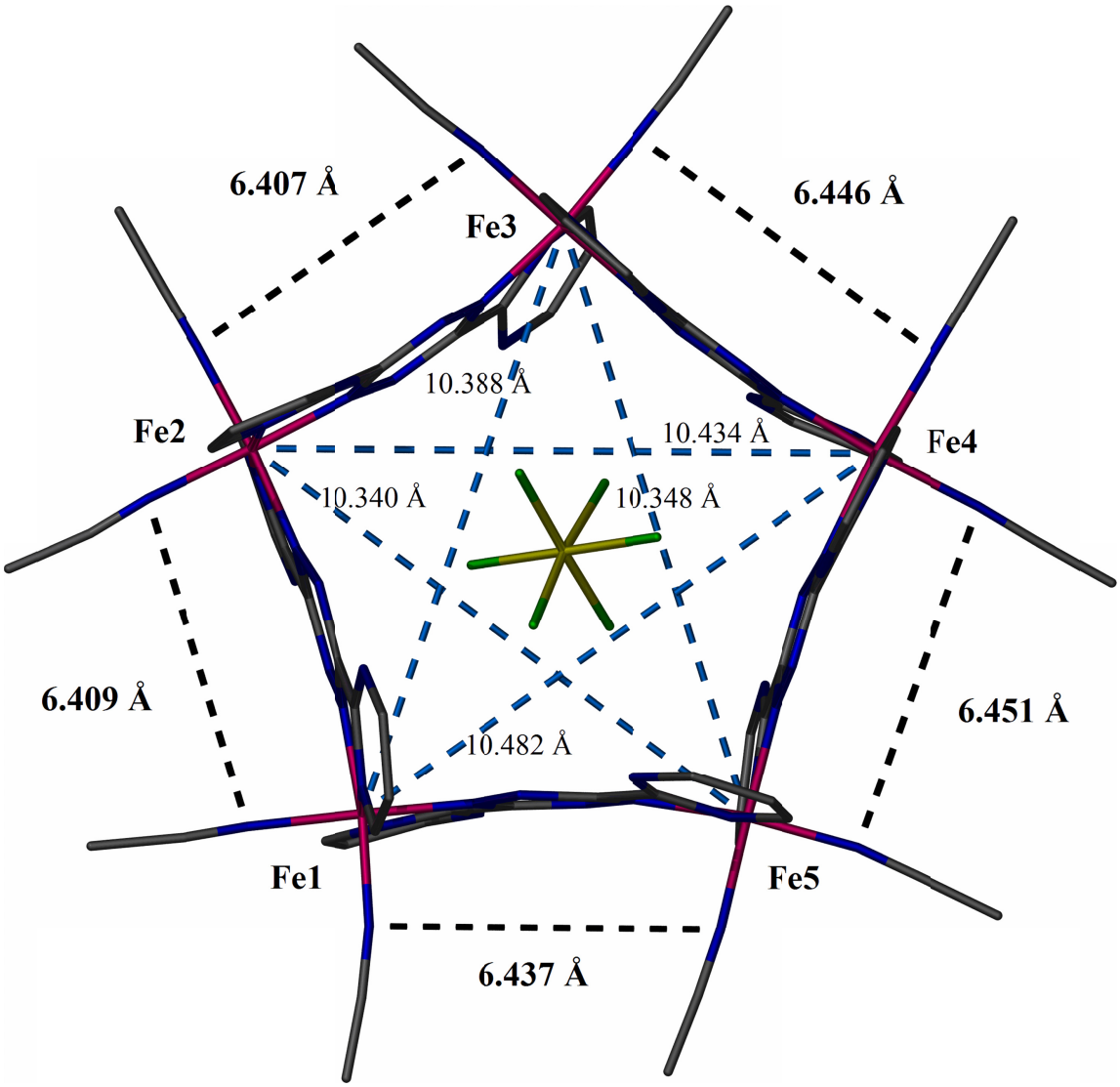

Figure 81. Side-view stick representations of $[Fe_5(bmtz)_5(NCCH_3)_{10}\subset SbF_6]^{9+}$ with cross-ligand (black dashed lines) and cross-cavity (blue dashed lines) distances indicated. Atom colors: Fe (pink), C (dark grey), N (blue), B (yellow), F (green). Non-encapsulated anions and H atoms are omitted for the sake of clarity.

vertex separations as compared to Ni^{II} and similar to the Fe^{II} pentagon with bptz. (~6.4 Å for Fe^{II} vs. ~6.7 Å for Ni^{II}, Figure 81). This situation notwithstanding, this cation is an excellent host for the encapsulated $[SbF_6]^-$ anion, with it centrally positioned within the cavity of the pentagonal unit with six anion–π contacts (Figure 79b, Figure 80), which are shorter by up to 0.38 Å than R_{vdW} F···C (3.17 Å). The central anion-to-ligand $F\cdots C_{tetrazine}$ contact distances in $[Fe_5(bmtz)_5(CH_3CN)_{10}\subset SbF_6][SbF_6]_9\cdot 6.5CH_3CN\cdot C_7H_8$ are at an average of 2.9 Å. The presence of only one encapsulated anion in $[Fe_5(bmtz)_5(CH_3CN)_{10}\subset SbF_6][SbF_6]_9\cdot 6.5CH_3CN\cdot C_7H_8$ versus two such anions in $[Fe_5(bmtz)_5(CH_3CN)_{10}\subset 2SbF_6][SbF_6]_8\cdot 8.5\ CH_3CN$ is attributed to the interplay between the increased π-acidity of bmtz and positioning the anion in the cavity to maximize anion–π interactions. As was observed in the structure of the Ni^{II} and Fe^{II} pentagons incorporating bptz, the bmtz ligand is distorted, with each tetrazine ring exhibiting an 'inward bowing' (Figure 82). The average dihedral angles with the planes of the two pyrimidyl rings is ~10°, as compared to the dihedral angle of ~8° in $[Fe_5(bptz)_5(CH_3CN)_{10}\subset 2SbF_6][SbF_6]_8\cdot 8.5CH_3CN$. This distortion of the rings serves the dual purpose of stabilizing overall ~108° angles at the Fe^{II} pentagon vertices and also of favorably positioning the central tetrazine rings to maximize the strength and number of anion–π contacts with the encapsulated $[SbF_6]^-$ anion.

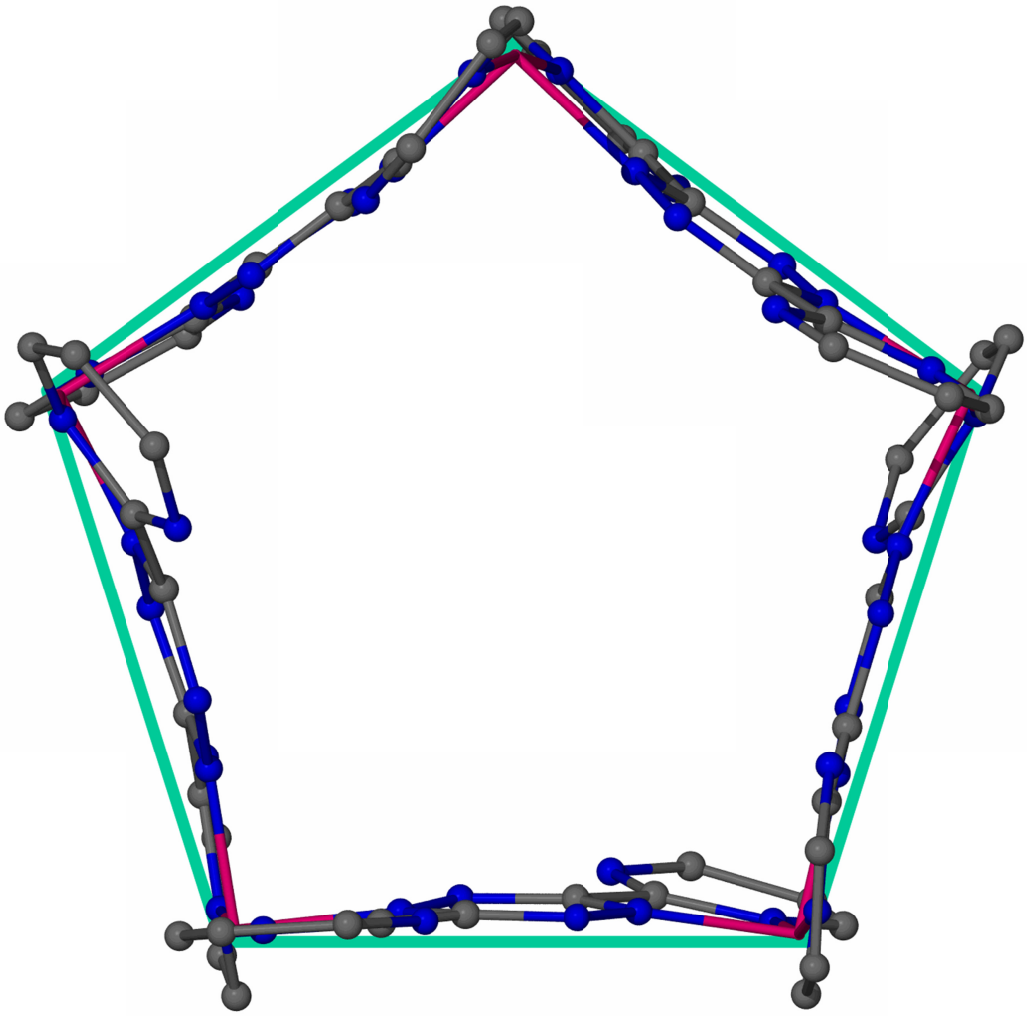

Figure 82. Ball and stick framework diagram of the cationic $[Fe_5(bmtz)_5]^{10+}$ metallacycle with a regular pentagon circumscribed about it, highlighting the significant inward bowing of the bmtz ligands toward the anion in the central cavity. Atom colors: Fe (pink), C (grey), N (blue). Anions, H atoms and bound solvent are omitted for the sake of clarity. Figure reproduced from Dunbar *et al*.[106]

The Fe^{II} pentagon with bmtz crystallizes in the monoclinic space group *Pc*. They pack in channels along the *b* axis (Figure 83a), with the pentagonal metallacycles pointing in opposing directions in neighboring channels. The pentagonal metallacyclic cations have their faces aligned along second channel of pentagons along the *c* axis (Figure 83b). Anions and disordered molecules of CH_3CN and toluene occupy the interstices between the cationic units. The packing is similar to that in the Fe^{II} pentagon with bptz, however the slight canting of the pentagonal metallacycles along the channels reduces the packing symmetry from orthorhombic *Pbcn* to monoclinic *Pc*.

iii. Solution analyses

a. Mass spectrometry

A parent ion signal at m/z 1466.7 corresponding to $[Fe_5(bmtz)_5(CH_3CN)_{10}(SbF_6)_{10} + 4(CH_3CN) - 3H]^{3+}$ was detected using ESI-FT-ICR-MS on a solution of $[Fe_5(bmtz)_5(CH_3CN)_{10}][SbF_6]_{10}$ in CH_3CN, demonstrating the stability of the Fe^{II} pentagon with bmtz in CH_3CN solution (Figure 84). All of the anions remain in the structure upon ionization, as do the coordinated solvent molecules, unlike the ion signal observed for either the Fe^{II} square or pentagon with bptz. It is presumed that the encapsulated anion remains in the cavity upon gas phase ionization in the bmtz pentagon.

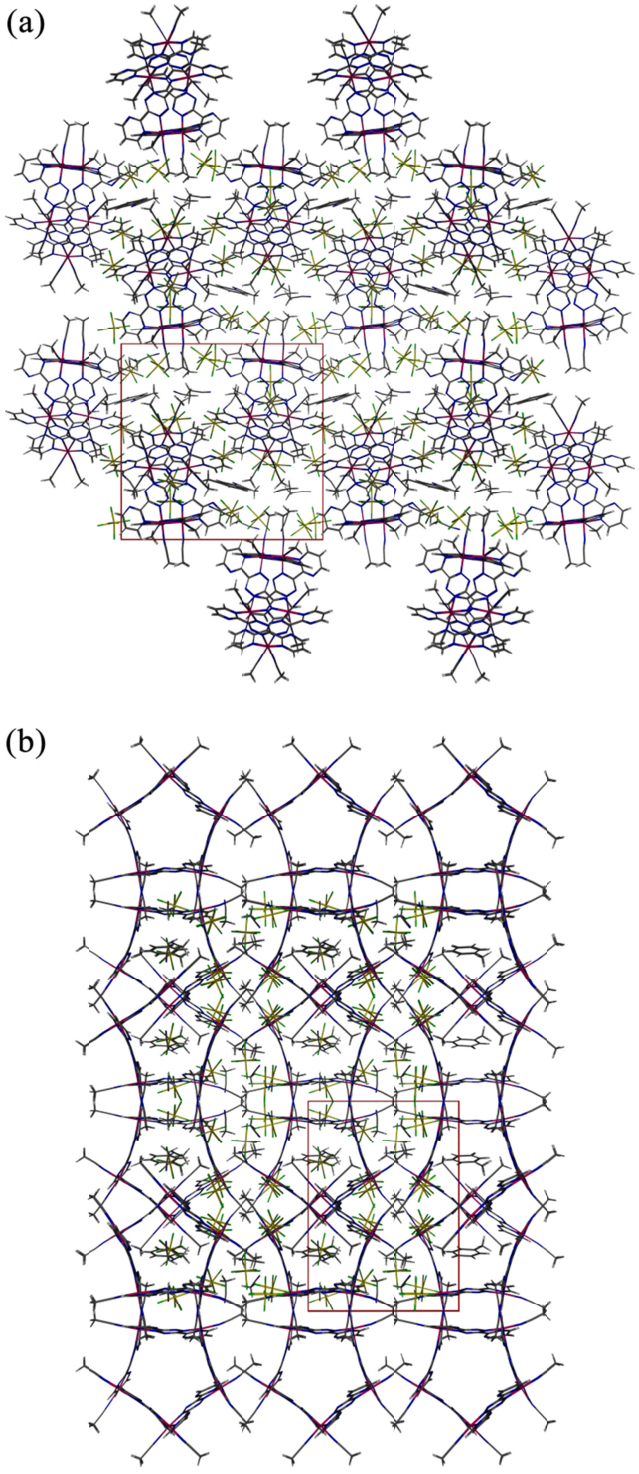

Figure 83. Packing diagrams of $[Fe_5(bmtz)_5(CH_3CN)_{10}][SbF_6]_{10}\cdot 6.5CH_3CN\cdot C_7H_8$ along the (a) *a* and (b) *c* axis of the unit cell (inscribed in red) highlighting the corrugated packing of the pentagons.

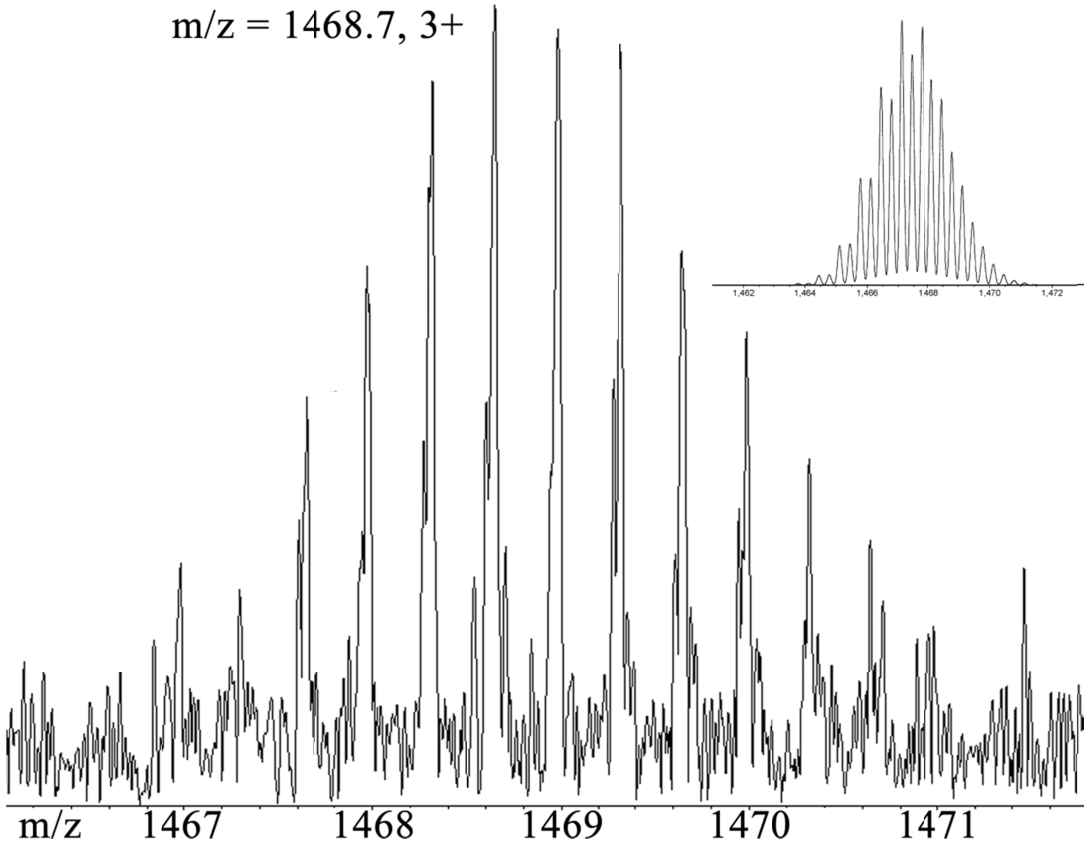

Figure 84. Parent ion signal consistent with $[Fe_5(bmtz)_5(CH_3CN)_{10}(SbF_6)_{10} + 4(CH_3CN) - 3H]^{3+}$ in CH_3CN at m/z = 1468.7. Theoretical isotopic distribution is depicted in the inset.

b. Electrochemistry

Similar to the metallacycles with bptz, $[Fe_5(bmtz)_5(CH_3CN)_{10}][SbF_6]_{10}$ has successive oxidation behavior when analyzed by cyclic and differential pulse voltammetry. In addition to irreversible ligand-based reduction waves at -1.17 and -1.67 V and an irreversible oxidation wave at 1.41 V, four successive reversible oxidation waves can be distinguished between 0 and 0.9 V: 0.032, 0.19, 0.50, 0.82 V (Figure 85 and Figure 86). The successive oxidation events occur on individual Fe^{II} centers, with each one becoming more difficult to oxidize due to the influence of Fe^{III} ions on the electrochemistry of the remaining Fe^{II} centers. It is proposed that the first two oxidation events occur at Fe^{II} atoms that are distal from each other. The third and fourth oxidations are proposed to occur on Fe^{II} atoms adjacent to the first two oxidized Fe^{II} centers. The highest potential oxidation occurs at the Fe^{II} center flanked by the first two oxidized centers (Figure 86). The reversibility of these oxidations further demonstrates the stability of $[Fe_5(bmtz)_5(CH_3CN)_{10}][SbF_6]_{10}$ toward oxidation in CH_3CN solution.

Reduction of the ligand, however, destabilizes the anion-π interactions between the ligands and the encapsulated $[SbF_6]^-$ anion, leading to the decomposition of the metallacycle in solution and an irreversible reduction wave. In contrast, the electrochemistry of $[Cu_8(bmtz)_6][BF_4]_6$ reveals successive ligand redox behavior along with an irreversible oxidation wave attributed to Cu^I oxidation.[118] Considering that the structure of $[Cu_8(bmtz)_6][BF_4]_6$ relies on inter-ligand π-π stacking interactions rather than anion-π interactions, the increased ligand charge does not destabilize the structure as it does in the pentagonal metallacycle. The additional electron density on the ligand

upon reduction would weaken anion-π interactions to a greater extent than π-π stacking interactions (especially on a ligand with a positive quadrupole moment such as bmtz). Based on the irreversibility of the ligand reduction in $[Fe_5(bmtz)_5(CH_3CN)_{10}][SbF_6]_{10}$, indicative of decomposition in solution due to the reduction event, it is reasonable to postulate that anion-π interactions are present in solution and, more importantly, are critical to the stability of $[Fe_5(bmtz)_5(CH_3CN)_{10}][SbF_6]_{10}$ in solution. The multiple reversible ligand reduction events in $[Cu_8(bmtz)_6][BF_4]_6$ suggest that, although they may be present, anion-π interactions are not essential for the stability of the complex in solution.

The increase in positive charge on the metal centers in the pentagonal Fe^{II} metallacycle serves to stabilize the anion in the cavity through favorable Coulombic effects, whereas in the $[Cu_8(bmtz)_6][BF_4]_6$ grid structure, the increased oxidation state of the copper decomposes the grid, as evidenced by the irreversible oxidation wave. This lends further support to the notion that the anions are critical for the stability of $[Fe_5(bmtz)_5(CH_3CN)_{10}][SbF_6]_{10}$ in solution but not for $[Cu_8(bmtz)_6][BF_4]_6$.

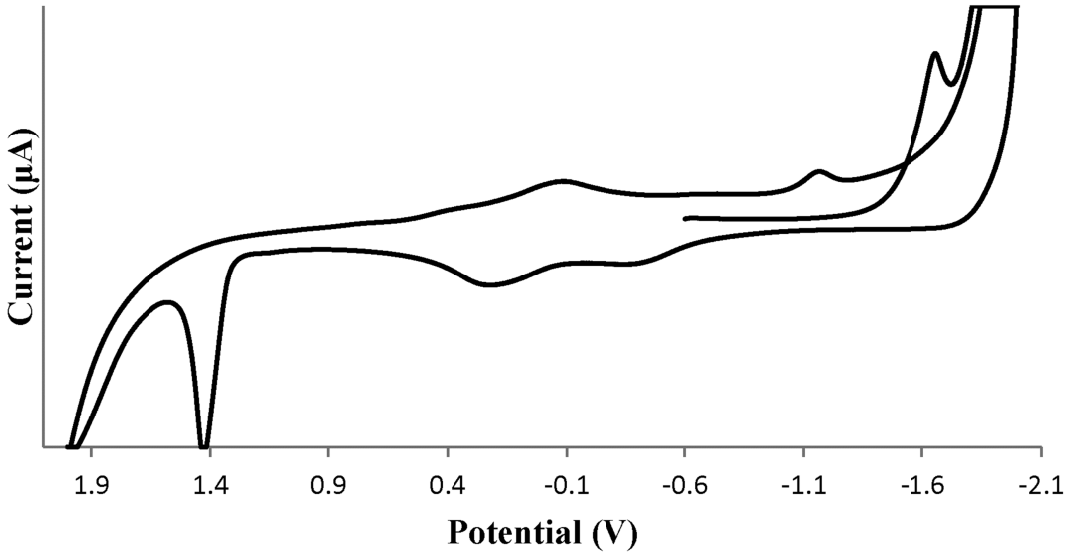

Figure 85. Cyclic voltammogram of $[Fe_5(bmtz)_5(NCCH_3)_{10}][SbF_6]_{10}$ in CH_3CN with $[^nBu_4N][SbF_6]$ as the supporting electrolyte referenced to Ag/AgCl at a scan rate of 0.2 V/s from 2.0 to -2.0 V.

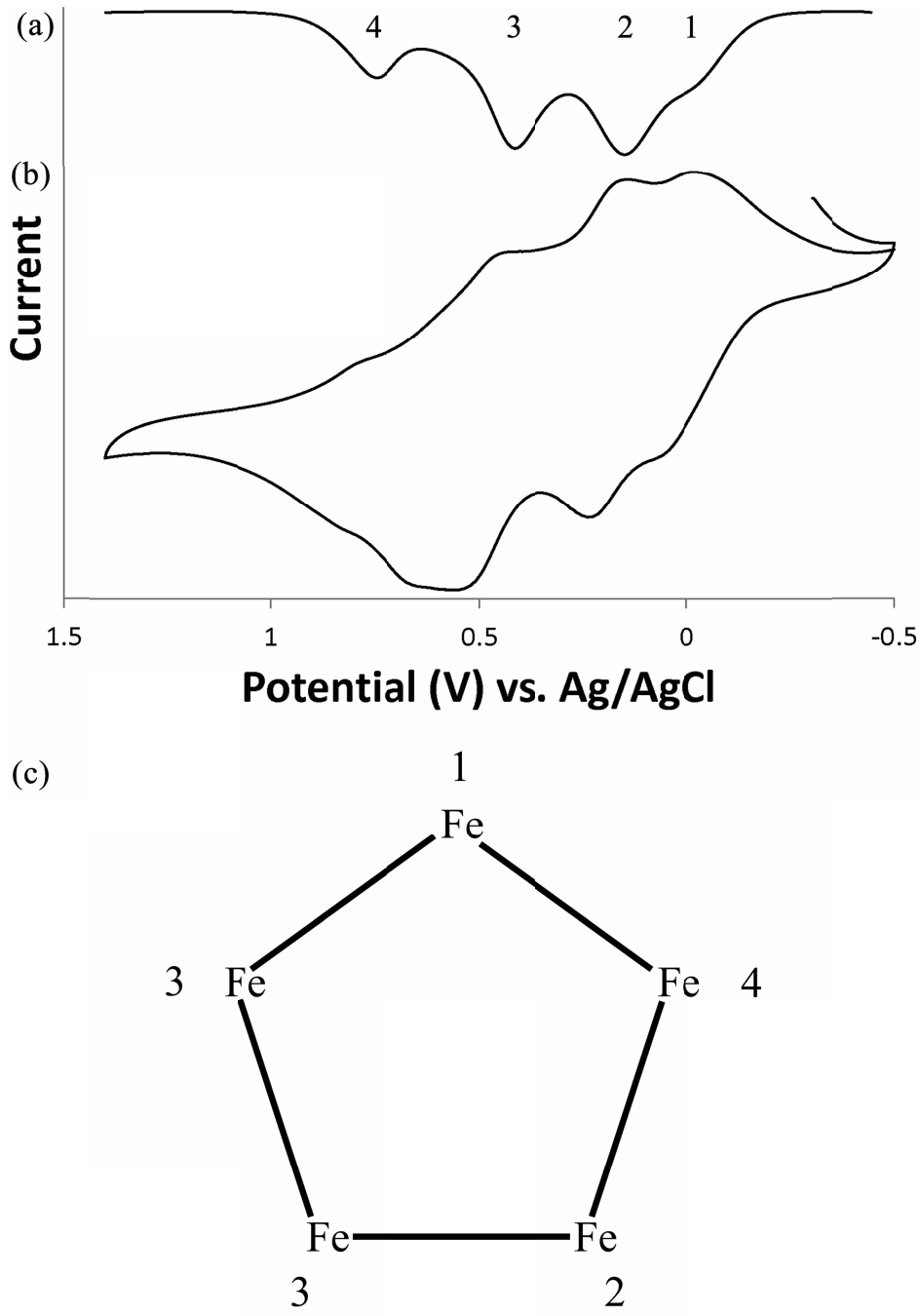

Figure 86. (a) Differential pulse voltammogram and (b) cyclic voltammogram of $[Fe_5(bmtz)_5(NCCH_3)_{10}][SbF_6]_{10}$ in CH_3CN with $[^nBu_4N][SbF_6]$ as the supporting electrolyte referenced to Ag/AgCl at a scan rate of 0.2 V/s from 1.4 to -0.5 V(c) A schematic representation of the proposed order of oxidation events, with the numbers corresponding to those shown in (a).

c. NMR spectroscopy

Similar to the Fe^{II} pentagon with bptz, $[Fe_5(bmtz)_5(CH_3CN)_{10}][SbF_6]_{10}$ is diamagnetic and therefore can be studied by NMR spectroscopy. ^1H NMR spectral data of $[Fe_5(bmtz)_5(CH_3CN)_{10}][SbF_6]_{10}$ in CD_3CN reveals similar shifts from the resonances of free bmtz as the Fe^{II} pentagon with bptz does. One key difference between bptz and bmtz is the loss of the 3′ pyridyl proton as the position is occupied by a N atom in the pyrimidyl group of bmtz (Figure 87). The chemical and magnetic equivalency of the 4′ and 6′ aromatic protons in free bmtz is removed upon coordination to Fe^{II} in the pentagonal metallacycle, creating an additional resonance in the aromatic region of the metallacycle, with the 4′ proton resonance deshielded from 9.13 to 9.48 ppm and the 6′ proton shielded from 9.13 to 8.77 ppm, that of the free ligand, which can be explained by the proximity of the 6′ proton to the nearby coordinated CH_3CN, which provides some shielding. The 5′ proton is also deshielded from 7.7 ppm in the free ligand to 8.07 ppm in the metallacycle. The deshielding of the 4′ and 5′ is due primarily to the inductive effect of the Fe^{II} coordination to bmtz. Considering that the 3′ proton in bptz is absent in bmtz, it is likely that the Fe^{II} square with bmtz will have a spectrum almost identical to that of the Fe^{II} pentagon with bmtz.

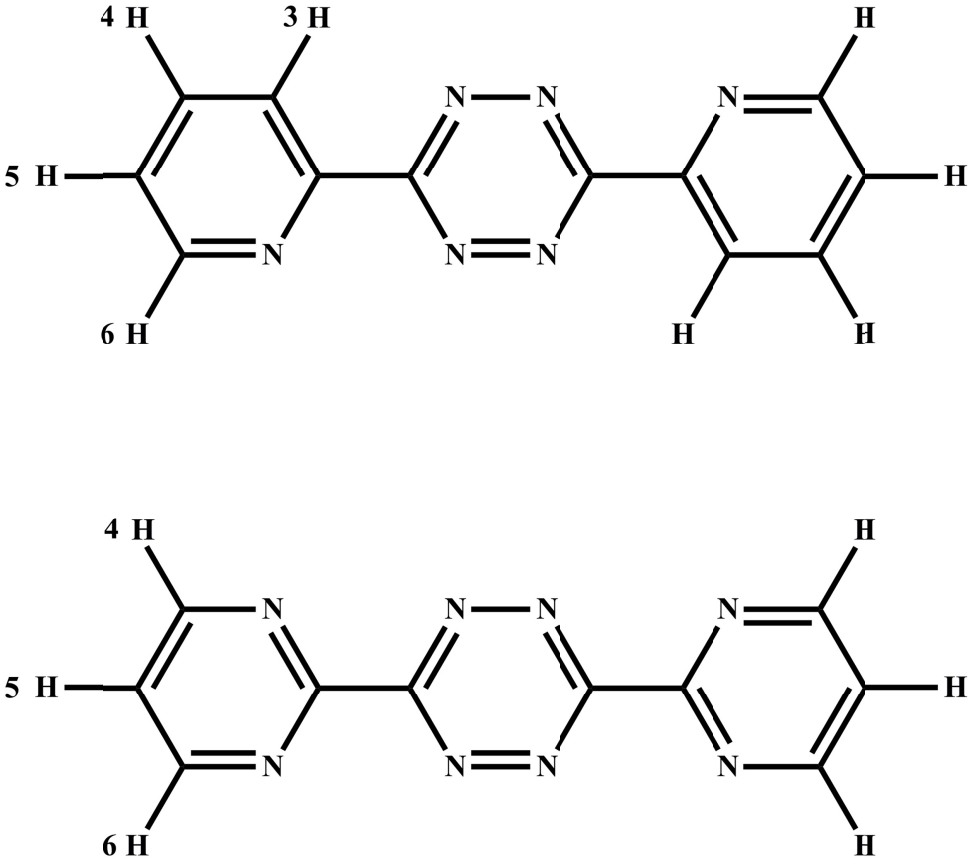

Figure 87. Schematic diagrams of bptz (top) and bmtz (bottom) showing the labeling of the protons and the absence of the proton in the 3-position in bmtz.

D. Conclusions

The ligand bppz was synthesized and reacted with $[Ni(NCCH_3)_6][BF_4]_2$, $[Ni(NCCH_3)_6][SF_6]_2$, $[Fe(NCCH_3)_6][BF_4]_2$, and $[Fe(NCCH_3)_6][SbF_6]_2$. Immediate color changes upon reaction in each case suggests that bppz is chelating with Fe^{II} or Ni^{II} in a similar manner to the metallacycles with bptz, however, no structural data has yet been obtained to find out whether or not metallacyclic structures have been templated by the counterions. The teal color evident in the Fe^{II} reactions with bppz is not as intense as that in the either bptz or bmtz and suggests that the compounds formed with bppz may not contain completely low spin Fe^{II} ions. The ligand bmtz has been reacted with $[Fe(NCCH_3)_6][BF_4]_2$ and $[Fe(NCCH_3)_6][SbF_6]_2$, both of which form dark solutions reminiscent of reactions between Fe^{II} and bptz.

The synthesis and structural characterization of the $[Fe_5(bmtz)_5(CH_3CN)_{10}][SbF_6]_{10}$ pentagon demonstrates that pentagonal metallacycles isostructural to those with bptz can be formed with a similar N-heterocyclic ligand, bmtz. The cross-cavity and cross-ligand distances (Table 16) mirror those of the Fe^{II} pentagon with bptz, as expected considering the similar coordination environment. A significant and interesting finding in the synthesis of $[Fe_5(bmtz)_5(CH_3CN)_{10}][SbF_6]_{10}$ is that there is only one anion completely encapsulated within the central cavity. It can be observed from the range of Fe^{II}-N distances in Table 16 that the pentagon formed with bmtz and Fe^{II} has a slightly larger range due to the slight expansion necessary to incorporate the $[SbF_6]^-$ anion completely. The cross-cavity and cross-ligand distances, however, are little perturbed as seen in Table 16. Initially, it was thought that the

Table 16. Comparison of average distances (d_{avg}) for the $[Fe_5L_5(NCCH_3)_{10}][SbF_6]_{10}$ pentagonal metallacycles, in Å (L = bptz or bmtz).

Ligand	Cross-ligand d_{avg}	Cross-cavity d_{avg}	Fe^{II}-N $d_{shortest} – d_{longest}$
bptz	6.4	10.4	1.87 – 2.01
bmtz	6.4	10.4	1.84 – 2.03

pentagonal metallacycles with Fe^{II} were too rigid and compact to allow for the complete encapsulation of $[SbF_6]^-$, thus resulting in the encapsulation of two $[SbF_6]^-$ anions primarily due to insufficient volume in the central cavity. The encapsulation of a single anion within the central cavity in $[Fe_5(bmtz)_5(CH_3CN)_{10}][SbF_6]_{10}$ indicates that the anion-π interactions between $[SbF_6]^-$ and the central tetrazine ring of bmtz are stronger than those in the Fe^{II} metallacycle with bptz. This is not surprising considering that the reduction potential of bmtz is lower than that of bptz, suggesting a greater affinity for a negative charge. This affinity, as shown by the localization of the LUMO of bmtz and bptz on the tetrazine ring, should be greatest at the central tetrazine ring. ESP maps of bmtz and bptz also reveal slightly more electropositive tetrazine C atoms for bmtz. The difference in the anion encapsulation between the metallacycles of Fe^{II} with bptz and bmtz, along with the electrochemistry of the two ligands, lends strong evidence to the presence of templating anion-π interactions as critical elements in the formation of these metallacycles.

The work presented in this chapter, along with previous work with the bppn ligand, demonstrate that anion-π interactions are important interactions that can be harnessed and controlled for the templation of supramolecular structures. Further work is necessary to determine the structures of the complexes formed with bppz as they will lend important insight into the extent of the anion templation with N-heterocyclic ligands. Further work to structurally characterize the product of the reaction of bmtz with $[Fe(NCCH_3)_6][BF_4]_2$ is also necessary, as isolating and characterizing both the square and pentagonal metallacycles of Fe^{II} with bmtz would allow the study of the

expected interconversion between the two compounds. It will be most interesting to see whether or not the anion is centrally located in the square metallacycle of Fe^{II} with bmtz. Extension of the structures incorporating bmtz to Co^{II} and Ni^{II} will allow comparisons of the cavity size and resulting interaction distances between the anions and ligands.

CHAPTER V

EXPLORING THE INCORPORATION OF NEW ANIONS INTO THE ANION-TEMPLATED METALLACYCLIC ARCHITECTURES OF IRON(II) AND BPTZ

A. Introduction

One of the key elements to understanding anion-π interactions in supramolecular chemistry is a working knowledge of how the differences in geometry, size, and charge of the anion affects them in complexes, whether anion templated or not. The studies of bptz coordinated to various Ag^{I} salts of complex anions discussed in Chapter IV underscore the structural differences between otherwise similar systems in the presence of different templating anions.[79,109] To this end, the Dunbar group has studied the effect of varying the anion in supramolecular assemblies of $HAT(CN)_6$ with halides, and explained anion replacement studies involving the Ni^{II} metallacycles with bptz.[70,80,119]

The spectroscopic and structural research of the columnar complexes resulting from the co-crystallization of Cl^-, Br^-, or I^- with the π-accepting arene 1,4,5,8,9,11-hexaazatriphenylene-hexacarbonitrile ($HAT(CN)_6$) revealed two different anion-π binding modes within the same structure, along with variations in the electronic absorption spectra exhibited by the series. Reactions of $HAT(CN)_6$ with $[^nBu_4N][X]$ (X = Cl^-, Br^-, and I^-) salts in CH_3CN and crystallization from benzene resulted in columnar stacks of alternating layers of $HAT(CN)_6$ and halide ions along with tetrabutylammonium cations situated around the periphery of the columns (Figure 88).

There are four different layers within the column, denoted A-D (Figure 89a-d). Layer A comprises one $HAT(CN)_6$ moiety and three tetrabutylammonium cations symmetrically arranged about the three-fold rotation axis perpendicular to the $HAT(CN)_6$ molecule (Figure 89a). Layer B comprises three of the four anion disorder positions symmetrically arranged about the perpendicular three-fold rotation axis over the (NC)C=C(CN) bond (Figure 89b). Layer C comprises a solitary $HAT(CN)_6$ molecule (Figure 89c). Layer D consists of an anion over the central aromatic region of $HAT(CN)_6$ along with three benzene solvent molecules symmetrically disposed about the central three-fold rotation axis (Figure 89d). The structures (determined by single-crystal XRD for both the I^- and Br^- derivatives) show the presence of an anion-π interaction above the centroid of $HAT(CN)_6$ and charge-transfer interactions above the edge of $HAT(CN)_6$ within the same structure. The anion in Layer D participates in an anion-π interaction with the center of $HAT(CN)_6$ and the anions in Layer B participate in charge-transfer type anion-π interactions with the outer (NC)C=C(CN) bonds.[80,119]

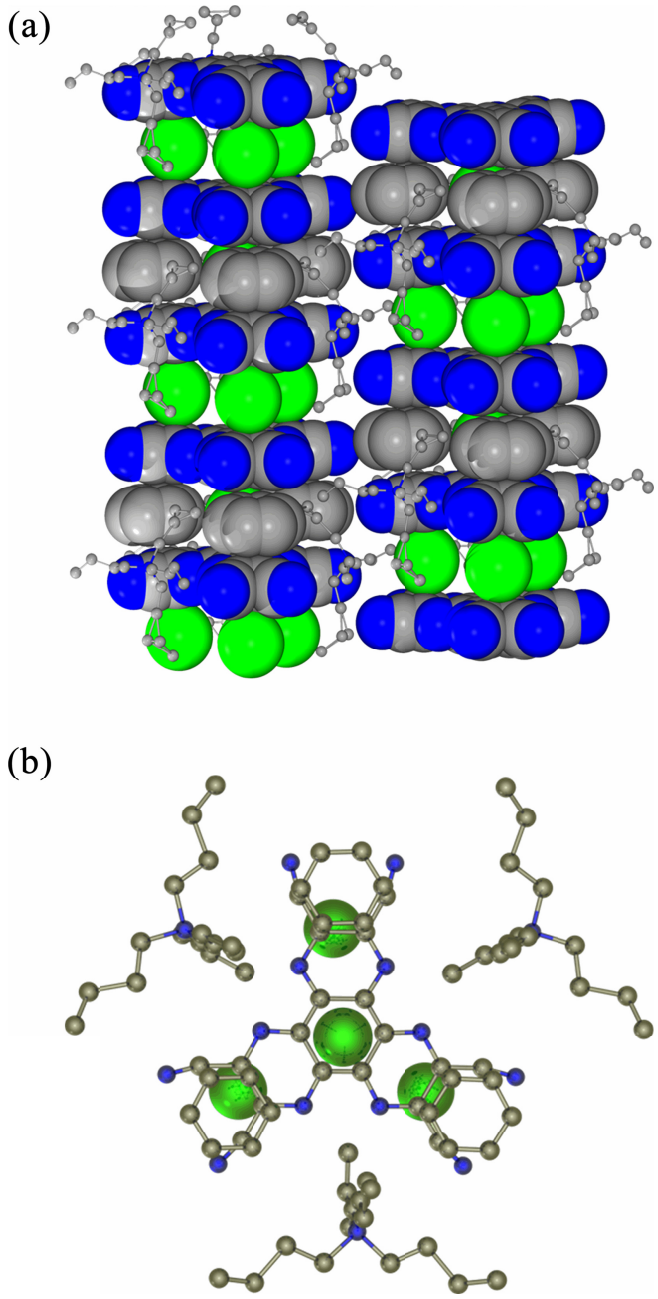

Figure 88. (a) Space-filling representation of the view perpendicular to the *c* axis of the columnar stacks of cocrystallized $HAT(CN)_6/[^nBu_4N][I]$ highlighting the layered structure of alternating anions and $HAT(CN)_6$ molecules, with benzene and $[^nBu_4N]^+$ incorporated within and about the columns, respectively. (b) Ball and stick representation of the view down the *c*-axis, highlighting the alignment of $HAT(CN)_6$, benzene, and $[I]^-$ within the columnar stack. Atom colors: carbon (grey), nitrogen (blue), iodine (green). Hydrogen atoms are omitted for the sake of clarity. Figure adapted from Dunbar *et al.*[119]

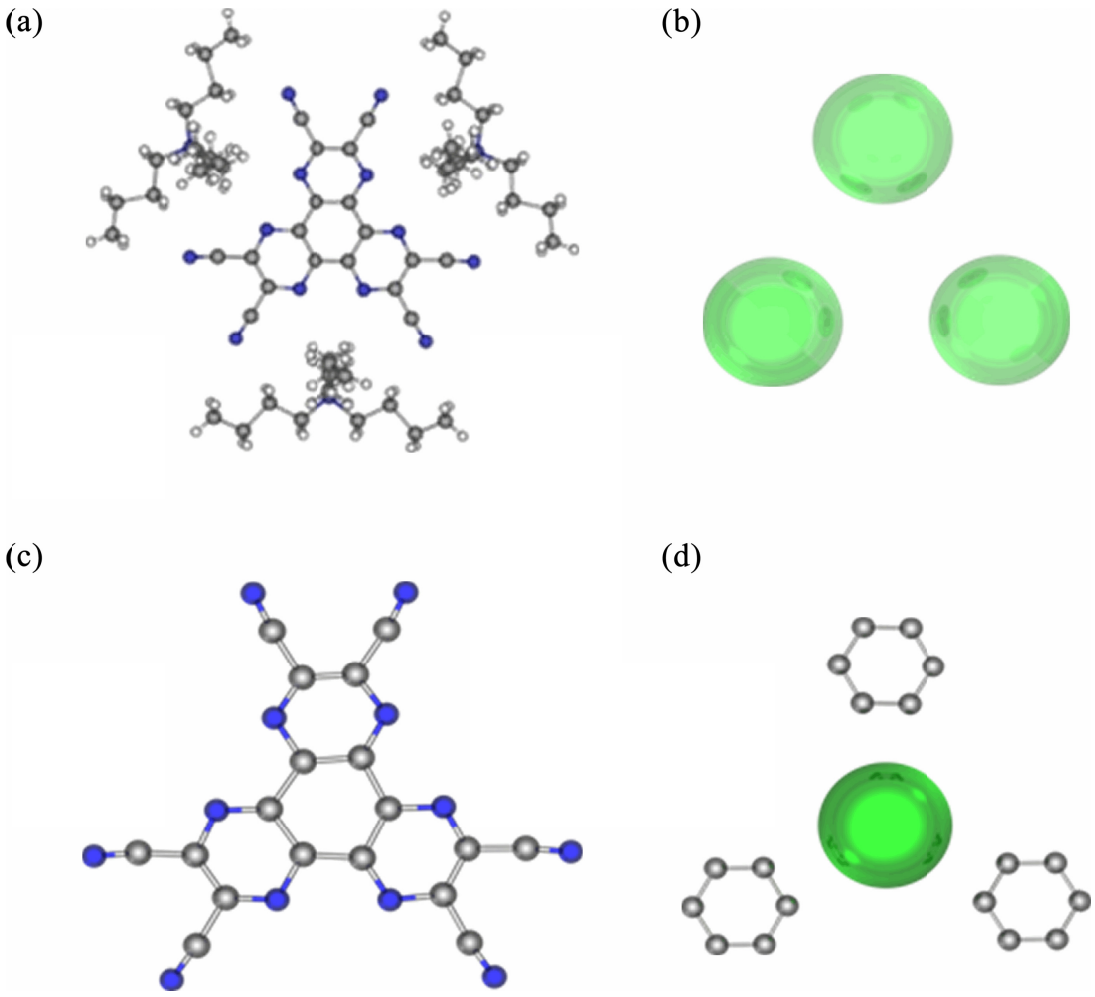

Figure 89. Deconstruction of the layers composing the $HAT(CN)_6/[^nBu_4N][I]$ columnar stack. (a) Ball and stick representation of Layer A showing the $HAT(CN)_6$ surrounded by three $[^nBu_4N]^+$ cations (hydrogen atoms shown). (b) Space-filling diagram of the three $[I]^-$ positions in Layer B, which align over the (NC)C=C(CN) bond in $HAT(CN)_6$. (c) Ball and stick diagram of the $HAT(CN)_6$ molecule in Layer C. (d) Ball and stick (benzene) and space-filling ($[I]^-$) diagram of the lone $[I]^-$ position surrounded by three benzene molecules. The $[I]^-$ ion is positioned directly above the centroid of $HAT(CN)_6$ (hydrogen atoms on benzene omitted for the sake of clarity). Atoms colors: carbon (grey), nitrogen (blue), iodine (green), and hydrogen (white). Figure adapted from Dunbar *et al*.[119]

The distinctive colors of the THF solutions of $HAT(CN)_6$ (yellow) with $[Br^-]$ (dark red) or $[I]^-$ (dark green) indicate the presence of strong charge transfer interactions between the anions and $HAT(CN)_6$ (Figure 90). Spectroscopic titrations of $[^nBu_4N][X]$ ($X = Cl^-$, Br^-, and I^-) into solutions of $HAT(CN)_6$ established a 2:3 ratio of $HAT(CN)_6$:$[X]^-$, in agreement with the structural data. The energies of the transitions, directly related to the HOMO→LUMO energy gap, increase linearly as a function of increasing oxidation potential ($[Cl]^- > [Br]^- > [I]^-$ are 408, 419, and 630 nm, respectively), confirming the charge transfer nature of the interactions. Given the differences in absorbance based on the halide, the π-acidic $HAT(CN)_6$ molecule is a good candidate for colorimetric halide sensing.[80]

In addition to the pioneering work with $HAT(CN)_6$, the effect of replacing $[BF_4]^-$, $[ClO_4]^-$, or $[SbF_6]^-$ anions in the Ni^{II} metallacycles with bptz with other anions on their structure and stability has been explored by the Dunbar group through anion-exchange reactions.[70] Indeed, the interconversion behavior of the Ni^{II} and Fe^{II} metallacycles with bptz discussed in Chapter III aptly demonstrates the structural changes that can be induced upon anion replacement. Taking advantage of the inherent instability of the pentagonal metallacycle of Ni^{II}, a solution of the Ni^{II} pentagonal metallacycle with bptz was treated with excess $[^nBu_4N][I]$, resulting in the formation of $[Ni_4(bptz)_4(NCCH_3)_8{\subset}I][SbF_6]_7$, a square metallacycle with an encapsulated $[I]^-$ anion and external $[SbF_6]^-$ anions, a species that cannot be formed from a reaction between NiI_2 and bptz (Figure 91). In an attempt to study the square metallacycle without any trapped anion, the Ni^{II} metallacycle encapsulating $[I]^-$ was treated with excess $TlPF_6$ in

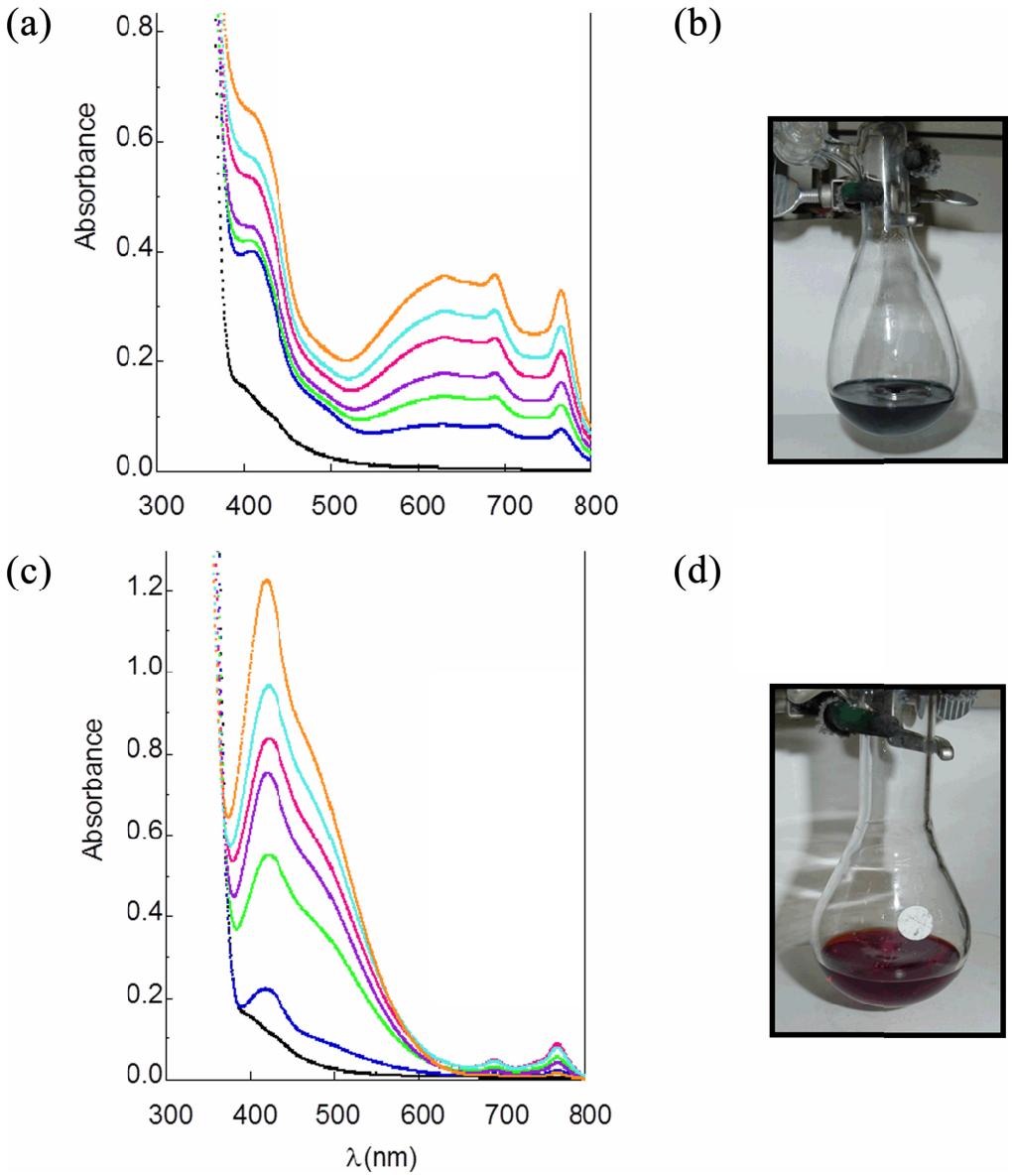

Figure 90. (a) Electronic absorption spectral titration of 0.13 mM $HAT(CN)_6$ in THF (black) with 0.31 mM (green), 0.46 mM (purple), 0.78 mM (fuchsia), 1.09 mM (teal), and 3.55 mM (orange) $[^nBu_4N][I]$, showing the increase in the charge transfer band at 630 nm. (b) A photograph of the $HAT(CN)_6/[^nBu_4N][I]$ solution showing the intense green color resulting from the charge transfer between $[I]^-$ and $HAT(CN)_6$. (c) Electronic absorption spectral titration of 0.13 mM $HAT(CN)_6$ in THF (black) with 0.39 mM (green), 0.78 mM (purple), 1.55 mM (fuchsia), 3.88 mM (teal), and 7.76 mM (orange) $[^nBu_4N][Br]$, showing the increase in the charge transfer band at 419 nm. (d) A photograph of the $HAT(CN)_6/[^nBu_4N][Br]$ solution showing the red color resulting from the charge transfer between $[Br]^-$ and $HAT(CN)_6$. Figure adapted from Dunbar *et al.*[80]

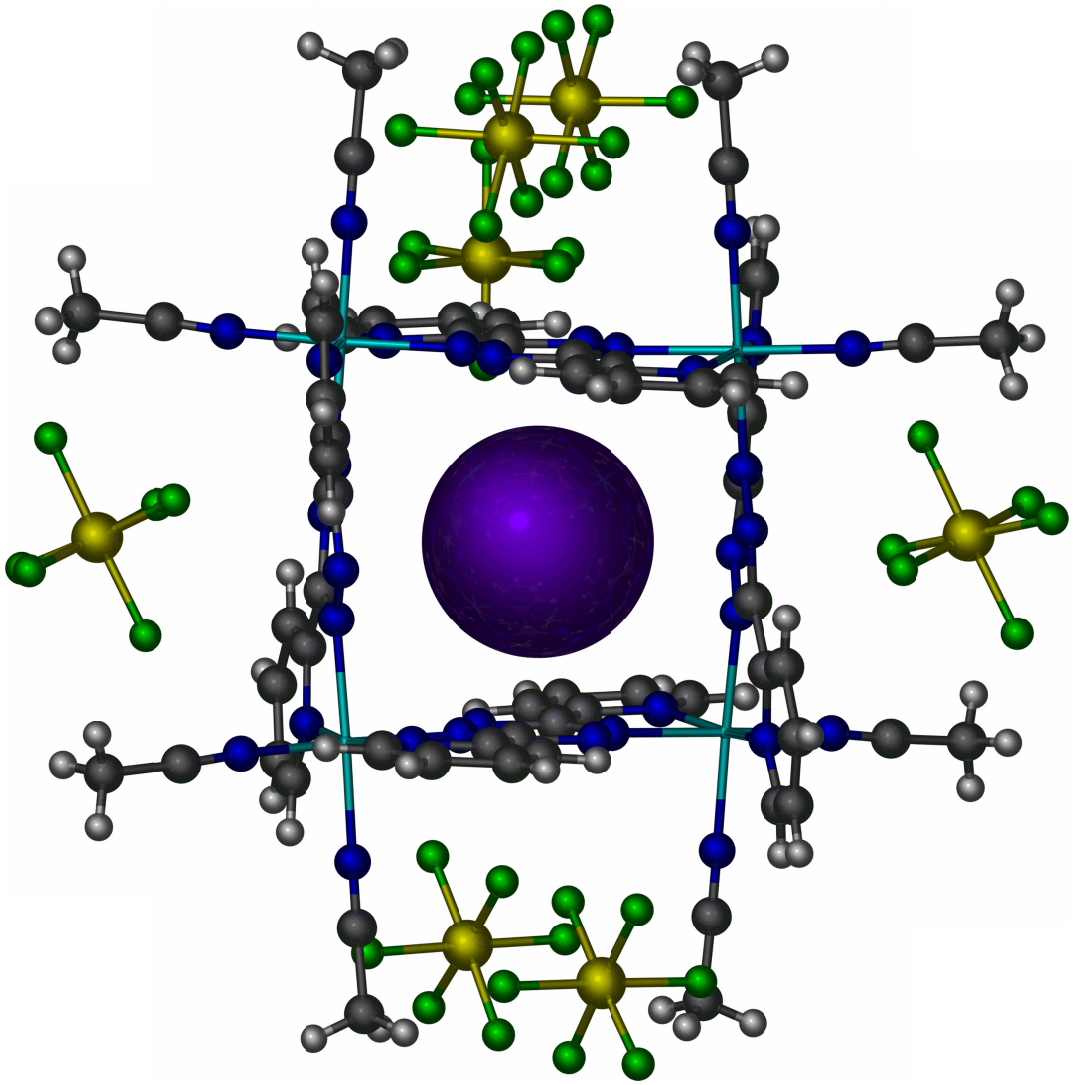

Figure 91. Ball and stick representation of $[Ni_4(bptz)_4(NCCH_3)_8 \subset I][SbF_6]_7$ depicting the square metallacycle encapsulating $[I]^-$ and surrounded by $[SbF_6]^-$. Atom colors: carbon (grey), nitrogen (blue), hydrogen (white), antimony (yellow), fluorine (green), and iodine (purple). Figure generated from data presented in Dunbar *et al.*, CCDC# 253371.[70]

CH_3CN, leading to a precipitate of TlI. Surprisingly, rather than replacing $[I]^-$ with solvent, the square metallacycle reorganizes into a pentagonal metallacycle encapsulating $[SbF_6]^-$ and crystallizes with varying amounts of $[PF_6]^-$ and $[SbF_6]^-$ anions occupying the metallacycle periphery presumably because no anion appropriate for the templation of the square metallacycle remains in solution.[70]

The square metallacycle $[Ni_4(bptz)_4(NCCH_3)_8][ClO_4]_8$ was also subjected to anion replacement studies. Treatment of $[Ni_4(bptz)_4(NCCH_3)_8][ClO_4]_8$ with an excess of $[IO_4]^-$ anion fails to replace the encapsulated $[ClO_4]^-$ anion with $[IO_4]^-$ since it is much larger than $[ClO_4]^-$, however, outer-sphere $[ClO_4]^-$ anions are replaced with $[IO_4]^-$ and some of the coordinated CH_3CN molecules are replaced by H_2O, forming $[Ni_4(bptz)_4(NCCH_3)_4(OH_2)_4 \subset ClO_4][IO_4]_7$ and demonstrating the sensitivity of these metallacycles to adventitious water, an important consideration due to the ease of oxidation of the Fe^{II} metallacycles (Figure 92). Treatment of $[Ni_4(bptz)_4(NCCH_3)_8][ClO_4]_8$ with excess $[^nBu_4N][Br_3]$ results in the intriguing metallacycle $[Ni_4(bptz)_4(NCCH_3)Br_7 \subset Br_3]$ in which all of the $[ClO_4]^-$ anions are replaced in the structure. More interesting, however, is that all but one of the coordinated CH_3CN molecules are replaced by coordinated $[Br]^-$ produced from the decomposition of $[Br_3]^-$. The encapsulated $[ClO_4]^-$ is replaced by a $[Br_3]^-$ anion that is threaded through the central cavity, with the central Br atom interacting with the bptz tetrazine rings and the two terminal Br atoms residing near the openings on each side of the cavity (Figure 93). This suggests that an encapsulated anion is necessary for the stability of the square

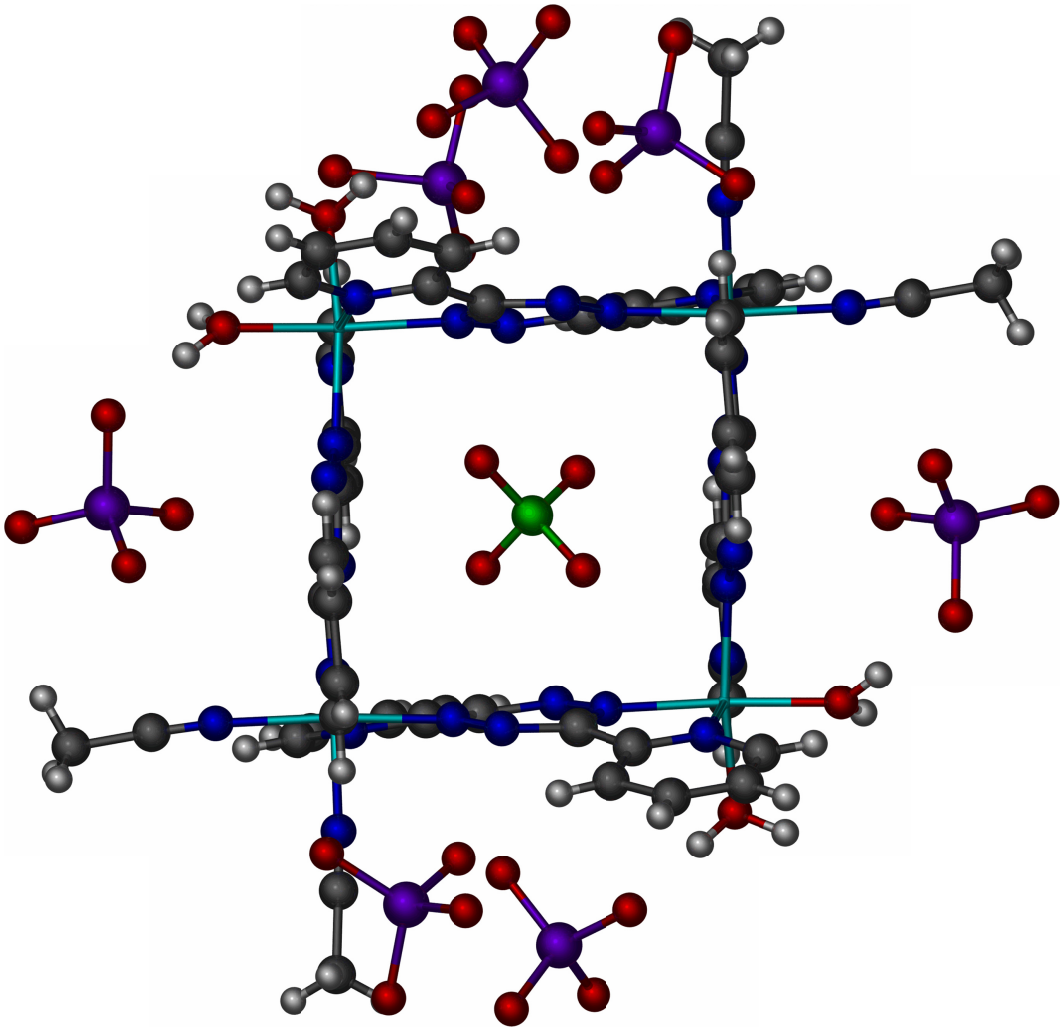

Figure 92. Ball and stick representation of $[Ni_4(bptz)_4(NCCH_3)_4(OH_2)_4 \subset ClO_4][IO_4]_7$. The square metallacycle encapsulates $[ClO_4]^-$ rather than $[IO_4]^-$, which are found surrounding the metallacycle. The replacement of CH_3CN for H_2O is also demonstrated. Interstitial solvent molecules are omitted for the sake of clarity. Atom colors: carbon (grey), nitrogen (blue), oxygen (red), hydrogen (white), chlorine (green), and iodine (purple). Figure generated from data presented in Dunbar *et al.*, CCDC# 253664.[70]

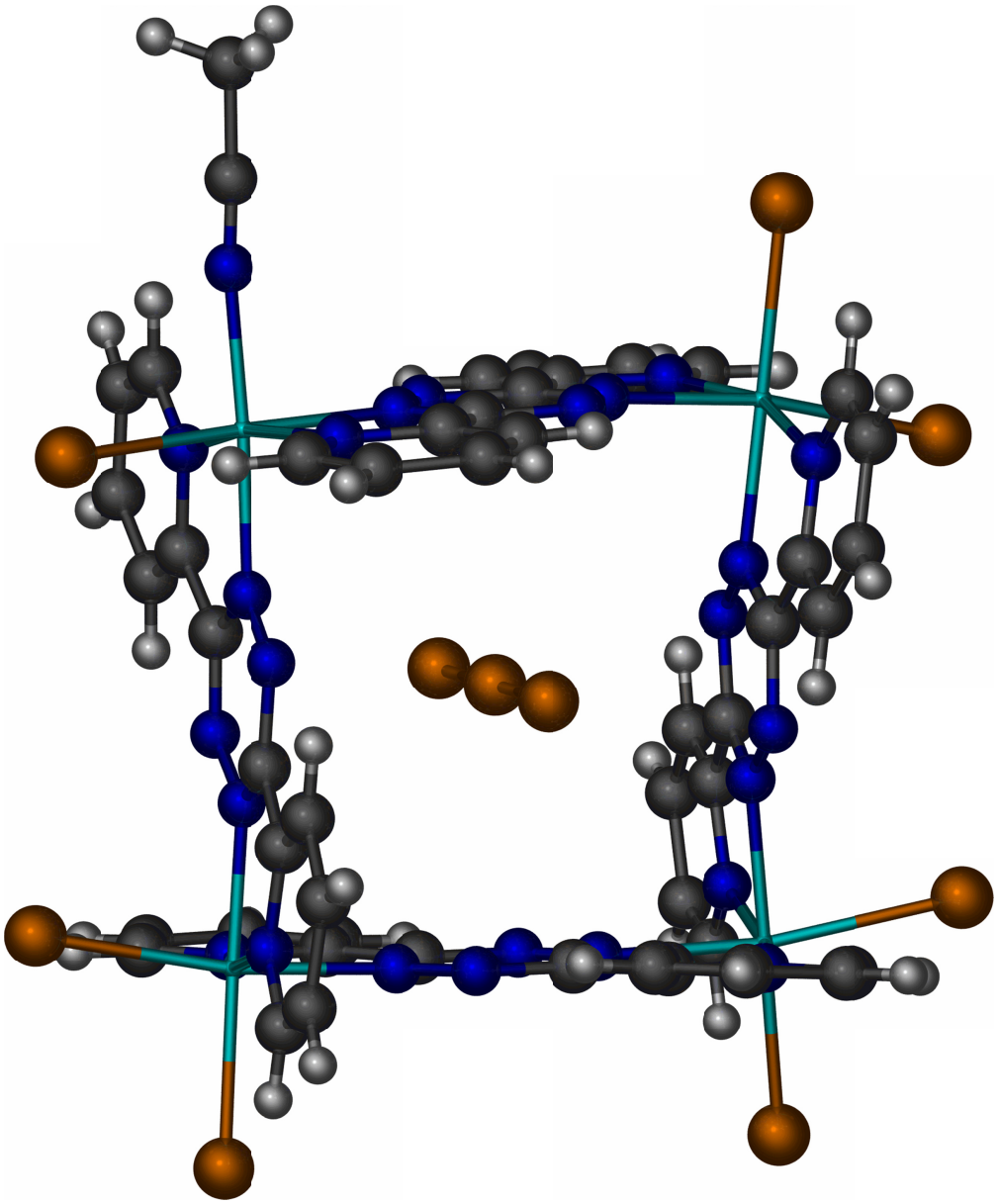

Figure 93. Ball and stick representation of $[Ni_4(bptz)_4(NCCH_3)Br_7 \subset Br_3]$, showing the square metallacycle encapsulating $[Br_3]^-$ and seven of the eight coordinated CH_3CN molecules replaced by $[Br]^-$. Interstitial solvent molecules are omitted for the sake of clarity. Atom colors: carbon (grey), nitrogen (blue), hydrogen (white), and bromine (orange). Figure generated from data presented in Dunbar *et al.*, CCDC# 254143.[70]

metallacycle since even in the presence of excess $[Br_3]^-$ not all of the CH_3CN ligands are replaced (which would form a completely neutral metallacycle with no anion present in the cavity).[70]

Studies of the structural changes induced by different anions have thus far been limited to these studies in the Dunbar group. One of the key features in the complexes resulting from replacement of the anions by an addition of an excess of a competing anion is the mixture of anions present in the final structures of these metallacycles. Although an excellent means to perform anion competition studies, the anion replacement methods tend to vary in the amount of anions replaced and could lead to difficulties in data interpretation as anions closer in size to those that template the metallacycles are used ($[AsF_6]^-$ *vs.* $[SbF_6]^-$, for example). In order to fully study the templation exhibited by other complex anions, it is necessary to use metal salts that incorporate the anions in question and thus eliminate the need for post-synthetic anion displacement. The divalent hexakisacetonitrile metal salts (specifically $[Fe(NCCH_3)_6][X]_2$, X = $[BF_4]^-$ and $[SbF_6]^-$) used as the metal and anion sources for the metallacycles discussed so far provide an excellent platform for the incorporation of a wide variety of anions.

There are, however, two limitations that must be overcome if one is to use the $[Fe(NCCH_3)_6]^{2+}$ salts in this manner. The first limitation is that the current synthesis used to produce the salts involves oxidation of Fe metal with NO^+ salts in CH_3CN. The nitrosonium salts are commercially available with only three counterions: $[BF_4]^-$, $[PF_6]^-$, and $[SbF_6]^-$. Also, the synthesis can produce Fe^{III} in addition to Fe^{II}, which is also

possible for other redox active metals. This limitation can be overcome by using Na^+, K^+, or Tl^+ salts of non-coordinating complex anions in a metathesis reaction with anhydrous $FeCl_2$ or FeI_2 in CH_3CN with the precipitation of NaX, KX, or TlX (X = Cl or I). Both anhydrous $FeCl_2$ and FeI_2, however, contain significant amounts of Fe^{III} impurities, often resulting in a mixture of Fe^{II} and Fe^{III} in the final product (typically resulting in a pale yellow rather than white or off-white solid). A highly pure form of Fe^{II} exists, however, in the form of the cluster $Fe_4Cl_8(THF)_6$, first synthesized by Cotton and coworkers by comproportionation of Fe(s) and $FeCl_3$ in THF, with a simpler synthesis involving reflux of anhydrous $FeCl_2$ in THF developed later by the Dunbar group (Figure 94).[120,121]

This chapter discusses the synthesis of new hexakisacetonitrile iron(II) salts with a wide variety of anions by simple reaction of the Na^+ salt of the anion with $Fe_4Cl_8(THF)_6$ and their subsequent reaction with bptz in an effort to explore the templation behavior for a range of anion sizes, shapes, and charges. One of the primary aims of this work is the incorporation of very large, non-coordinating anions such as $[((CF_3)_2C_6H_3)_4B]^-$, $[(C_6F_5)_4B]^-$, $[CHB_{11}Cl_{11}]^-$, and $[B_{12}Cl_{12}]^{2-}$ to determine whether metallacyclic structures can be templated with such anions, possibly with the formation of larger polygons such as hexagons.

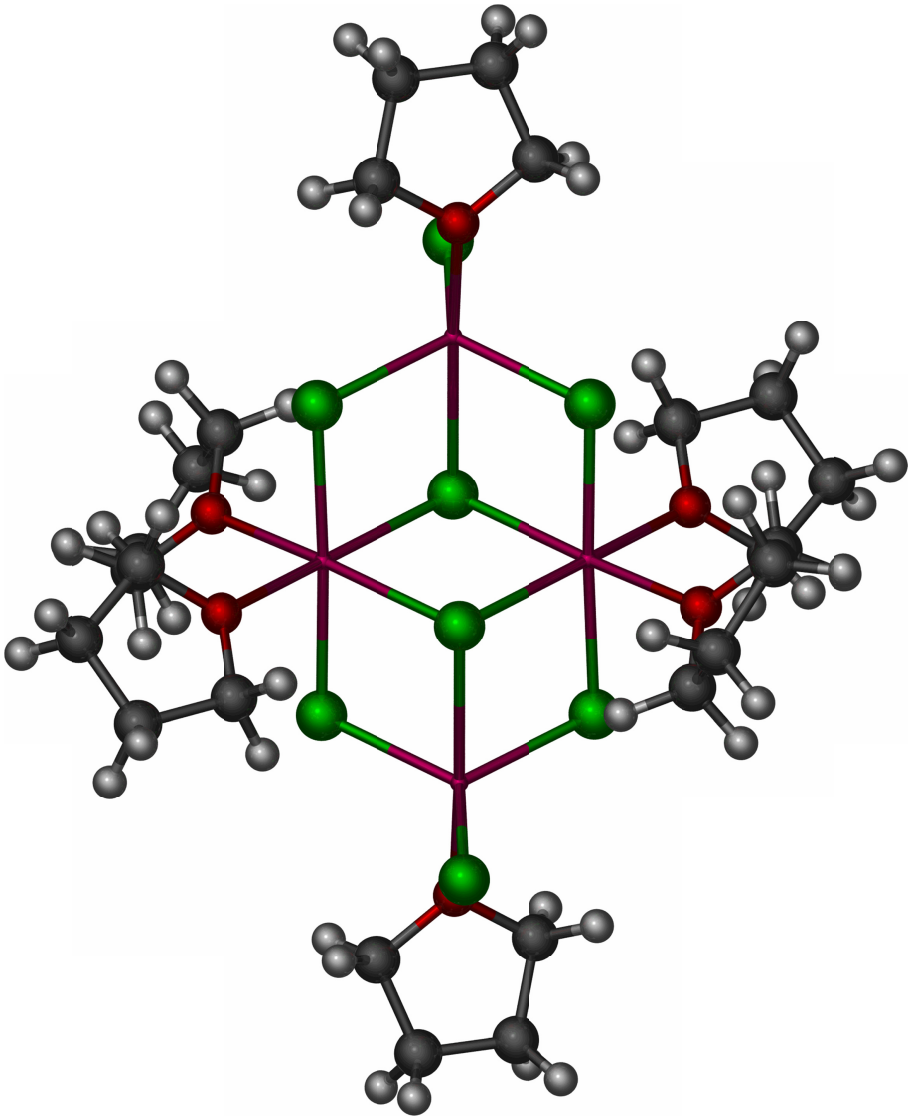

Figure 94. Ball and stick representation of the cluster $Fe_4Cl_8(THF)_6$. Atom colors: carbon (grey), oxygen (red), hydrogen (white), chlorine (green), and iron (pink). Figure generated from Cotton *et al.*, CSD ID: CIZFEW01.[120]

B. Experimental

i. General methods and starting materials

All reactions were performed under nitrogen using standard Schlenk-line techniques or in an MBraun inert atmosphere glovebox. All glassware was oven-dried prior to use. Acetonitrile was dried over 3 Å molecular sieves and distilled under nitrogen. Toluene was dried by passing it through a column of proprietary desiccant and dispensed under nitrogen using an MBraun Solvent Purification System. Dichloromethane was dried over P_2O_5 and distilled under nitrogen. Anhydrous tetrahydrofuran (THF) and diethyl ether were purchased from Aldrich in SureSeal® containers, dispensed under nitrogen and used as received. The cluster $Fe_4Cl_8(THF)_6$ was synthesized by refluxing anhydrous $FeCl_2$ in anhydrous THF under nitrogen according to the preparation of Dunbar *et al.*[121] The Na^+ salts of anions were purchased from Aldrich, Alfa Aesar, or Acros and dried under vacuum prior to use, unless otherwise noted. The bptz ligand (magenta) was synthesized by the method of Geldard and Lions, recrystallized from benzene, and dried *in vacuo* prior to use.[95] Physical properties measurements were performed as described in Chapter III.

ii. $[Fe(NCCH_3)_6]^{2+}$ starting materials

a. $Fe_4Cl_8(THF)_6$ + 8 $Na[BF_4]$

A suspension of ground $NaBF_4$ (white powder, 1.25 g, 11.42 mmol) in 20 mL of CH_3CN (clear, colorless solution) was combined with a solution of $Fe_4Cl_8(THF)_6$ (pale tan solid, 1.43 g, 1.43 mmol) in 20 mL of CH_3CN (tan solution) while stirring. After stirring, the solution became colorless with a white powder present. It was subsequently

filtered through a fine sintered glass frit to remove the white precipitate. The volume of the clear, colorless filtrate was reduced under vacuum, treated with 5 mL of diethyl ether, and then refiltered to remove any remaining NaCl(s). Diethyl ether (20 mL) was added and the solution was cooled to -20 ^{o}C overnight to precipitate the white microcrystalline solid of $[Fe(NCCH_3)_6][BF_4]_2$, which was isolated by filtration through a fine sintered glass frit and dried under nitrogen. Yield: 1.12 g, 41 %. IR (Nujol mull, CsI,cm^{-1}): $\nu_{C\equiv N}$ 2308 (m), 2280 (m), CH_3CN; ν_{B-F} 1087 (s), 551 (w), $[BF_4]^-$.

b. $Fe_4Cl_8(THF)_6$ + 8 $Na[PF_6]$

A suspension of $NaPF_6$ (white solid, 1.52 g, 9.03 mmol) in 30 mL of CH_3CN (clear, colorless solution) was combined with a solution of $Fe_4Cl_8(THF)_6$ (pale tan solid, 1.01 g, 1.08 mmol) in 30 mL of CH_3CN (tan solution) while stirring. A small amount of white precipitate formed immediately, indicating the formation of NaCl(s). The reaction was stirred until the solution became colorless and then filtered through a fine sintered glass frit to remove the white precipitate. The volume of the clear, colorless filtrate was reduced under vacuum, treated with 5 mL diethyl ether, and then refiltered to remove any remaining NaCl(s). Diethyl ether (50 mL) was added and the solution cooled to -20 ^{o}C overnight to precipitate the white microcrystalline solid of $[Fe(NCCH_3)_6][PF_6]_2$, which was isolated by filtration through a fine sintered glass filter and dried under nitrogen. Yield: 2.00 g, 79 %. IR (Nujol mull, CsI, cm^{-1}): $\nu_{C\equiv N}$ 2325 (s), 2293 (s), CH_3CN; ν_{P-F} 875 (vs), 558 (s), $[PF_6]^-$.

c. $Fe_4Cl_8(THF)_6$ + 8 Na[AsF_6]

A solution of $NaAsF_6$ (white solid, 2.07 g, 9.76 mmol) in 15 mL of CH_3CN (clear, colorless solution) was combined with a solution of $Fe_4Cl_8(THF)_6$ (pale tan solid, 1.44 g, 1.22 mmol) in 25 mL of CH_3CN (tan solution) while stirring. A white precipitate formed after five minutes of stirring, indicating the formation of NaCl(s). The reaction was stirred overnight and then filtered through a fine sintered glass frit to remove the white precipitate. The volume of the clear, colorless filtrate was reduced under vacuum, treated with 5 mL of diethyl ether, and then refiltered to remove any remaining NaCl(s). Diethyl ether (50 mL) was added and the solution cooled to -20 ^oC overnight to precipitate the white microcrystalline solid of $[Fe(NCCH_3)_6][AsF_6]_2$, which was isolated by filtration through a fine sintered glass frit and dried under nitrogen. Yield: 2.85 g, 86 %. IR (Nujol mull, CsI, cm^{-1}): $\nu_{C\equiv N}$ 2322 (s), 2292 (s), CH_3CN; ν_{As-F} 699 (vs), 399 (s), $[AsF_6]^-$.

d. $Fe_4Cl_8(THF)_6$ + 8 Na[CF_3CO_2]

A suspension of $Na(CF_3CO_2)$ (white solid, 0.21 g, 0.22 mmol) in 5 mL of CH_3CN (clear, colorless solution) was combined with a solution of $Fe_4Cl_8(THF)_6$ (pale tan solid, 0.24 g, 1.76 mmol) in 10 mL of CH_3CN (tan solution) while stirring. A white precipitate formed immediately, indicating the formation of KCl(s). The reaction was then filtered through a fine sintered glass frit to remove the white precipitate. The volume of the clear, colorless filtrate was reduced under vacuum, treated with diethyl ether (25 mL) and then cooled to -20 ^oC overnight to precipitate the white microcrystalline solid of $[Fe(NCCH_3)_6][CF_3CO_2]_2$, which was isolated by filtration

through a fine sintered glass frit and dried under nitrogen. Yield: 0.068 g, 6.5 %. IR (Nujol mull, CsI, cm^{-1}): $\nu_{C\equiv N}$ 2313 (m), 2286 (m), CH_3CN; $\nu_{C=O}$ 1718 (vs), ν_{C-F} 1212 (vs), 1152 (vs) $[CF_3CO_2]^-$.

e. $Fe_4Cl_8(THF)_6$ + 8 $Na[(C_6H_5)_4B]$

A solution of $Na[(C_6H_5)_4B]$ (white solid, 0.60 g, 1.76 mmol) in 10 mL of CH_3CN (clear, off-white solution) was combined with a solution of $Fe_4Cl_8(THF)_6$ (pale tan solid, 0.20 g, 0.21 mmol) in 10 mL of CH_3CN (tan solution) while stirring. An instantaneous white precipitate was observed to form, indicating the formation of NaCl(s). The reaction was then filtered through a fine sintered glass frit to remove the white precipitate. The off-white, colorless filtrate was treated with diethyl ether until cloudy and then cooled to -20 ^oC overnight to precipitate the white microcrystalline solid of $[Fe(NCCH_3)_6][(C_6H_5)_4B]_2$, which was isolated by filtration through a fine sintered glass filter and dried under nitrogen. Yield: 0.94 g, 33 %. IR (Nujol mull, CsI, cm^{-1}). $\nu_{C\equiv N}$ 2306 (s), 2279 (s), CH_3CN; $\nu_{C-H(ar)}$ 3054 (m), $\nu_{C-C(ar)}$ 1478 (w), 1428 (w), $\nu_{B-C(ar)}$ 1030 (m), $[B(C_6H_5)_4]^-$.

f. $Fe_4Cl_8(THF)_6$ + 8 $Na[CHB_{11}Cl_{11}]$

The $Na(CHB_{11}Cl_{11})$ salt was synthesized by the reaction of $[(CH_3)_3NH][CHB_{11}Cl_{11}]$ (donated by Prof. Oleg Ozerov, Texas A&M University, Department of Chemistry) with Na_2CO_3 in 8:2 MeOH:H_2O and recrystallized from CH_2Cl_2 in 73% yield. A solution of $Na(CHB_{11}Cl_{11})$ (white solid, 0.19 g, 0.36 mmol) in 3 mL of CH_3CN (clear, colorless solution) was combined with a solution of $Fe_4Cl_8(THF)_6$ (pale tan solid, 0.042 g, 0.045 mmol) in 0.5 mL of CH_3CN (tan solution) while stirring.

The solution became cloudy after two minutes of stirring, indicating the formation of NaCl(s). The reaction was stirred overnight and then filtered through a fine sintered glass frit to remove the white precipitate. Diethyl ether (25 mL) was added and the solution cooled to -20 ^{o}C overnight to precipitate the white microcrystalline solid of $[Fe(NCCH_3)_6][CHB_{11}Cl_{11}]_2$, which was isolated by filtration through a fine sintered glass frit and dried under nitrogen. Yield: 0.10 g, 42 %. IR (Nujol mull, CsI, cm^{-1}): $\nu_{C\equiv N}$ 2312 (s), 2285 (s), CH_3CN; ν_{C-H} 3028 (w), ν_{B-B} 1116 (m), ν_{B-C} 1034 (m), 1011 (m), ν_{B-Cl} 722 (w), $[CHB_{11}Cl_{11}]^-$.

g. $Fe_4Cl_8(THF)_6$ + 4 $K_2[NbF_7]$

A suspension of K_2TaF_7 (white solid, 0.28 g, 0.91 mmol) in 5 mL of CH_3CN (clear, colorless solution) was combined with a solution of $Fe_4Cl_8(THF)_6$ (pale tan solid, 0.21 g, 0.22 mmol) in 10 mL of CH_3CN (tan solution) while stirring. A white precipitate formed after overnight stirring, indicating the formation of KCl(s). The reaction was then filtered through a fine sintered glass frit to remove the white precipitate. The volume of the clear, colorless filtrate was reduced under vacuum, treated with diethyl ether until cloudy and then cooled to -20 ^{o}C overnight to precipitate the white microcrystalline solid of $[Fe(NCCH_3)_6][NbF_7]$, which was isolated by filtration through a fine sintered glass filter and dried under nitrogen. Yield: 0.066 g, 14 %. IR (Nujol mull, CsI, cm^{-1}): $\nu_{C\equiv N}$ 2309 (s), 2281 (s), CH_3CN; ν_{Nb-F} 565 (w), $[NbF_7]^-$.

h. $Fe_4Cl_8(THF)_6$ + 4 $K_2[TaF_7]$

A suspension of K_2TaF_7 (white solid, 0.34 g, 0.86 mmol) in 5 mL CH_3CN (clear, colorless solution) was combined with a solution of $Fe_4Cl_8(THF)_6$ (pale tan solid, 0.20 g,

0.21 mmol) in 10 mL of CH_3CN (tan solution) while stirring. A white precipitate formed after overnight stirring, indicating the formation of KCl(s) which was removed by filtration through a fine sintered glass frit. The volume of the clear, colorless filtrate was reduced under vacuum, treated with diethyl ether until cloudy and then cooled to -20 ^oC overnight to precipitate the white microcrystalline solid of $[Fe(NCCH_3)_6][TaF_7]$, which was isolated by filtration through a fine sintered glass filter and dried under nitrogen. Yield: 0.18 g, 35%. IR (Nujol mull, CsI, cm^{-1}): $\nu_{C\equiv N}$ 2309 (s), 2282 (s), CH_3CN; ν_{Ta-F} 589 (s), $[TaF_7]^-$.

iii. Metallacycle syntheses

a. $[Fe_5(bptz)_5(NCCH_3)_{10}][PF_6]_{10}$

The addition of a magenta solution of bptz (0.076 g, 0.32 mmol) in CH_3CN (25 mL) to a colorless solution of $[Fe(CH_3CN)_6][PF_6]_2$ (0.19 g, 0.32 mmol) in CH_3CN (20 mL) under anaerobic conditions induces an immediate color change of the solution to dark blue. After overnight stirring, a blue solid was obtained by filtration after layering the acetonitrile solution over toluene under anaerobic conditions. Yield: 0.13 g, 62%. CV (CH_3CN, vs. Ag/AgCl): $E_{1/2}$(ox): -0.08, 0.05, 0.32, 0.59 V (reversible), -0.51 V (irreversible). ^1H NMR, δ, ppm (CD_3CN): 7.52 (d, 3,3′-H), 8.07 (t, 5,5′-H), 8.34 (d, 4,4′-H), 8.85 (d, 6,6′-H), 1.95 (s, CH_3CN). ESI-FT-ICR-MS: m/z 1046.2 for $[Fe_5(bptz)_5(CH_3CN)_9(PF_6)_9 + 2H^+]^{3+}$.

b. $[Fe_5(bptz)_5(NCCH_3)_{10}][AsF_6]_{10}$

The quantitative transfer of a magenta solution of bptz (0.073 g, 0.31 mmol) in CH_3CN (25 mL) to a colorless solution of $[Fe(CH_3CN)_6][AsF_6]_2$ (0.21 g, 0.31 mmol) in

CH_3CN (10 mL) under anaerobic conditions induces an immediate color change of the solution to dark blue. After overnight stirring, a blue solid was obtained by filtration after layering the acetonitrile solution over toluene under anaerobic conditions. Yield: 0.13 g, 58%.

C. Results and Discussion

i. $[Fe(NCCH_3)_6]^{2+}$ salt syntheses

The synthesis of a wide variety of $[Fe(NCCH_3)_6]^{2+}$ salts of polyatomic metal ions is possible without the use of NO^+ salts (Figure 95). The reactions between alkali metal salts and the cluster $Fe_4Cl_8(THF)_6$ offer a simple and widely applicable means of incorporating any anion available as its alkali metal, silver(I), or thallium(I) salt into the salt of $[Fe(NCCH_3)_6]^{2+}$, that is, assuming the salt is at least slightly soluble in CH_3CN. Considering that only white or off-white powders were obtained that were tentatively identified as the $[Fe(NCCH_3)_6]^{2+}$ salts of the anions in question by IR spectroscopy, there was no apparent contamination of the salts by Fe^{III}, suggesting that this synthesis is a more reliable method for obtaining purely Fe^{II}-containing products. Test reactions of each product with bptz in CH_3CN confirmed the presence of Fe^{II} with immediate color changes to dark blue for each of the reported products, and white product residues on the sintered glass frits immediately turned yellow upon exposure to air, signaling the oxidation to Fe^{III}. Attempts to crystallize the $[Fe(NCCH_3)_6][PF_6]_2$ and $[Fe(NCCH_3)_6][AsF_6]_2$ salts from CH_3CN and Et_2O were successful in producing crystals, however, due to the high air sensitivity of the compound and the incorporation of Et_2O into the crystal, the crystals rapidly oxidized and degraded before XRD data could be

(a)

$$Fe(s) + 2\ NOX \xrightarrow{CH_3CN} [Fe(NCCH_3)_6][X]_2 + 2\ NO(g)$$

$X = [BF_4]^-, [PF_6]^-, [SbF_6]^-$

(b)

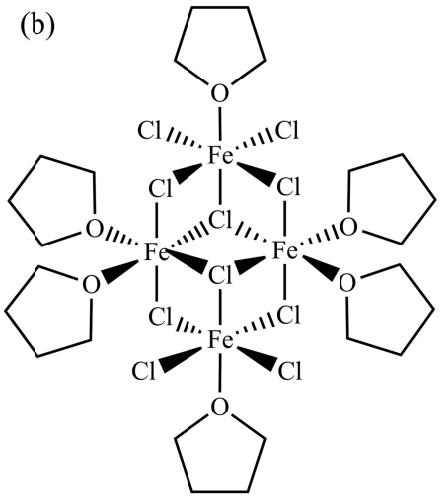

$$+ 8\ NaX \longrightarrow 4\ [Fe(NCCH_3)_6][X]_2 + 8\ NaCl(s)$$

X = Any anion forming a Na^+ salt soluble in CH_3CN

Figure 95. Reaction schemes of the synthesis of $[Fe(NCCH_3)_6]^{2+}$ salts by (a) metal oxidation using nitrosonium salts and (b) reaction between $Fe_4Cl_8(THF)_6$ and sodium salts.

obtained to structurally characterize these complexes. It should be possible to extend this method to Co^{II} and Mn^{II} as the cluster $Co_4Cl_8(THF)_6$ and the coordination polymer $\{[Mn_4Cl_8(THF)_6][Mn(THF)_2Cl_2]\}_\infty$ are known will presumably exhibit similar chemistry to $Fe_4Cl_8(THF)_6$.[121] More pure anhydrous MCl_2 salts such as $NiCl_2$ should also be amenable to this method, assuming they can be dissolved at least to a minimal extent in CH_3CN.

The yields of these reactions vary significantly (ranging from 6 to 86%), however, with further refinement of the synthetic methods the lower yields should be able to be improved. The amount of CH_3CN used in the reaction and the final volume of the reaction solution prior to treatment with diethyl ether both have a significant effect on the yield obtained, as does the initial solubility of the alkali metal salt. Efforts to synthesize the $[Fe(NCCH_3)_6]^{2+}$ salts of the larger anions such as $[((CF_3)_2C_6H_3)_4B]^-$ met with initial difficulty due to the use of solutions that were too dilute for an efficient reaction to take place. Upon increasing the concentrations of the reactants, the reactions proceeded with better yield, although work is still needed to optimize these reactions.

ii. Metallacycle syntheses

The reaction between $[Fe(NCCH_3)_6][PF_6]_2$ and bptz in CH_3CN immediately forms a dark blue solution. Treatment of this solution with toluene produces a dark blue powder that can be redissolved in CH_3CN. When the powder is stored in a dried vial over extended periods of time, however, decomposition occurs, with the appearance of an iridescent sheen on the vial and a rendering of the powder insoluble in CH_3CN. As far as is known, this is the only Fe^{II} metallacycle with bptz that exhibits this decomposition

behavior upon long term storage, suggesting that the metallacycle produced is less stable than the metallacycles with $[SbF_6]^-$. Reaction of $[Fe(NCCH_3)_6][AsF_6]_2$ with bptz in CH_3CN also produces an instantaneous dark blue solution, which yields a dark blue powder upon treatment with toluene. In both cases, crystallization attempts have resulted in the formation of poorly-diffracting crystals that are too small for in-house XRD analysis, and crystals sent to the Advanced Photon Source at Argonne National Laboratories for XRD analysis with synchrotron radiation yielded no useful data due to beam damage.

Reaction of $[Fe(NCCH_3)_6][((CF_3)C_6H_3)_4B]_2$ with bptz in CH_3CN leads to the rapid production of a dark blue solution, as expected. The product is very soluble in CH_3CN and precipitation of the dark blue powder required removal of nearly all of the CH_3CN under vacuum and subsequent treatment with toluene. Attempts to crystallize the product by layering the reaction solution with toluene resulted in no solid material. A ^1H NMR spectrum of the product revealed that the aromatic proton resonances of the $[((CF_3)_2C_6H_3)_4B]^-$ anions obscure the aromatic proton resonances of the bptz ligand. Test reactions between $[Fe(NCCH_3)_6]^{2+}$ salts with $[NbF_7]^{2-}$, $[TaF_7]^{2-}$, $[CHB_{11}Cl_{11}]^-$, $[(C_6H_5)_4B]^-$, and $[CF_3CO_2]^-$ with bptz in CH_3CN all resulted in dark blue solutions indicative of ligand coordination and, in fact, helped to establish the presence of Fe^{II} in these salts.

iii. IR spectral analysis of the $[Fe(NCCH_3)_6]^{2+}$ salts

The starting material for the $[Fe(NCCH_3)_6]^{2+}$ salt syntheses, $Fe_4Cl_8(THF)_6$, exhibits a characteristic terminal $\nu_{Fe\text{-}Cl}$ vibrational mode at 339 cm^{-1}, as well as the

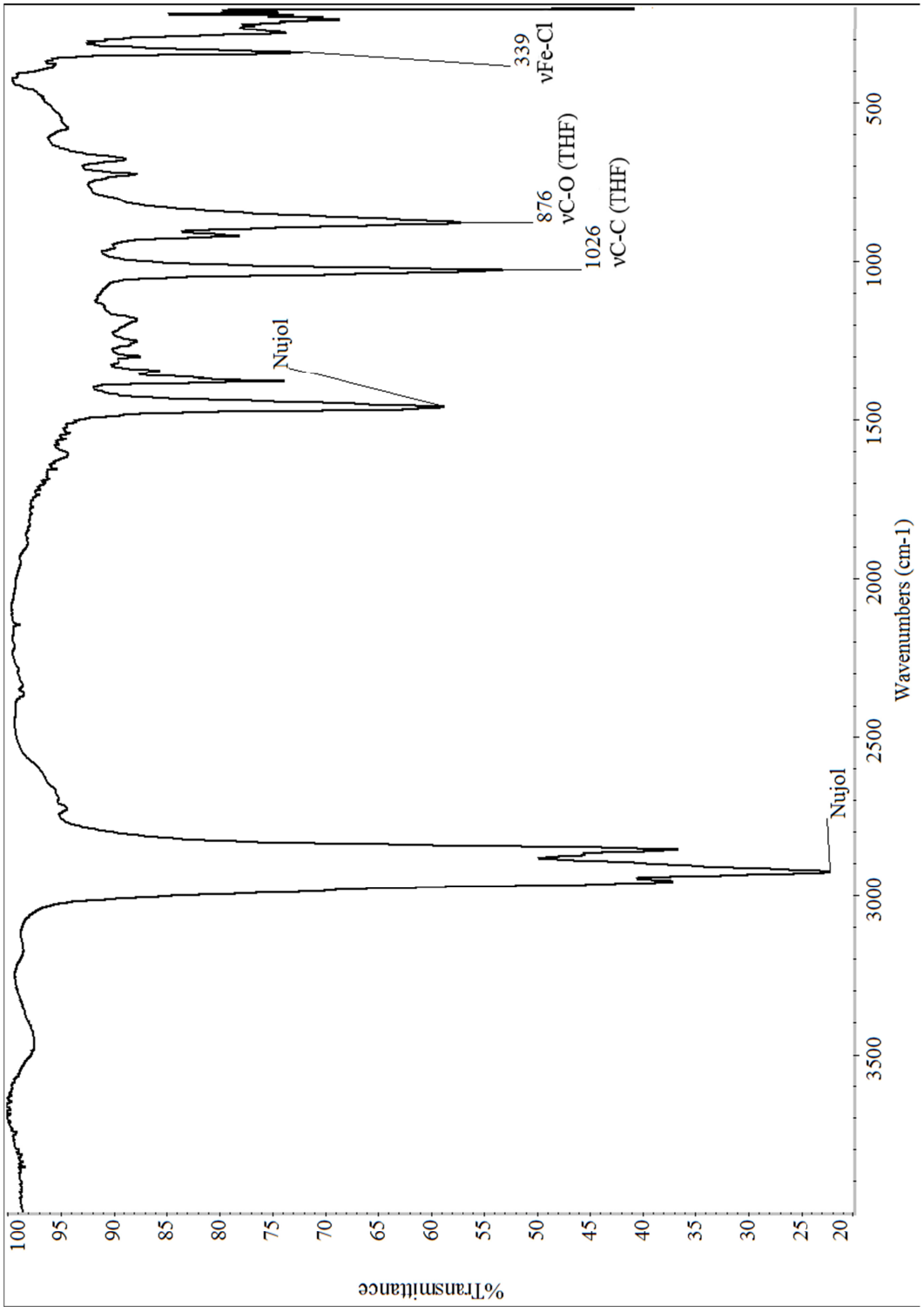

Figure 96. IR spectrum of $Fe_4Cl_8(THF)_6$ (Nujol mull on CsI) with the THF C-C and C-O stretches and terminal Fe-Cl stretch indicated.

characteristic ν_{C-C} and ν_{C-O} vibrational modes for THF at 1026 and 876 cm^{-1}, respectively. These stretches provide a good indicator for the presence of remaining $Fe_4Cl_8(THF)_6$ (or coordinated Cl^- or THF, Figure 96), however trace impurities may still be present. The resulting $[Fe(NCCH_3)_6]^{2+}$ cation exhibits two characteristic $\nu_{C\equiv N}$ modes at ~2290 and 2310 cm^{-1}, which indicate the presence of CH_3CN molecules coordinated to Fe^{II}. Characteristic vibrational modes also signal the presence of the different anions incorporated into the new salts (for example, $[AsF_6]^-$ and $[PF_6]^-$ antisymmetric octahedral ν_{oct1} vibrational modes at 699 and 865 cm^{-1}, respectively, see Figure 97 for the two IR-active vibrational modes in octahedral anions).

The IR spectrum of $[Fe(NCCH_3)_6][AsF_6]_2$ (Figure 98) contains the two characteristic acetonitrile $\nu_{C\equiv N}$ stretching modes at 2322 and 2292 cm^{-1}. The two IR-active vibrational modes, ν_{oct1} and $\nu_{oct2,}$ of $[AsF_6]^-$ are present at 699 and 399 cm^{-1}, respectively (see Figure 97 for vibrational modes). The absence of the vibrational modes for THF and the terminal Fe-Cl stretching mode at 339 cm^{-1} in the final product supports the conclusion that the $Fe_4Cl_8(THF)_4$ cluster has been converted to the $[Fe(NCCH_3)_6][AsF_6]_2$ salt, with no remaining THF molecules or $[Cl]^-$ anions coordinated to the Fe^{II} ion. For all of the reported $[Fe(NCCH_3)_6]^{2+}$ salts, the combination of the characteristic CH_3CN and individual anion vibrational modes and the absence of the THF and Fe-Cl vibrational modes confirm the conversion of $Fe_4Cl_8(THF)_6$ to the $[Fe(NCCH_3)_6]^{2+}$ salts, with no apparent remaining THF molecules or $[Cl]^-$ anions coordinated to the Fe^{II} ion.

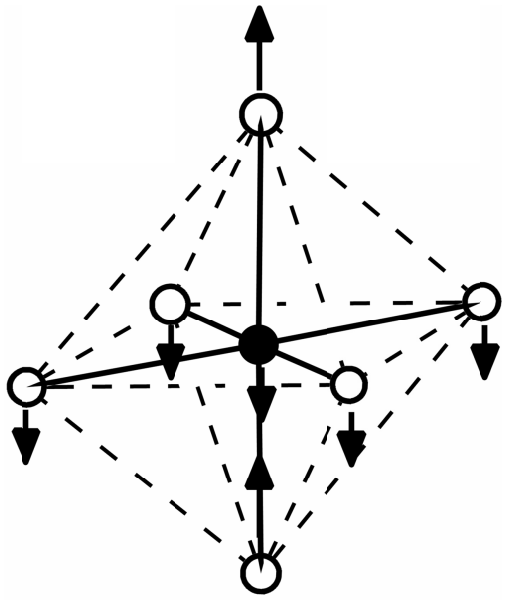

ν_{oct_1}

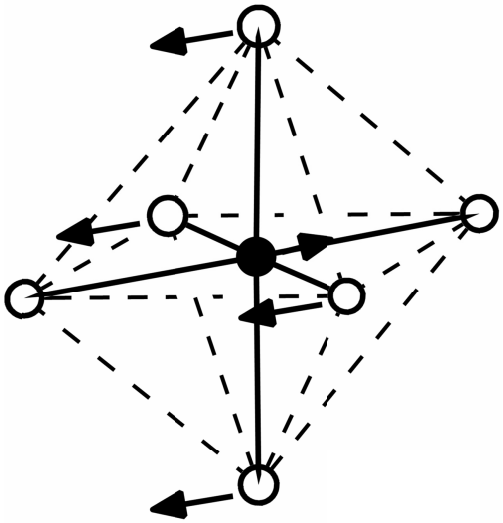

ν_{oct_2}

Figure 97. The two IR-active vibrational modes for the octahedral anions.

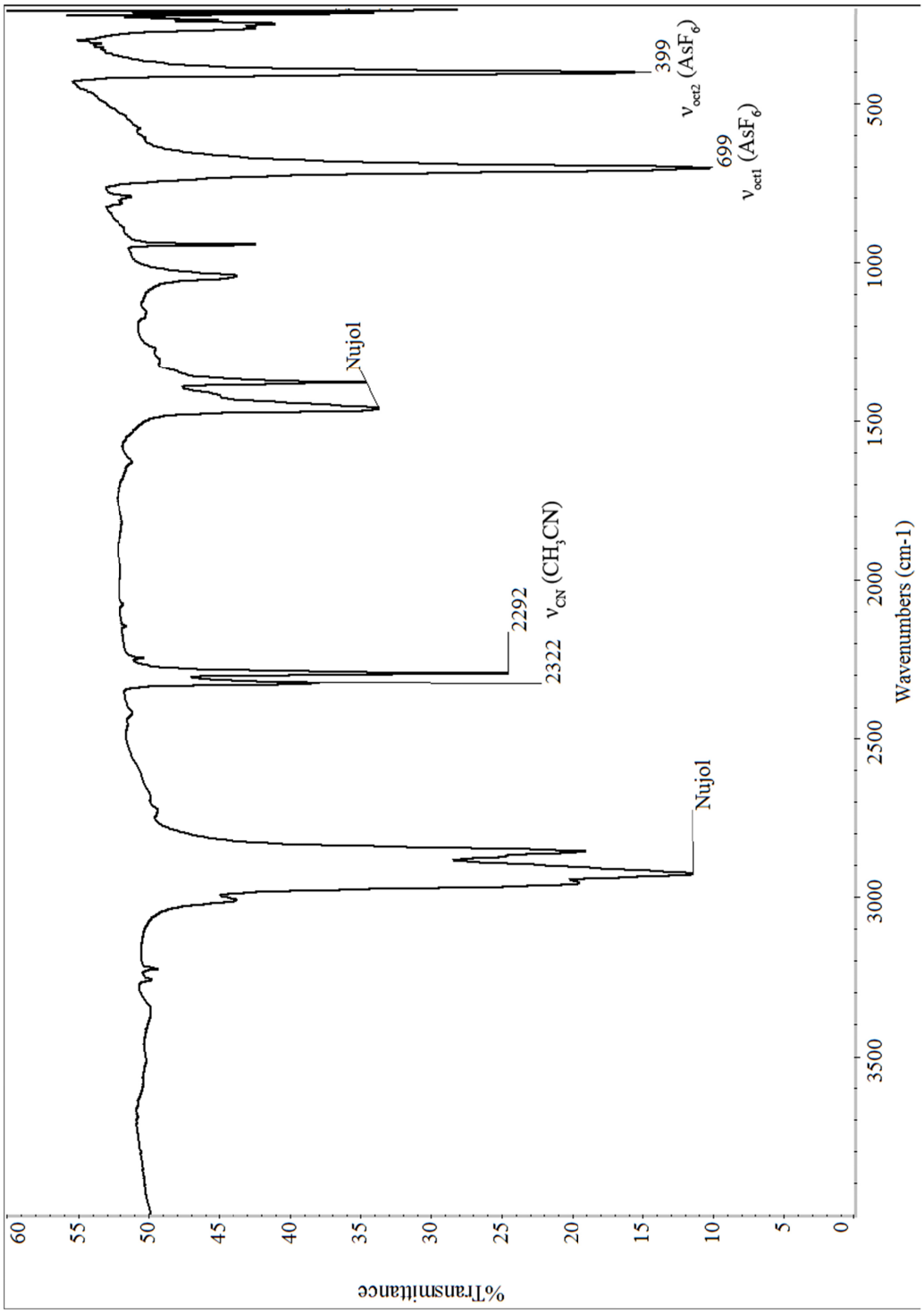

Figure 98. IR spectrum of $[Fe(NCCH_3)_6][AsF_6]_2$ (Nujol mull on CsI) with the CH_3CN and $[AsF_6]^-$ vibrational modes indicated.

iv. Solution evidence for the Fe^{II} pentagon templated by $[PF_6]^-$

Although no crystallographic data could be obtained for $[Fe_5(bptz)_5(NCCH_3)_{10}][PF_6]_{10}$, solution evidence supports the conclusion that the reaction of $[Fe(NCCH_3)_3][PF_6]_2$ with bptz in CH_3CN produces a closed structure that, based on the size of the $[PF_6]^-$ anion and the dimensions of the cavity in the $[Fe_4(bptz)_4(NCCH_3)_6][BF_4]_8$ square metallacycle, is likely pentanuclear. ESI-FT-ICR-MS of a sample of the dark blue powder redissolved in CH_3CN displays a signal atm/z = 1046.2 (3+) that corresponds to $[Fe_5(bptz)_5(CH_3CN)_9(PF_6)_9 + 2H^+]^{3+}$, indicating the loss of one $[PF_6]^-$ anion and one coordinated CH_3CN molecule from a pentanuclear complex of Fe^{II} and bptz (Figure 99).

Electrochemical studies of $[Fe_5(bptz)_{10}(NCCH_3)_{10}][PF_6]_{10}$ reveal that stepwise reversible oxidations of the Fe^{II} centers occur at $E_{1/2}$ values of -0.08, 0.05, 0.32, and 0.59 V vs. Ag/AgCl, behavior similar to the redox properties exhibited by the other known Fe^{II} metallacycles of bptz and bmtz (Figure 100 and Figure 101). The irreversible reduction of bptz at -1.01 V suggests that, as in the cases of other Fe^{II} metallacycles, an increase in the electron density on the ligand is detrimental to the stability of the metallacycle and causes the complex to decompose in solution. The persistence of the metallacycle in solution upon reversible oxidation of the Fe^{II} centers, however, suggests that an increase in the oxidation state of the metal does not lead to destabilization of the compound in solution. Both of these observations are consistent with the concept that these cationic complexes are templated by anion-π interactions as additional electron density on the ligand would destabilize anion-π interactions between the ligand and the

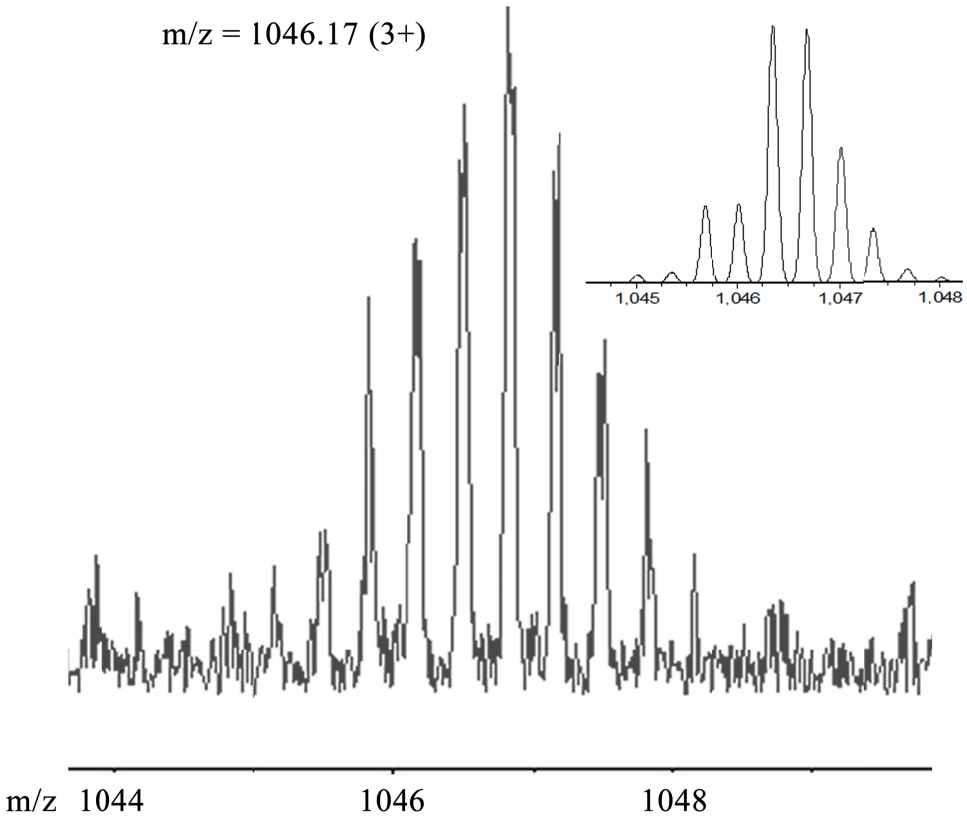

Figure 99. Parent ion signal consistent with $[Fe_5(bptz)_5(CH_3CN)_9(PF_6)_9 + 2H^+]^{3+}$ in CH_3CN at m/z = 1046.2. Theoretical isotopic distribution is shown in the inset.

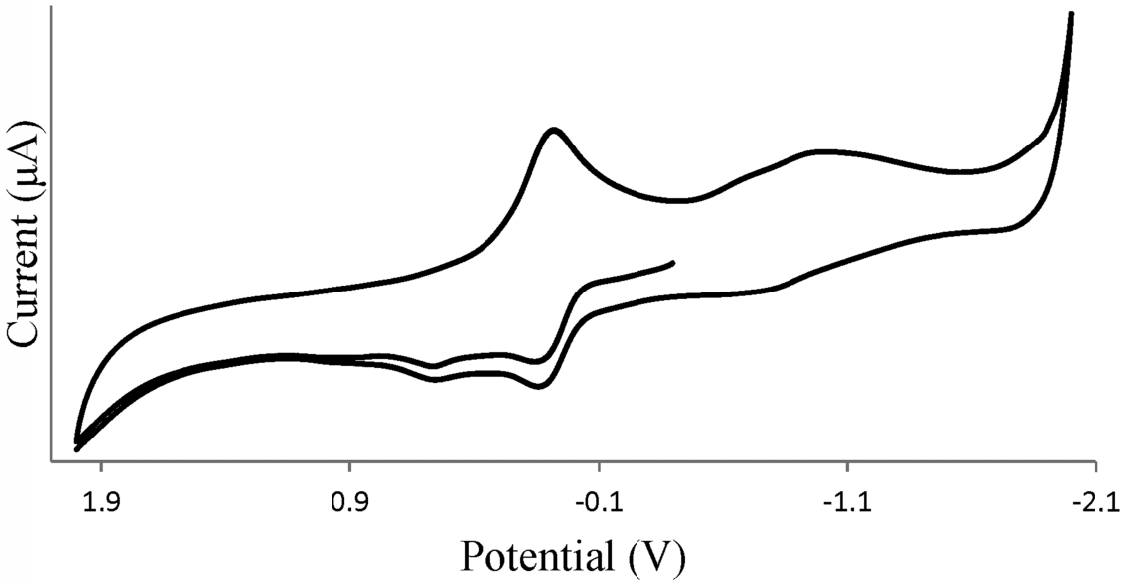

Figure 100. Cyclic voltammogram of $[Fe_5(bptz)_5(NCCH_3)_{10}][PF_6]_{10}$ in CH_3CN with $[^nBu_4N][PF_6]$ as the supporting electrolyte referenced to Ag/AgCl at a scan rate of 0.1 V/s from 2.0 to -2.0 V.

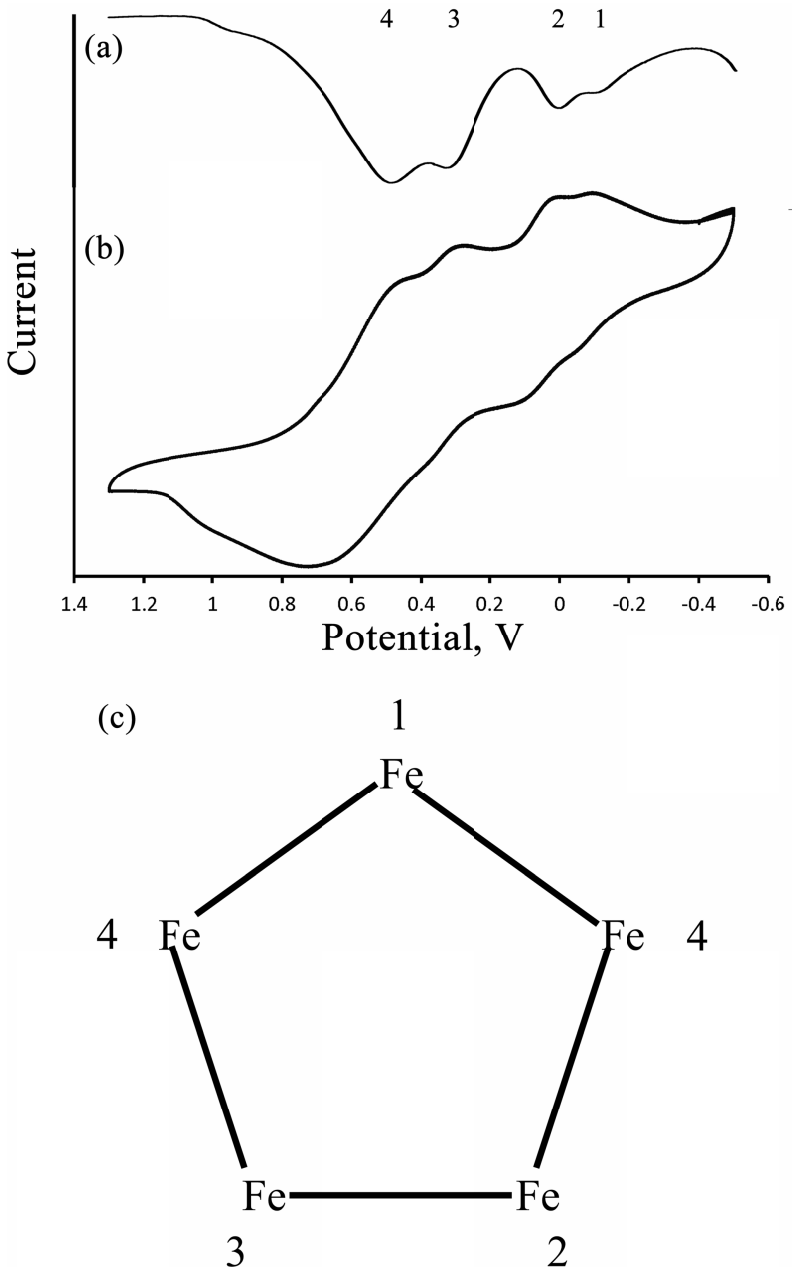

Figure 101. (a) Differential pulse voltammogram and (b) cyclic voltammogram of $[Fe_5(bptz)_5(NCCH_3)_{10}][PF_6]_{10}$ in CH_3CN at a Pt disk electrode with $[^nBu_4N][PF_6]$ as the supporting electrolyte referenced to Ag/AgCl at a scan rate of 0.2 V/s from 1.3 to -0.5 V. (c) A schematic representation of the proposed order of oxidation events, with the numbers corresponding to those shown in (a).

encapsulated anion, whereas additional positive charge on the metal centers would only serve to increase favorable Coulombic interactions with the anion.

^{1}H NMR spectroscopy reveals resonances in the aromatic region consistent with the presence of a pentagonal metallacycle in solution (Figure 102). The aromatic region of the spectrum, however, also contains other bptz resonances that do not match the pentagonal metallacycle or the free ligand. These extra resonances indicate some instability of the metallacycle in solution as they are probably the result of the metallacycle opening up when dissolved in CH_3CN. This solution instability, coupled with the observation of the slow decomposition of the solid upon storage, suggests that the Fe^{II} pentagon with bptz templated by $[PF_6]^-$ is less stable than its counterpart templated by $[SbF_6]^-$. Considering the size difference between $[PF_6]^-$ and $[SbF_6]^-$, $[PF_6]^-$ is a poorer size match for the cavity of the pentagonal metallacycle, however, it is too large to template a square metallacycle. The poorer size match would also lead to longer anion-ligand distances and ostensibly weaker anion-π interactions between bptz and $[PF_6]^-$, but the extent of the lengthening of the anion to ligand distances cannot be determined without structural information provided by single crystal XRD analysis.

D. Conclusions

The work presented in Chapter V constitutes an important first step in analyzing the effect of the anion in the anion-π templation of Fe^{II} metallacycles. The new synthetic protocol for preparing $[Fe(NCCH_3)_6]^{2+}$ salts from $Fe_4Cl_8(THF)_6$ and sodium salts leads to the expected products according to IR spectroscopy with no Fe^{III} contamination. This opens up a wealth of new anions that can be tested to determine how changing the size,

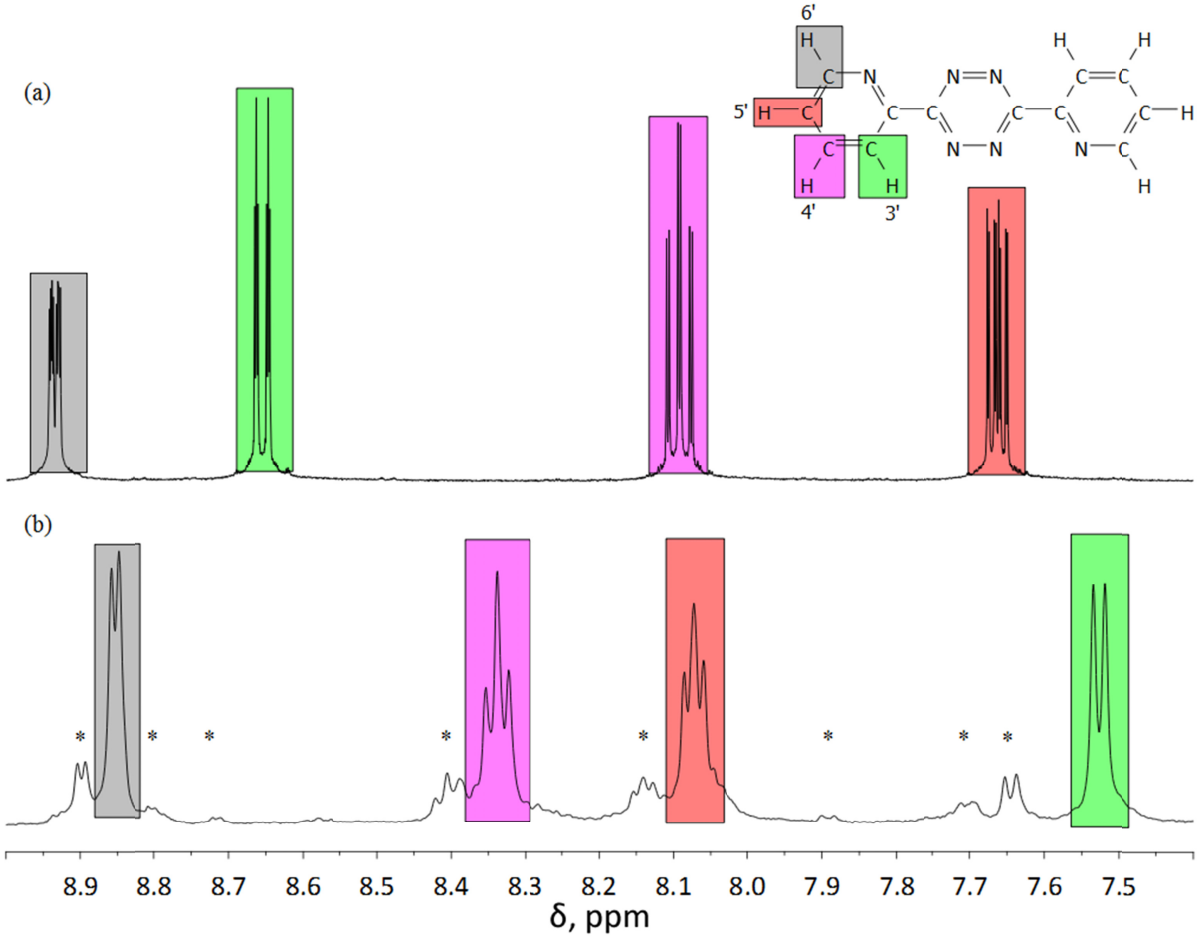

Figure 102. (a) Aromatic region of the ^{1}H NMR spectrum of free bptz and (b) $[Fe_5(bptz)_5(NCCH_3)_{10}][PF_6]_{10}$ in CD_3CN, referenced to CH_3CN impurities in the deuterated solvent. Proton resonances are color coded according to the inset scheme. Resonances marked with an asterisk (*) are ligand resonances that are attributed to an equilibrium with an open form of the metallacycle in solution.

shape, and charge of the anion affects the formation and stability of metallacycles of Fe^{II} with bptz based on the presence of that anion alone. As has been demonstrated, the synthetic route works for anions ranging in size from $[BF_4]^-$ (whose sodium salt is only slightly soluble in CH_3CN) to anions as large as the undecachlorinated carborane $[CHB_{11}Cl_{11}]^-$. Each of the salts synthesized in this manner exhibit reactivity towards bptz in CH_3CN and form the dark blue solutions characteristic of bptz coordinated to Fe^{II}. As the $[SbF_6]^-$ anion is already a close fit for the cavity of the pentagonal metallacycles of Fe^{II}, it is possible that larger metallacycles such as hexagons could be templated with anions that are larger than $[SbF_6]^-$, if they template at all. The new synthesis method provides a facile route that uses a pure Fe^{II} starting material and cleanly forms the $[Fe(NCCH_3)_6]^{2+}$ salts, allowing for the incorporation of new anions during the synthesis of the metallacycles rather than reacting known metallacycles with salts of other anions.

While there is still a need for further optimization, the $Fe_4Cl_8(THF)_6$/sodium salt reaction holds great promise for the generation of pure $[Fe(NCCH_3)_6]^{2+}$ salts with a plethora of anions. These can be used in turn to synthesize a wide variety of new complexes similar, but not necessarily limited to, the Fe^{II} metallacycles with bptz already known to form with $[SbF_6]^-$ and $[BF_4]^-$. The increased flexibility in anion choice afforded by this synthetic method allows for a tailoring of these systems towards those more amenable to specific characterization methods. For example, the replacement of $[SbF_6]^-$ with $[AsF_6]^-$ should simplify the ^{19}F NMR spectrum of the anion, aiding in the study of the anion in solution to determine whether or not the anion persists within the cavity in solution. Incorporation of $[(C_6F_5)_4B]^-$ rather than $[((CF_3)_2C_6H_3)_4B]^-$ would

eliminate the aromatic proton resonances from the anion that obscure the ligand resonances without greatly changing the shape, size, or charge of the anion.

Solution evidence, based on comparisons with known compounds, supports the conclusion that $[PF_6]^-$ templates the formation of a pentagonal metallacycle of Fe^{II} with bptz, even in the absence of structural information. Electrochemical studies, along with MS and ^1H NMR spectral data, indicate the presence of a cyclic, pentanuclear species detectable in solution. ^1H NMR spectroscopy, along with observations of the product over extended periods of time, indicates a lower stability for $[Fe_5(bptz)_5(NCCH_3)_{10}][PF_6]_{10}$ than its $[SbF_6]^-$ counterpart, supporting evidence for the conclusion that the anion is indeed important to the formation and stability of the metallacycles of Fe^{II} and bptz. Structural information, however, is necessary in order to gauge the extent of the anion-to-ligand distances and, by extension, the relative strength of the anion-π interactions operative in the metallacycle. It is clear, however, from the data gathered thus far that the anion does indeed play a significant role in the formation and stability of metallacycles of Fe^{II} and bptz. Coupled with the new synthetic method for $[Fe(NCCH_3)_6]^{2+}$ salts, the ability to correlate basic structural information with solution behavior will provide an avenue for the exploration of a myriad complexes between Fe^{II} and N-heterocyclic ligands such as bptz with varying anions as the templates.

CHAPTER VI

CONCLUSIONS AND FUTURE OUTLOOK

The research discussed in this dissertation lends further support to the conclusion that anion-π interactions exist and are important and useful in the design and synthesis of supramolecular architectures through an exploration of the subtle effects of ligand, anion, and metal ion on the supramolecular architecture of tetrazine-based ligands. Research into anion-π interactions has shifted from attempts to establish the legitimacy of the interaction to gaining an understanding of its nuances *vis-à-vis* the incorporation of anion-π interactions into functional supramolecular systems, notably the transmembrane anion-π slides of Matile and coworkers.[53]

The computations presented in Chapter II highlight the importance of the arene quadrupole moment and the substituent effects on the strength of the resulting anion-π interactions. More importantly, however, the computational work establishes that there is a distinct directionality inherent to the anion-π interaction between polyatomic anions and N-heterocycles. The ability of anion-π interactions to direct the structures of supramolecular architectures has been demonstrated through the work of this group, prior to and in the current dissertation with the square and pentagonal metallacycle work.

The extension of the square and pentagonal metallacycles of bptz to Fe^{II} as discussed in Chapter III has allowed for the study of the interconversion between the two metallacycles *via* ^{1}H NMR spectroscopy for the first time. The ^{1}H NMR spectra revealed differences in the aromatic proton environments of bptz in the square and pentagonal

metallacycles which are characteristic of their respective nuclearities. In addition, rich redox behavior was observed for the square and pentagonal metallacycles of Fe^{II}, namely the reversible sequential oxidation of the individual Fe^{II} centers. This behavior, along with the irreversible ligand reduction, supports the presence of anion-π interactions and the importance of the encapsulated anion in the templation and stability of the metallacycles in solution. The ability to tune the size of the metallacyclic cavity by simply changing the metal ion was also demonstrated, along with its effects on the anion-π interactions within the cavity of the metallacycles, notably the inclusion of two $[SbF_6]^-$ anions in the cavity of $[Fe_5(bptz)_5(NCCH_3)_{10}][SbF_6]_{10}$.

The effect of changing the π-acidity of the chelating ligand (from bptz to bmtz) is demonstrated in the pentagonal metallacycle $[Fe_5(bmtz)_5(NCCH_3)_{10}][SbF_6]_{10}$ presented in Chapter IV. Contrary to expectations, this metallacycle only encapsulated one $[SbF_6]^-$ anion which, due to the increased π-acidity of the central tetrazine of bmtz as compared to bptz, resides in the center of the cavity which maximizes anion-π interactions with the ligand despite the much tighter fit (Figure 103). This demonstrates that anion-π interactions can be strong enough to overcome structural constraints within molecules, assuming a ligand with a high enough π-acidity is used. Work towards incorporating bppz into architectures with Fe^{II} was also presented. Despite the difficulties in ligand synthesis, the incorporation of bppz into complexes with Fe^{II} should continue to be pursued in order to establish whether or not the lower π-acidity of bppz would still allow for anion templation.

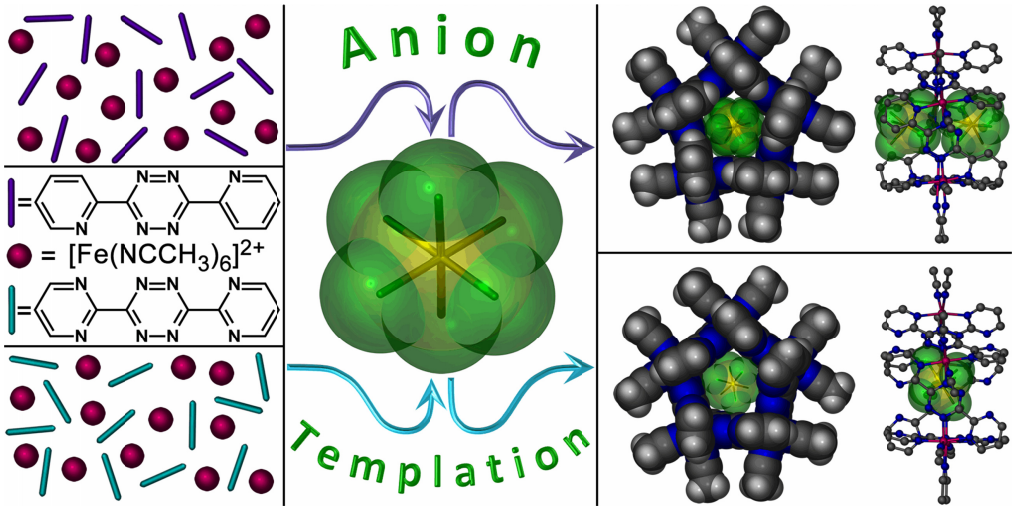

Figure 103. Schematic diagram depicting the templation of pentagonal metallacycles of Fe^{II} with bptz and bmtz templated by the same anion, $[SbF_6]^-$, showing that even a slight change in the electronic properties of the ligand can have a surprising effect on the final structure. Figure reproduced from Dunbar *et al.*[106]

A significant hurdle in the incorporation of different anions into the metallacyclic structures was overcome with the development of a new synthetic protocol for $[Fe(NCCH_3)_6]^{2+}$ salts of a wide range of anions from sodium salts and $Fe_4Cl_8(THF)_6$. Also, the nuclearity of the $[Fe_5(bptz)_5(NCCH_3)_{10}][PF_6]_{10}$ metallacycle was established *via* a combination of mass spectrometry, electrochemistry and ^1H NMR spectroscopy experiments through comparisons with known structures and in the absence of single crystal XRD data. The ^1H NMR spectrum of $[Fe_5(bptz)_5(NCCH_3)_{10}][PF_6]_{10}$, as well as observed decomposition upon storage, demonstrated the lower stability of this metallacycle as a result of the $[PF_6]^-$ ion, which, while too large to template a square metallacycle, is too small to effectively support a pentagonal metallacycle, further demonstrating the importance of the anion towards the stability of the metallacycles.

The work presented herein opens up a wide range of research trajectories, from work incorporating new and more exotic anions (carboranes, tetraphenylborates, and heptafluoroniobate), potentially forming larger metallacycles such as hexagons, to expanding the metallacycles into new and larger supramolecular architectures using chelating ligands to link the polygonal architectures. A possible topology for a "supermolecule" based on the pentagonal metallacycles is that of a large buckyball composed of pentagonal metallacycles linked by 1,2,3,4-tetraminobutane (Figure 104), which can be synthesized from diaminomaleonitrile by successive hydrogenation of the ethene and nitrile functional groups. Although the work presented in this dissertation has increased the number of metallacycles synthesized (Table 17), even more

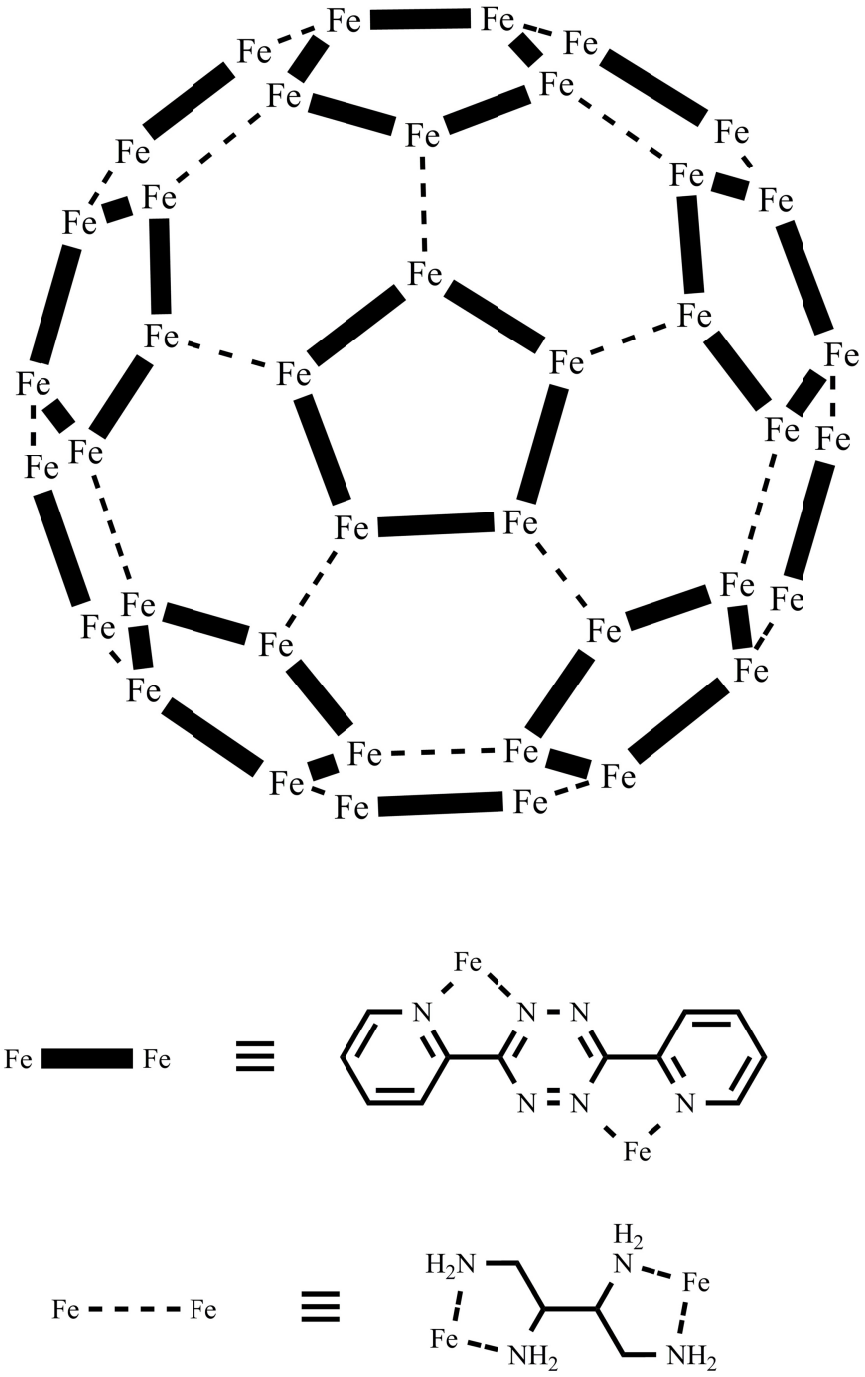

Figure 104. Schematic representation of the hypothetical self-assembled supermolecule reminiscent of C_{60} composed of pentagonal units of $[Fe_5(bptz)_5(NCCH_3)_{10}][SbF_6]_{10}$ interconnected by 1,2,3,4-tetraminobutane *via* chelation to Fe^{II} and displacement of the terminal CH_3CN solvent molecules. Anions should remain encapsulated within the pentagonal metallacycles but are omitted here for the sake of clarity.

Table 17. Table of the metallacycles synthesized to date. Black checkmarks indicate previously synthesized metallacycles. Teal checkmarks indicate metallacycles presented in this dissertation.

	V^{II}	Cr^{II}	Mn^{II}	Fe^{II}	Co^{II}	Ni^{II}	Cu^{II}	Zn^{II}
Bptz Square				✓	✓	✓		✓
Bptz Pentagon				✓		✓		
Bmtz Pentagon				✓				

metal ions can be incorporated by varying the oxidation states and moving into the 4d and 5d transition elements. The remarkable metallacyclic architectures of divalent first-row transition elements expanded upon in this dissertation certainly warrant further research.

It is a time of exciting development in anion-π research as more intricate and elegant experimental studies shed light on the numerous applications of these initially counterintuitive interactions. The literature is replete with reviews on the subject, highlighting the rapid acceptance and progress of research within this burgeoning topic. In the span of a decade since the early computational work of Deyà, Alkorta, and Mascal focused attention on the anion-π interaction, interest in the field has increased dramatically and is sure to continue to do so in years to come.

REFERENCES

1. Lehn, J.-M. *Supramolecular Chemistry*; Wiley-VCH Verlag GmbH & Co. KGaA: New York, 2006.

2. Steed, J. W.; Atwood, J. L. *Supramolecular Chemistry*, 2nd ed.; John Wiley & Sons, Ltd: Chichester, United Kingdom, 2009.

3. Robertazzi, A.; Krull, F.; Knapp, E. W.; Gamez, P. *CrystEngComm* **2011**, *13*, 3293-3300.

4. Ma, J. C.; Dougherty, D. A. *Chem. Rev.* **1997**, *97*, 1303-1324.

5. Post, B.; Schwartz, R. S.; Fankuchen, I. *Acta Crystallographica* **1952**, *5*, 372-374.

6. Kitaĭgorodskiĭ, A. I. *Organic chemical crystallography*; Consultants Bureau: New York, 1961.

7. Sygula, A.; Fronczek, F. R.; Sygula, R.; Rabideau, P. W.; Olmstead, M. M. *J. Am. Chem. Soc.* **2007**, *129*, 3842-3843.

8. Schneider, H. J.; Strongin, R. M. *Acc. Chem. Res.* **2009**, *42*, 1489-1500.

9. Maffei, F.; Betti, P.; Genovese, D.; Montalti, M.; Prodi, L.; De Zorzi, R.; Geremia, S.; Dalcanale, E. *Angew. Chem., Int. Ed.* **2011**, *50*, 4654-4657.

10. *Supramolecular Chemistry of Anions*; Bianchi, A., Bowman-James, K., Garcia-España, E., Eds.; Wiley-VCH Verlag GmbH & Co. KGaA: New York, 1997.

11. Pedersen, C. J. *J. Am. Chem. Soc.* **1967**, *89*, 7017-7036.

12. Park, C. H.; Simmons, H. E. *J. Am. Chem. Soc.* **1968**, *90*, 2431-2432.

13. Schneider, H.-J.; Werner, F.; Blatter, T. *J. Phys. Org. Chem.* **1993**, *6*, 590-594.

14. Hiraoka, K.; Mizuse, S.; Yamabe, S. *J. Phys. Chem.* **1987**, *91*, 5294-5297.

15. Alkorta, I.; Rozas, I.; Elguero, J. *J. Am. Chem. Soc.* **2002**, *124*, 8593-8598.

16. Mascal, M.; Armstrong, A.; Bartberger, M. D. *J. Am. Chem. Soc.* **2002**, *124*, 6274-6276.

17. Quiñonero, D.; Garau, C.; Rotger, C.; Frontera, A.; Ballester, P.; Costa, A.; Deyà, P. M. *Angew. Chem., Int. Ed.* **2002**, *41*, 3389-3392.

18. Schottel, B. L.; Chifotides, H. T.; Dunbar, K. R. *Chem. Soc. Rev.* **2008**, *37*, 68-83.

19. Garau, C.; Quiñonero, D.; Frontera, A.; Ballester, P.; Costa, A.; Deyà, P. M. *New J. Chem.* **2003**, *27*, 211-214.

20. Wheeler, S. E.; Houk, K. N. *J. Phys. Chem. A* **2010**, *114*, 8658-8664.

21. Raju, R. K.; Bloom, J. W. G.; An, Y.; Wheeler, S. E. *ChemPhysChem* **2011**, *12*, 3116-3130.

22. Garau, C.; Quiñonero, D.; Frontera, A.; Ballester, P.; Costa, A.; Deyà, P. M. *J. Phys. Chem. A* **2005**, *109*, 9341-9345.

23. Quiñonero, D.; Frontera, A.; Garau, C.; Ballester, P.; Costa, A.; Deyà, P. M. *ChemPhysChem* **2006**, *7*, 2487-2491.

24. Kim, D.; Lee, E. C.; Kim, K. S.; Tarakeshwar, P. *J. Phys. Chem. A* **2007**, *111*, 7980-7986.

25. Xu, Z.; Singh, N. J.; Kim, S. K.; Spring, D. R.; Kim, K. S.; Yoon, J. *Chem.--Eur. J.* **2011**, *17*, 1163-1170.

26. Frontera, A.; Quiñonero, D.; Costa, A.; Ballester, P.; Deyà, P. M. *New J. Chem.* **2007**, *31*, 556-560.

27. Clements, A.; Lewis, M. *J. Phys. Chem. A* **2006**, *110*, 12705-12710.

28. Garau, C.; Quiñonero, D.; Frontera, A.; Escudero, D.; Ballester, P.; Costa, A.; Deyà, P. M. *Chem. Phys. Lett.* **2007**, *438*, 104-108.

29. Garau, C.; Quiñonero, D.; Frontera, A.; Costa, A.; Ballester, P.; Deyà, P. M. *Chem. Phys. Lett.* **2003**, *370*, 7-13.

30. Garau, C.; Frontera, A.; Quiñonero, D.; Ballester, P.; Costa, A.; Deyà, P. M. *Recent Research Developments in Chemical Physics*; Pandalai, S. G., Ed.; Transworld Research Network: Kerala, India, 2004.

31. Dawson, R. E.; Hennig, A.; Weimann, D. P.; Emery, D.; Ravikumar, V.; Montenegro, J.; Takeuchi, T.; Gabutti, S.; Mayor, M.; Mareda, J.; Schalley, C. A.; Matile, S. *Nature Chem.* **2010**, *2*, 533-538.

32. Matile, S.; Jentzsch, A. V.; Montenegro, J.; Fin, A. *Chem. Soc. Rev.* **2011**, *40*, 2453-2474.

33. Hay, B. P.; Custelcean, R. *Cryst. Growth Des.* **2009**, *9*, 2539-2545.

34. Gamez, P.; Mooibroek, T. J.; Teat, S. J.; Reedijk, J. *Acc. Chem. Res.* **2007**, *40*, 435-444.

35. Johnson, D. W.; Berryman, O. B. *Chem. Commun.* **2009**, 3143-3153.

36. Frontera, A.; Gamez, P.; Mascal, M.; Mooibroek, T. J.; Reedijk, J. *Angew. Chem., Int. Ed.* **2011**, *50*, 9564-9583.

37. Rosokha, Y. S.; Lindeman, S. V.; Rosokha, S. V.; Kochi, J. K. *Angew. Chem., Int. Ed.* **2004**, *43*, 4650-4652.

38. Han, B.; Lu, J. J.; Kochi, J. K. *Cryst. Growth Des.* **2008**, *8*, 1327-1334.

39. Berryman, O. B.; Hof, F.; Hynes, M. J.; Johnson, D. W. *Chem. Commun.* **2006**, 506-508.

40. de Hoog, P.; Gamez, P.; Mutikainen, H.; Turpeinen, U.; Reedijk, J. *Angew Chem Int Edit* **2004**, *43*, 5815-5817.

41. Casellas, H.; Massera, C.; Gamez, P.; Lanfredi, A. M. M.; Reedijk, J. *Eur. J. Inorg. Chem.* **2005**, 2902-2908.

42. Gamez, P.; van Albada, G. A.; Mutikainen, I.; Turpeinen, U.; Reedijk, J. *Inorg. Chim. Acta* **2005**, *358*, 1975-1980.

43. Casellas, H.; Massera, C.; Buda, F.; Gamez, P.; Reedijk, J. *New J. Chem.* **2006**, *30*, 1561-1566.

44. Gamez, P.; Reedijk, J. *Eur. J. Inorg. Chem.* **2006**, 29-42.

45. Maheswari, P. U.; Modec, B.; Pevec, A.; Kozlevčar, B.; Massera, C.; Gamez, P.; Reedijk, J. *Inorg. Chem.* **2006**, *45*, 6637-6645.

46. Casellas, H.; Roubeau, O.; Teat, S. J.; Masciocchi, N.; Galli, S.; Sironi, A.; Gamez, P.; Reedijk, J. *Inorg. Chem.* **2007**, *46*, 4583-4591.

47. de Hoog, P.; Robertazzi, A.; Mutikainen, I.; Turpeinen, U.; Gamez, P.; Reedijk, J. *Eur. J. Inorg. Chem.* **2009**, 2684-2690.

48. Costa, J. S.; Castro, A. G.; Pievo, R.; Roubeau, O.; Modec, B.; Kozlevčar, B.; Teat, S. J.; Gamez, P.; Reedijk, J. *CrystEngComm* **2010**, *12*, 3057-3064.

49. Quiñonero, D.; Garau, C.; Frontera, A.; Ballester, P.; Costa, A.; Deyà, P. M. *Chem. Phys. Lett.* **2002**, *359*, 486-492.

50. Frontera, A.; Saczewski, F.; Gdaniec, M.; Dziemidowicz-Borys, E.; Kurland, A.; Deyà, P. M.; Quiñonero, D.; Garau, C. *Chem.--Eur. J.* **2005**, *11*, 6560-6567.

51. Garau, C.; Frontera, A.; Ballester, P.; Quiñonero, D.; Costa, A.; Deyà, P. M. *Eur. J. Org. Chem.* **2005**, 179-183.

52. García-Raso, A.; Albertí, F. M.; Fiol, J. J.; Tasada, A.; Barceló-Oliver, M.; Molins, E.; Estarellas, C.; Frontera, A.; Quiñonero, D.; Deyà, P. M. *Cryst. Growth Des.* **2009**, *9*, 2363-2376.

53. Mareda, J.; Matile, S. *Chem.--Eur. J.* **2009**, *15*, 28-37.

54. Perez-Velasco, A.; Gorteau, V.; Matile, S. *Angew. Chem., Int. Ed.* **2008**, *47*, 921-923.

55. Gorteau, V.; Bollot, G.; Mareda, J.; Perez-Velasco, A.; Matile, S. *J. Am. Chem. Soc.* **2006**, *128*, 14788-14789.

56. Gorteau, V.; Bollot, G.; Mareda, J.; Matile, S. *Org. Biomol. Chem.* **2007**, *5*, 3000-3012.

57. Míšek, J.; Jentzsch, A. V.; Sakurai, S. I.; Emery, D.; Mareda, J.; Matile, S. *Angew. Chem., Int. Ed.* **2010**, *49*, 7680-7683.

58. Sakai, N.; Mareda, J.; Vauthey, E.; Matile, S. *Chem. Commun.* **2010**, *46*, 4225-4237.

59. Bhosale, R.; Bhosale, S.; Bollot, G.; Gorteau, V.; Julliard, M. D.; Litvinchuk, S.; Mareda, J.; Matile, S.; Miyatake, T.; Mora, F.; Perez-Velasco, A.; Sakai, N.; Sisson, A. L.; Tanaka, H.; Tran, D. H. *Bull. Chem. Soc. Jpn.* **2007**, *80*, 1044-1057.

60. Chakrabarty, R.; Mukherjee, P. S.; Stang, P. J. *Chem. Rev.* **2011**, *111*, 6810-6918.

61. Fujita, M.; Yazaki, J.; Ogura, K. *J. Am. Chem. Soc.* **1990**, *112*, 5645-5647.

62. Fujita, M.; Yazaki, J.; Ogura, K. *Chem. Lett.* **1991**, *20*, 1031-1032.

63. Stang, P. J.; Cao, D. H. *J. Am. Chem. Soc.* **1994**, *116*, 4981-4982.

64. Caulder, D. L.; Raymond, K. N. *Acc. Chem. Res.* **1999**, *32*, 975-982.

65. Fujita, M.; Tominaga, M.; Hori, A.; Therrien, B. *Acc. Chem. Res.* **2005**, *38*, 369-378.

66. Oliveri, C. G.; Ulmann, P. A.; Wiester, M. J.; Mirkin, C. A. *Acc. Chem. Res.* **2008**, *41*, 1618-1629.

67. Cotton, F. A.; Lin, C.; Murillo, C. A. *Acc. Chem. Res.* **2001**, *34*, 759-771.

68. Zhao, L.; Ghosh, K.; Zheng, Y.; Lyndon, M. M.; Williams, T. I.; Stang, P. J. *Inorg. Chem.* **2009**, *48*, 5590-5592.

69. Campos-Fernández, C. S.; Clérac, R.; Koomen, J. M.; Russell, D. H.; Dunbar, K. R. *J. Am. Chem. Soc.* **2001**, *123*, 773-774.

70. Campos-Fernández, C. S.; Schottel, B. L.; Chifotides, H. T.; Bera, J. K.; Bacsa, J.; Koomen, J. M.; Russell, D. H.; Dunbar, K. R. *J. Am. Chem. Soc.* **2005**, *127*, 12909-12923.

71. Hasenknopf, B.; Lehn, J. M.; Kneisel, B. O.; Baum, G.; Fenske, D. *Angew. Chem., Int. Ed.* **1996**, *35*, 1838-1840.

72. Satake, A.; Tanaka, H.; Hajjaj, F.; Kawai, T.; Kobuke, Y. *Chem. Commun.* **2006**, 2542-2544.

73. Vilar, R. *Angew. Chem., Int. Ed.* **2003**, *42*, 1460-1477.

74. Vilar, R. *Struct. Bonding* **2008**, *129*, 175-206.

75. Vickers, M. S.; Beer, P. D. *Chem. Soc. Rev.* **2007**, *36*, 211-225.

76. Campos-Fernández, C. S.; Clérac, R.; Dunbar, K. R. *Angew. Chem., Int. Ed.* **1999**, *38*, 3477-3479.

77. Lehn, J. M. *Chem. Soc. Rev.* **2007**, *36*, 151-160.

78. Escudero, D.; Frontera, A.; Quiñonero, D.; Costa, A.; Ballester, P.; Deyà, P. M. *J. Chem. Theory Comput.* **2007**, *3*, 2098-2107.

79. Schottel, B. L.; Chifotides, H. T.; Shatruk, M.; Chouai, A.; Perez, L. M.; Bacsa, J.; Dunbar, K. R. *J. Am. Chem. Soc.* **2006**, *128*, 5895-5912.

80. Chifotides, H. T.; Schottel, B. L.; Dunbar, K. R. *Angew. Chem., Int. Ed.* **2010**, *49*, 7202-7207.

81. Schottel, B. L. The influence of anion-π interactions between multi-atomic anions and π-acidic ring systems on the self-assembly of coordination

compounds. Ph.D. Dissertation, Texas A&M University, College Station, TX, 2007.

82. Gaussian 09, Revision B.01, Frisch, M. J.; Trucks, G. W.; Schlegel, H. B.; Scuseria, G. E.; Robb, M. A.; Cheeseman, J. R.; Scalmani, G.; Barone, V.; Mennucci, B.; Petersson, G. A.; Nakatsuji, H.; Caricato, M.; Li, X.; Hratchian, H. P.; Izmaylov, A. F.; Bloino, J.; Zheng, G.; Sonnenberg, J. L.; Hada, M.; Ehara, M.; Toyota, K.; Fukuda, R.; Hasegawa, J.; Ishida, M.; Nakajima, T.; Honda, Y.; Kitao, O.; Nakai, H.; Vreven, T.; Montgomery, J., J. A.; Peralta, J. E.; Ogliaro, F.; Bearpark, M.; Heyd, J. J.; Brothers, E.; Kudin, K. N.; Staroverov, V. N.; Kobayashi, R.; Normand, J.; Raghavachari, K.; Rendell, A.; Burant, J. C.; Iyengar, S. S.; Tomasi, J.; Cossi, M.; Rega, N.; Millam, N. J.; Klene, M.; Knox, J. E.; Cross, J. B.; Bakken, V.; Adamo, C.; Jaramillo, J.; Gomperts, R.; Stratmann, R. E.; Yazyev, O.; Austin, A. J.; Cammi, R.; Pomelli, C.; Ochterski, J. W.; Martin, R. L.; Morokuma, K.; Zakrzewski, V. G.; Voth, G. A.; Salvador, P.; Dannenberg, J. J.; Dapprich, S.; Daniels, A. D.; Farkas, Ö.; Foresman, J. B.; Ortiz, J. V.; Cioslowski, J.; Fox, D. J. Gaussian Inc., Wallingford CT, 2010.

83. Becke, A. D. *J. Chem. Phys.* **1993**, *98*, 5648-5652.

84. Lee, C. T.; Yang, W. T.; Parr, R. G. *Physical Review B* **1988**, *37*, 785-789.

85. Krishnan, R.; Binkley, J. S.; Seeger, R.; Pople, J. A. *J. Chem. Phys.* **1980**, *72*, 650-654.

86. Mclean, A. D.; Chandler, G. S. *J. Chem. Phys.* **1980**, *72*, 5639-5648.

87. Agui 9.2.1, Dennington, R. D., II; Keith, T. A.; Millam, J. M. Semichem, Inc., Shawnee Mission KS, 2008.

88. Check, C. E.; Faust, T. O.; Bailey, J. M.; Wright, B. J.; Gilbert, T. M.; Sunderlin, L. S. *J. Phys. Chem. A* **2001**, *105*, 8111-8116.

89. Hay, P. J.; Wadt, W. R. *J. Chem. Phys.* **1985**, *82*, 270-283.

90. Hay, P. J.; Wadt, W. R. *J. Chem. Phys.* **1985**, *82*, 299-310.

91. Wadt, W. R.; Hay, P. J. *J. Chem. Phys.* **1985**, *82*, 284-298.

92. Bu, X. H.; Morishita, H.; Tanaka, K.; Biradha, K.; Furusho, S.; Shionoya, M. *Chem. Commun.* **2000**, 971-972.

93. Campos-Fernández, C. S. Clusters and extended arrays with metal ions and nitrogen donor ligands. Ph.D. Dissertation, Michigan State University, East Lansing, MI, 2001.

94. Heintz, R. A.; Smith, J. A.; Szalay, P. S.; Weisgerber, A.; Dunbar, K. R. *Inorg. Synth.* **2002**, *33*, 75-83.

95. Geldard, J. F.; Lions, F. *J. Org. Chem.* **1965**, *30*, 318-319.

96. APEX2 v2011.6-1, Bruker AXS, Madison, WI, 2011.

97. Blessing, R. *Acta Crystallogr., Sect. A* **1995**, *51*, 33-38.

98. Siemens Area Detector Absorption Correction, Sheldrick, G. University of Gottingen, Germany, 1997.

99. Sheldrick, G. M. *Acta Crystallogr., Sect. A* **2008**, *64*, 112-122.

100. Barbour, L. J. *J. Supramol. Chem.* **2001**, *1*, 189-191.

101. Hubschle, C. B.; Sheldrick, G. M.; Dittrich, B. *J. Appl. Crystallogr.* **2011**, *44*, 1281-1284.

102. Spek, A. *Acta Crystallogr., Sect. D* **2009**, *65*, 148-155.

103. van der Sluis, P.; Spek, A. L. *Acta Crystallogr., Sect. A* **1990**, *46*, 194-201.

104. Lehn, J. M.; Funeriu, D. P.; Fromm, K. M.; Fenske, D. *Chem.--Eur. J.* **2000**, *6*, 2103-2111.

105. Funeriu, D. P.; Lehn, J. M.; Baum, G.; Fenske, D. *Chem-Eur J* **1997**, *3*, 99-104.

106. Giles, I. D.; Chifotides, H. T.; Shatruk, M.; Dunbar, K. R. *Chem. Commun.* **2011**, *47*, 12604-12606.

107. Ruben, M.; Breuning, E.; Lehn, J. M.; Ksenofontov, V.; Renz, F.; Gutlich, P.; Vaughan, G. B. M. *Chem-Eur J* **2003**, *9*, 4422-4429.

108. Ruben, M.; Breuning, E.; Lehn, J. M.; Ksenofontov, V.; Gutlich, P.; Vaughan, G. *J. Magn. Magn. Mater.* **2004**, *272*, E715-E717.

109. Schottel, B. L.; Bacsa, J.; Dunbar, K. R. *Chem. Commun.* **2005**, 46-47.

110. Zhao, L.; Ghosh, K.; Zheng, Y. R.; Stang, P. J. *J. Org. Chem.* **2009**, *74*, 8516-8521.

111. Funck, E. S. Investigation of anion-pi interactions in inorganic, organic and biological systems. M.S. Thesis, Texas A&M University, College Station, TX, 2011.

112. Kaim, W.; Kohlmann, S. *Inorg. Chem.* **1987**, *26*, 68-77.

113. Kaim, W.; Fees, J. *Z. Naturforsch., B: Chem. Sci.* **1995**, *50*, 123-127.

114. Clemo, G. R.; Holmes, T.; Leitch, G. C. *J. Chem. Soc.* **1938**, 753-755.

115. Neels, A.; Stoeckli-Evans, H. *Chimia* **1993**, *47*, 198-202.

116. Case, F. H.; Koft, E. *J. Am. Chem. Soc.* **1959**, *81*, 905-906.

117. Armand, J.; Chekir, K.; Pinson, J. *Can. J. Chem.* **1974**, *52*, 3971-3980.

118. Woods, T. J. Texas A&M University, College Station, TX. Unpublished work, 2011

119. Szalay, P. S.; Galan-Mascaros, J. R.; Schottel, B. L.; Bacsa, J.; Perez, L. M.; Ichimura, A. S.; Chouai, A.; Dunbar, K. R. *J. Cluster Sci.* **2004**, *15*, 503-530.

120. Cotton, F. A.; Luck, R. L.; Son, K. A. *Inorg. Chim. Acta* **1991**, *179*, 11-15.

121. Zhao, H.; Clerac, R.; Sun, J. S.; Ouyang, X.; Clemente-Juan, J. M.; Gomez-Garcia, C. J.; Coronado, E.; Dunbar, K. R. *J. Solid State Chem.* **2001**, *159*, 281-292.

VITA

IAN DEREK GILES
Department of Chemistry
Texas A&M University
P.O. Box 30012
College Station, TX 77842-3012

EDUCATION

Texas A&M University, College Station, TX
Ph. D., Chemistry. 05/2012
Dissertation: Experimental and Theoretical Investigations of Anion-pi Interactions in Metallacyclic Architectures of First-Row Transition Metals with N-Heteroaromatic Ligands.
Advisor: Prof. Kim R. Dunbar

Austin College, Sherman, Texas
B. A., Chemistry and French, with Honors in Chemistry 05/2005

RESEARCH EXPERIENCE

Graduate Research, **Texas A&M University**, College Station, TX 08/2005-05/2012
NSF-REU Fellow, **University of Utah**, Salt Lake City, UT 06-08/2004
NSF-REU Fellow, **University of Rochester**, Rochester, NY 06-08/2003
Undergraduate Research, **Austin College**, Sherman, TX 01/2003-05/2005

OTHER EXPERIENCE

Instructional Assistant, **Texas A&M University**
Teaching Assistant, **Texas A&M University**

AWARDS AND DISTINCTIONS

Frederick Bradley Armendt Fellowship in Chemistry, Austin College
Excellence in General Chemistry Teaching, Texas A&M University
Martell Travel Award recipient
Phi Lambda Upsilon Travel Award recipient

PROFESSIONAL AFFILIATIONS AND ACTIVITIES

Member, American Chemical Society, Division of Inorganic Chemistry
Phi Beta Kappa, Iota of Texas Chapter National Honor Society
Phi Lambda Upsilon, Beta Beta Chapter National Chemistry Honor Society
Alpha Chi National Honor Society
Chemistry Open House, Texas A&M University